

**Numerical Modelling and Prediction of Cavitation Erosion Using Euler-Euler and  
Multi-Scale Euler-Lagrange Methods**

Von der Fakultät für Ingenieurwissenschaften, Abteilung Maschinenbau  
und Verfahrenstechnik

der

Universität Duisburg-Essen

zur Erlangung des akademischen Grades

eines

Doktors der Ingenieurwissenschaften

Dr.-Ing.

genehmigte Dissertation

von

Andreas Peters

aus

Duisburg

Gutachter: Univ.-Prof. Dr.-Ing. Bettar Ould el Moctar  
Prof. Dr.-Ing. Milovan Perić

Tag der mündlichen Prüfung: 24.10.2019



## **Abstract**

This thesis presents numerical predictions of cavitation-induced erosion, for hydrodynamic flows, using Euler-Euler and multi-scale Euler-Lagrange methods. Improved approaches to numerically predict hydrodynamic cavitation-induced erosion are developed and applied to internal and external flows that involve stationary and rotating components. Comparisons of numerically predicted erosion with experimentally obtained erosion patterns and qualitative experimental erosion predictions demonstrate the accuracy of the numerical methods. First, an efficient Euler-Euler approach predicts areas exposed to erosion based on information of pressure and vapour content in the flow. Second, a multi-scale Euler-Lagrange method uses calculated collapses of spherical Lagrangian bubbles to identify locations and time instances of cavitation bubble collapses and, thereby, predict erosion impacts. The multi-scale approach enables to correlate calculated bubble collapses with erosion pitting rates from measurements. The developed methods give more accurate predictions of cavitation-induced erosion beyond the state of the art.

## **Zusammenfassung**

Die vorliegende Arbeit präsentiert numerische Vorhersagen kavitationsbedingter Erosion für hydrodynamische Strömungen, basierend auf Euler-Euler- und Multiskalen-Euler-Lagrange-Methoden. Verbesserte Verfahren zur numerischen Vorhersage von hydrodynamischer, kavitationsbedingter Erosion werden entwickelt und auf interne und externe Strömungen angewandt, welche stationäre und rotierende Komponenten beinhalten. Vergleiche mit experimentell bestimmten Erosionsmustern und qualitativen, experimentellen Vorhersagen ermöglichen eine Beurteilung der Genauigkeit der numerischen Erosionsvorhersage. Zunächst wird eine effiziente Methode zur Vorhersage von Kavitationserosion basierend auf einem Euler-Euler-Verfahren vorgestellt. Das Verfahren verwendet Informationen aus der Strömungslösung zur Identifizierung von erosionsgefährdeten Bereichen. Daraufhin wird ein Multiskalen-Euler-Lagrange-Verfahren präsentiert, welches berechnete Kollapse sphärischer Lagrange'scher Einzelblasen verwendet, um die Zeitpunkte und Positionen von Blaskollapsen und somit von Erosionseinschlägen zu bestimmen. Dieser Multiskalen-Ansatz ermöglicht die Korrelation der Blaskollapsen mit Erosionsmustern aus experimentellen Messungen. Die entwickelten Verfahren liefern genauere Vorhersagen kavitationsbedingter Erosion, über den derzeitigen Stand der Forschung hinaus.

## Acknowledgements

I want to thank Professor Bettar Ould el Moctar for his supervision associated with all work related to this thesis. I am grateful for his guidance and critical comments that improved this work. Further acknowledgements are referred to Professor Milovan Perić for his interest in and review of this thesis. I acknowledge the funding of research work associated with this thesis from the German Research Foundation (Deutsche Forschungsgemeinschaft, DFG) and the Federal Ministry for Economic Affairs and Energy (Bundesministerium für Wirtschaft und Energie, BMWi). Many thanks go out to all colleagues at the institute, especially the cavitation group. In particular, I want to thank Udo Lantermann for his guidance, many fruitful discussions, and his critical comments that this thesis has largely benefitted from. Sincere thanks are given to Fabian Reuter and Leonie Walter for long discussions and their critical opinions from different points of view. Besides, Thomas Schellin is thanked for critically reviewing research work associated with this thesis. Furthermore, I want to thank my colleague and friend Lahbib Zentari as well as my cousin Stephanie for taking their time to review this thesis. Thanks go out also to my colleague and friend Wenjing Lyu for many discussions concerning numerics. Besides I want to thank all other colleagues with whom I had many fruitful discussions and always an enjoyable time at the institute. Most importantly, I am grateful for the support my parents gave me during the last years, related to this work and beyond, as well as the support that I received from my girlfriend Viktoria.

## Declaration

Part of the work described in this thesis has previously been published in the following references of the author:

Peters, A., Sagar, H., Lantermann, U., and el Moctar, O. Numerical Modelling and Prediction of Cavitation Erosion. *Wear*, 338–339:189–201, 2015c

Peters, A., Lantermann, U., and el Moctar, O. Numerical Modelling and Prediction of Erosion Induced by Hydrodynamic Cavitation. *Journal of Physics, conference series*, 656(1), 2015a

Peters, A., Lantermann, U., Sagar, H., Lange, S., and el Moctar, O. Entwicklung von numerischen und experimentellen Methoden zur Vorhersage von kavitationsbedingter Erosion an Schiffsanhängen – KonKav III: Schlussbericht zum Teilvorhaben Entwicklung von numerischen Methoden zur Berechnung von kavitationsbedingter Erosion – NumEro. Technical report, Universität Duisburg-Essen, Institut für Schiffstechnik, Meerestechnik und Transportsysteme, 2015b

Peters, A., Lantermann, U., and el Moctar, O. Numerical Prediction of Cavitation Erosion on a Ship Propeller in Model- and Full-Scale. *Wear*, 408–409:1–12, 2018a

Peters, A., Lantermann, U., and el Moctar, O. Simulation of an Internal Nozzle Flow Using an Euler-Lagrange Method. In *Proceedings of the 10 International Symposium on Cavitation, CAV2018, Baltimore, Maryland, USA*, 2018b

Peters, A. and el Moctar, O. Numerical Prediction of Cavitation-Induced Erosion Using a Multi-Scale Euler-Lagrange Method. *revised manuscript submitted to Journal of Fluid Mechanics*, 2019



# Contents

<b>List of Figures</b>	<b>XI</b>
<b>List of Tables</b>	<b>XV</b>
<b>List of Symbols</b>	<b>XVII</b>
<b>1 Introduction</b>	<b>1</b>
1.1 State of the Art in Numerical Prediction of Cavitation Erosion . . . . .	2
1.2 State of the Art in Prediction of Cavitation and Erosion on Propellers . . . . .	3
1.3 State of the Art in Multi-Scale Methods for Cavitating Flows . . . . .	4
1.4 Objectives and Scope of the Thesis . . . . .	5
<b>2 Physical Background</b>	<b>9</b>
2.1 Cavitation . . . . .	9
2.1.1 Nucleation . . . . .	10
2.1.2 Spherical Single Bubble Dynamics . . . . .	11
2.1.3 Mechanisms to Generate Cavitation . . . . .	14
2.1.4 Structures of Cavitation in Hydrodynamic Flows . . . . .	16
2.2 Cavitation Erosion . . . . .	19
2.2.1 Periods of Cavitation Erosion . . . . .	19
2.2.2 Erosion Mechanisms: Near-Wall Bubble Collapse . . . . .	20
2.2.3 Properties of Solid Materials . . . . .	23
2.3 Laws of Similarity and Scale Effects . . . . .	24
2.3.1 Laws of Similarity . . . . .	25
2.3.2 Scale Effects on Cavitation and Cavitation Erosion . . . . .	25
2.4 Cavitation and Cavitation Erosion in Maritime Environments . . . . .	28
<b>3 Basic Equations and Numerical Methods for Continuous Flows</b>	<b>31</b>
3.1 Flow Equations of Conservation . . . . .	32
3.1.1 Navier-Stokes Equations . . . . .	32
3.1.2 Turbulence . . . . .	33
3.1.3 Volume of Fluid Method . . . . .	36
3.1.4 Summary of Equations for Continuous Flows . . . . .	39
3.2 Finite Volume Method . . . . .	39
3.2.1 Approximation of Temporal Derivatives . . . . .	41
3.2.2 Approximation of Volume and Surface Integrals . . . . .	42
3.2.3 Interpolation Techniques . . . . .	43

3.2.4	Boundary Conditions . . . . .	44
3.2.5	Linear Algebraic System of Equations . . . . .	46
3.3	Solution of the Navier-Stokes Equations . . . . .	47
3.3.1	Linearisation of Momentum Equation . . . . .	47
3.3.2	Pressure Equation . . . . .	48
3.3.3	Pressure-Velocity Coupling . . . . .	50
3.4	Error Estimation . . . . .	52
3.4.1	Modelling Errors . . . . .	52
3.4.2	Statistical Convergence Errors . . . . .	52
3.4.3	Discretisation Errors . . . . .	53
<b>4</b>	<b>Modelling of Cavitation and Cavitation-Induced Erosion</b>	<b>55</b>
4.1	Modelling of Spherical Cavitation Bubbles . . . . .	55
4.1.1	Dynamics of Spherical Bubbles . . . . .	56
4.1.2	Lagrangian Description of Spherical Bubble Motion . . . . .	59
4.2	Euler-Euler Approach . . . . .	64
4.2.1	Sauer and Schnerr Cavitation Model . . . . .	64
4.2.2	Turbulence Effects on Cavitation . . . . .	68
4.3	Euler-Lagrange Approach . . . . .	70
4.3.1	Bubble-Liquid Interactions . . . . .	70
4.3.2	Momentum of Lagrangian Bubbles Acting on Carrier Flow . . . . .	72
4.3.3	Bubble Collision and Coalescence . . . . .	73
4.4	Hybrid Multi-Scale Cavitation Approach . . . . .	75
4.4.1	Multi-Scale Treatment of Vapour Volumes . . . . .	75
4.4.2	Calculation of Vapour Volume . . . . .	82
4.4.3	Non-Condensable Gas Content of Bubbles . . . . .	82
4.4.4	Solution Algorithm . . . . .	83
4.5	Erosion Prediction . . . . .	86
4.5.1	Eulerian Approach . . . . .	86
4.5.2	Lagrangian Approach . . . . .	94
<b>5</b>	<b>Numerical Prediction of Hydrodynamic Cavitation Erosion</b>	<b>101</b>
5.1	Euler-Euler Method . . . . .	101
5.1.1	NACA 0009 Modified Hydrofoil in Oblique Flow . . . . .	101
5.1.2	NACA 0015 Hydrofoil in Oblique Flow . . . . .	108
5.1.3	Internal Nozzle Flow . . . . .	125
5.1.4	Propeller in Oblique Flow . . . . .	136
5.1.5	Conclusion . . . . .	155
5.2	Euler-Lagrange Method . . . . .	157
5.2.1	Spherical Bubble Dynamics in an Acoustic Field . . . . .	157
5.2.2	Behaviour of a Spherical Single Bubble in a Vortex . . . . .	158
5.2.3	Bubble Rising in a Liquid Column . . . . .	163
5.2.4	Lagrangian Bubble-Bubble Interaction . . . . .	164
5.2.5	Internal Nozzle Flow . . . . .	167

5.2.6	Conclusion . . . . .	171
5.3	Hybrid Multi-Scale Method . . . . .	172
5.3.1	Coalescence of a Lagrangian and an Eulerian Vapour Volume . . . . .	172
5.3.2	Internal Nozzle Flow . . . . .	174
5.3.3	Conclusion . . . . .	185
<b>6</b>	<b>Conclusions and Outlook</b>	<b>187</b>
6.1	Conclusions . . . . .	188
6.1.1	Summary of Author’s Contributions . . . . .	190
6.2	Outlook . . . . .	190
<b>7</b>	<b>Appendix</b>	<b>192</b>
7.1	Algorithm for Identification of Isolated Eulerian Vapour Volumes . . . . .	192
7.2	Algorithm to Organise Communication in Parallel Simulations . . . . .	194
	<b>Bibliography</b>	<b>196</b>



# List of Figures

2.1	Pressure-temperature phase diagram of water . . . . .	10
2.2	Dynamics of a travelling bubble . . . . .	12
2.3	Sheet and cloud cavitation on a hydrofoil . . . . .	16
2.4	Shedding of a cavitation cloud by a re-entrant jet . . . . .	18
2.5	Erosion process with characteristic periods . . . . .	20
2.6	Collapse of a single cavitation bubble near a solid wall . . . . .	22
2.7	Tip and hub vortex cavitation on the DTC model propeller . . . . .	29
2.8	Cavitation erosion on the pressure side of the tip of a propeller blade . . . . .	30
3.1	Time history and backward averaging of a scalar quantity . . . . .	53
4.1	Saffman shear lift force generated on a bubble by the carrier fluid . . . . .	62
4.2	Density functions for Reboud correction to calculate turbulent viscosity . . . . .	69
4.9	Solution algorithm of hybrid multi-scale method . . . . .	85
4.10	Collecting cells around a hydrofoil in a spherical cell zone . . . . .	87
4.11	Cells in and around a cell zone . . . . .	87
4.12	Evaluation of erosion model conditions for face and cell zone . . . . .	88
4.13	Microjet velocities from theoretical and experimental investigations . . . . .	90
4.14	Measured impacting microjet velocities onto a solid surface . . . . .	90
4.15	Exemplary calculation of coefficient $c_{ero,E}$ to estimate erosion potential . . . . .	94
5.1	Numerical domain and grid topology around NACA 0009 . . . . .	103
5.2	Grid refinement regions around the NACA 0009 . . . . .	104
5.3	Sheet and cloud cavitation around NACA 0009 . . . . .	105
5.4	Pressure distributions on NACA 0009 from simulation and measurements . . . . .	107
5.5	Numerical domain and grid topology around NACA 0015 . . . . .	109
5.6	Grid refinement regions around the NACA 0015 . . . . .	109
5.7	Sheet and cloud cavitation around NACA 0015 at $8^\circ$ angle of attack . . . . .	111
5.8	Normalised vapour volume and lift coefficient on NACA 0015 . . . . .	112
5.9	FFT of normalised vapour volume obtained using different grids . . . . .	113
5.10	Sheet and cloud cavitation around NACA 0015 at $\sigma_{cav} = 0.95$ . . . . .	116
5.11	Re-entrant jet formation around NACA 0015 at $\sigma_{cav} = 0.95$ . . . . .	116
5.12	Sheet and cloud cavitation around NACA 0015 at $\sigma_{cav} = 1.07$ . . . . .	117
5.13	Sheet and cloud cavitation around NACA 0015 at $\sigma_{cav} = 1.19$ . . . . .	118
5.14	Lift coefficient on NACA 0015 for different cavitation numbers . . . . .	119
5.15	Sheet and cloud cavitation around NACA 0015 in experiment . . . . .	121
5.16	Numerical erosion prediction on NACA 0015 for different cavitation numbers . . . . .	122

## List of Figures

5.17	Erosion pattern in coating of NACA 0015 surface . . . . .	123
5.18	Numerical erosion prediction on NACA 0015 for different yield strengths . . .	124
5.19	Sketch of nozzle geometry and flow conditions . . . . .	125
5.20	Grid in solution domain and around connecting radius of nozzle . . . . .	126
5.21	Velocity magnitude and pressure in cross section plane . . . . .	126
5.22	Formation, shedding, and collapse of cavitation structures in nozzle . . . . .	127
5.23	Time series and FFT of normalised vapour volume . . . . .	128
5.24	Time series and FFT of average pressure in numerical sensor . . . . .	129
5.25	Cavitation behaviour and numerical erosion prediction . . . . .	130
5.26	FFT of normalised vapour volume for different grids . . . . .	131
5.27	Exceedances of vertical force and pressure for different grids . . . . .	132
5.28	Numerical microjet erosion prediction obtained using different grids . . . . .	132
5.29	Erosion prediction for different cell zone radii in 3D . . . . .	133
5.30	Erosion prediction for different cell zone radii in 2D . . . . .	134
5.31	Predicted erosion using two different models and measured erosion depth . . .	135
5.32	Measured erosion and erosion prediction on target surface . . . . .	135
5.33	Simulation domain for P1225 in axial flow . . . . .	137
5.34	Grid refinement regions at rotor-stator interface in propeller plane . . . . .	138
5.35	Grid around propeller blade . . . . .	139
5.36	Axial velocity field around P1225 for $J = 0.7813$ . . . . .	140
5.37	Thrust and torque coefficient on P1225 in homogeneous flow . . . . .	140
5.38	Simulation domain for P1225 in oblique flow . . . . .	142
5.39	Thrust generated by a propeller blade for different angles of attack . . . . .	143
5.40	Thrust on a propeller blade with and without cavitation . . . . .	145
5.41	Grid of entire propeller and refinements around a propeller blade . . . . .	145
5.42	Resolved cavitation structures with and without additional grid refinements .	147
5.43	Pressure coefficient around P1225 and mesh interface . . . . .	148
5.44	Correlations between cavitation and pressure distribution on propeller blades	149
5.45	Cavitation structures from simulation and experiment for $\sigma_{\text{cav}} = 0.963$ . . . .	150
5.46	Erosion prediction on propeller blade for $\sigma_{\text{cav}} = 0.963$ . . . . .	151
5.47	Cavitation structures from simulation and experiment for $\sigma_{\text{cav}} = 1.464$ . . . .	152
5.48	Erosion prediction on propeller blade for $\sigma_{\text{cav}} = 1.464$ . . . . .	153
5.49	Radius and pressure of a bubble in an acoustic field . . . . .	157
5.50	Velocity magnitude and pressure in a vortex . . . . .	159
5.51	Bubble motion and dynamics in a vortex . . . . .	160
5.52	Influence of volume variation force on bubble motions and dynamics . . . . .	161
5.53	Influence of lift force on bubble motion and dynamics . . . . .	161
5.54	Bubble trajectories in a vortex considering different forces . . . . .	162
5.55	Rise velocities of a bubble for different coupling techniques . . . . .	163
5.56	Lagrangian bubble positions and directions prior to coalescence and collision	165
5.57	Coalescence of two Lagrangian bubbles . . . . .	166
5.58	Collision of two Lagrangian bubbles . . . . .	166
5.59	Cavitation structures in nozzle for $n_0 = 5 \cdot 10^{10} \text{ m}^{-3}$ . . . . .	168
5.60	Cavitation structures in nozzle for $n_0 = 1 \cdot 10^{11} \text{ m}^{-3}$ . . . . .	169

5.61	Cavitation behaviour in nozzle for different nuclei densities . . . . .	170
5.62	Coalescence of Lagrangian bubble with Eulerian vapour volume . . . . .	173
5.63	Eulerian cavitation structures and Lagrangian bubbles inside nozzle . . . . .	175
5.64	Eulerian cavitation structures and Lagrangian bubbles inside nozzle . . . . .	175
5.65	Lagrangian bubbles growing and forming a larger Eulerian vapour structure .	176
5.66	Transformation of an Eulerian vapour volume into a Lagrangian bubble . . .	177
5.67	Time history of number of Lagrangian bubbles in simulation domain . . . . .	179
5.68	Cavitation behaviour obtained using different numerical methods . . . . .	180
5.69	Lagrangian bubble collapses on target surfaces . . . . .	181
5.70	Distribution of impacts at different distances to target surface . . . . .	182
5.71	Distribution of impacts obtained from different multi-scale simulations . . .	183
5.72	Numerical erosion predictions and measured erosion pattern . . . . .	184
5.73	Non-linear erosion prediction and measured erosion pattern . . . . .	185



## List of Tables

5.1	Particulars of NACA 0009 and measurement section of cavitation tunnel . . .	102
5.2	Results of cavitating flow around NACA 0009 on different grids . . . . .	106
5.3	Experimental and numerical results of cavitating flow around NACA 0009 . .	106
5.4	Particulars of NACA 0015 and measurement section of cavitation tunnel . . .	108
5.5	Results of cavitating flow around NACA 0015 for different grids . . . . .	112
5.6	Results of cavitating flow around NACA 0015 for different time step sizes . .	114
5.7	Results of cavitating flow around NACA 0015 for different nuclei densities .	114
5.8	Results of lift and vapour volume for different cavitation numbers . . . . .	120
5.9	Results of grid dependence study of cavitating flow in axisymmetric nozzle .	131
5.10	Particulars of SVA cavitation tunnel and P1225 . . . . .	137
5.11	Parameters for open water conditions of P1225 . . . . .	139
5.12	Results from grid dependence study for P1225 in axial flow . . . . .	141
5.13	Results of thrust and torque for P1225 in axial flow . . . . .	142
5.14	Parameters for P1225 in oblique flow conditions . . . . .	142
5.15	Results from grid dependence study for P1225 in cavitating flow . . . . .	144
5.16	Results for cavitating flow obtained using different grids . . . . .	146
5.17	Computed and measured propeller forces for $\sigma_{\text{cav}} = 1.464, J = 0.8009$ . . . .	146
5.18	Computed scale effects related to cavitation and erosion prediction . . . . .	154
5.19	Initial positions and velocities of Lagrangian bubbles . . . . .	164
5.20	Numerical results of cavitation behaviour for different nuclei densities . . . .	168
5.21	Results for multi-scale Euler-Lagrange method using parameters . . . . .	178
5.22	Processor times for simulations using different numerical approaches . . . . .	181



# List of Symbols

Label	Description	Unit
<b>Latin</b>		
$A$	Matrix of linear equation system	-
$D$	Deformation tensor	$\text{kg m}^{-1} \text{s}^{-2}$
$I$	Identity matrix	-
$T$	Stress tensor	$\text{Nm}^{-2}$
$\mathbf{b}$	Acceleration vector	$\text{m s}^{-2}$
$\mathbf{b}_Q$	Vector of source terms $Q_P$	-
$\mathbf{F}$	Force vector	N
$\mathbf{n}$	Surface normal vector	-
$\mathbf{r}$	Vector of absolute residuals	-
$\mathbf{S}$	Surface area vector	$\text{m}^2$
$\mathbf{s}_b$	Vector of bubble momentum source term	-
$\mathbf{s}_f$	Vector of volume forces	-
$\mathbf{u}$	Flow velocity vector	$\text{m s}^{-1}$
$\mathbf{x}$	Position vector	m
$c_{\text{ero}}$	Dimensionless erosion coefficient	-
$c_{\text{intensity}}$	Dimensionless intensity coefficient	-
$c_F$	Force coefficient	-
$c_p$	Pressure coefficient	-
$f$	Frequency	$\text{s}^{-1}$
$H$	Distance from bubble centre to solid wall	m
$h$	Hydrostatic height	m
$J$	Advance coefficient	-
$k$	Turbulent kinetic energy	$\text{m}^2 \text{s}^{-2}$
$K_Q$	Torque coefficient	-
$K_T$	Thrust coefficient	-
$L$	Length	m
$m$	Mass	kg
$n$	Wall normal distance	m
$n^+$	Dimensionless wall normal distance	-
$n_0$	Cavitation nuclei per liquid volume	$\text{m}^{-3}$
$n_{\text{EtoL}}$	Transformations from Eulerian to Lagrangian frame	-

List of Symbols

Label	Description	Unit
$n_{\text{limit}}$	Limit number of cells for vapour transformation	-
$n_{\text{LtoE}}$	Transformations from Lagrangian to Eulerian frame	-
$p$	Pressure	Pa
$p_{\text{asym}}$	Pressure of asymmetric bubble collapse	Pa
$p_{\text{imp}}$	Wall impact pressure caused by bubble collapse	Pa
$p_{\text{rgh}}$	Pressure reduced by hydrostatic pressure	Pa
$p_{\text{sat}}$	Saturation pressure	Pa
$p_{\text{spher}}$	Pressure of spherical bubble collapse	Pa
$p_{\text{wh}}$	Water hammer pressure	Pa
$Q$	Torque	Nm
$Q_P$	Source terms of cells $P$	-
$T$	Thrust	N
$R$	Bubble radius	m
$R_0$	Equilibrium bubble radius	m
$R_{\text{Cz}}$	Cell zone radius	m
$R_{\text{max}}$	Maximum bubble radius during collapse	m
$R_{\text{min}}$	Minimum bubble radius during collapse	m
$\dot{R}$	Bubble growth rate	$\text{m s}^{-1}$
$\ddot{R}$	Bubble wall acceleration	$\text{m s}^{-2}$
$r$	Radial coordinate	-
$r'$	Normalised residual	-
$S$	Surface	$\text{m}^2$
$S_{\text{c,p}}$	Condensation source term for $p$	$\text{m s kg}^{-1}$
$S_{\text{c}}$	Condensation source term	$\text{s}^{-1}$
$S_{\text{v,p}}$	Vapourisation source term for $p$	$\text{m s kg}^{-1}$
$S_{\text{v}}$	Vapourisation source term	$\text{s}^{-1}$
$t$	Time	s
$u$	Velocity	$\text{m s}^{-1}$
$u_{\text{crit}}$	Critical microjet velocity	$\text{m s}^{-1}$
$u_{\text{jet}}$	Microjet velocity	$\text{m s}^{-1}$
$V$	Volume	$\text{m}^3$
$V_{\text{v}}^*$	Normalised vapour volume in computational domain	-
$x$	First Cartesian coordinate	m
$y$	Second Cartesian coordinate	m
$z$	Third Cartesian coordinate	m
<b>Greek</b>		
$\zeta$	Vector of anisotropy parameter	$\text{m}^2 \text{s}^{-3}$
$\omega$	Flow vorticity	$\text{s}^{-1}$
$\alpha$	Volume fraction	-

Label	Description	Unit
$\alpha_{AoA}$	Angle of attack	$^{\circ}$
$\alpha_{limit}$	Threshold of vapour volume fraction	-
$\alpha_{nuc}$	Volume fraction related to $R_0$	-
$\gamma$	Dimensionless stand-off distance	-
$\varepsilon$	Turbulence dissipation	$m^2 s^{-3}$
$\varepsilon_L$	Strain	-
$\dot{\varepsilon}_L$	Strain rate	$s^{-1}$
$\zeta$	Scalar anisotropy parameter	$m^2 s^{-3}$
$\kappa$	von Karman constant	-
$\lambda$	Scale factor	-
$\mu$	Dynamic viscosity	Pas
$\mu_t$	Turbulent viscosity	Pas
$\nu$	Kinematic viscosity	$m^2 s^{-1}$
$\rho$	Density	$kg m^{-3}$
$\sigma$	Surface tension	$N m^{-1}$
$\sigma_{cav}$	Cavitation number	-
$\sigma_{load}$	Load stress	$N m^{-2}$
$\sigma_y$	Yield strength	$N m^{-2}$
$\tau$	Shear stress	$N m^{-2}$
$\omega$	Specific turbulence dissipation	$s^{-1}$
<b>Constants</b>		
$\mathbf{g}$	Gravitational acceleration vector	$m s^{-2}$
$c_{\infty}$	Speed of sound of liquid water	$m s^{-1}$
$g_z$	Gravitational acceleration	$m s^{-2}$
$\mathcal{R}_g$	Gas constant	$kg m^2 s^{-2} mol^{-1} K^{-1}$
<b>Dimensionless Parameters</b>		
Co	Courant number	
Eö	Eötvös number	
Ma	Mach number	
Re	Reynolds number	
St	Strouhal number	
<b>Subscripts</b>		
$\infty$	Far field value	
0	Equilibrium value	
b	Bubble value	
c	Carrier fluid value	

## List of Symbols

<b>Label</b>	<b>Description</b>	<b>Unit</b>
coll	Value after bubble collapse	
CV	Control volume value	
E	Eulerian value	
eff	Effective value	
ero	Erosion related value	
f	Face index	
g	Gas value	
i	Cell, face, or bubble index	
j	Cell, face, or bubble index	
L	Lagrangian value	
l	Liquid value	
limit	Threshold value	
max	Maximum value	
min	Minimum value	
N	Neighbour cell index	
P	Owner cell index	
ref	Reference value	
v	Vapour value	
x	Component in x-direction	
y	Component in y-direction	
z	Component in z-direction	

### Acronyms

AMI	Arbitrary Mesh Interface
CFD	Computational Fluid Dynamics
CV	control volume
DES	Detached Eddy Simulations
DNS	Direct Numerical Simulations
DTC	Duisburg Test Case
FVM	Finite Volume Method
LES	Large Eddy Simulations
MULES	Multi-Dimensional Limiter for Explicit Solution
PISO	Pressure-Implicit with Splitting Operators
RANS	Reynolds-averaged Navier-Stokes
SIMPLE	Semi-Implicit Method for Pressure Linked Equations
UDE	Index of bubble dynamics time step
VOF	Volume of Fluid





# 1 Introduction

In engineering flows, hardly a material exists that is able to resist the loads exerted by aggressive cavitation collapses. Local pressures of more than a gigapascal are the result of collapses of cavitation bubbles of micro- to millimetre radii. Generated by fluid pressures near the saturation pressure, cavitation bubbles grow from gas bubbles or solid particles that are present in almost any engineering flow. Over a century of research on cavitation and cavitation-induced erosion, referred to as cavitation erosion, has revealed the complexity of a problem that has yet to be fully understood. Owing to the intricacy of the physical processes involved, designs in various fields of fluid engineering are often improper concerning aggressive collapses of cavitation structures that lead to material erosion. The consequent material erosion yields several difficulties. Besides lower efficiencies of machinery and a higher energy consumption, in engineering applications, cavitation erosion may even cause losses of components, resulting in significant repair and maintenance costs.

To avoid these damages, design improvements require more accurate predictions of cavitation erosion for hydrodynamic flows. Given the fact that experimental predictions of cavitation erosion are expensive, not applicable to every flow problem, and encompass scale effects, numerical predictions based on Computational Fluid Dynamics (CFD) have received increasing attention. Despite the steady increase of computational power, simulations comprising asymmetric cavitation bubble collapses near solid surfaces are computationally expensive and are therefore usually limited to simulate only a few individual cavitation bubbles. Thus, numerical approaches to predict cavitation erosion comprise several modelling assumptions and resolve physical processes down to different levels of accuracy. These approaches differ mainly in their treatment of the vapour phase and the computational effort needed. While numerical erosion predictions are mostly of qualitative nature and only valid for certain flow problems, relevant efforts call for more efficient and accurate predictions.

The underlying thesis addresses the prediction of cavitation erosion for multiple hydrodynamic flow problems using two numerical approaches: first, an efficient approach based on an Eulerian treatment of the vapour phase to predict areas exposed to erosion; second, a more accurate multi-scale approach that is used to simulate the dynamics of single Lagrangian bubbles and predicts erosion based on computed Lagrangian bubble collapses.

## 1.1 State of the Art in Numerical Prediction of Cavitation Erosion

To predict cavitation erosion with numerical methods for practical and macroscopic hydrodynamic flow problems, different models were developed. Fortes-Patella et al. (2004) considered the shock waves radiated from macroscopic cloud collapses. The potential energy of these cavitation clouds is supposedly converted into acoustic energy of shock waves, which are able to damage an impacted surface. To estimate the erosion potential, they calculate the acoustic pressure radiated by the spherical cloud. The collapse of a cloud is also regarded as the main erosion mechanism by Wang and Brennen (1999). In their model, the fully non-linear Rayleigh-Plesset equation is used to simulate the interaction of a spherical bubble cloud that consists of single cavitation bubbles with the liquid. To quantify the damage potential of a spherical cloud, the acoustic pressure radiated by the cloud is calculated. Dular et al. (2006), Dular and Coutier-Delgosha (2009) proposed an erosion model based on the hypothesis that microjets are able to erode a surface. The collapse of single bubbles near a surface is always asymmetric because the symmetric flow to the bubble is disturbed by the surface. This leads to liquid waterjets, so-called microjets, being directed towards the surface. Depending on the jet velocity and the yield strength of the considered material, a surface is supposedly eroded. Peters et al. (2015c,a) further developed this model by considering the flow within a given distance from the surface. They derived a coefficient to qualitatively assess the erosion potential based on the number of impacts and their intensities on the impacted areas. Nohmi et al. (2008) stated a formula to derive so-called aggressiveness indices. These indices depend on the volume fraction, the pressure, and the temporal derivatives of these quantities. Depending on the considered index, a low or a high value stands for high erosion potential. A model by Li (2012) evaluates time derivatives of pressure on the regarded surface. Erosion is predicted in areas where these pressure derivatives exceed a certain threshold value. The numerical erosion prediction agreed qualitatively with experimental erosion predictions. Mihatsch et al. (2012, 2015), Mihatsch (2017) numerically predicted cavitation erosion by detecting collapses of vapour cavities. They employed a density-based compressible solver to simulate the flow through an axisymmetric nozzle. Numerically predicted wall zones exposed to erosion were compared with measured erosion depths and agreed well. Mottyll (2017) used a similar density-based compressible solver to predict erosion for cavitation at an ultrasonic horn. Predicted regions of erosion were in good qualitative agreement to the authors' in-house experiments. Leclercq et al. (2017) developed a cavitation intensity model that estimates impact loads based on void fraction and pressure derivatives. Using this model, they performed qualitative erosion predictions to the cavitating flow around a NACA 65012 hydrofoil which agreed favourably with experimental results obtained from a pitting test. Based on the approach of Leclercq et al. (2017), Schenke et al. (2019) proposed a model that considers the conversion of the potential energy of a vapour cavity into acoustic power to estimate the pressure of a collapsing vapour cavity. The model assumes that the energy of a vapour cavity is transformed from potential energy into kinetic energy during collapse and converted into shock wave energy at the final stage of the collapse. Before conversion into acoustic energy,

focussing of the potential energy into the cavity's collapse centre is performed using an energy transport function.

## 1.2 State of the Art in Prediction of Cavitation and Erosion on Propellers

Cavitation on marine propellers was studied by Kimura et al. (2009) and Lu et al. (2012) using Reynolds-averaged Navier-Stokes (RANS) methods. They showed that the behaviour and extent of cavitation in uniform cavitating flow can be predicted numerically. Their results were in favourable agreement to experimental observations. A detailed analysis of sheet and tip vortex cavitation on a propeller was performed by Hsiao et al. (2015b). To predict cavitation, they used a multi-scale Euler-Lagrange approach, including a RANS method for the macroscopic scale which precisely described the behaviour of both macroscopic and microscopic vapour volumes. The authors found that cavitation has a large effect on the pressure distribution on a blade, leading to a significant reduction of lift. Sakamoto and Kamiirisa (2015) investigated the noise generated by propeller cavitation. They calculated the sound pressure taking into account the propeller's characteristics and using two different methods in order to estimate noise generation of two different propellers. Hasuike et al. (2009) numerically studied the risk of erosion on propeller blades caused by cavitation. They evaluated the occurrence of cavitation erosion on a propeller with four differently loaded blades in a predefined wake field. Simulations and experiments of a test case showed a higher erosion risk on the less loaded blades because cavitation volumes collapsed in the vicinity of the blade surface. Their experimental erosion prediction used a painted surface, whereas their numerical prediction was based on the aggressiveness indices proposed by Nohmi et al. (2008). Based on these aggressiveness indices, they obtained a qualitative erosion prediction. Ponkratov and Caldas (2015) applied the indices stated by Nohmi et al. (2008) to predict cavitation erosion caused by a ship propeller near the leading edge of a rudder. These authors used Detached Eddy Simulations (DES) to predict cavitation erosion on a rudder by simulating the flow around the entire geometry of the ship. In observations of full-scale measurements, erosion on the ship's rudder was caused by the hub vortex of the propeller collapsing near the leading edge of the rudder. The aggressiveness indices identified similar regions of erosion risk. Ponkratov (2015) used the same approach of DES and erosion model indices to predict erosion for a full-scale propeller behind the full ship geometry. Full scale measurements of the operating propeller revealed cavitation induced erosion at the tip of the blade's leading edge. The aggressiveness indices qualitatively addressed the erosion damage in the numerical simulations. Usta et al. (2017) used three models of different formulas to numerically predict cavitation erosion. They conducted simulations on a four-bladed model propeller and compared the erosion predictions to an experimental prediction method that showed a good qualitative agreement. Peters et al. (2018a) simulated the oblique, cavitating flow around a propeller with an implicit RANS-based flow solver using the Volume of Fluid method to model the interface between liquid and vapour phase. They used an erosion model based on the hypothesis of Dular et al.

(2006), Dular and Coutier-Delgosha (2009), Peters et al. (2015c) to qualitatively predict erosion risk on the propeller blades for different advance coefficients and cavitation numbers. The results were compared to experimental erosion predictions of Heinke et al. (2013) and agreed favourably.

## 1.3 State of the Art in Multi-Scale Methods for Cavitating Flows

Approaches for cavitation modelling mainly differ in the treatment of the vapour phase. Cavitation models for Euler-Euler methods assume that both the liquid and the vapour phase are continuous. For projection methods, utilising a volume of fluid method, a volume fraction defines the volume of vapour in a control volume (CV). The volume fraction is obtained from a transport equation in which source terms from a cavitation model represent the processes of condensation and vapourisation. The most popular cavitation models follow Sauer and Schnerr (2000), Singhal et al. (2002), Merkle et al. (1998), Kunz et al. (2000), Zwart et al. (2004). On the contrary, Euler-Lagrange methods consider the vapour phase as an accumulation of discrete individual bubbles and assume just the liquid phase to be a continuum. In these methods, motions of individual cavitation bubbles are calculated in a Lagrangian coordinate system. Dynamics of every single bubble are modelled by equations of bubble dynamics according to Rayleigh (1917), Plesset (1949), Hsiao et al. (2000), Tomita and Shima (1977). Hsiao et al. (2000, 2003) used Lagrangian methods to model the vapour phase in simulations of cavitating flows. A coupled Euler-Lagrange method to calculate cavitating flows was developed by Abdel-Maksoud et al. (2010). The authors conducted simulations of cavitating flows around a hydrofoil and compared bubble trajectories with carrier flow streamlines. The Lagrangian treatment of bubble motions allowed them to determine the motions of bubbles relative to the carrier fluid flow. Deviations between bubble trajectories and flow streamlines were particularly found at the free outer edge of the hydrofoil. Shams et al. (2011) developed an Euler-Lagrange approach to simulate turbulent bubbly flows. They considered a one-way coupling and two-way coupling including the influence of volumetric displacement concerning vapour bubbles. Yakubov et al. (2011) compared numerical simulations of cavitating flows around a hydrofoil and a propeller utilising both Euler-Euler and Euler-Lagrange approaches. The simulation results revealed strong dependences of the Euler-Euler simulation on model constants. On the other hand, the Euler-Lagrange method allowed taking into account water-quality effects, using a measured cavitation nuclei distribution. Yakubov et al. (2013) extended and optimised the approach for parallel simulations. Ma et al. (2015b) used an Euler-Lagrange approach to simulate the dynamics of a cavitation cloud consisting of an accumulation of single, spherical bubbles. Therein, influences of the liquid phase on the bubbles and vice versa were considered in form of a two-way coupling. The approach was further developed by Ma et al. (2015c) for more efficient parallel computations.

Recently, hybrid and multi-scale methods have been proposed, combining an efficient Eulerian treatment of the vapour phase with a more accurate Lagrangian treatment. Based on the size

and resolution of vapour volumes, these volumes are transformed between the Eulerian and Lagrangian frameworks. Accordingly, larger vapour structures are treated on an Eulerian grid while smaller vapour volumes are treated as spherical Lagrangian bubbles. Apte et al. (2009) developed a hybrid Euler-Lagrange approach to simulate turbulent bubbly flows. Larger bubbles were fully resolved by the numerical grid whereas under-resolved bubbles were treated in a Lagrangian frame. Vallier (2013) developed a multi-scale approach to transform vapour volumes between the Eulerian and Lagrangian frameworks. Using this approach, the author simulated the break-up of a cavitation sheet as well as cavitation structures on a hydrofoil. Hsiao et al. (2014) developed a similar approach to capture the formation of sheet cavitation and shedding of cloud cavitation on a hydrofoil. They used a wall nucleation approach to enable the unsteady shedding of cloud cavitation. Their results showed good agreement to published experimental results with regard to the length of sheet cavitation and shedding frequencies. Hsiao et al. (2015a) used a similar multi-phase approach to simulate sheet and tip vortex cavitation on a three-bladed propeller for three different advance coefficients. They showed that a reduction of the advance coefficient resulted in the extension of sheet cavitation towards the leading edge and the development of tip vortex cavitation because single cavitation bubbles merged into a macroscopic cavity. Following up on this work, Ma et al. (2017) presented a multi-scale approach to simulate the cavitating flow in a waterjet propulsion nozzle, bubbly flow in a line vortex, unsteady sheet cavitation on a hydrofoil, and cavitation behind a blunt body. Lidtke (2017) used a fully parallel, multi-scale approach to simulate the flow around a hydrofoil in order to investigate cavitation noise. In contrast to a purely Eulerian approach, the simulation of Lagrangian bubble dynamics enabled the calculation of medium to high frequency pressure fluctuations induced by cavitation. Ghahramani et al. (2018) developed a multi-scale model, similar to Vallier (2013), in which larger cavities are considered in the Eulerian framework while smaller cavities are treated as Lagrangian bubbles. Nevertheless, in contrast to other aforementioned approaches (Vallier, 2013, Hsiao et al., 2014, Lidtke, 2017), small vapour clouds are transformed into multiple Lagrangian bubbles. Therein, based on the Eulerian vapour volume fraction, a Lagrangian bubble is introduced into each control volume of a small cavity.

## 1.4 Objectives and Scope of the Thesis

In this thesis, improved approaches to numerically predict hydrodynamic cavitation-induced erosion are presented and applied to internal and external flows that involve stationary and rotating components. Two new approaches to predict cavitation erosion are derived and applied to different flow problems. Comparisons of numerically predicted erosion with experimentally obtained erosion patterns and qualitative experimental erosion predictions yield the accuracy of the numerical methods. First, an efficient Euler-Euler approach predicts areas exposed to erosion based on information of pressure and vapour content in the flow. Second, a multi-scale Euler-Lagrange method uses calculated collapses of spherical Lagrangian bubbles to identify locations and time instances of cavitation bubble collapses and, thereby, predict erosion im-

## 1.4 Objectives and Scope of the Thesis

pacts. The multi-scale approach enables to correlate calculated bubble collapses with erosion pitting rates from measurements.

The thesis is structured into four main parts. Chapter 2 deals with the physical background of cavitation and cavitation-induced erosion, paying special attention to phenomena related to hydrodynamic cavitation. After addressing cavitation nucleation and dynamics of spherical single bubbles, mechanisms to generate cavitation and various structures related to hydrodynamic cavitation are outlined. Phases characterising an erosion cycle are given and the main mechanisms that lead to erosion during a near-wall cavitation bubble collapse are discussed. Moreover, light is shed on dependencies of these erosion processes on material properties. Basic laws of similarity are presented and scale effects of cavitation and cavitation erosion are summarised. The end of the chapter highlights cavitation and cavitation erosion related to maritime environments.

Chapter 3 describes the existing numerical solution method used as the basis for the Eulerian analysis of cavitating flows. It covers the basic equations for flows together with the numerical methods used to solve them. Starting from the Navier-Stokes equations, models to deal with turbulent and two-phase flows yield additional equations of conservation. Components of the Finite Volume Method (FVM) used to discretise and solve these equations are described and a linear algebraic system of equations is obtained. Following a pressure-velocity coupling approach, an algorithm to sequentially solve the system of equations is given that stems from the derivation of the pressure equation. A summary of typical errors originating from numerical methods, with special emphasis on modelling errors, statistical convergence errors, and discretisation errors completes the chapter.

Cavitation modelling approaches that consider Eulerian and Lagrangian perspectives are given in Chapter 4. Following the modelling of the dynamics and motions of spherical single bubbles, the derivation of a state of the art Euler-Euler cavitation model is explained. Based on the Lagrangian treatment of single spherical bubbles, the implementation of an Euler-Lagrange approach utilising different levels of coupling techniques is outlined. The chapter further introduces a hybrid multi-scale approach that combines the advantages of an Eulerian and a Lagrangian treatment of the vapour phase. Mechanisms of the multi-scale approach to transform vapour volumes between the Eulerian and the Lagrangian framework are depicted with attention paid to transformations in parallel simulations. A measurement-based distribution of cavitation nuclei is implemented so that the initial gas content for Lagrangian bubbles can be selected. The solution algorithm for the multi-scale approach is given and erosion models based on an Eulerian and on a Lagrangian treatment of the vapour phase are stated. The computationally more efficient Eulerian erosion model predicts regions exposed to erosion based on quantities of the flow solution. In the Lagrangian erosion model, spatial and temporal resolution of bubble collapses in terms of locations and time instances of collapses and bubble sizes during these collapses are identified from the simulated behaviour of single spherical bubbles. Here, motion and shock wave radiation during an asymmetric near-wall bubble collapse are accounted for by modelling these processes according to experimental observations and theoretical considerations.

Results obtained from numerical simulations using a pure Euler-Euler, a pure Euler-Lagrange, and a hybrid multi-scale Euler-Lagrange approach are described in Chapter 5. The Euler-Euler approach yields results of cavitating flows around differently shaped hydrofoils, inside an axisymmetric nozzle, and around a propeller. Numerical erosion predictions for a NACA 0015 hydrofoil and the propeller are compared to experimental erosion predictions, while numerical erosion predictions for the axisymmetric nozzle are compared to experimental observations where the extent of erosion is quantified via the depth of erosion pits on the experimentally treated specimen. Numerical exercises are performed for simple simulation cases to validate and verify the main components of the Euler-Lagrange approach, namely bubble dynamics and bubble motions. In four-way coupled Euler-Lagrange simulations, collision and coalescence of Lagrangian bubbles are evaluated. Considering different nuclei densities, a two-way coupled Euler-Lagrange approach is used to simulate the cavitating flow through an axisymmetric nozzle. For the multi-scale Euler-Lagrange method, transformation mechanisms are analysed for a simplified case and for the flow through an axisymmetric nozzle. Parameters that influence these transformations are studied for the nozzle flow with respect to the number and the sizes of Lagrangian bubbles in the numerical domain. Distributions of erosion predictions on a target surface within the nozzle are obtained from different hybrid simulations. Finally, the numerical prediction is compared to published measurements of erosion pits, and dependences of the erosion prediction on transform mechanisms, bubble sizes, and impact pressures are analysed.

The thesis ends with a conclusion, a summary of the author's contributions, and gives an outlook that indicates possible directions for future research studies.



## 2 Physical Background

Cavitation and cavitation-induced erosion, also referred to as *cavitation erosion*, incorporate physical phenomena ranging from microscopic scales – gas bubbles of a few micro metres – to macroscopic scales – vortex cavitation on propellers of diameters up to almost ten metres. Accordingly, these events take place within different time scales, considering, on the one hand, a bubble collapse occurring within micro seconds, and on the other hand, the periodic process of cloud cavitation taking place at frequencies even lower than 20Hz. To understand the behaviour of macroscopic physical phenomena of cavitation as well as cavitation-induced erosion, it is important to know about the basics of the microscopic processes involved. In this chapter, the connections between different spatial and temporal scales of these phenomena are explained and a brief introduction is given into cavitation and cavitation erosion. First, basic principles and mechanisms involved in the generation of cavities are presented. Second, the most common structures in hydrodynamic cavitation are described. Characteristics of cavitation erosion, such as erosion periods, the mechanisms that cause damage, and the influence of material properties are outlined. Dimensionless quantities and scale effects based on these quantities are presented. Finally, common structures of cavitation and patterns of cavitation erosion in maritime environments are encapsulated. The reader is referred to Knapp et al. (1970), Franc and Michel (2005), Brennen (1995, 2005), and Kuiper (2010) for more aspects related to cavitation and cavitation erosion.

### 2.1 Cavitation

The *Turbinia* was the first ship driven by a steam turbine that was incorporated by Sir Charles Parsons. During its first public sail in 1897 the *Turbinia* was able to reach speeds of over 30 knots, higher than those of the military ships chasing it. Although the *Turbinia*'s speeds were high compared to other ships at that time, they fell short of Parsons' expectations. The propellers were not designed for these speeds and lacking efficiency ascribable to the appearance of a specific phenomenon on the propeller blades: *cavitation*.

Cavitation is mostly referred to as the generation of a void or cavity (latin: *cavitare*) in a liquid under very low pressures. A substance, such as water, can undergo different phase changes based on the combination of pressure and temperature. Phase changes from liquid to vapour are commonly understood as vapourisation. In contrast to boiling as a process where a liquid vapourises because of a change of the surrounding temperature, cavitation is a purely pressure driven process. Therein, under isothermal conditions, a decrease of the pressure in a liquid below the saturation pressure can cause vapourisation as well.

## 2.1 Cavitation

Figure 2.1 sketches different phases of water as well as exemplary processes of vapourisation depending on pressure,  $p$ , and temperature,  $T$ . At constant atmospheric pressure of 100 kPa, liquid water will undergo a phase change to vapour when the temperature is increased over 100 °C. On the other hand, at a constant temperature of 20 °C, cavitation occurs when the pressure in water decreases below the saturation pressure of  $p_v(T = 20\text{ °C}) = 2339\text{ Pa}$ . The so-called triple point is found at a pressure of 0.612 kPa and a temperature of 0.01 °C and defines a state in which liquid, vapour, and solid water are in equilibrium.

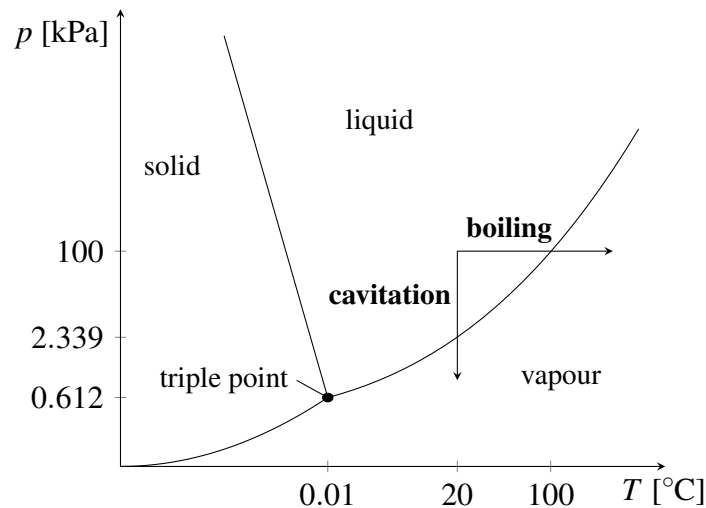


**Figure 2.1:** Pressure-temperature phase diagram of water; paths of boiling and cavitation are depicted

Theoretically, a void is generated because of depressurisation below the so-called vapour pressure,  $p_v(T)$ , and vapourises afterwards through its interface until vapour saturation is achieved. For the phenomena considered in this work, these processes can be assumed to take place instantly.

Although conditions exist under which vapourisation can take place at higher pressures than the vapour pressure and, likewise, vapourisation can be avoided at pressures lower than the vapour pressure, the vapour pressure serves as a quantity to assess macroscopic cavitation processes.

### 2.1.1 Nucleation

Pure liquid water can resist very high tension until vapour cavities appear. Briggs (1950) showed that when liquid water is not contaminated by any particles or free gases, at 10 °C it can withstand tension up to 277 bar yielding pressures well below the theoretical vapour pressure. Pressures below the vapour pressure do therefore not automatically cause the formation of vapour bubbles because water molecules are attracted to each other by adhesion and try to stick together more than they try to break up. However, water may be polluted by different types of so-called *cavitation nuclei* such as free gas bubbles (e.g. air) or solid particles that

carry small gas pockets. In some sciences, the contents of free gas as well as dissolved gas in a liquid flow are referred to as *water quality*. Cavitation inception is largely influenced by the presence of nuclei as they lower the surface tension of the liquid and create failure points in it, Pelz et al. (2017), Kuiper (2010), Church (1988), Marschall et al. (2001). Hence, vapourisation processes start at the outer surfaces of nuclei when pressures around the equilibrium vapour pressure are approached.

In technical applications and test facilities cavitation nuclei are always present. The number of particles and gas bubbles as well as their size distributions vary from one application to another. For example, sea water contains a larger number of free gas bubbles than still water. Processes of wave breaking as well as wave motions and turbulence consistently transport new nuclei into the water and keep existing ones from dissolving. Nuclei density (i.e. the number of nuclei per volume of liquid) and nuclei sizes influence cavitation inception. In most cases, cavitation inception is related to the growth of nuclei in the free stream, Brennen (1995).

In a static liquid, gas bubbles can rise to a free surface or dissolve. Here, the *saturation rate* is defined as the amount of air which can dissolve in water of a given temperature and pressure. Water can be *saturated* (i.e. in equilibrium), *oversaturated*, or *undersaturated* with air. In oversaturated water, air goes into solution with liquid water even beyond the saturation point. In contrast to vapourisation, which is a fast process, taking place directly at a bubble interface, gas diffusion into water is a rather slow process through a comparably thick diffusion layer around the bubble surface. In undersaturated water, free gas bubbles can go into solution. The dissolution time of a bubble is, therein, lowered by the surface tension force which, for a bubble, is anti-proportional to its radius,  $R$ . For smaller bubbles, the surface tension force is larger and dissolution therefore more likely. The number of free gas bubbles in an experiment may depend on the saturation rate of water. Nevertheless, in contrast to free air, dissolved air has no known direct effect on cavitating flows, Kuiper (2010).

Nuclei densities can be measured in experimental facilities using acoustic techniques as explained in Arndt et al. (2007). Measurements of gas bubble sizes utilising acoustic waves were performed for different flow problems by Reuter et al. (2018). While it is possible to control or even remove nuclei from experimental facilities, they cannot be controlled for practical engineering applications and it is usually difficult to perform nuclei measurements under these operating conditions. Furthermore, characterising different nuclei types such as particles or gases of various chemical composition is a challenging subject.

### 2.1.2 Spherical Single Bubble Dynamics

All types of macroscopic cavitation are accumulations of single cavitation bubbles interacting with each other. To understand the behaviour of macroscopic cavitation, it is inevitable to understand the fundamentals about single bubbles and their generation. Depending on the application, a specific number of cavitation nuclei travels through a liquid flow. When microscopic gas bubbles are exposed to low pressures, vapourisation processes start. Thereby, vapour diffuses through the outer walls of the microscopic bubbles causing them to grow to

## 2.1 Cavitation

larger cavitation bubbles. Thus, a cavitation bubble contains both vapour and non-condensable gas, which undergoes adiabatic changes of state according to an ideal gas. The pressure inside a bubble is defined by the partial pressures of vapour and non-condensable gas. As the bubble expands, its inner bubble pressure is lowered and approaches the vapour pressure.

Once a bubble is exposed to higher liquid pressure again, it collapses rapidly and the inner bubble pressure rises. Because of the dynamic behaviour of a cavitation bubble, the velocity of the bubble wall as well as the inner pressure will increase and cause the generation of a shock wave at the very end of the collapse process and the radiation of this shock wave through the liquid. During collapse, the pressure in the bubble increases to a magnitude that can be multiple orders larger than the ambient pressure. Owing to the abrupt implosion of the bubble, most of the energy that is initially stored in the bubble is converted into acoustic energy in order to compress the liquid and form shock waves of high pressure amplitudes, Vogel and Lauterborn (1988), Vogel et al. (1996), Supponen et al. (2017). The shock waves are nearly spherically radiated away from the bubble and may initiate oscillations and collapses of other cavitation bubbles in the vicinity. After the first collapse, the dynamics of the bubble can enable a repetition of growth and collapse processes – so-called *rebounds*.

Figure 2.2 sketches the dynamics of a bubble as it travels through a convergent-divergent nozzle. A cavitation nucleus in form of a microscopic gas bubble travels with the flow from left to right. Initially, the gas bubble is in equilibrium at a radius,  $R_0$ , under atmospheric pressure,  $p_{\text{atm}}$ . As it travels into regions of lower liquid pressure, first, the non-condensable gas in the bubble expands ( $p < p_{\text{atm}}$ ). When the bubble reaches regions of even lower liquid pressure ( $p < p_v$ ), vapourisation starts at its outer wall and causes it to be filled with vapour and to grow to a larger cavitation bubble. In the divergent part of the nozzle, the liquid pressure is increased to atmospheric pressure again, causing the bubble to collapse rapidly. Because of the non-condensable gas in the bubble, which expands during bubble growth and compresses during bubble collapse, the bubble oscillates. Thus, processes of growth and collapse are repeated multiple times in form of rebounds until the bubble approaches an equilibrium radius again or dissolves in the liquid.

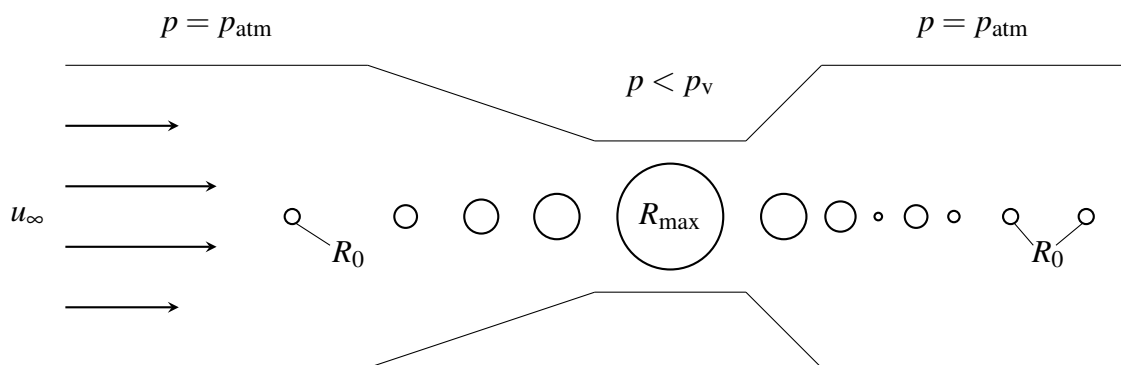


**Figure 2.2:** Dynamics of a cavitation bubble travelling through a channel and experiencing different liquid pressures

The behaviour of cavitation bubbles is often studied assuming a spherical bubble in an infinite liquid so that simplified equations with only the radius as a geometrical parameter of the bubble can be used to analyse the bubble's dynamics. Rayleigh (1917) was the first to state an equation for a spherical bubble to study its behaviour. Plesset (1949) extended this equation considering a non-uniform liquid pressure around the bubble as well as surface tension. Incorporating viscous effects, a generalised form of this so-called Rayleigh-Plesset equation can be written as:

$$\frac{p_b - p_\infty}{\rho_l} = R\ddot{R} + \frac{3}{2}\dot{R}^2 + \frac{4\nu_l\dot{R}}{R} + \frac{2\sigma}{\rho_l R}, \quad (2.1)$$

with  $R$ ,  $\dot{R}$ , and  $\ddot{R}$  as bubble radius, bubble wall velocity, and bubble wall acceleration, respectively.  $p_b$  is the inner bubble pressure and  $p_\infty$  the pressure in the liquid.  $\rho_l$  and  $\nu_l$  are density and kinematic viscosity of the liquid phase.  $\sigma$  is the surface tension of liquid water in contact with its vapour. Dynamics of spherical bubbles therefore depend on the difference between pressures in the bubble and the liquid, surface tension – larger for smaller bubbles –, viscous forces – larger for smaller bubbles and higher bubble growth rates –, and the bubble wall acceleration. Because the Rayleigh-Plesset equation was initially derived based on the assumption of an incompressible liquid phase, the equation has been extended to consider compressibility and the energy loss attributable to the generation of shock waves in the liquid. A derivation of the Rayleigh-Plesset equation and a bubble dynamics equation considering liquid compressibility are later explained in section 4.1.1. Simulation results of spherical single bubble dynamics are presented in section 5.2.1.

Neglecting surface tension, viscous effects, liquid compressibility, and non-condensable gas content in the bubble, Rayleigh (1917) derived a formula to calculate the collapse time of a vapour bubble,  $t_{\text{coll}}$ , from maximum Radius,  $R_{\text{max}}$ , to minimum radius,  $R \rightarrow 0$ , under a given pressure difference:

$$t_{\text{coll}} = 0.915 \sqrt{\frac{\rho_l R_{\text{max}}}{p_\infty - p_v}}. \quad (2.2)$$

Volumes of liquid water pursue small free surfaces with other substances or phases because of their surface tension. The attraction of molecules of equal substances towards each other – called *cohesion* – generates much larger forces than the bond of molecules of different substances – called *adhesion*. Molecules at an interface between two phases are bond more to molecules of the same substance and therefore a force pointing away from the interface is generated. Accordingly, the difference between cohesion and adhesion causes surface tension. As a result, gas bubbles in liquid water strive for a spherical shape, whereas the sphericity of a bubble strongly depends on its size. As can be seen in equation (2.1) the surface tension force of a spherical bubble,  $\left(\frac{2\sigma}{\rho_l R}\right)$ , is anti-proportional to the bubble radius,  $R$ . Consequently, surface tension forces are smaller for larger bubbles and asphericity is more likely to occur.

Furthermore, surface tension is important for the consideration of the stability of gas bubbles. Based on the Rayleigh-Plesset equation, an expression for the critical bubble radius, above

## 2.1 Cavitation

which rapid growth is expected, was derived by Blake (1949b) and Neppiras and Noltingk (1951):

$$R_c = \sqrt{\frac{9\gamma_h m_g \mathcal{T}_b \mathcal{R}_g}{8\pi\sigma}}. \quad (2.3)$$

$\gamma_h$  is the ratio of specific heats,  $m_g$  the mass of gas in the bubble,  $\mathcal{T}_b$  the temperature in the bubble, and  $\mathcal{R}_g$  is the gas constant. Bubbles of radii smaller than  $R_c$  can exist in stable equilibrium, while bubbles of radii larger than  $R_c$  are in unstable condition. Decreasing the liquid pressure below a critical threshold pressure – the Blake threshold pressure – results in rapid growth of a gas bubble (Brennen (2005), Louisnard and González-García (2011)) and introduces cavitation inception. The threshold pressure by Blake is defined as:

$$p_{\infty,c} = p_v - \frac{4\sigma}{3} \sqrt{\frac{8\pi\sigma}{9\gamma_h m_g \mathcal{T}_b \mathcal{R}_g}}. \quad (2.4)$$

### 2.1.3 Mechanisms to Generate Cavitation

Cavitation inception usually occurs because of vapourisation of cavitation nuclei which do not dissolve in the liquid. Since clean liquid water, free of cavitation nuclei, can withstand high tension without vapourising, cavitation nuclei represent certain *weak spots* for cavitation to begin. On the other hand, cavities can even be generated without the presence of initial nuclei by very high tension or by the deposition of high amounts of energy into the liquid. Hereinafter, three main mechanisms to cause cavitation are briefly described. Although this work mainly deals with hydrodynamic cavitation, light is shed on other types of cavitation as well.

#### Acoustic Cavitation

In acoustic cavitation, bubbles are caused to oscillate by acoustic waves travelling through a liquid. These waves alternately exert high tension and high pressure on existing bubbles in the liquid, Neppiras (1980). Acoustic waves are usually generated by devices moving at a high frequency such as ultrasonic horns, Yasui et al. (2008), Žnidarčič et al. (2014), Biluš et al. (2017). When cavitation nuclei are exposed to acoustic waves, they may start to vapourise and grow to larger bubbles when a tension phase of the wave passes by. As a compression phase of the shock wave passes the bubbles, they may collapse. The bubble oscillations depend on amplitude and frequency of the sound waves as well as gas content in the bubbles. Bubble dynamics can involve multiple growth and collapse processes occurring at a much higher frequency than the one of the generating device. Even if there are no cavitation nuclei present, shock waves are able to create voids in the liquid if their amplitudes generate enough tension in the water. These phenomena can especially take place when aggressive shock waves are radiated by preceding cavitation collapses. Acoustic cavitation is used in terms of surface activation, treatment or cleaning (Maisonhaute et al. (2002), Zoetewij et al. (2009), Reuter

et al. (2017)), for medical treatments such as sonophoresis (Tezel and Mitragotri (2003)), lithotripsy (Jamaluddin et al. (2011)), and tumour treatment (Kennedy (2005)), as well as for the erosion assessment of materials (ASTM Standard G32-10 (2010), Arndt et al. (2007)).

### Laser-Induced Cavitation

When focusing a laser onto a point in a liquid it may cause an optical breakdown that generates a plasma. Once the plasma expands, it creates a cavity in form of a single vapour bubble in the liquid. If done precisely, an isolated spherical bubble can be produced. Although the generation process of laser-induced bubbles differs from those in other technical devices, the bubble behaviour is similar. This technique therefore allows the investigation of single bubbles in defined environments to understand the physics of isolated bubble dynamics. Laser-induced cavitation bubbles have been experimentally investigated by Lauterborn and Bolle (1975), Vogel and Lauterborn (1988), Isselin et al. (1998), Noack and Vogel (1998), Philipp and Lauterborn (1998), Lauterborn and Kurz (2010), Lauterborn and Vogel (2013), Reuter and Mettin (2016), Reuter et al. (2016), and Supponen et al. (2016).

### Hydrodynamic Cavitation

In technical flows, such as flows around stationary parts, e.g. rudders, nozzles, or valves, as well as flows around rotating machinery, e.g. propellers, pumps, or turbines, high local flow velocities usually accompany low local pressures. Once cavitation nuclei travel through these regions, they grow to larger bubbles which may accumulate and form macroscopic types of cavitation. When these structures reach regions of higher liquid pressure again, they rapidly collapse. Both steady and periodically fluctuating cavitation can cause losses in efficiency of a regarded device. In addition, periodically shedding cavitation can cause vibrations, radiate noise or cause material damage. Significant experimental investigations of hydrodynamic cavitation are those of Arndt et al. (1991), Kjseldsen et al. (2000), Callenaere et al. (2001), Dular and Petkovšek (2015), Ganesh et al. (2016), and Pelz et al. (2017).

To classify and compare cases of hydrodynamic flows, the difference between liquid far field pressure and vapour pressure relative to a reference pressure,  $\Delta p$ , of the flow is used to define a dimensionless quantity, called *cavitation number*:

$$\sigma_{\text{cav}} = \frac{p_{\infty} - p_v}{\Delta p} . \quad (2.5)$$

In case of defined upstream pressure,  $p_{\text{us}}$ , and downstream pressure,  $p_{\text{ds}}$ , the reference pressure may be defined as:

$$\Delta p = p_{\text{us}} - p_{\text{ds}} . \quad (2.6)$$

## 2.1 Cavitation

On the other hand, in a flow of defined flow velocity in the far field,  $u_\infty$ , the dynamic pressure can be used to define the characteristic pressure difference:

$$\Delta p = \frac{1}{2} \rho_1 u_\infty^2. \quad (2.7)$$

Although other scale effects can play a role in cavitation (see section 2.3.2), qualitatively similar cavitation conditions can usually be obtained for the same cavitation number. Small cavitation numbers imply a higher risk of cavitation inception as well as a greater extent in vapour volume.

### 2.1.4 Structures of Cavitation in Hydrodynamic Flows

In addition to single cavitation bubbles, different shapes of macroscopic cavitation volumes, that contain accumulations of single cavitation bubbles, can be identified. These cavitation structures occur in flows over different geometries and can be distinguished depending on their shape and dynamical behaviour.

#### Bubble Cavitation

Isolated cavitation bubbles are commonly observed in regions of cavitation inception and when macroscopic forms of cavitation have not yet fully developed. Bubble cavitation can also be generated from rough surfaces that incorporate gas pockets. Further downstream a flow, single bubbles can accumulate and form larger vapour structures by collision and coalescence with other bubbles. Furthermore, single cavitation bubbles can be observed at the downstream end of sheet cavitation as well as during the last stages of a cavitation cloud collapse.

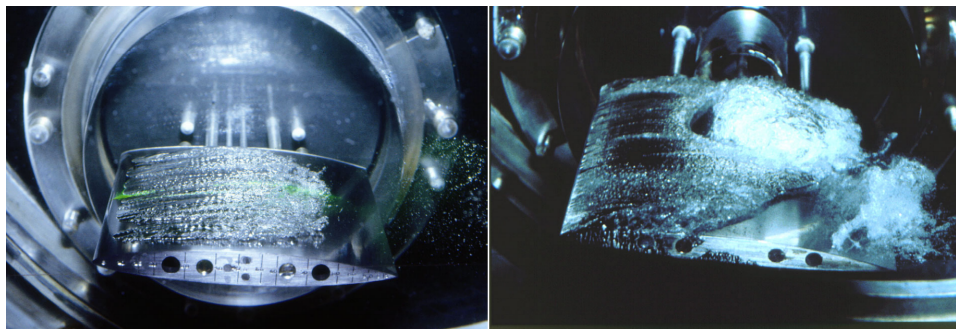


**Figure 2.3:** Sheet and cloud cavitation on a hydrofoil from Franc (2001)

## Sheet Cavitation

An agglomeration of cavitation bubbles can form a vapour structure referred to as *sheet cavitation* which is usually attached to the leading edge of a body. The generation of sheet cavitation can be shifted just downstream behind the lowest pressure region owing to bubble trajectories that deviate from the streamlines of the flow, known as *bubble screening*, Kuiper (2010). Sheet cavitation can be more or less steady when growth and collapse of the bubbles that travel through it are always taking place in the same locations. In this case, the observed length of the sheet cavitation is constant. Figure 2.3 (left) shows sheet cavitation generated at the leading edge on the suction side of a two-dimensional hydrofoil. It is usually found that the length of a sheet cavitation starts to oscillate when the vapour volume reaches a certain extent. Sheet cavitation can develop into cloud cavitation when it is shed from a surface.

## Cloud Cavitation

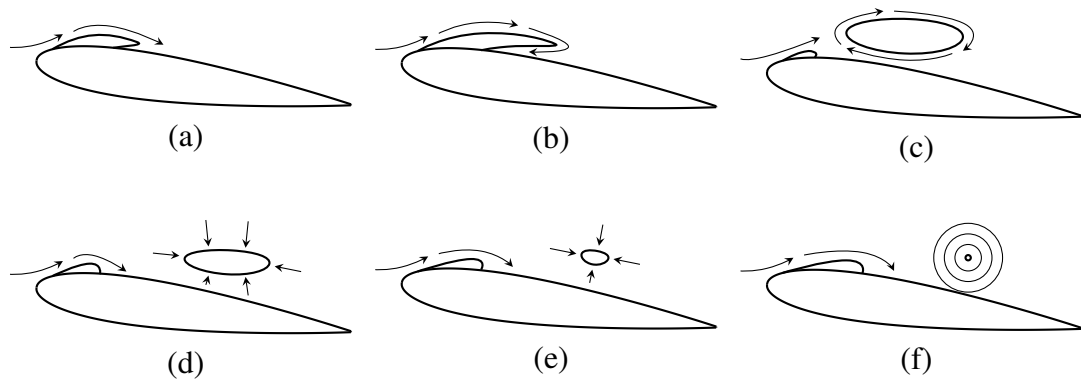
*Cloud cavitation* usually develops from a sheet cavitation attached to a body. If a sheet cavitation is surrounded by a circulation in the flow, a reverse flow can develop along the surface of the regarded body, piercing the sheet cavitation, and causing its shedding from the body. This reverse flow is referred to as the *re-entrant jet* and its occurrence was identified by Knapp et al. (1970). The re-entrant jet is found as one of the main mechanisms to cause periodic cloud shedding, Franc (2001), Callenaere et al. (2001). Figure 2.3 (right) displays the formation of cloud cavitation by shedding from an attached sheet cavitation. Further downstream, near the trailing edge of the hydrofoil, another cloud cavitation is collapsing into smaller cavitation structures.

Figure 2.4 sketches a process of periodic cloud shedding caused by a re-entrant jet. Directions of local flow velocities around the vapour cavities are depicted with arrows. A flow from left to right causes the growth of a sheet cavitation, consisting of an agglomeration of single bubbles, in the low pressure region on the suction side of a hydrofoil (see Figure 2.4 (a)-(b)). At the beginning (see Figure 2.4 (a)), the sheet cavitation and the flow are attached to the foil. Flow separation starts in Figure 2.4 (b), where a reversed flow behind the sheet cavitation develops along the hydrofoil surface – the re-entrant jet. As shown in Figure 2.4 (c), a cloud cavitation is shed from the hydrofoil surface by the re-entrant jet and transported further downstream with the flow. The cloud cavitation travels further downstream into regions of higher pressure and starts to collapse (see Figure 2.4 (d)-(e)). Finally, the cloud collapses to its minimal volume and generates a shock wave of high pressure amplitude, which is radiated spherically away from the position of collapse (see Figure 2.4 (f)). At the same time, a new sheet cavitation starts to grow on the suction side of the hydrofoil (see Figure 2.4 (d)-(f)). The process repeats itself in periodic manner.

Another mechanism to cause the transition from sheet to cloud cavitation appears because of the generation of shock waves generated further downstream of the considered geometry as shown in the experimental work of Ganesh et al. (2015, 2016) and Mäkiharju et al. (2015) and in numerical simulations of Budich et al. (2018). Therein, a cavitation cloud, that collapses

## 2.1 Cavitation

downstream from the regarded geometry, radiates a shock wave. As the shock travels further upstream, it reaches the sheet cavity attached to the leading edge of the hydrofoil. The authors found that under certain conditions, shock waves are the dominant shedding mechanism of partial cavities. Especially for low vapour fractions in the partial cavities, where the local speed of sound was significantly reduced, shedding ascribed to shock waves occurred.



**Figure 2.4:** Shedding of a cavitation cloud by a re-entrant jet

### Vortex Cavitation

Low pressures prevail in centres of flow vortices, Franc and Michel (2005). Cavitation nuclei are attracted to the low pressure regions and their traces can deviate substantially from the streamlines of the flow. Vapourisation processes start at the outer surface of the gas nuclei and lead to the growth of cavitation bubbles. Vortices can develop from flow separation on a hydrofoil to form cloud cavitation. On the tips of propeller blades or the hubs of propellers, tip vortices are often generated and they can maintain very low pressures in their centres and enable the cavitation regions to remain stable much further downstream from the propeller. Tip vortex cavitation structures that encounter material surfaces will often collapse and possibly cause material damage.

### Supercavitation

When a body is fully surrounded by a macroscopic cavitation structure, this is called *supercavitation*. For supercavitation to occur, cavitation numbers are usually requested to be very low. Supercavitation can occur on hydrofoils as well as on propellers. As explained by Achkinadze (2001), for propellers, special wedge-shaped blade profiles were developed in order to reduce cavitation occurring directly on the blades by delaying the cavitation region further downstream. Therein, cavitation erosion of the propeller blades themselves can be decreased and the propeller's efficiency can be increased. On the other hand, as a body fully submerged in a vapour cavity is exposed to a lot lower resistance than in liquid water, supercavitation has

also shown to be beneficiary in some engineering applications. In naval defence research, investigations on designs for supercavitating torpedoes were conducted, Alyanak et al. (2006). Therein, a vapour cavity is supposed to be generated around the entire torpedo in order to lower its resistance and increase the torpedoes' speeds.

## 2.2 Cavitation Erosion

In the vicinity of a material surface, collapses of vapour structures can cause substantial material damage, referred to as cavitation erosion. The extent and temporal progress of surface damage depend on the behaviour of cavitation structures (e.g. vapour volume, shedding frequency), their shape and collapse distance to the solid surface, local flow conditions, and properties of the surface material. Unsteady forms of cavitation that end with bubble collapses close to a material surface, are mostly correlated with cavitation damage. Cloud and vortex cavitation have been found to show the highest erosion aggressiveness, Berchiche et al. (2003), Grekula and Lindell (2007), van Terwisga et al. (2009), Petkovšek and Dular (2013), Jian et al. (2015), Dular and Petkovšek (2015). Although erosion is a process caused by high pressure impacts, concentrated on microscopic areas within short durations of time, macroscopic properties like yield strength, ultimate strength, and hardness can be used to characterise a material's resistance to cavitation erosion. Erosion defines a process of material loss, but surfaces are usually plastically deformed and hardened, before material loss takes place, Berchiche et al. (2002), Franc and Michel (2005), Chahine et al. (2014a). A process of cavitation erosion is therefore characterised by different periods.

### 2.2.1 Periods of Cavitation Erosion

Erosion is a damaging process wherein material of a surface is removed. Pressure impacts that generate stresses higher than a threshold stress of a material can cause a surface to first deform and harden. This threshold stress is usually assumed equal to the yield stress of the regarded material. After a longer time of exposure, the surface is subjected to volume loss. Impacts that generate higher surface stresses than the ultimate tensile strength can cause direct material loss. Macroscopically, however, surface deformation commonly occurs before mass is removed from a surface. Processes of cavitation-induced erosion can be classified into different phases, Steller and Kaczmarzyk (2000), Billet et al. (2005), Arndt et al. (2007), ASTM Standard G32-10 (2010), Choi et al. (2012), Chahine et al. (2014b). Figure 2.5 sketches the volume loss rate over time for a surface that is exposed to cavitation erosion. Initially, during the *incubation period* (1), the material surface is deformed. The deformation rate is supposed to be constant and material loss to be negligible. Therein, microscopic material deformation and surface hardening occurs, increasing the materials resistance to stresses. Material loss starts during the *acceleration period* (2) and, at the beginning, the volume loss rate increases significantly. Depending on the flow field and the strain-hardening properties of the regarded material, a maximum volume loss rate is reached. Afterwards, the volume loss rate decreases

## 2.2 Cavitation Erosion

during a *deceleration period* (3). An interaction between flow field and the roughened surface occurs. Herein, gas pockets in large craters can damp incoming pressure waves, Chahine et al. (2014b), but also generate additional free nuclei, Groß and Pelz (2017). Finally, a *stationary erosion period* (4) with a constant volume loss rate is achieved owing to an equilibrium between flow field and the impacted material surface.

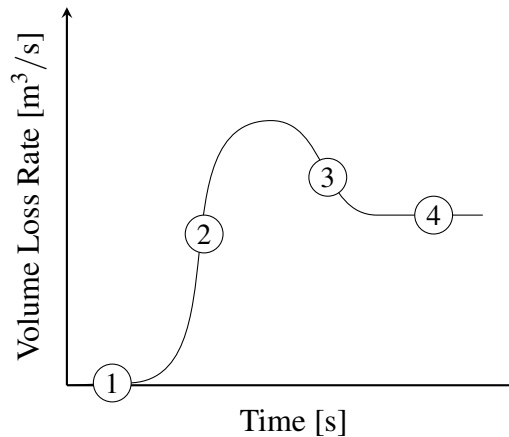


**Figure 2.5:** Erosion process with characteristic periods: (1) incubation period, (2) acceleration period, (3) deceleration period, (4) stationary erosion period

Depending on flow conditions, material properties, as well as interactions between flow and material, different shapes of the curve shown in Figure 2.5 can develop. It is even possible that the latter two periods do not appear. In cases of cavitation erosion, where cavitation is not generated on the affected surface itself, the final period does not necessarily show a constant volume loss rate, because the interaction between cavitation and the surface is negligible.

### 2.2.2 Erosion Mechanisms: Near-Wall Bubble Collapse

Cloud and vortex cavitation are considered to be two of the most aggressive types of cavitation, which commonly occur in technical flows. Since a macroscopic cavitation structure incorporates single bubbles, a collapse of such a structure embraces collapses of many single bubbles interacting with each other. In dense bubble accumulations, consecutive collapses of neighbouring bubbles can result in an amplification of the pressures after collapse, Lauer et al. (2012a), Ma et al. (2015a). To understand the behaviour of macroscopic cavitation structures, it is inevitable to investigate the physics involved during the complex process of a single bubble collapse in the vicinity of a solid wall. Extensive research has been conducted to study single cavitation bubbles experimentally and numerically. Collapses of single laser-induced bubbles in undisturbed fields, acoustic fields, and near solid boundaries were experimentally studied by Lauterborn and Bolle (1975), Vogel and Lauterborn (1988), Philipp and Lauterborn (1998), Noack and Vogel (1998), Lauterborn and Vogel (2013), Brujan et al. (2002), Lauterborn and Kurz (2010), Reuter and Mettin (2016), Reuter et al. (2016), Supponen et al. (2016),

Dular et al. (2018), Sagar et al. (2018), and Sagar (2018). Numerical simulations of near-wall single bubble collapses were conducted by Osterman et al. (2009), Lauer et al. (2012b), Chahine and Hsiao (2015), Pöhl et al. (2015), and Koch et al. (2016).

As reported by Vogel and Lauterborn (1988), during a spherical bubble collapse in an undisturbed field, about 73 % of the potential energy, which is stored in the bubble at the beginning of the collapse, is transformed into acoustic energy, in order to generate shock waves of high pressure amplitudes. For bubble collapses close to solid boundaries, the emitted acoustic energy depends on the size of a bubble, its gas content, and its relative distance to the boundary. When a bubble collapses close enough to a material surface, this process is always asymmetric because the flow through the bubble is disturbed by the solid surface. This in turn will generate a liquid waterjet, called *microjet*, which flows through the bubble, always pointing in direction of the material surface. As the bubble collapse process differs with varying distance of the bubble from the wall, a dimensionless stand-off distance was introduced as:

$$\gamma = \frac{R_{\max}}{H} . \quad (2.8)$$

Here,  $R_{\max}$  is the maximum bubble radius at the beginning of the bubble collapse and  $H$  the stand-off distance of the bubble centre from the solid wall. For single bubble collapses near solid boundaries,  $\gamma$  serves well to characterise the flow phenomena and surface damage relative to the initial bubble size and its stand-off distance from the wall.

Philipp and Lauterborn (1998), Isselin et al. (1998), and Dular et al. (2018) studied the potential erosion caused by single laser-induced cavitation bubbles near solid boundaries. During the asymmetric process of a near-wall bubble collapse, multiple mechanisms were identified that possibly lead to erosion of the surface:

1. A high velocity liquid jet, referred to as *microjet*, piercing the bubble and hitting the surface at velocities of more than 100 m/s. As shown by Field (1991) and Haller Knežević (2002), the impact of the jet onto the wall leads to the generation of a shock wave radiated perpendicularly away from the wall. This phenomenon generates a significantly high pressure near the wall – the so called *water hammer pressure* found by Joukowski (1898). Plesset and Chapman (1971) already found the pressure to be higher than the yield strengths of common copper alloy or steel materials.
2. The collapse of the toroidal structure, obtained after the piercing by the microjet, radiates pressure waves through the liquid, which can superpose and thus amplify each other in order to damage the nearby surface.
3. Cavitation structures can rebound after the first collapse of the vapour torus. Superpositions of low pressure regions of different shock waves cause high tensile stresses in the water, which leads to the growth of new cavitation structures. Collapses of the newly generated cavitation structures radiate further shock waves with the potential to damage the solid boundary.

For different  $\gamma$ , varying degrees of erosion potential are expected for these mechanisms. For example, Dular et al. (2018) showed that the erosion potential of the microjet decreases with

## 2.2 Cavitation Erosion

increasing  $\gamma$  and vanishes at  $\gamma \approx 2.0$ . On the contrary, the erosion potential of collapses of the toroidal cavitation structures increased from  $\gamma = 0.05$  to  $\gamma \approx 1.0$  and then decreased. Almost no erosion was found for  $\gamma > 2.5$ .

Figure 2.6 sketches the collapse of a single bubble close to a rigid wall on a cross-section through the centre of the bubble. Flow velocity vectors are depicted as arrows around the bubble. In Figure 2.6 (a) the bubble is shown at its maximum size within a normalised distance of  $\gamma \approx 1.5$  from the solid wall. The pressure in the bubble has decreased fairly below the liquid pressure around it, resulting in compression of the bubble. The surrounding liquid therefore flows towards the bubble from all directions. Because the flow from the bottom is disturbed by the solid wall, more liquid flows from the top towards the bubble. As a result, the bubble moves slightly towards the rigid wall and is asymmetrically compressed (see Figure 2.6 (b) and (c)). The bubble asymmetry progresses and a high velocity microjet develops, flowing through the bubble (see Figure 2.6 (c)). Finally, the microjet pierces the bubble and hits the sheet of liquid between bubble and solid wall, which is at rest (see Figure 2.6 (d)). Depending on the velocity of the microjet, this rapid deceleration can result in the formation of a shock wave of high pressure. As shown in Figure 2.6 (e), the bubble forms a vapour torus, which is further compressed. Accordingly, the microjet flows towards the rigid wall and is decelerated to zero, leading to a second potential shock wave formation. Both positions of deceleration of the microjet present potential water hammer impacts. Figure 2.6 (f) depicts the collapse of the torus, forming complex shock waves which can interact with each other in the original bubble centre, at the solid wall, and above the bubble, away from the solid wall. Depending on the normalised wall distance of the bubble, the shock waves can superpose to generate high pressures to damage the rigid boundary. Furthermore, tension phases of the shock waves can superpose and generate new cavities in the water. Collapses of these cavitation structures are called *rebounds* and have a damaging potential, too.

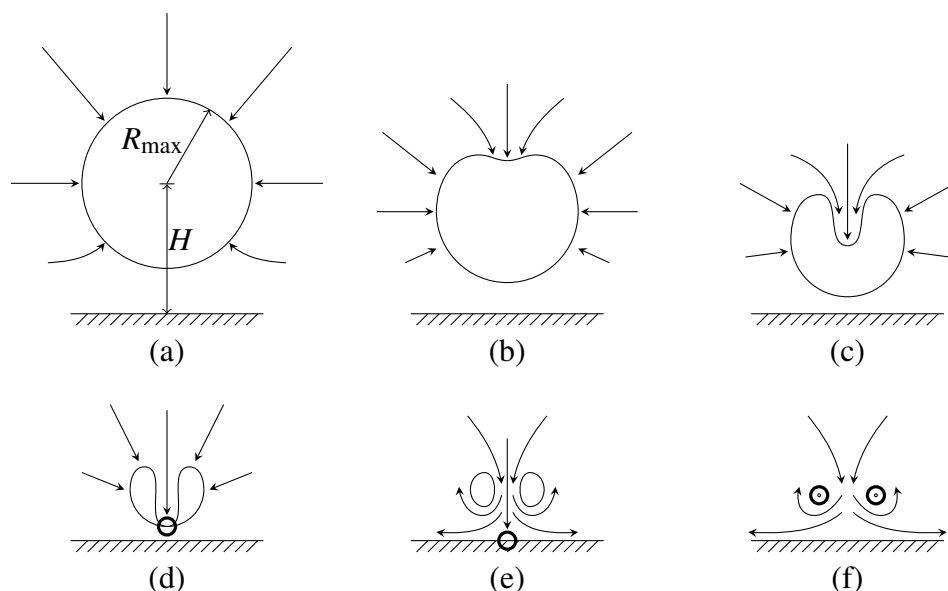


**Figure 2.6:** Collapse of a single cavitation bubble near a solid wall

Although collapses of macroscopic cavitation structures such as cloud or vortex cavitation are regarded as main mechanisms to cause erosion, collapses of single bubbles need to take place in the vicinity of a surface, for surface damage to occur. It was shown by Vogel et al. (1996), Noack and Vogel (1998), Lauterborn and Vogel (2013), and Supponen et al. (2017) that the pressures and velocities of shock waves that are generated by collapses of laser-induced cavitation bubbles are rapidly damped as these shock waves travel through the liquid. For shock waves that expanded in radial direction,  $r$ , Vogel et al. (1996) found a pressure decay proportional to  $r^{-2}$  for shock pressures larger than 100 MPa. For lower pressures, they found a decay of shock pressures proportional to  $r^{-1.06}$ . Noack and Vogel (1998) found that, during the collapse of the bubble, initial shock velocities of up to 5000 m/s and pressures up to 11 GPa were reached. As the shock waves expanded, the shock pressures decreased initially proportional to  $r^{-1.3\pm 0.2}$  up to distances of two times the initial radius of the shock,  $r_0$ . Later on, in larger distances of  $r > 2r_0$ , the shock pressures even decayed at rates of  $r^{-2.2\pm 0.1}$ . For laser-induced bubbles collapsing near a rigid surface within  $3 < \gamma < 40$ , Supponen et al. (2017) stated a pressure decay proportional to  $r^{-1.249\pm 0.003}$  that was obtained from a function fitted to the experimental data.

Even though the collapse pressures after shock generation can be of orders as high as 10 GPa, pressures of fully developed shock waves are rapidly decaying as they travel away from the centre of shock generation. Generally, for high pressure shock waves which commonly occur near the centre of shock emission, pressure decay is approximately proportional to  $r^{-2}$  and for lower pressures in the far field approximately proportional to  $r^{-1}$ . Therein, especially near the collapse location of a bubble, the pressure decays non-linearly. Collapses that take place too far away from a surface are generally not directly responsible for cavitation damage but can only trigger oscillations of other cavitation bubbles. For the aforementioned reasons, it is supposed that all processes of collapses of cavitation structures, which cause surface damage, require single cavitation bubbles to be located within the immediate vicinity of the surface considered.

### 2.2.3 Properties of Solid Materials

In general, materials of lower strength and hardness tend to be more endangered to erosion than materials of higher strength and hardness, Hattori et al. (2009), Hattori and Takinami (2010). Strength properties of a material can be derived from a tensile test. The yield strength,  $\sigma_y$ , is the limiting stress of a material at which plastic deformation occurs. A stress higher than the yield strength is supposed to induce irreversible deformations in the material. Plastic deformation of a material can proceed until stresses in the structure exceed the ultimate strength,  $\sigma_u$ , above which a material is supposed to break under tension. Although they represent macroscopic material properties, it is often supposed that impact pressures, attributed to cavitation, which exceed the yield strength of the regarded material, cause surface deformation in forms of pits, Franc and Riondet (2006), Franc et al. (2014), Chahine and Hsiao (2015). Furthermore, impacts that introduce stresses larger than the ultimate strength are supposed to cause immediate material loss.

### 2.3 Laws of Similarity and Scale Effects

In addition to a material's strength properties, its hardness classifies its resistance against permeation by another material. Hardness of a material is usually tested using permeation of an object of standardised shape. Especially during the incubation period, material layers near the impacted surface are consecutively hardened. Therein, the material's resistance to further impacts can locally increase. With increasing distance from the surface the hardness of the material decreases, Chahine (2014b).

Although it is not strictly a material property, Franc et al. (2012), Chahine et al. (2014a), and Berchiche et al. (2002) found the strain rate to play a significant role for the progress of erosion on a surface. It is defined as:

$$\dot{\epsilon}_L = \frac{\Delta\epsilon_L}{\Delta t} . \quad (2.9)$$

$\Delta\epsilon_L$  is the mean strain caused by an impact of peak duration  $\Delta t$ . It was found that the flow stress – the stress required to sustain plastic flow – increases with the strain rate, Chahine et al. (2014a). For strain rates  $\dot{\epsilon}_L < 1 \cdot 10^3/\text{s}$  this increase is more or less logarithmic, whereas for  $\dot{\epsilon}_L > 1 \cdot 10^3/\text{s}$  the flow stress increases stronger. Carnelli et al. (2012) conducted nanoindentation tests to find pressures of comparable cavitation impacts. They found that on average, a strain of 3 – 4% is caused by a cavitation impact. Konno et al. (1999) and Soyama et al. (2011) conducted measurements using piezoelectric ceramics and PVDF transducers to find that an average peak duration of a cavitation impact is approximately 10  $\mu\text{s}$ . Based on these measurements, Chahine et al. (2014a) proposed a conservative approach, using  $\Delta\epsilon_L = 5\%$  and  $\Delta t = 10\mu\text{s}$ , to obtain an estimate for the strain rate of a cavitation impact of  $\dot{\epsilon}_L = 5 \cdot 10^3/\text{s}$ .

Accordingly, it can be concluded that the flow stress that needs to be exceeded by a cavitation impact to cause plastic deformation is, firstly, usually larger than the yield strength of the material, and, secondly, varies non-linearly with the strain rate of the regarded impact. Nonetheless, it is very difficult to accurately quantify the influence of strain rate for cavitation erosion, because strain rates strongly vary depending on the respective impacts. Thus, considering the yield strength of a material as the limit for plastic flow, is a conservative approach to investigate cavitation erosion.

## 2.3 Laws of Similarity and Scale Effects

Various dimensionless quantities are used to characterise and compare problems of flows in general as well as involving cavitation. Based on these quantities, specific flow phenomena have shown to be qualitatively similar if the ratio between characteristic flow forces or quantities is constant. As long as this ratio is constant, the flows can show similar behaviour while differing in other spatial, temporal, or flow quantity related scales. In the following, the most important laws of similarity for hydrodynamic cavitating flows are presented. Finally, a discussion of how these laws apply or deviate for phenomena related to cavitation erosion is given.

### 2.3.1 Laws of Similarity

Dimensionless quantities in fluid dynamics often serve to compare flows of similar behaviour but different flow conditions. For cavitating flows, the cavitation number (see equation (2.5) in section 2.1.3) is often used for these purposes. Further important quantities are listed below:

- *Reynolds number:*

$$\text{Re} = \frac{\rho u_{\text{ref}} L_{\text{ref}}}{\mu} . \quad (2.10)$$

$\rho$  is the density and  $\mu$  the viscosity of the regarded fluid, respectively.  $u_{\text{ref}}$  is the reference velocity and  $L_{\text{ref}}$  the reference length of the case considered. The Reynolds number is a ratio of inertia forces to viscous forces in the flow and is used to characterise the turbulence in a flow. Although the values of the Reynolds number vary for different flow problems, it serves to determine whether similar flows are of laminar, transitional, or turbulent behaviour. In model tests of maritime flows, it is generally not possible to achieve Reynolds similarity of the regarded full-scale geometry.

- *Strouhal number:*

$$\text{St} = \frac{f L_{\text{ref}}}{u_{\text{ref}}} . \quad (2.11)$$

$f$  is the oscillation frequency of the regarded quantity. Flows involving vortex shedding can be characterised by the Strouhal number. In cavitating flows, it is used to characterise the shedding behaviour of cloud cavitation.

- *Mach number:*

$$\text{Ma} = \frac{u_{\text{ref}}}{c_{\infty}} . \quad (2.12)$$

$c_{\infty}$  is the speed of sound in the regarded liquid. Compressible flows of high velocities are often characterised by the Mach number. It relates the velocity of a flow to the speed of sound in the regarded fluid. For  $\text{Ma} < 0.3$  a flow is considered incompressible, for  $0.3 \leq \text{Ma} < 1.0$  subsonic, for  $1.0 \leq \text{Ma} < 5.0$  supersonic, and for  $\text{Ma} \geq 5.0$  hypersonic.

- *Kinematic Similarity:*

$$\frac{u_1}{v_1} = \frac{u_2}{v_2} . \quad (2.13)$$

Here,  $u, v$  are two velocities of a regarded case and the indices 1 and 2 indicate two different scales. Kinematic similarity assures that the ratio of two velocities is equal in different comparable scales (e.g. in full-scale and model-scale). For model tests of propellers, kinematic similarity between the inflow velocity and the rotational velocity induced by the propeller revolution is accomplished.

### 2.3.2 Scale Effects on Cavitation and Cavitation Erosion

In many cases, dimensionless quantities can be used to compare flows of different scales. In other cases, dependencies of physical phenomena on specific dimensionless quantities were identified. Hereinafter, scale effects on cavitation and cavitation erosion are elaborated.

#### **Cavitation**

Experiments of cavitating flows often rely on the cavitation number in order to categorise a flow problem. For some cases of the same cavitation number, a qualitatively similar behaviour of cavitation can be obtained. Nevertheless, cavitation can also be influenced by e.g. turbulence, free gas nuclei, water temperature, or surface roughness.

As shown in 2.1, the vapour pressure of water depends on its temperature. Higher temperatures increase the vapour pressure and therefore the possibility of cavitation to occur. Besides temperature, nucleation was found to have a large influence on cavitation inception. As reported by Briggs (1950), water can withstand tension of up to 277 bar when it is not contaminated with any particles or free gases. Hence, the distribution of nuclei in the water can lead to earlier inception of cavitation, Kuiper (2010). In technical flows, nuclei are always present, but measurements of these free gases and particles in the water is a rather difficult subject. For experiments, the content of dissolved gas in the water is often mentioned as free gases are more likely to appear when the gas content is high.

Gas bubbles do not only appear in the free stream of a flow but they can also be attached to a surface. Surfaces of high roughness increase the possibility of gas pockets to form. These gas pockets can generate nuclei in different ways. A nucleus can be separated from the surface when the pressure falls below a critical threshold. Otherwise, a nucleus can be generated in super-saturated liquids by overcoming the nucleation energy or by a fluid flow along a gas pocket, Brennen (1995). In experiments, Groß and Pelz (2017) used flows along gas pockets to periodically generate free nuclei.

Furthermore, owing to the presence of free gas bubbles in a flow, the speed of sound in a bubbly mixture can locally decrease to just a few metres per second, which is lower than the speed of sound in either of the single phases, Kiefer (1977). In experimental investigations, Ganesh et al. (2016) found that the shedding of sheet cavitation by shock waves occurred when the local Mach number exceeded unity.

Although the speed of sound in liquid water lies about 1500 m/s and is not reached by any of the flows considered, a cavitating flow can become compressible by various mechanisms. One mechanism is the abrupt acceleration or deceleration of liquid water that is the case for the impact of a microjet onto a rigid boundary. This phenomenon is also called water hammer and was first identified by Joukowski (1898) during experiments of rapidly closing valves in water pipes. Shock waves are, therein, generated by rapid deceleration of the liquid.

Moreover, the behaviour of cavitation can deviate whether a flow is laminar or turbulent. If the flow over a body such as a hydrofoil is mostly laminar, flow separation may occur early and influence cavitation inception as described by Kuiper (2010). Turbulent boundary layers at higher Reynolds numbers can delay flow separation because more energy is transported from the outer flow into the boundary layer. In these cases, turbulent flow separation usually occurs further downstream compared to laminar flow separation which can change the position of cavitation inception, Schlichting and Gersten (2017), Kuiper (2010).

Keil et al. (2011), Pelz et al. (2014), and Pelz et al. (2017) showed that, for a constant cavitation number but higher Reynolds numbers, periodic cloud shedding is more likely to occur than sheet cavitation. In experiments, Pelz et al. (2014) found a critical Reynolds number that characterises the dynamic behaviour of sheet and cloud cavitation. Below this number, sheet cavitation occurred without the presence of cloud cavitation and above it, periodic shedding of cloud cavitation was observed. This behaviour could be attributed to the influence of viscous effects on the development of the re-entrant jet. Furthermore, Keller et al. (1999) found that, at the same cavitation number, a higher reference velocity and a larger geometric scale – both leading to an increase of Reynolds number – cause earlier cavitation inception and greater vapour production.

In experimental investigations of cavitation on a hydrofoil, Hao et al. (2018) found an influence of surface roughness on the generation of cloud cavitation. A higher surface roughness thus led to a larger maximum volume of cloud cavitation which can be related to the generation of additional nuclei by gas pockets in rough surfaces.

For model-tests of propellers, usually only the cavitation number and kinematic similarity are considered. Differences in cavitation behaviour may then result because of higher Reynolds numbers (turbulence) and higher Mach numbers (compressibility), different temperatures, and different nuclei distributions in full-scale flows compared to model-scale.

### **Erosion**

Some of the aforementioned scale effects on cavitation have to be considered with regard to cavitation erosion as well. Changes in nuclei distribution, geometric scale, or velocity may even have a stronger influence on the progress of erosion than just on the observed cavitation behaviour. Influences on cavitation and cavitation erosion have to be kept in mind when conducting experiments at a specific geometrical scale. Especially for cavitation erosion, large dependencies on velocity and geometric scale have been shown. Dular et al. (2005) and Dular et al. (2006) found that an increase of the gas content in water lowers the aggressiveness of cavitation erosion, even though the extent and behaviour of cavitation is qualitatively similar. The authors concluded that a higher gas content lowers the sonic velocity in the water and increases compressibility. In turn, the shock wave pressures generated at cavitation bubble collapses are attenuated stronger as the shock waves travel at lower velocities.

Furthermore, at constant cavitation numbers, erosion rates increase significantly with an increase in velocity. This can be explained by looking at the cavitation number (see equation (2.5)). To keep the cavitation number constant when increasing the velocity, the difference between free stream pressure and vapour pressure needs to be increased as well. An increased far-field pressure thus causes more aggressive bubble collapses with higher collapse pressures.

It has been shown that erosion rates are proportional to a higher power of velocity, Shal'nev et al. (1966), Auret et al. (1993), Dular et al. (2005). Hattori et al. (2009) and Hattori and Takinami (2010) conducted experiments of a cavitating jet impacting on a test specimen. They

found a proportionality of erosion rate to the flow velocity with a power of 5.2 – 6.8. Franc et al. (2012) conducted measurements of cavitation erosion in an axisymmetric nozzle. They reported that the diameters of circular surface deformations, referred to as *pits*, increased with velocity to a power of about 0.75. For pitting rates, they found a proportionality to the fifth power of velocity.

A dependence of erosion rates on geometric scales was shown by Rao and Buckley (1984). They found that erosion rates increased with increasing diameter of the cavitation inducer used. In their investigations, erosion rates were found to be proportional to a power of 1.7 – 4.9 of the diameter of the cavitation inducer.

## 2.4 Cavitation and Cavitation Erosion in Maritime Environments

Cavitation occurs in different forms on almost every marine propeller. Freight ships sail at one design speed most of the time. Their propellers are developed to reach a high efficiency under designed operating conditions. Amongst other types of cavitation, especially vortex cavitation on the propeller blades' tips is accepted as long as its elongation over the blade is not too large and a high efficiency along with a low fuel consumption can be maintained. In fact, cavitation on ship appendages is already difficult to prevent for one design condition because of the inevitable inhomogeneous wake behind the ship, currents of changing direction, and waves. For non-design speeds and conditions, cavitation volumes as well as the effects caused by cavitation become even larger. Besides freight ships, vessels with different purposes usually face cavitation because of large variations in operating conditions. Except for special propellers of military or research ships, where avoiding the inception of cavitation is mandatory, cavitation occurs on almost every propeller.

The most common kinds of propeller cavitation occur at the leading edge and the tip of the blade as well as the propeller's hub in forms of vortex or sheet cavitation. Golf (2018) investigated various cavitation structures on the Duisburg Test Case (DTC) propeller in model-scale tests. Figure 2.7 shows vortex cavitation generated on the tips of the blades and on the hub of the DTC propeller. Both kinds of vortex cavitation are relatively stable as they can be maintained for distances of multiple propeller diameters further downstream.



**Figure 2.7:** Tip and hub vortex cavitation on the DTC propeller in model-scale from Golf (2018)

When the extents of tip vortex cavitation become larger, sheet cavitation can develop from the leading edge of a propeller blade. The propeller rotation and the inhomogeneous flow in the ship's wake ahead of the propeller cause the blades to be exposed to different effective angles of attack for every position during one propeller revolution. Accordingly, generation and collapse of cloud cavitation can be induced by a periodic change of flow conditions around the blades. Depending on the ship's manoeuvres and operating conditions, cavitation may be generated at the pressure or the suction side of a propeller blade and at the tip or root of a blade. For larger extents of vapour volumes on the blades, besides the generation of noise, propellers suffer from efficiency losses, structural vibrations, and material erosion. When cavitation volumes collapse periodically in the vicinity of a surface the risk of erosion is high. For ship propellers, especially periodic collapses of cloud cavitation have a high potential to cause surface damage. Common damage patterns on full-scale propellers assignable to cavitation erosion can be found in Billet et al. (2005), Miller and Wilczyński (2006), and Ponkratov (2015). Model-scale predictions of cavitation erosion on propeller blades are given in Berchiche et al. (2003), Miller and Wilczyński (2006), Ukon et al. (2006), and Heinke et al. (2013)

Figure 2.8 shows erosion induced by cavitation on the pressure side of the tip of an inland vessel's propeller blade. The complete extent of erosion can be seen in Figure 2.8 (left). Material removal from the blade created a hole with a maximum width of about 10 cm. The extent of erosion decreased with increasing distance from the position of the hole, whereas the right side of the tip was not affected by erosion at all. Figure 2.8 (right) presents a detailed view of the area around the hole. In different regions, different stages of erosion were approached. In larger distance from the hole, only a small amount of material was removed. Here, the surface was mostly only plastically deformed and hardened, showing small and circular pits, related to the collapses of cavitation bubbles. Moreover, single isolated spots of removed material,

## 2.4 Cavitation and Cavitation Erosion in Maritime Environments

in comparable size as the pit deformations, can be seen. With decreasing distance from the hole, material loss increased and became more macroscopic. Generally, edges, newly formed by erosion, provide further disturbances to the flow and possible locations to generate more cavitation. The roughened surface enabled gas pockets to be formed and generate additional nuclei in the flow.



**Figure 2.8:** Cavitation erosion on the pressure side of the tip of a propeller blade

On ship rudders, sheet cavitation can be generated on the leading edge at high angles of attack. At lower surrounding pressures or even higher angles of attack, cloud cavitation can develop. In the small gaps between the stationary and rotating part of the rudder high velocities and low pressure regions can develop. Even for relatively high far field pressures, cavitation structures can form in or around these gaps. Under the much higher pressures outside of the gaps, these cavitation structures can collapse rapidly and give rise to surface damage. Vortex cavitation is usually stable on propeller blades and on the hub. Further downstream, these types of cavitation may collapse on surfaces of other ship appendages, such as rudders, and cause surface erosion. The collapse of tip vortex cavitation on a rudder surface therefore presents another high risk of erosion. Typical examples of cavitation-induced erosion on rudder surfaces caused by tip vortex cavitation, cloud cavitation, and rudder gap cavitation are presented in Billet et al. (2005), Grekula and Lindell (2007), el Moctar and Schellin (2008), Oh et al. (2009), van Terwisga et al. (2009), and Brehm et al. (2009).

### 3 Basic Equations and Numerical Methods for Continuous Flows

*Fluids* are liquids and gases whose motions are reactions to surface and body forces acting on them. For the largest majority of engineering problems, fluids can be considered as continua. This means that the volumes of interest, which share the same fluid quantities already, incorporate a substantial number of molecules. These considered volumes are called fluid elements. For a Newtonian fluid – assuming shear velocity to be proportional to shear stress – the governing equations of motion are called Navier-Stokes equations. These consist of a set of partial integro-differential equations for the conservation of momentum. They can be formulated for both single-phase and multi-phase flows with and without phase change. For the flows considered, they are accompanied by the equation of mass conservation. Given that no analytical solutions exist for the governing equations, they need to be discretised and transformed into an algebraic system of equations.

In this chapter, the basic equations characterising fluid motions and the numerical techniques needed to solve them are described and discussed. For flow simulations, applications and libraries out of the open source CFD framework OpenFOAM are used. Simulations are based on the numerical solution of the time dependant Reynolds-averaged Navier-Stokes equations of a two-phase isothermal flow. Although compressibility of vapour and liquid phases can play a role for collapses of cavitation structures, its influence on the macroscopic behaviour of cavitation structures can be neglected in most cases and thus both phases are assumed to be incompressible. A homogeneous mixture approach is applied whereby both phases share the same equations of conservation of mass and momentum. Interfaces between the phases are captured using the Volume of Fluid (VOF) approach. Cavitation is modelled by deriving source terms for condensation and vapourisation processes based on simplified bubble dynamics (see chapter 4). In contrast to other fields of physics, in fluid dynamics it is rather convenient to consider the quantities of a flow in a control volume than in a control mass. The approach used in this work considers fluid quantities in control volumes: the Finite Volume Method (FVM). For the FVM, governing equations are used in integral form. More detailed descriptions regarding flows and numerical techniques can be found in Ferziger and Perić (2002), Jasak (1996), and Truckenbrodt (2008).

## 3.1 Flow Equations of Conservation

### 3.1.1 Navier-Stokes Equations

To describe flows, one can differentiate between two different points of view. In a Lagrangian approach, the flow is analysed while following the trajectory of a fluid particle. The reference coordinate system is a local coordinate system moving with the fluid particle. The Eulerian point of view, instead of moving with a fluid particle, analyses the fluid flow from a fixed location in an earth-fixed coordinate system. In the ambit of this work, an Eulerian treatment is always utilised for the liquid phase and, in case of the Euler-Euler method (see section 4.2), it is used for the vapour phase as well. The equations of conservation are given for arbitrary control volumes in a Cartesian formulation. The position vector is denoted  $\mathbf{x} = (x, y, z)$  with coordinate directions  $x, y, z$ .  $\mathbf{u} = (u_x, u_y, u_z)$  is the flow velocity vector consisting of velocity components  $u_i$  in the respective coordinate direction  $i = x, y, z$ . Basic equations of conservation for the flows considered are those of mass and momentum. In integral form, the mass conservation equation yields:

$$\frac{\partial}{\partial t} \int_V \rho \, dV + \int_S \rho \mathbf{u} \cdot d\mathbf{S} = 0. \quad (3.1)$$

$\rho$  is the fluid density.  $t$  is the time and  $V$  is the volume of the CV.  $\mathbf{S} = \mathbf{n}S$  is the surface area vector of a CV's surface with the surface unit normal vector,  $\mathbf{n}$ , and the surface area,  $S$ . The first term on the left hand side is the transient term. The second term is called the convective term. Using Gauss' theorem to convert a surface integral into a volume integral and letting the arbitrary volume become zero the equation can be written in differential form. After rearrangement one can obtain:

$$\nabla \cdot \mathbf{u} = -\frac{1}{\rho} \frac{d\rho}{dt}. \quad (3.2)$$

In incompressible flows, density and pressure are independent of one another. Considering an incompressible, isothermal, single-phase flow, equation (3.2) can further be simplified as the right hand side vanishes which yields a divergence free velocity field:

$$\nabla \cdot \mathbf{u} = 0. \quad (3.3)$$

For cavitating flows, this simplification cannot be made as the right hand side of equation (3.2) does not vanish because of phase change and motions of the free surface. Integrating over a control volume and applying Gauss' theorem to convert the volume integral into a surface integral one can obtain a form of the equation as follows:

$$\int_S \mathbf{u} \cdot d\mathbf{S} = -\int_V \frac{1}{\rho} \frac{d\rho}{dt} \, dV. \quad (3.4)$$

For the regarded fluid, despite not containing a dominant variable, the continuity equation is used as a condition in the momentum equation as well as for derivation of the pressure equation (see section 3.3). To calculate velocities, the momentum equation is used. It can be written as:

$$\frac{\partial}{\partial t} \int_V \rho \mathbf{u} dV + \int_S \rho \mathbf{u} \mathbf{u} \cdot d\mathbf{S} = \sum \mathbf{F}. \quad (3.5)$$

Similarly to the mass equation, the transient and convective term are found on the left hand side. The right hand side consists of forces,  $\mathbf{F}$ , acting on a control volume. These forces can be divided into surface forces, e.g. owing to pressure, shear stress, normal stress, or surface tension and volume forces, e.g. gravity or Coriolis forces. Surface forces attributable to pressure and viscosity are written as surface integrals while volume forces are written as volume integrals. Rewriting the right hand side of equation (3.5), one obtains:

$$\frac{\partial}{\partial t} \int_V \rho \mathbf{u} dV + \int_S \rho \mathbf{u} \mathbf{u} \cdot d\mathbf{S} = \int_S \mathbf{T} \cdot d\mathbf{S} + \int_V \rho \mathbf{b} dV. \quad (3.6)$$

The first term on the right hand side are momentum fluxes through the surface of a control volume and the last term represents volume forces.  $\mathbf{T}$  is the stress tensor and  $\mathbf{b}$  are accelerations, e.g. owing to gravity. For a Newtonian fluid the stress tensor reads:

$$\mathbf{T} = - \left( p - \frac{2}{3} \mu \nabla \cdot \mathbf{u} \right) \mathbf{I} + 2\mu \mathbf{D}. \quad (3.7)$$

Here,  $p$  is the pressure,  $\mu$  is the dynamic viscosity of the fluid, and  $\mathbf{I}$  is the identity matrix. For an incompressible flow, the term  $\left( \frac{2}{3} \mu \nabla \cdot \mathbf{u} \right)$  vanishes because of the condition of a divergence free velocity field from (3.3). The deformation tensor is denoted as:

$$\mathbf{D} = \frac{1}{2} \left( \nabla \mathbf{u} + (\nabla \mathbf{u})^T \right). \quad (3.8)$$

Finally, the momentum equation can be written as:

$$\frac{\partial}{\partial t} \int_V \rho \mathbf{u} dV + \int_S \rho \mathbf{u} \mathbf{u} \cdot d\mathbf{S} = \int_S \mu \left[ \nabla \mathbf{u} + (\nabla \mathbf{u})^T \right] \cdot d\mathbf{S} - \int_S \left( p - \frac{2}{3} \mu \nabla \cdot \mathbf{u} \right) \mathbf{I} \cdot d\mathbf{S} + \int_V \rho \mathbf{b} dV. \quad (3.9)$$

The first term on the right hand side is the diffusion term.

### 3.1.2 Turbulence

In reality, most flows in technical applications are turbulent. They incorporate fluctuations of flow quantities in space and time that range from microscopic to macroscopic scales. Turbulence is three-dimensional and unsteady, generates eddies in a flow and increases *mixing* of fluid quantities, which is referred to as turbulent diffusion. Resolving turbulence in a fluid simulation can be done using Direct Numerical Simulations (DNS) or Large Eddy Simulations (LES). Former, DNS, aim to resolve all eddies in a flow and are limited to simple flow

### 3.1 Flow Equations of Conservation

problems of low Reynolds numbers because the demand for computational resources increases with increasing turbulence. Latter, LES, resolve only large eddies in a turbulent flow up to a certain turbulence scale while smaller eddies are modelled. Although LES is computationally more efficient than DNS, it is usually too expensive for most engineering problems. An approach that models all turbulence structures assumes that the values of fluid quantities in turbulent flows can be split into an average value and oscillations around this average value that are attributed to turbulence. This approach is called Reynolds-averaging and was used for all simulations throughout this work. Every variable in a statistically steady flow is expressed as:

$$\varphi(\mathbf{x}, t) = \overline{\varphi(\mathbf{x})} + \varphi(\mathbf{x}, t)' , \quad (3.10)$$

$\overline{\varphi(\mathbf{x})}$  is an average value and  $\varphi(\mathbf{x}, t)'$  is the oscillation around the average. For steady cases,  $\overline{\varphi(\mathbf{x})}$  can be obtained by averaging over the complete time series:

$$\overline{\varphi(\mathbf{x})} = \lim_{T \rightarrow \infty} \frac{1}{T} \int_0^T \varphi(\mathbf{x}, t) dt . \quad (3.11)$$

The time interval,  $T$ , should be large for the averaging not to be influenced by the interval any more. For transient cases, an ensemble-averaged value is calculated by averaging over a representative number of flow realisations,  $\varphi_n(\mathbf{x}, t)$ :

$$\overline{\varphi(\mathbf{x}, t)} = \lim_{N \rightarrow \infty} \frac{1}{N} \sum_1^N \varphi_n(\mathbf{x}, t) , \quad (3.12)$$

where  $N$  has to be large enough so that effects assignable to fluctuations become negligible. From equation (3.11) follows that the average of a fluctuation of a quantity vanishes  $\overline{\varphi(\mathbf{x}, t)'} = 0$ . Neglecting volume forces, the RANS equations can be derived:

$$\frac{\partial}{\partial t} \int_V \rho \bar{\mathbf{u}} dV + \int_S \rho (\bar{\mathbf{u}}\bar{\mathbf{u}} + \overline{\mathbf{u}'\mathbf{u}'}) \cdot d\mathbf{S} = \int_S \mu (\nabla \bar{\mathbf{u}} + (\nabla \bar{\mathbf{u}})^T) \cdot d\mathbf{S} - \int_S \left( \bar{p} - \frac{2}{3} \mu \nabla \cdot \bar{\mathbf{u}} \right) \mathbf{I} \cdot d\mathbf{S} . \quad (3.13)$$

$\rho \overline{\mathbf{u}'\mathbf{u}'}$  are the Reynolds stresses. In contrast to the average of a fluctuation of a linear term, this non-linear term does not vanish, because its properties are statistically not independent of each other. These Reynolds stresses introduce an additional unknown quantity, while lacking sufficient equations to solve for all unknowns. Dealing with this so-called *closure problem* requires approximations, mostly based on empirical considerations, to yield additional equations. As turbulence increases the mixing of fluid quantities globally, one approach, first stated by Boussinesq (1877), assumes the Reynolds stresses to be considered as an additional diffusion:

$$-\rho \overline{\mathbf{u}'\mathbf{u}'} = \mu_t (\nabla \bar{\mathbf{u}} + (\nabla \bar{\mathbf{u}})^T) + \frac{2}{3} \rho k \mathbf{I} . \quad (3.14)$$

$\mu_t$  is the turbulent viscosity or eddy viscosity.  $k$  is the turbulent kinetic energy defined as:

$$k = \frac{1}{2} \overline{\mathbf{u}' \cdot \mathbf{u}'} = \frac{1}{2} (\overline{u'_x u'_x} + \overline{u'_y u'_y} + \overline{u'_z u'_z}) . \quad (3.15)$$

Approaches taking up these assumptions are called eddy viscosity *turbulence models*. Besides turbulence models based on the eddy viscosity assumption, many other approaches to model turbulence exist. The  $k$ - $\omega$  two equation eddy viscosity turbulence model proposed by Wilcox (1988) seeks to express the turbulent viscosity using the turbulent kinetic energy and the specific turbulence dissipation,  $\omega$ :

$$\mu_t = \rho C_\mu k / \omega, \quad (3.16)$$

with the constant  $C_\mu = 0.09$ .  $k$  and  $\omega$  are obtained from the following transport equations:

$$\frac{\partial(\rho k)}{\partial t} + \nabla \cdot (\rho \bar{\mathbf{u}} k) = P_k - \rho \beta^* k \omega + \nabla \cdot \left[ \left( \mu + \frac{\mu_t}{\sigma_k^*} \right) \nabla \omega \right], \quad (3.17)$$

$$\frac{\partial(\rho \omega)}{\partial t} + \nabla \cdot (\rho \bar{\mathbf{u}} \omega) = \alpha_\omega \frac{\omega}{k} P_k - \rho \beta \omega^2 + \nabla \cdot \left[ \left( \mu + \frac{\mu_t}{\sigma_\omega^*} \right) \nabla \omega \right]. \quad (3.18)$$

$P_k$  is the production rate of  $k$ . The constants are set to  $\alpha_\omega = \frac{5}{9}$ ,  $\beta = 0.075$ ,  $\beta^* = 0.09$ ,  $\sigma_k = \sigma_\omega = 2.0$ .

While the  $k$ - $\omega$  turbulence model is known for being relatively accurate especially in near wall regions of a flow, it is less accurate to predict free-stream turbulence. Another commonly used model is the  $k$ - $\varepsilon$  turbulence model proposed by Launder and Sharma (1974), which is supposed to model turbulence more accurately in free-stream flows than the  $k$ - $\omega$  model. Instead of solving a transport equation for  $\omega$ , an equation for the turbulence dissipation rate,  $\varepsilon$ , is solved. Both approaches are combined in the  $k$ - $\omega$ -SST turbulence model introduced by Menter (1994), which uses the  $k$ - $\omega$  approach in the near wall regions and switches to a  $k$ - $\varepsilon$  behaviour in the free-stream at larger distance to walls. In the present work, the  $k$ - $\omega$ -SST model is used as it combines the benefits of the  $k$ - $\omega$  and  $k$ - $\varepsilon$  models and is considered to be relatively accurate for the simulation of flow separation, which is of importance for cavitation shedding mechanisms. Additional corrections of turbulence are applied for cavitating flows, as explained in section 4.2.2.

Schlichting and Gersten (2017) described that turbulent boundary layers consist of sub layers in which various coherences between wall distances and tangential velocity components of the flow exist. In the wall-nearest layer, the viscous sub layer, turbulent stresses are small compared to viscous stresses. A buffer layer separates the viscous sub layer from the turbulent part of the boundary layer in which the turbulent stresses are dominant. A dimensionless wall distance serves to characterise the sub layers of a boundary layer flow:

$$n^+ = \frac{u_\tau n}{\nu}. \quad (3.19)$$

$u_\tau = \sqrt{\tau_w / \rho}$  is the shear stress velocity,  $\nu = \mu / \rho$  is the kinematic viscosity, and  $n$  is the normal distance from the wall. For a Newtonian fluid, the shear stress with respect to the wall is  $\tau_w = \mu \left( \frac{\partial u_{ta}}{\partial n} \right)_w$ , with the velocity component tangential to the wall,  $u_{ta}$ .  $n$  is the distance

### 3.1 Flow Equations of Conservation

to the wall.  $n^+$  can be regarded as a local, turbulent Reynolds number near the wall. A dimensionless wall velocity is defined as:

$$u^+ = \frac{\overline{u_{ta}}}{u_\tau}. \quad (3.20)$$

The viscous sub layer is located in the region of  $n^+ \leq 5$  where the wall turbulence Reynolds number is small and the relation  $u^+ = n^+$  applies. A buffer layer is located in the region of  $5 < n^+ < 30$ , where no clear relation between  $u^+$  and  $n^+$  is given. The turbulent sub boundary layer region elongates outside from about  $n^+ \geq 30$ , Ferziger and Perić (2002). It is also called logarithmic wall region because the dimensionless wall velocity follows the relation:  $u^+ = \frac{1}{\kappa} \ln n^+ + B$ .  $\kappa = 0.41$  is the von Karman constant and  $B$  an empirical coefficient to consider different wall roughness.

When using RANS turbulence models, it has to be decided to either fully resolve the boundary layer down to the viscous sub layer ( $n^+ \approx 1$ ) or to consider the logarithmic *law of the wall* ( $n^+ \approx 50$ ). A full resolution of the boundary layer (called low Reynolds number approach) requires finer numerical meshes and therefore higher computational effort. For high Reynolds numbers, to compute the wall shear stress the logarithmic law of the wall (so-called *wall function* or *high-Re approach*) is used because it is computationally less expensive and thus used in many engineering applications, such as full-scale analysis of maritime flows.

#### 3.1.3 Volume of Fluid Method

Two main categories of approaches exist to treat interfaces in free surface flows such as gravity waves, sloshing, or cavitation: interface-tracking and interface-capturing. In interface-tracking methods, the interface is sharp and the grid has to be modified in order to follow the free surface. In interface-capturing methods, the interface is not sharp and thus its position is not directly clear but has to be obtained from the phases' volume fractions in control volumes. In fact, the interface may even be smeared over multiple control volumes. In this work, the VOF interface-capturing method is used that introduces a volume fraction of an arbitrary phase as:  $\alpha = \frac{V_\alpha}{V_{cv}}$ .  $V_\alpha$  is the phase volume inside of the regarded control volume and  $V_{cv}$  is the total volume of the control volume. It needs to be assured that the total volume of the control volume is the sum of all phase volumes,  $V_{CV} = \sum_i V_i$ , and therefore the sum of all volume fractions equals unity:  $\sum_i \alpha_i = 1$ . Fluid quantities in a homogeneous mixture are then obtained from:

$$\phi = \sum_i \alpha_i \phi_i. \quad (3.21)$$

To calculate the volume fraction of a phase, a scalar transport equation is introduced. For a free surface flow without phase change it reads:

$$\frac{\partial}{\partial t} \int_V \alpha dV + \int_S \alpha \mathbf{u} \cdot d\mathbf{S} = 0. \quad (3.22)$$

Boundedness of each volume fraction between zero and unity is required, while retaining conservation of the volume fraction.

### Interface Compression

Depending on the flow type considered, a sharp interface between phases is demanded. Various schemes exist that aim to preserve a sharp interface using compressive mechanisms, Ubbink (1997), Waclawczyk and Koronowicz (2008). In the present method, a so-called *Counter-Gradient* approach by Weller (2008) is implemented that can be used to sharpen the interface between two phases. A convection-based compression term is introduced into the volume fraction equation:

$$\frac{\partial}{\partial t} \int_V \alpha dV + \int_S \alpha \mathbf{u} \cdot d\mathbf{S} + \int_V \nabla \cdot \mathbf{u}_{co} \alpha (1 - \alpha) dV = 0. \quad (3.23)$$

$\mathbf{u}_{co}$  is the velocity used to compress the interface. Owing to the factor  $\alpha(1 - \alpha)$  the introduced compression term is maximal at  $\alpha = 0.5$ . The term becomes smaller as the volume fraction approaches either zero or unity and completely vanishes in single-phase regions. To influence only the volume fraction normal to the interface, the velocity  $\mathbf{u}_{co}$  should point in normal direction of the interface  $\frac{\nabla \alpha}{|\nabla \alpha|}$  and is, thereby, defined as:

$$\mathbf{u}_{co} = \min(c_\alpha |\mathbf{u}|, \mathbf{u}_{max}) \frac{\nabla \alpha}{|\nabla \alpha|} \quad (3.24)$$

$\mathbf{u}$  is the velocity in the regarded control volume and  $\mathbf{u}_{max}$  the velocity of maximum magnitude in the solution domain.  $c_\alpha$  is a coefficient of the order of unity, which may be chosen to be larger to apply higher compression and smaller to apply less compression. Using (3.24) it is ensured that the interface is compressed, even in regions of low velocities. For macroscopic cavitating flows, a sharp interface is usually undesirable. A strong compression would prevent lower concentrations of vapour over multiple control volumes and is not needed for the simulation of cavitating flows, except when single bubbles are resolved by the numerical grid. Hence, in this work, lower compression is achieved by using lower values or zero for  $c_\alpha$ . In the remainder, the interface compression term is neglected in the volume fraction equation.

### MULES Algorithm to Guarantee Boundedness

Solution algorithms for the volume fraction equation demand boundedness and conservation. In OpenFOAM a bounded as well as efficient solution of the volume fraction equation is achieved by using an algorithm consisting of an implicit predictor and an explicit corrector step. The predictor step uses an implicit Euler scheme for time integration and an upwind scheme for spatial discretisation of the convection term in (3.22). Owing to the schemes used, the solution is naturally bounded after the predictor step, which allows the use of larger time steps while maintaining stability. Correction of the volume fraction is attained in an

### 3.1 Flow Equations of Conservation

explicit step using the Multi-Dimensional Limiter for Explicit Solution (MULES) algorithm. Boundedness of the solution in the corrector step is assured by splitting the convective fluxes into a bounded upwind term and an unbounded higher order term. Higher order fluxes need to be limited to guarantee boundedness of the final fluxes used to solve the volume fraction equation. For all faces of a control volume, limiting weighting factors are evaluated based on maxima and minima of the local fluxes in neighbouring cells. Evaluated weighting factors of a face are correlated and, hence, need to be updated in multiple iterations until convergence is achieved. Details about the derivation of the MULES algorithm and calculation of the weighting factors can be found in The OpenFOAM Foundation Ltd (2018), Weller (2006), and Zalesak (1979).

#### Surface Tension

Surface tension occurs at the interface between different phases. Molecules of a fluid are attracted to each other by cohesive forces. Molecules located at an interface to another substance, have less neighbouring molecules of the same substance as away from the interface. The result are cohesive forces between molecules of the same substance which are significantly higher than the adhesive forces that would attract the molecules towards the other substance. Surface tension forces are then generated and try to minimise the interface's area. As it acts directly at the interface, it cannot explicitly be applied for interface-capturing methods where the interface is smeared over multiple control volumes. To deal with this problem, Brackbill et al. (1992) introduced a continuum surface force model that defines the surface tension force as:

$$\int_V \sigma \kappa_{\text{cur}} \nabla \alpha \, dV, \quad (3.25)$$

with the curvature of the interface:

$$\kappa_{\text{cur}} = -\nabla \cdot \frac{\nabla \alpha}{|\nabla \alpha|}. \quad (3.26)$$

The gradient of the volume fraction,  $\nabla \alpha$ , points into direction normal to the interface. Surface tension vanishes in control volumes occupying only one phase where  $\nabla \alpha = 0$ . Moreover, in a homogeneous mixture approach, a friction force acts tangentially to the interface, which is included by the change of viscosity across the interface from one phase to another according to (4.36). Including surface tension, the momentum equation for a two-phase flow reads:

$$\begin{aligned} \frac{\partial}{\partial t} \int_V \rho \mathbf{u} \, dV + \int_S \rho \mathbf{u} \mathbf{u} \cdot d\mathbf{S} &= \int_S \mu (\nabla \mathbf{u} + (\nabla \mathbf{u})^T) \cdot d\mathbf{S} - \int_S \left( p - \frac{2}{3} \mu \nabla \cdot \mathbf{u} \right) \mathbf{I} \cdot d\mathbf{S} \\ &+ \int_V \rho \mathbf{b} \, dV + \int_V \sigma \kappa_{\text{cur}} \nabla \alpha \, dV. \end{aligned} \quad (3.27)$$

### 3.1.4 Summary of Equations for Continuous Flows

In this section, the equations of conservation, used in this work, in order to describe continuous flows and utilising an Euler-Euler approach were described. To summarise, they are again listed below:

- Mass equation:

$$\frac{\partial}{\partial t} \int_V \rho \, dV + \int_S \rho \mathbf{u} \cdot d\mathbf{S} = 0. \quad (3.28)$$

- Momentum equation:

$$\begin{aligned} \frac{\partial}{\partial t} \int_V \rho \mathbf{u} \, dV + \int_S \rho \mathbf{u} \mathbf{u} \cdot d\mathbf{S} &= \int_S \mu (\nabla \mathbf{u} + (\nabla \mathbf{u})^T) \cdot d\mathbf{S} - \int_S \left( p - \frac{2}{3} \mu \nabla \cdot \mathbf{u} \right) \mathbf{I} \cdot d\mathbf{S} \\ &+ \int_V \rho \mathbf{b} \, dV + \int_V \sigma \kappa_{\text{cur}} \frac{\nabla \alpha}{|\nabla \alpha|} \, dV. \end{aligned} \quad (3.29)$$

- Turbulence equations (using standard  $k$ - $\omega$  turbulence model):

$$\frac{\partial(\rho k)}{\partial t} + \nabla \cdot (\rho \bar{\mathbf{u}} k) = P_k - \rho \beta^* k \omega + \nabla \cdot \left[ \left( \mu + \frac{\mu_t}{\sigma_k^*} \right) \nabla \omega \right], \quad (3.30)$$

$$\frac{\partial(\rho \omega)}{\partial t} + \nabla \cdot (\rho \bar{\mathbf{u}} \omega) = \alpha_\omega \frac{\omega}{k} P_k - \rho \beta \omega^2 + \nabla \cdot \left[ \left( \mu + \frac{\mu_t}{\sigma_\omega^*} \right) \nabla \omega \right]. \quad (3.31)$$

- Volume fraction equation (using Sauer-Schnerr cavitation model; see section 4.2):

$$\frac{\partial}{\partial t} \int_V \alpha_v \, dV + \int_S \alpha_v \mathbf{u} \cdot d\mathbf{S} = \int_V (S_v - S_c) \, dV. \quad (3.32)$$

Discretisation of these equations is described in the next section.

## 3.2 Finite Volume Method

Given that no general analytical solutions exist for the partial integro-differential equations presented in section 3.1.4, they are approximated in time and space using numerical approaches to obtain an algebraic system of equations. In this work, the equations of conservation are discretised according to the FVM wherein they are considered in integral form. For a specified solution domain, differentials and integrals are discretised using control volumes of arbitrary shapes. When all fluxes are expressed in terms of divergences and discretised properly, the quantities of the equations are conserved and yield a so-called conservative approach. In terms of time integration, implicit schemes are used. In the present section, methods and schemes used to approximate the equations for cavitating flows are given in an aggregate form of The OpenFOAM Foundation Ltd (2018), Jasak (1996), and Ferziger and Perić (2002).

### 3.2 Finite Volume Method

In light of computational efficiency, different approaches have been developed to use regular connectivity between control volumes or to disregard regular connectivity and use complex shapes of finite volumes instead. Structured grids use regular connectivity between neighbouring control volumes, where a direct next neighbour of a control volume of index  $i$  is addressed by the index  $i + 1$ . Connections between control volumes are implicit and enable easy programming and storage for the numerical code. As each control volume has exactly 4 neighbours in 2D and 6 neighbours in 3D, the shapes of the control volumes are restricted.

When different mesh resolutions are needed across the fluid domain, structured meshes can be combined at interfaces between regions of different mesh resolution, referred to as block structured grids. At the interfaces, hanging nodes – nodes which do not define the corners of all their neighbouring control volumes – exist and interpolation between the two structured grid regions is necessary. Block structured approaches allow to still use efficient techniques to handle structured grids in different blocks while enabling the use of different scales of grid resolution.

To resolve complex geometries, unstructured grids utilise arbitrary shapes of control volumes. Refinements of the numerical grids can be applied universally which results in meshes of less control volumes compared to structured grid approaches. The use of arbitrarily shaped control volumes, however, prevents a regular implicit connectivity between them so that every control volume needs to be explicitly defined by the points and faces containing it and a list of neighbouring control volume indices needs to be stored with it. Furthermore, control volumes incorporating high non-orthogonality or skewness, need special treatment. In OpenFOAM, a solely unstructured approach is used to deal with all types of meshes. Generating structured grids for OpenFOAM simulations is therefore limited to the benefit of the orthogonal shape of the control volumes. Storage and connectivity are explicitly treated as common for unstructured grids.

In the present work, a finite volume method that utilises unstructured grids is used for spatial discretisation. A solution domain is generated that incorporates a finite number of control volumes of arbitrary form, for which the equations of conservation are solved. Here, different approximations of differentials and integrals as well as of flow variables for surfaces and volumes are applied. The different numerical techniques, used to discretise the governing equations, can be described altogether based on a generic transport equation which reads:

$$\frac{\partial}{\partial t} \int_V \rho \varphi dV + \int_S \rho \varphi \mathbf{u} \cdot d\mathbf{S} = \int_S \Gamma \nabla \varphi \cdot d\mathbf{S} + \int_V \rho S_\varphi dV . \quad (3.33)$$

$\varphi$  is the flow variable being transported.  $\Gamma$  is the diffusion coefficient and  $S_\varphi$  are source terms depending on  $\varphi$ . The equation contains surface and volume integrals as well as temporal and spatial derivatives to be discretised. Flow variables need to be approximated in cells and on faces. Different approximations needed for these integrals and derivatives will be explained below.

### 3.2.1 Approximation of Temporal Derivatives

Despite few exceptions, most cavitating flows show transient or periodic behaviour. Here, for the flow problems dealt with, solely unsteady methods are used in which time dependent flow phenomena need to be discretised accurately in time. Several schemes for time integration exist and can be separated in terms of order of accuracy as well as implicit and explicit methods. A dimensionless quantity, the so-called *Courant number* or *Courant-Friedrichs-Lewy number*, is introduced to relate temporal and spatial discretisation of a regarded flow simulation. For a flow problem, with a characteristic velocity,  $u_{\text{ref}}$ , it can be written as:

$$\text{CFL} = u_{\text{ref}} \frac{\Delta t}{\Delta x_{\text{ref}}} . \quad (3.34)$$

$\Delta x_{\text{ref}}$  is the reference edge length of the regarded control volume and  $\Delta t$  is the time step. For explicit schemes, limits of  $\text{CFL} < 1$  usually have to be fulfilled in order to guarantee stability. For implicit schemes, no such strict limits exist, because the schemes are stable for larger Courant numbers as well. Various schemes for time integration can be obtained from a Taylor series expansion. For a continuously differentiable variable,  $\varphi(t)$ , the Taylor expansion around the time  $t = t_{n+1}$  with  $n$  as the index of the last time instance and  $\varphi(t_n) = \varphi^n$  is given by:

$$\varphi(t) = \varphi^{n+1} - \Delta t \left( \frac{\partial \varphi}{\partial t} \right)_{n+1} + \frac{\Delta t^2}{2!} \left( \frac{\partial^2 \varphi}{\partial t^2} \right)_{n+1} - \frac{\Delta t^3}{3!} \left( \frac{\partial^3 \varphi}{\partial t^3} \right)_{n+1} + \text{HOT} . \quad (3.35)$$

*HOT* are higher order terms. After substituting  $t = t_{n+1} - \Delta t = t_n$ , with the index of the next time instance,  $n + 1$ , and neglecting higher order terms, the Euler implicit scheme for the first time derivative reads:

$$\left( \frac{\partial \varphi}{\partial t} \right)_{n+1} \approx \frac{\varphi^{n+1} - \varphi^n}{\Delta t} , \quad (3.36)$$

and the time integration to obtain  $\varphi^{n+1}$  yields:

$$\varphi^{n+1} = \varphi^n + \Delta t F(t_{n+1}, \varphi^{n+1}) . \quad (3.37)$$

The equation is non-linear and can, in contrast to explicit time integration schemes, not be solved analytically. This means that the function  $F(t_{n+1}, \varphi^{n+1})$  depends on the unknown  $\varphi^{n+1}$  of the next time instance and a solution is not as straightforward as for the explicit Euler approach. However, the stability of the implicit Euler method, which is of first order as well, is higher because it takes into account the quantities of  $t_{n+1}$ . When combining both Euler methods, it is possible to calculate  $\varphi^{n+1}$  taking into account the functions  $F(t_n, \varphi^n)$  and  $F(t_{n+1}, \varphi^{n+1})$  of the last and new time step, respectively. A combination where the functions are blended by a factor of 0.5 is called the Crank-Nicolson scheme. Time integration based on the Crank-Nicolson method reads:

$$\varphi^{n+1} = \varphi^n + \frac{1}{2} \Delta t [F(t_n, \varphi^n) + F(t_{n+1}, \varphi^{n+1})] . \quad (3.38)$$

### 3.2 Finite Volume Method

This method is implicit and of second order and therefore of higher accuracy than the Euler schemes. Nevertheless, because of being of second order, it may lead to oscillations in the solution and have less stability than the implicit Euler method. In OpenFOAM, different implicit methods for time integration can be utilised. In the ambit of this thesis, both the first order, implicit Euler scheme as well as the second order Crank-Nicolson scheme are used depending on the regarded case.

In the above approximations, higher order terms were neglected. These terms are called the truncation error,  $\epsilon_{\text{trunc}}$ . In general form it is defined as:

$$\epsilon_{\text{trunc}} = (\Delta t)^m f \left( \frac{\partial^{m+1} \varphi(t)}{\partial t^{m+1}} \right) + (\Delta t)^{m+1} f \left( \frac{\partial^{m+2} \varphi(t)}{\partial t^{m+2}} \right) + HOT . \quad (3.39)$$

$\epsilon_{\text{trunc}}$  is dominated by the leading term which is proportional to the lowest exponent,  $m$ . A reduction of  $\Delta t$  leads to a reduction of the error proportional to  $(\Delta t)^m$ .  $m$  is called the order of the approximation of which  $\epsilon_{\text{trunc}}$  is the truncation error. When decreasing  $\Delta t$ , a higher order of approximation leads to a faster decrease of the truncation error.

#### 3.2.2 Approximation of Volume and Surface Integrals

Gauss' theorem is often used to transform volume integrals into surface integrals or vice versa. It allows to derive different forms of equations such as the mass and momentum equations in differential or integral form. In the present thesis, the theorem will be used to express equations in a more understandable way. For a volume integral of the divergence of an arbitrary vector quantity,  $\mathbf{c}$ , it can be applied as follows:

$$\int_V \nabla \cdot \mathbf{c} dV = \int_S \mathbf{c} \cdot d\mathbf{S} , \quad (3.40)$$

with  $\mathbf{S} = \mathbf{n}S$  as the surface area normal vector as the product of the unit normal vector of a surface,  $\mathbf{n}$ , and the area of the surface,  $S$ . Analogously, Gauss' theorem can be applied on the volume integral over the gradient of a scalar quantity,  $\varphi$ :

$$\int_V \nabla \varphi dV = \int_S \varphi \mathbf{I} \cdot d\mathbf{S} . \quad (3.41)$$

Applying the theorem to the volume integral of a vector gradient yields:

$$\int_V \nabla \mathbf{c} dV = \int_S \mathbf{c} d\mathbf{S} . \quad (3.42)$$

In the finite volume method, volume integrals consider the integration over a volume of a control volume. The source term in (3.33) represents volume forces and therefore incorporates

integration over a control volume. An approximation of the volume integral for a control volume of index  $P$  reads:

$$\int_V \rho S_\varphi dV = \rho_P S_{\varphi_P} \Delta V . \quad (3.43)$$

Here, it is assumed that variable values at the cell centre represent the mean value over the control volume, which is equivalent to assuming a linear variation within the control volume.  $\rho_P$  and  $S_{\varphi_P}$  are the values of density and source term in the centre of the control volume of index  $P$ , respectively. This approximation is known as the midpoint method, which is of second order.  $\Delta V$  is the volume of the control volume. As most finite volume codes store variables in the control volumes' centres, no additional interpolation is needed.

Surface integrals are approximated by splitting the surface integral into partial integrals over part surfaces. The entire surface integral over a control volume is calculated from the sum of the integrals of all face areas of the control volume. The second term on the left hand side of (3.33) is the convection term. Its approximation reads:

$$\int_S \rho \boldsymbol{\varphi} \mathbf{u} \cdot d\mathbf{S} = \sum_f \int_{S_f} \rho_f \varphi_f \mathbf{u}_f \cdot d\mathbf{S} = \sum_f \rho_f \varphi_f \mathbf{S}_f \cdot \mathbf{u}_f . \quad (3.44)$$

$\rho_f$ ,  $\varphi_f$ , and  $\mathbf{u}_f$  are the approximated density, scalar quantity, and velocity in the centre of face  $f$ , respectively. Analogue to the approximation for a volume, the midpoint method can be used to choose the flow variable in the centre of the face as the mean value for the complete face. Variables on face centres can be interpolated from cell centres of neighbouring control volumes, where variables are stored. Interpolation schemes will be explained in section 3.2.3. In the same way, the diffusion term from (3.33) can be discretised as:

$$\int_S \Gamma \nabla \varphi \cdot d\mathbf{S} = \sum_f \Gamma_f \mathbf{S}_f \cdot (\nabla \varphi)_f , \quad (3.45)$$

where  $\Gamma_f$  and  $(\nabla \varphi)_f$  are the diffusion coefficient and the gradient of the scalar quantity on face  $f$ , respectively. Depending on the numerical procedure, the gradient could be directly calculated on the faces from values of  $\varphi$  in centres of the neighbouring control volumes. If  $\nabla \varphi$  is stored in the centres of the control volumes, the face gradients can also be interpolated from neighbouring control volumes. Attention has to be given to the discretisation of the pressure gradient in the Poisson equation, which will be explained later on.

### 3.2.3 Interpolation Techniques

The order of accuracy of a numerical method is defined by the lowest order in any approximation or interpolation. To maintain the same order of accuracy of the spatial discretisation, interpolation techniques of the same order need to be used. A scalar quantity on a face,  $\varphi_f$ ,

### 3.2 Finite Volume Method

between two neighbouring cells of indices  $P$  and  $N$  can be interpolated by assuming a linear progression of the variable between two cell centres:

$$\varphi_f = \varphi_P + \frac{\varphi_P - \varphi_N}{(\mathbf{x}_P - \mathbf{x}_N) \cdot \mathbf{n}} (\mathbf{x}_f - \mathbf{x}_P) \cdot \mathbf{n} . \quad (3.46)$$

$\varphi_P$  and  $\varphi_N$  are the variable in the owner and neighbour cell, respectively.  $\mathbf{x}_i$  are the positions of the face,  $f$ , owner cell,  $P$ , and neighbour cell,  $N$ , and  $\mathbf{n}$  is the unit normal vector of face  $f$ . This method is called linear interpolation and it is sometimes referred to as the central differencing scheme because it becomes central differencing in finite difference methods. The method is of second order, maintaining the order of the midpoint method but being prone to cause oscillations and lead to instabilities. If stability of a numerical scheme is preferred over accuracy, upwind schemes may be used, which approximate the face quantity as one of the neighbouring cell quantities based on direction of flow velocity normal to the face,  $u_f$ , as follows:

$$\varphi_f = \begin{cases} \varphi_P & \text{if } u_f \geq 0 \\ \varphi_N & \text{else .} \end{cases} \quad (3.47)$$

The interpolation is of first order and bounded but its accuracy is lower than that of the linear interpolation. Many interpolations incorporate a blending of the two schemes to reach a compromise between accuracy and stability.

Considering orthogonal grids, the same schemes can be applied to the interpolation of gradients of flow quantities on faces. For non-orthogonal control volumes, the described interpolations cannot guarantee sufficient accuracy. Different techniques for correction of non-orthogonal meshes are described in Jasak (1996) and Ferziger and Perić (2002). In the present work, an additional iterative loop accounts for correction of non-orthogonality.

#### 3.2.4 Boundary Conditions

Previously described methods, to discretise the equations of the flow, apply for control volumes inside the simulation domain. For control volumes and their faces located at the boundaries of a fluid domain, boundary conditions have to be specified. For each field, which is calculated from a transport equation, either the value at the boundary face,  $bf$ , (Dirichlet boundary condition) or a function for the gradient (Neumann boundary condition) has to be given:

$$\begin{aligned} \varphi_{bf} &= f(\mathbf{x}, t) \quad \text{Dirichlet ,} \\ \left( \frac{\partial \varphi}{\partial x} \right)_{bf} &= f(\mathbf{x}, t) \quad \text{Neumann .} \end{aligned} \quad (3.48)$$

The function  $f(\mathbf{x}, t)$  needs to be predefined in space and time, e.g. to impose waves at an inlet boundary, it is necessary to define the profiles of velocity and volume fraction over time. For the pressure at the inlet, one would need to take into account the change of the hydrostatic

pressure attributable to different water heights in time. Moreover, it is possible to impose conditions for both a value and a gradient on a boundary face, referred to as Cauchy conditions.

Inside of the fluid domain, higher order schemes may be used for approximation. When schemes of an order, that is larger than two, are used in cells that are neighbouring boundaries, additional values outside of the domain would be needed. Therefore, the approximations are usually brought to a lower order at the boundaries. It is for example common to use a linear interpolation scheme inside of the domain and an upwind scheme at the boundary. The basic types of boundary conditions used in the present work are described below.

**Inlet** At the inlet boundary, a fixed value for velocity, volume fraction, and turbulence variables is set. A zero normal gradient of pressure is imposed.

**Outlet** In contrast to the inlet condition, the pressure, reduced by the hydrostatic part,  $p_{rgh} = p - \rho g_z h$ , is fixed at the outlet boundary. For the velocity as well as volume fraction and turbulence variables, zero gradient boundary conditions are used.

**No-Slip Wall** At a wall boundary, the relative velocity in normal direction is zero. For no-slip walls, which consider friction, the relative tangential velocity at the boundary is zero as well. For pressure, a zero gradient boundary condition is defined. Based on the turbulence model used, a wall function is specified to calculate turbulence quantities (see section 3.1.2). A zero gradient boundary condition is specified for the volume fraction.

**Symmetry** The normal component of velocity through a symmetry boundary condition is zero. In contrast to the no-slip wall boundary condition, a zero gradient boundary condition for the tangential velocity component normal to the boundary is specified. Zero gradient conditions are also defined for all other variables.

**Cyclic** Cyclic boundaries are always defined in neighbour pairs as if they are physically connected. Fluxes convected out on a face on one cyclic boundary will be convected in from its cyclic neighbour boundary.

**Cyclic Arbitrary Mesh Interface (AMI)** The same conditions as for the cyclic condition apply for the cyclic AMI boundary condition. In contrast to the standard cyclic condition, two AMI neighbouring boundaries need to share only the same geometries, while the boundaries can move relative to each other. For stator-rotor cases, a sliding interface may be instantiated between two cyclic AMI boundaries (one in the stator and one in the rotor region) where interpolation between the neighbours needs to be conducted in every iteration of flow simulation in which the non-linearity in the momentum equation is updated.

**Processor** Processor boundaries are generated when decomposing a mesh into sub-domains for a parallel simulation. The boundaries exist in pairs on the neighbouring processors and are needed to exchange information between sub-domains.

#### 3.2.5 Linear Algebraic System of Equations

Using the discretisation techniques previously described in section 3.2, the integro-differential equation (3.33) is converted into an algebraic equation for each control volume:

$$a_P \phi_P + \sum_N a_N \phi_N = Q_P, \quad (3.49)$$

with  $Q_P$  being the explicit source terms for the control volume  $P$ . This equation serves to calculate the quantity of the considered variable in the centre of each control volume,  $\phi_P$ . When implicit time integration schemes are used, the solution of the quantity for the next iteration,  $\phi_P^{n+1}$ , depends on the values of the quantity in neighbouring control volumes from the next iteration,  $\phi_N^{n+1}$ , as well. Including boundary conditions, a system of equations can be established consisting of as many unknowns (for  $n_{CV}$  control volumes) as there are equations. The linear algebraic system of equations has the form:

$$\mathbf{A} \boldsymbol{\phi} = \mathbf{b}_Q. \quad (3.50)$$

Here,  $\mathbf{A}$  is the matrix containing the coefficients  $a_P$  on the main diagonal and  $a_N$  on the off-diagonals.  $\boldsymbol{\phi}$  is the vector containing the values of quantity  $\phi$  of all control volumes and  $\mathbf{b}_Q$  the vector of the source terms,  $Q_P$ , of all control volumes. The matrix  $\mathbf{A}$  is called sparse as it contains entries only on the diagonal and, depending on the discretisation schemes used, on few off-diagonals compared to its size of  $n_{CV} \times n_{CV}$ . For sparse matrices, direct solution methods are usually not efficient as they treat every entry in a matrix. Iterative methods have shown to be beneficiary as they are faster, and, in accordance with numerical approaches, an exact solution of the equation system is generally not necessary. However, it should be assured, that iterative convergence is achieved. The approximate solution,  $\phi^n$ , for an iterative method is obtained from:

$$\mathbf{A}^m \boldsymbol{\phi}^m = \mathbf{b}_Q^m - \mathbf{r}^m. \quad (3.51)$$

An outer iteration is understood as an iteration in which the matrix for the momentum matrix is constructed and the non-linear convection term is updated (see section 3.3.3).  $m$  denotes the dependence on quantities of the last outer iteration.  $\mathbf{r}^m$  is the vector containing the absolute residuals for all equations of the regarded iteration which can be a measure to confirm the convergence of an iterative solution method. The residual can be calculated from:

$$\mathbf{r}^m = \mathbf{b}_Q^m - \mathbf{A}^m \boldsymbol{\phi}^m. \quad (3.52)$$

To obtain a relative residual,  $\mathbf{r}$  can be scaled using the sum over all equations of the system:

$$n_r = \sum |(A\boldsymbol{\phi} - A\bar{\boldsymbol{\phi}})| + |(b_Q - A\bar{\boldsymbol{\phi}})|. \quad (3.53)$$

The normalised residual can then be obtained from:

$$r' = \frac{1}{n_r} \sum |(\mathbf{b}_Q - \mathbf{A}\boldsymbol{\varphi})|. \quad (3.54)$$

This normalisation is referred to as L1-norm. In the underlying work, solely implicit time integration schemes are used. Based on the L1-norm, residual control for outer iterations of the SIMPLE loop (see section 3.3.3) is applied to momentum and pressure equations.

### 3.3 Solution of the Navier-Stokes Equations

Two main problems arise from the system of equations stated in the previous sections. First, a non-linearity is introduced in the momentum equation by the convection term. Second, an equation to solve for pressure has yet to be derived. In so-called *projection methods*, an equation for pressure is derived using the momentum equation and the divergence of the velocity field. Equations for velocity and pressure are then solved sequentially. Linearisation procedure, derivation of the pressure equation and the solution algorithm for the system of equations are condensed from Jasak (1996), Ferziger and Perić (2002), and Weller (2005).

#### 3.3.1 Linearisation of Momentum Equation

Convection in the momentum equation introduces the non-linearity  $\mathbf{u}\mathbf{u}$ . It is possible to use a non-linear equation solver to solve the momentum equation while the velocities have to fulfil continuity at the same time. These systems of equations are very complex and it is computationally highly demanding to solve them. Hence, the convection term is linearised and can be discretised as:

$$\int_S \rho \mathbf{u}\mathbf{u} \cdot d\mathbf{S} = \sum_f \rho_f \mathbf{S}_f \cdot \mathbf{u}_f \mathbf{u}_f = \sum_f \rho_f \phi_f \mathbf{u}_f = \left[ a_P \mathbf{u}_P + \sum_N a_N \mathbf{u}_N \right]^{\text{conv}}. \quad (3.55)$$

Here,  $\phi_f$ ,  $a_P$ , and  $a_N$  are functions of  $\mathbf{u}$ . The surface integral is discretised by considering the sum of the fluxes,  $\phi_f$ , multiplied by the velocities,  $\mathbf{u}_f$ , and densities,  $\rho_f$ , on the faces,  $f$ , of a regarded control volume. The matrix coefficients  $a_P$ ,  $a_N$  are related to the regarded control volume  $P$  and its neighbours  $N$ . The term can be linearised with the Picard iteration approach using known velocities from the last outer iteration or time step to calculate the coefficients  $a_P$  and  $a_N$ . For transient simulations, outer iterations to update the linearisation can be applied, while small comparative time steps need less outer iterations than comparatively large time steps because the changes of velocities between consecutive time steps are smaller.

### 3.3.2 Pressure Equation

The described system of equations contains the momentum equation to calculate the velocity. The continuity equation does not serve for the calculation of pressure because it does not contain the pressure. An additional equation for pressure is therefore derived by combining mass and momentum equations. Hereinafter, the pressure,  $p_{\text{rgh}}$ , used in this section is the total pressure reduced by the hydrostatic pressure:

$$p_{\text{rgh}} = p - \rho g_z h, \quad (3.56)$$

with the gravitational acceleration in  $z$  direction,  $g_z$ , and the hydrostatic height,  $h$ . At first, the momentum equation is partially discretised. Using Gauss' theorem to transform surface integrals into volume integrals, letting the volumes go to zero, and assuming a divergence free velocity field it can be written as:

$$\frac{\partial \rho \mathbf{u}}{\partial t} + \nabla \cdot (\rho \mathbf{u} \mathbf{u}) = \nabla \cdot (\mu \nabla \mathbf{u}) - \nabla p_{\text{rgh}} + \mathbf{s}_f, \quad (3.57)$$

with the source term vector ascribable to surface and volume forces,  $\mathbf{s}_f$ . The equation is discretised with the schemes described in section 3.2 to obtain an algebraic system of equations:

$$\mathbf{M}(\mathbf{u}) = -\nabla p_{\text{rgh}}. \quad (3.58)$$

The coefficient matrix  $\mathbf{M}(\mathbf{u}) = A(\mathbf{u}) - \mathbf{H}(\mathbf{u})$  can be divided into a diagonal part,  $A(\mathbf{u}) = a_P \mathbf{u}_P$ , and a part containing the off-diagonal components as well as the transient source term and all other source terms without the pressure gradient,  $\mathbf{H}(\mathbf{u})$ . The momentum predictor step solves equation (3.58) using the old pressure field. Dividing the diagonal part and the other parts of  $\mathbf{M}(\mathbf{u})$  and using the formulation of the convection term (3.55) one obtains:

$$a_P \mathbf{u}_P = -\sum_N a_N \mathbf{u}_N + \frac{\mathbf{u}^n}{\Delta t} + \mathbf{s}_f - \nabla p_{\text{rgh}} = \mathbf{H}(\mathbf{u}) - \nabla p_{\text{rgh}}. \quad (3.59)$$

Dividing by the diagonal coefficient,  $a_P$ , yields the equation for the velocity:

$$\mathbf{u}_P = \frac{\mathbf{H}(\mathbf{u})}{a_P} - \frac{\nabla p_{\text{rgh}}}{a_P}. \quad (3.60)$$

Velocities on faces are calculated based on different interpolations as follows:

$$\mathbf{u}_f = \left( \frac{\mathbf{H}(\mathbf{u})}{a_P} \right)_f - \left( \frac{1}{a_P} \right)_f (\nabla p_{\text{rgh}})_f. \quad (3.61)$$

Multiplication of the face velocities with the surface vectors,  $\mathbf{S}_f$ , yields the equation for the face flux:

$$\phi_f = \mathbf{S}_f \cdot \mathbf{u}_f = \mathbf{S}_f \cdot \left( \frac{\mathbf{H}(\mathbf{u})}{a_P} \right)_f - \mathbf{S}_f \cdot \left( \frac{1}{a_P} \right)_f (\nabla p_{\text{rgh}})_f. \quad (3.62)$$

Substituting (3.61) into the continuity equation (3.2) yields the Poisson equation:

$$\nabla \cdot \left( \frac{\mathbf{H}(\mathbf{u})}{a_P} \right) - \nabla \cdot \left( \frac{\nabla p_{\text{rgh}}}{a_P} \right) = -\frac{1}{\rho} \frac{d\rho}{dt}. \quad (3.63)$$

The equation is integrated over each control volume. Transformation of the volume integrals into surface integrals is conducted using Gauss' theorem. Finally, the surface integrals are discretised which yields a semi-discretised pressure equation:

$$\sum_f \mathbf{S}_f \cdot \left( \frac{\mathbf{H}(\mathbf{u})}{a_P} \right)_f - \sum_f \mathbf{S}_f \cdot \left[ \left( \frac{1}{a_P} \right)_f (\nabla p_{\text{rgh}})_f \right] = \int_V -\frac{1}{\rho} \frac{d\rho}{dt} dV. \quad (3.64)$$

A problem with this approach lies in the decoupling of pressure and velocity fields, when interpolation of all flow variables and gradients is solely cell-centred. This phenomenon is also called *checkerboard* problem. Similar to the approach of Rhie and Chow (1983), a mechanism to avoid decoupling is implemented in OpenFOAM, The OpenFOAM Foundation Ltd (2018). Hence, in equation (3.64), discretisation of the coefficient  $\left( \frac{1}{a_P} \right)_f$  and the pressure gradient  $(\nabla p_{\text{rgh}})_f$  is conducted separately. At the beginning, the divergence was integrated and transformed into a surface integral using Gauss' theorem. The discretisation asks for velocities on cell faces, which is why the velocities are replaced by the velocity fluxes on the faces. The pressure gradient is needed on the cell faces as well. A calculation of the pressure gradients in the cell centres and interpolation of the gradients onto cell faces would cause a decoupling of pressure and velocity fields. Thus, to avoid decoupling, the pressure gradients are directly calculated on the cell faces using pressure values from the neighbouring cell centres.

For an incompressible, isothermal, and single-phase flow, the density along the path of a fluid particle does not change, which leads to a divergence free velocity field (see (3.3)) and equation (3.64) can further be simplified as:

$$\sum_f \mathbf{S}_f \cdot \left[ \left( \frac{1}{a_P} \right)_f (\nabla p_{\text{rgh}})_f \right] = \sum_f \mathbf{S}_f \cdot \left( \frac{\mathbf{H}(\mathbf{u})}{a_P} \right)_f. \quad (3.65)$$

This equation can be solved for pressure. However, for cavitating flows, changes of density both owing to a moving free surface and to vapourisation and condensation processes have to be considered. For cavitating flows, the density is not constant and the velocity field is not divergence free, so that the temporal change of density on the right hand side of (3.63) does not vanish because it comprises processes of condensation and vapourisation that need to be addressed by further hypotheses. In this work, a cavitation model yields source terms that are substituted for the expression on the right hand side of (3.63) to obtain equation (4.54) (see section 4.2.1). The final discretised pressure equation, including source terms of the cavitation model, reads:

$$\sum_f \mathbf{S}_f \cdot \left[ \left( \frac{1}{a_P} \right)_f (\nabla p_{\text{rgh}})_f \right] + \Delta V (S_{p,c} - S_{p,v}) p_{\text{rgh}} = \sum_f \mathbf{S}_f \cdot \left( \frac{\mathbf{H}(\mathbf{u})}{a_P} \right)_f + \Delta V (S_{p,c} - S_{p,v}) (p_v - \rho g_z h) . \quad (3.66)$$

Here, the source terms of the cavitation model are split into parts proportional to  $p_{\text{rgh}}$  and proportional to  $(p_v - \rho g_z h)$ . This separation enables to treat all terms on the left hand side, that depend on  $p_{\text{rgh}}$ , implicitly. The source terms on the right hand side are treated explicitly.

#### 3.3.3 Pressure-Velocity Coupling

The equations of the coupled system are solved sequentially. Different algorithms to solve this system exist, incorporating iterative and relaxation techniques to ensure stability. Two of the most popular algorithms are the Semi-Implicit Method for Pressure Linked Equations (SIMPLE) algorithm introduced by Caretto et al. (1972) and the Pressure-Implicit with Splitting Operators (PISO) algorithm by Issa (1986). Considering transient flows, both algorithms have their advantages and disadvantages.

Although the SIMPLE algorithm was originally developed for steady-state problems, It can be used for transient problems, where an outer loop is introduced to update the non-linearity of the momentum equation. This means that the momentum matrix is reconstructed and the momentum equation is implicitly solved to give a momentum correction in every outer iteration. Under-relaxation is applied for the pressure calculation in order to improve convergence. The computational cost is high, especially because of reconstruction of the momentum matrix.

On the contrary, the PISO algorithm does not reconstruct the momentum matrix in every outer iteration, but solves only the pressure equation multiple times. Fluxes and velocities are corrected multiple times, using the updated pressure, while the momentum prediction is only solved once every time step. This approach is way more efficient, but restricted to lower Courant numbers where the influence of the non-linearity,  $\mathbf{u}\mathbf{u}$ , from one time step to another is small.

A combination of both algorithms, SIMPLE and PISO, referred to as the PIMPLE algorithm, was developed by Weller (2005) and implemented into OpenFOAM, The OpenFOAM Foundation Ltd (2018). It combines all functionality of both approaches to use either algorithm solely or a combination of both to fit the flow problem at hand. Including the calculation of volume fraction and turbulence variables, the algorithm used in the present work is structured as follows:

---

**Algorithm 1:** PIMPLE algorithm for pressure-velocity coupling

---

Begin with new time step  $t \rightarrow t^{n+1}$ **while** *SIMPLE* **do**

Calculate volume fraction using MULES algorithm

Construct matrix for momentum equation (3.58)

Under-relax momentum matrix

    Solve equation (3.60) for a prediction of the velocity  $\mathbf{u}^{n+1}$  by using an old pressure field    **while** *PISO* **do**        **while** *Non-orthogonal correction* **do**

Construct the pressure equation (3.66)

Solve the pressure equation

**end**        Substitute the pressure into equation (3.62) and correct the flux  $\phi^{n+1}$ 

Under-relax the pressure

        Substitute the pressure into equation (3.60) and correct the velocity  $\mathbf{u}^{n+1}$     **end****end**Calculate turbulence quantities

---

The outer loop is the SIMPLE or PIMPLE loop. At the beginning of the SIMPLE loop, the volume fraction is calculated using the MULES algorithm. Afterwards, the non-linearity of the momentum equation is updated by constructing the momentum matrix. For the SIMPLE loop, a maximum number of iterations as well as residual control can be set to check whether to advance to the next time step. The non-orthogonal corrector loop is used to correct the pressure field when a high percentage of control volumes are non-orthogonal to each other. The PISO loop updates the fluxes and velocities based on the newly calculated pressures. A fixed number of PISO iterations is defined. Under-relaxation can be applied both to pressure and velocity fields. Turbulence equations are solved in the end of each time step after the SIMPLE loop. Further information about the PIMPLE algorithm can be found in OpenCFD Ltd (ESI Group) (2018) and Weller (2005).

For the simulations performed in this work, residual control for pressure and momentum equations along with a fixed maximum number of outer SIMPLE iterations are used. Furthermore, two non-orthogonal corrector and two PISO iterations are set.

## 3.4 Error Estimation

Errors in numerical simulations have different sources. They can be characterised as modelling, discretisation, iterative, input, statistical convergence, and round-off errors. Especially modelling, statistical convergence, and discretisation errors can be of significant magnitude. While the latter two can be quantified and minimised, modelling errors can only be identified by comparison of numerical results to results from experiments or from more accurate approaches, and when discretisation and iteration errors are negligibly small.

### 3.4.1 Modelling Errors

For simulations of laminar single phase flows based on the Navier-Stokes equations, modelling errors can be assumed to be negligible. In contrast, simulations of flows that involve turbulence and cavitation require these processes to be modelled. To simulate cavitating flows, all approaches used in this work rely on physical assumptions. While simulations of cavitation behaviour under the assumption of a continuous vapour phase (Euler-Euler, see section 4.2) involve less details than simulations under the assumption of the vapour phase consisting of spherical Lagrangian bubbles (Euler-Lagrange, see section 4.3), both approaches involve significant modelling errors. All cavitating flows considered in this work are turbulent and simulated using RANS-based eddy viscosity turbulence models. Not only are these turbulence models unable to resolve turbulent eddies, but they also interact with the cavitation models used in this approach (see section 4.2.2). Certain phenomena in a cavitating flow, such as the dynamic shedding of cloud cavitation, can therefore only be captured by including certain modifications of the turbulence model or using an approach that resolves larger turbulent eddies such as DES or LES. Because of the assumptions involved in turbulence and cavitation models and their interactions, modelling errors are supposedly the largest errors in the numerical simulations of this work. Validation of the numerical methods against experimental results or results from more accurate approaches is thus inevitable.

### 3.4.2 Statistical Convergence Errors

The convergence of the temporal progression of a flow quantity, obtained from a numerical solution, needs to be statistically assured. Statistical errors appear because of initialisation and statistical behaviour of the simulated flow. To estimate statistical convergence, in the underlying work, a strategy to use a backward averaging technique, with time intervals consecutively becoming larger, is used, as proposed by Pereira (2018). Depending on the length of the time series, between 1000 and 10000 time intervals are considered for averaging. Figure 3.1 depicts different states for a time series of a quantity based on the strategy from Pereira (2018). Figure 3.1 (left) shows the time history of a variable,  $\Phi$ . At the beginning, the simulation is in a transient state and not yet converged. After an initial transient state, the solution reaches a statistically converged state. Figure 3.1 (right) shows the averaged variable,  $\overline{\Phi}$ , using time

intervals of averaging,  $\Delta T$ , which become consecutively larger. The averaging starts from the end of the time series moving towards the beginning. Time intervals for averaging need to be sufficiently large, but should not reach the transient state, because the averaging would be affected by the initialisation.

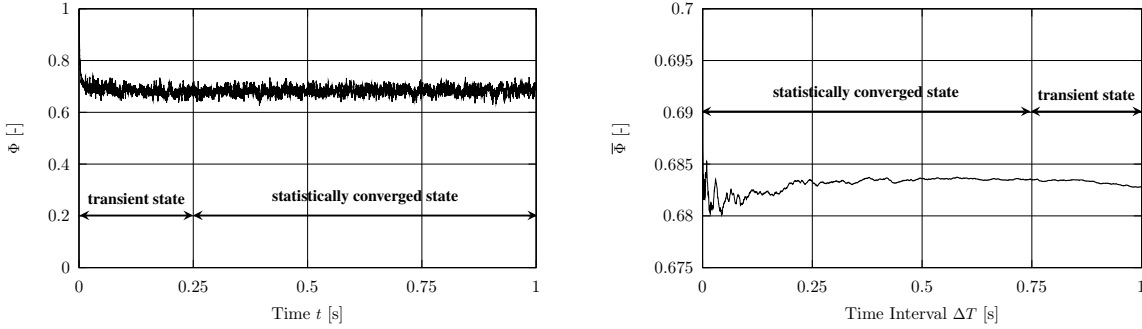


**Figure 3.1:** Time history of a quantity  $\Phi$  (left) and averaged quantity  $\bar{\Phi}$  for different time intervals of averaging (right)

### 3.4.3 Discretisation Errors

Numerical approaches for fluid dynamics problems require discretisation of the governing equations in both space and time. Discretisation errors are amongst the largest errors and need to be estimated in order to address the accuracy of the numerical results. ITTC (2017), Godderidge et al. (2006), and Oberhagemann (2017) proposed procedures to verify convergence of a parameter study using at least three solutions with a uniform refinement ratio,  $r_k$ , between the solutions. While ITTC (2017) does not mention an approach for temporal discretisation when performing a grid dependence study, Godderidge et al. (2006) and Oberhagemann (2017) suggest to keep the Courant number constant. In case of a grid or time step dependence study incorporating three solutions, the refinement ratio is calculated as:

$$r_k = \frac{\Delta h_{k_2}}{\Delta h_{k_1}} = \frac{\Delta h_{k_3}}{\Delta h_{k_2}}, \quad (3.67)$$

with  $\Delta h_{k_i}$  as the reference grid length or time step of the corresponding solution. Here,  $i = 1$  denotes the smallest grid/time spacing,  $i = 2$  the medium spacing, and  $i = 3$  the largest spacing. The difference between solutions  $\hat{S}_{k_3}$  and  $\hat{S}_{k_2}$  is then calculated as:  $\epsilon_{k_{32}} = \hat{S}_{k_3} - \hat{S}_{k_2}$ . The calculation of  $\epsilon_{k_{21}} = \hat{S}_{k_2} - \hat{S}_{k_1}$  is conducted analogously. Afterwards, convergence of a parameter study can be identified using the convergence ratio, which is defined as:

$$R_k = \frac{\epsilon_{k_{21}}}{\epsilon_{k_{32}}}. \quad (3.68)$$

A monotonically converging study is characterised by  $0 < R_k < 1$ , an oscillatory converging one by  $R_k < 0$ , and a diverging one by  $R_k > 1$ . In case of monotonic convergence, Richardson

### 3.4 Error Estimation

extrapolation can be applied to expand the error  $\delta_k$  using a power series expansion. For three solutions, the leading term of the power series expansion can be estimated as:

$$\delta_{RE_k}^* = \frac{\epsilon_{k21}}{r_k^{p_k} - 1}. \quad (3.69)$$

Here, the order of accuracy is calculated using:

$$p_k = \frac{\ln\left(\frac{\epsilon_{k32}}{\epsilon_{k21}}\right)}{\ln(r_k)}. \quad (3.70)$$

Although it is generally preferred to achieve monotonic convergence, in this work, oscillatory convergence is accepted, if the difference between the two solutions of higher discretisation,  $\epsilon_{k21}$ , is sufficiently small. ITTC (2017) propose calculations of errors and uncertainties treating parameter analyses independently and therefore conducting convergence studies regarding spatial and temporal discretisation separately. Eçã et al. (2014) proposed a different strategy to obtain clearly separate contributions of temporal and spatial discretisation using at least five solutions containing three different grids. Further strategies for grid verification studies can be found in Eçã and Hoekstra (2014) and Eçã et al. (2016).

## 4 Modelling of Cavitation and Cavitation-Induced Erosion

Phenomena of cavitation and cavitation erosion incorporate processes that take place on a microscopic scale and within microseconds of time. Especially investigations of cavitation damage require information about the collapses of cavitation structures in the vicinity of a surface. To predict cavitation erosion, an approach to deal with the behaviour of cavitation bubbles near solid walls has to be chosen. In the Euler-Euler approach, the vapour phase is considered as a continuum whose behaviour is obtained from a cavitation model (see section 4.2.1). Thus, for Euler-Euler approaches, information about the behaviour of single cavitation bubbles is missing. However, erosion predictions require model assumptions regarding bubble collapses near walls. In a Lagrangian approach for the vapour phase, the dynamics and motions of each individual spherical bubble are calculated. The information of single bubble behaviour enables erosion predictions based on computations of spherical Lagrangian bubble collapses.

In the underlying chapter, at first, the basics of modelling dynamics and motions of spherical single bubbles are presented. An Euler-Euler methodology to simulate cavitating flows is given, assuming vapour and liquid phases to be continuous. To consider single bubble information, an approach using a Lagrangian treatment of the vapour phase is introduced that enables an accurate simulation of single spherical cavitation bubbles. The Lagrangian approach is first introduced as part of a purely Euler-Lagrange method where the vapour phase is solely treated in forms of spherical Lagrangian bubbles. Afterwards, a hybrid approach, that combines the advantages of Eulerian and Lagrangian approaches to deal with the vapour phase, is presented. Finally, modelling approaches to predict cavitation erosion are proposed: First, a practical and efficient model based on an Eulerian vapour treatment. Second, a more accurate and detailed model, that takes into account single bubble behaviour of Lagrangian bubbles.

### 4.1 Modelling of Spherical Cavitation Bubbles

Cavitation structures such as sheet, cloud, or vortex cavitation consist of agglomerations of single cavitation bubbles. The behaviour of the macroscopic cavitation structures arises from the dynamics and motions of single bubbles located within them. Collapses of single cavitation bubbles near material surfaces cause erosion. To model and investigate cavitation phenomena as well as predict cavitation erosion, it is indispensable to understand single bubble dynamics. This section deals with the dynamics of spherical cavitation bubbles. Parts of this section

are described in Peters and el Moctar (2019) (paper under review). Further details of bubble dynamics and motions are given in Brennen (2005) and Franc and Michel (2005).

### 4.1.1 Dynamics of Spherical Bubbles

Motion of a spherical void in liquid was first investigated by Besant (1859). To investigate the phenomenon of cavitation, which appeared behind ship propellers, Rayleigh (1917) was the first to propose an equation to describe the dynamics of a spherical bubble. Following Rayleigh's ideas, Plesset (1949) derived an equation for the dynamics of a bubble moving through a non-uniform pressure field considering the bubble wall acceleration as well as surface tension. The author compared numerical results to experimental observations. Poritsky (1952) studied viscous effects on bubble dynamics and found that, especially during the collapse phase, viscous effects have a significant influence. Plesset and Zwick (1954) studied thermal effects on bubble dynamics by linking the bubble dynamics problem with a heat diffusion problem. They showed that during the collapse phase of a bubble, a large part of the energy stored in the bubble is converted into acoustic energy to form and radiate shock waves that travel through the liquid. Accordingly, the collapse pressure of a bubble is reduced and consecutive oscillations are damped. Gilmore (1952) and Keller and Kolodner (1956) considered the compressibility of liquid water to account for the radiation of shock waves at bubble collapse. Tomita and Shima (1977) derived a bubble dynamics equation considering compressibility, surface tension, and viscous forces.

In the following, the derivation of the Rayleigh-Plesset equation for bubble dynamics is given based on Brennen (2005). A spherical cavity of radius  $R$  in an infinite Newtonian and isothermal liquid is considered. The pressure in the liquid far from the bubble,  $p_\infty$ , as well as the viscosity of the liquid,  $\mu_l$ , are assumed to be constant. In the first place, the liquid will be considered incompressible. While it will further be assumed that the mass of the non-condensable gas, i.e. air, inside a bubble is constant, the air volume and its pressure are related according to an adiabatic equation of state of an ideal gas. Besides air, the bubble contains saturated vapour with a partial pressure equal to the vapour pressure of water at a certain temperature.

To fulfil mass conservation, the velocity in radial direction, from the centre of the bubble, needs to be inversely proportional to the radial distance from the centre squared:

$$u(r,t) = \frac{F(t)}{r^2}, \quad (4.1)$$

with  $F(t)$  depending on the bubble radius  $R(t)$  based on a kinematic boundary condition. When neglecting mass transfer across the bubble wall, the radial velocity at the interface is defined as  $u(R,t) = \frac{dR}{dt}$ . This yields the kinematic boundary condition with:

$$F(t) = R^2 \frac{dR}{dt}. \quad (4.2)$$

For the motion in radial direction,  $r$ , from the bubble centre, the Navier-Stokes equation is written as:

$$-\frac{1}{\rho_1} \frac{\partial p}{\partial r} = \frac{\partial u}{\partial t} + u \frac{\partial u}{\partial r} - \nu_1 \left[ \frac{1}{r^2} \frac{\partial}{\partial r} \left( r^2 \frac{\partial u}{\partial r} \right) - \frac{2u}{r^2} \right], \quad (4.3)$$

substituting  $u = \frac{F}{r^2}$  with  $u(r, t) = u$  and  $F(t) = F$  and differentiating the terms on the right hand side with respect to  $r$  one obtains:

$$-\frac{1}{\rho_1} \frac{\partial p}{\partial r} = \frac{1}{r^2} \frac{\partial F}{\partial t} - \frac{2F}{r^5}, \quad (4.4)$$

with diffusion terms vanishing after differentiation. Integrating the left hand side with respect to  $p$  and the right hand side with respect to  $r$  and substituting  $F = R^2 \frac{dR}{dt}$ :

$$-\frac{1}{\rho_1} \int_{p_{r=R}}^{p_\infty} dp = \int_R^\infty \left[ \frac{1}{r^2} \frac{\partial}{\partial t} \left( R^2 \frac{dR}{dt} \right) - \frac{2R^2}{r^5} \frac{dR}{dt} \right] dr, \quad (4.5)$$

yields:

$$\frac{p_{r=R} - p_\infty}{\rho_1} = R\ddot{R} + \frac{3}{2}\dot{R}^2, \quad (4.6)$$

with  $\dot{R} = \frac{dR}{dt}$  and  $\ddot{R} = \frac{d^2R}{dt^2}$ . Considering viscous forces and surface tension, the pressure at the bubble interface is defined as:

$$p_{r=R} = p_b - \frac{2\sigma}{R} - \frac{4\mu_1\dot{R}}{R}, \quad (4.7)$$

with the pressure inside the bubble,  $p_b = p_{g,0} \left( \frac{R_0}{R} \right)^{3\gamma_h} + p_v$ . The bubble pressure incorporates the partial pressures owing to the vapour pressure,  $p_v$ , and the non-condensable gas pressure. The non-condensable gas undergoes adiabatic expansion and compression processes according to an ideal gas law.  $p_{g,0}$  is the initial gas pressure of the bubble at initial radius  $R_0$ .  $\gamma_h$  is the ratio of specific heats.  $\sigma$  is the surface tension of water. Substituting (4.7) into (4.6) yields the Rayleigh-Plesset equation:

$$\frac{p_b - p_\infty}{\rho_1} = R\ddot{R} + \frac{3}{2}\dot{R}^2 + \frac{4\nu_1\dot{R}}{R} + \frac{2\sigma}{\rho_1 R}. \quad (4.8)$$

While this equation is valid for an isolated stationary bubble, it is less accurate for a bubble moving through a variable pressure field. For a bubble being transported by a carrier fluid, the far field pressure outside of the bubble has to be taken from the flow field of the carrier fluid. A simple approximation is to choose the carrier flow pressure at the position of the bubble's centre which, in this work, was used for small bubbles. A more complex technique is part of the spherical bubble dynamics model supposed by Hsiao et al. (2000). Therein, for larger bubbles, an averaging of liquid pressures at multiple locations along the bubble's outer wall is conducted. This method enables a better approximation of the carrier fluid pressure for larger bubbles and prevents them from extensive unphysical growth in low pressure regions.

#### 4.1 Modelling of Spherical Cavitation Bubbles

Furthermore, the authors considered an additional term attributable to the relative velocity between carrier fluid and bubble,  $\rho_1(\mathbf{u} - \mathbf{u}_b)^2/4$ . Here,  $\mathbf{u}$  is the liquid velocity and  $\mathbf{u}_b$  is the bubble velocity. Adding this term to the right hand side of equation (4.8) results in:

$$\frac{p_b - p_\infty}{\rho_1} = R\ddot{R} + \frac{3}{2}\dot{R}^2 + \frac{4\nu_1\dot{R}}{R} + \frac{2\sigma}{\rho_1 R} - \frac{(\mathbf{u} - \mathbf{u}_b)^2}{4}. \quad (4.9)$$

A full derivation of this modified Rayleigh-Plesset equation can be found in Hsiao et al. (2000).

Effects ascribable to compressibility of the liquid phase were considered by Tomita and Shima (1977). They derived the bubble dynamics equation based on Bernoulli's equation for a spherical potential flow. To account for isentropic changes of the liquid phase and therefore liquid compressibility, they used the Tait equation. It relates pressures and densities as follows:

$$\frac{p + B}{p_\infty + B} = \left( \frac{\rho_g}{\rho_\infty} \right)^n. \quad (4.10)$$

$B = 300\text{MPa}$  and  $n = 7$  are constants for a water temperature of  $20^\circ\text{C}$ . Boundary conditions to derive the bubble dynamics equation assume a zero velocity potential in the far field and, in contrast to an incompressible liquid phase, a velocity at the bubble interface of  $u(R, T) = \varepsilon_R \dot{R}$ . Hence, the bubble dynamics equation reads:

$$\frac{p_{r=R} - p_\infty}{\varepsilon \rho_1} + \frac{R\dot{p}_{r=R}}{\varepsilon \rho_1 c_\infty} = R\ddot{R} \left[ 1 - (1 + \varepsilon_R) \frac{\dot{R}}{c_\infty} \right] + \frac{3}{2}\dot{R}^2 \left( \frac{4 - \varepsilon_R}{3} - \frac{4}{3} \frac{\dot{R}}{c_\infty} \right). \quad (4.11)$$

$c_\infty$  is the speed of sound in the far field and  $\varepsilon_R = 1 - \rho_g/\rho_1$ . As opposed to the Rayleigh-Plesset equation, the terms on the right hand side depend on  $c_\infty$  and  $\varepsilon_R$ . Moreover, a second term is introduced on the left hand side, including the time derivative of the pressure at the bubble interface,  $\dot{p}_{r=R}$ . Assuming an incompressible liquid phase where  $c_\infty \rightarrow \infty$  and  $\varepsilon_R \rightarrow 1$ , equation (4.11) would reduce to the Rayleigh-Plesset equation (4.6). A first order approximation of the pressure at the bubble interface reads:

$$p_{r=R} = p_{g,0} \left( \frac{R_0}{R} \right)^{3\gamma_h} + p_v - \frac{2\sigma}{R} - \varepsilon_R \frac{4\mu_1\dot{R}}{R}. \quad (4.12)$$

Its time derivative is then written as:

$$\dot{p}_{r=R} = -3\gamma_h p_{g,0} \frac{\dot{R}}{R} \left( \frac{R_0}{R} \right)^{3\gamma_h} + \frac{2\sigma}{R^2} \dot{R} - \varepsilon_R 4\mu_1 \frac{\ddot{R}R - \dot{R}^2}{R^2}. \quad (4.13)$$

Equations (4.8), (4.9), and (4.11) serve to calculate the bubble wall acceleration,  $\ddot{R}$ . Afterwards, the bubble wall velocity is obtained from time integration:

$$\dot{R}^{m+1} = \dot{R}^m + \Delta t \ddot{R}. \quad (4.14)$$

$m$  is the index representing the old time step for the solution of bubble dynamics and  $m + 1$  is the index related to the new time step. Time integration is conducted in two steps using a Trapezoidal rule which is implicit and of second order. Close to the moment of bubble collapse, bubble wall velocity and acceleration as well as their changes in time are rather large. Therefore, to efficiently calculate the bubble dynamics, adaptive time-stepping was utilised. Time integration of bubble dynamics was conducted until reaching the same time instance as in the Eulerian flow solution.

As liquid compressibility plays a minor role during the growth phase of a bubble, in this work, equation (4.8) was solved for bubbles up to a threshold radius that depends on the case simulated. For the growth of bubbles that exceed this threshold radius, equation (4.9) was used in order to consider effects assignable to relative velocity. In addition, the liquid pressure was averaged from multiple positions at the bubble wall, Hsiao et al. (2000). During collapse, liquid compressibility needs to be considered to model the effect of shock wave radiation on bubble dynamics. Thus, equation (4.11) was used to calculate bubble dynamics during a bubble's collapse phase.

#### 4.1.2 Lagrangian Description of Spherical Bubble Motion

In many cases, cavitation bubbles are transported by the liquid flow. In terms of a Lagrangian approach, the liquid phase is therefore also referred to as *carrier fluid*. However, bubble trajectories can deviate considerably from the streamlines of a liquid fluid flow, especially when high gradients of flow quantities are present. On the suction side of a hydrofoil, cavitation inception can occur further downstream from the region of lowest pressure – known as *bubble screening* – because the trajectories of gas bubbles are deflected around the low pressure region, which is attributable to large ambient pressure gradients. In a resting liquid column, bubbles will rise to the free surface without the presence of any liquid flow. Further differences between bubble trajectories and flow streamlines appear because of large gradients of flow quantities, vortices in the flow, gravity, or bubble dynamics. In Euler-Euler simulations, both phases are treated as continua and relative motions between bubbles and liquid flow are neglected. In the present work, in order to simulate the motions of spherical single bubbles, a Lagrangian approach was used. General considerations about the transport of spherical bubbles as well as the Lagrangian description of motions are summarised from Oweis et al. (2005), Hsiao et al. (2000), Abdel-Maksoud et al. (2010), and Lantermann (2006).

Flows can be treated using an Eulerian or Lagrangian description. In the Lagrangian point of view, the quantities of a fluid particle are analysed in a local coordinate system. This can be explained by looking at the total derivative of a scalar quantity,  $\phi$ , which may be split into partial derivatives:

$$\frac{d\phi}{dt} = \left( \frac{\partial \phi}{\partial t} \right)_{x=const} + u \left( \frac{\partial \phi}{\partial x} \right)_{t=const} . \quad (4.15)$$

$\frac{d\phi}{dt}$  is also called the Lagrangian derivative, which can be used to express the rate of change of a scalar quantity of a fluid element being followed. On the contrary, in the Eulerian point

#### 4.1 Modelling of Spherical Cavitation Bubbles

of view, the total derivative can be expressed with the time derivative at a constant location and a convection term. Here,  $\left(\frac{\partial \varphi}{\partial t}\right)_{x=const}$  is the Eulerian derivative at a constant position.  $u \left(\frac{\partial \varphi}{\partial x}\right)_{t=const}$  is the convection containing the partial derivative of  $\varphi$  with respect to the coordinate  $x$  at constant time.

It is noted that the following Lagrangian approach is described, assuming a one-way coupling approach in which the carrier phase is a pure liquid. In case of a two- or four-way coupling, the liquid quantities, denoted by the index  $l$ , are substituted by the quantities of the homogeneous mixture. Based on Newton's second law, the Lagrangian equation of motion for a bubble can be derived and reads:

$$m_b \frac{d\mathbf{u}_b}{dt} = \sum_i \mathbf{F}_i . \quad (4.16)$$

$\mathbf{u}_b$  is the velocity of the bubble and  $m_b = \rho_b V_b$  the mass of the bubble. The volume of a sphere is  $V_b = \frac{4}{3}\pi R^3$  with  $R$  as the bubble radius.  $\rho_b$  is the density of the bubble. As the mass of vapour in a bubble mostly outweighs the mass of non-condensable gas, the density of the bubble is assumed to be equal to the vapour density.  $\mathbf{F}_i$  are different forces acting on the bubble, explained in the following.

A bubble in an acoustic field experiences a force ascribable to a pressure gradient that depends on amplitude and frequency of the sound wave and causes a motion of the bubble, even though the carrier flow velocity is zero. This pressure gradient force is called the primary Bjerknes force. It was first identified by Blake (1949a) and goes back to the effects discovered by Bjerknes (1909). The Bjerknes force is present in all kinds of situations in which bubbles face pressure gradients and it can be written as:

$$\mathbf{F}_{pg} = -V_b \nabla p . \quad (4.17)$$

As found by Corrsin and Lumley (1956) the momentum equation, when neglecting viscous effects, volume forces, and assuming an incompressible fluid, can be written as:

$$\rho_1 \frac{d\mathbf{u}}{dt} = \rho_1 \frac{\partial \mathbf{u}}{\partial t} + \rho_1 \nabla \cdot \mathbf{u}\mathbf{u} = -\nabla p , \quad (4.18)$$

where  $\mathbf{u}$  is the velocity of the carrier fluid. This expression can be substituted into (4.17) to obtain:

$$\mathbf{F}_{pg} = V_b \rho_1 \frac{d\mathbf{u}}{dt} = \frac{m_b \rho_1}{\rho_b} \frac{d\mathbf{u}}{dt} . \quad (4.19)$$

Because of the acceleration of a body in a liquid, a part of the liquid volume around the body needs to be displaced, which causes a force proportional to the regarded liquid volume. Although different parts of the liquid perform different motions, a simplification supposes that, depending on the motion and shape of the considered body, a part of the liquid mass surrounding the body is accelerated together with it. The force based on this effect is called

added mass or virtual mass force. For a bubble, the virtual mass force is proportional to the acceleration of the bubble, relative to the carrier fluid, and reads:

$$\mathbf{F}_{\text{vm}} = 0.5\rho_l V_b \left( \frac{d\mathbf{u}}{dt} - \frac{d\mathbf{u}_b}{dt} \right). \quad (4.20)$$

It can be shown, for a potential flow, that the added mass of a sphere is half the volume of the sphere multiplied by the density of the liquid:  $m_a = \frac{1}{2}\rho_l V_b$ .

Owing to rapid growth and collapse processes, a force depending on the bubble's volume variation has to be taken into account. It is written according to Johnson and Hsieh (1966):

$$\mathbf{F}_{\text{volume}} = \frac{\rho_l}{2} \frac{dV_b}{dt} (\mathbf{u} - \mathbf{u}_b) = \frac{3}{2}\rho_l V_b \frac{\dot{R}}{R} (\mathbf{u} - \mathbf{u}_b). \quad (4.21)$$

Both the radius growth rate as well as the relative velocity between carrier fluid and bubble,  $(\mathbf{u} - \mathbf{u}_b)$ , determine magnitude and direction of this force. In case of a relative velocity between bubble and carrier fluid, a drag force is exerted on the bubble as well:

$$\mathbf{F}_{\text{drag}} = \frac{3}{4} c_D m_{\text{eff}} \mu_l \frac{1}{(\rho_b (2.0R))^2} |\mathbf{u} - \mathbf{u}_b| (\mathbf{u} - \mathbf{u}_b), \quad (4.22)$$

with the effective mass of the bubble,  $m_{\text{eff}} = m_b + m_a$ , consisting of the mass of the bubble,  $m_b$ , and its added mass,  $m_a$ .  $\mu_l$  is the viscosity of the carrier fluid. According to Haberman and Morton (1953) the drag coefficient can be defined as:

$$c_D = 24.0(1.0 + 0.197\text{Re}_b^{0.63} + 2.6 \cdot 10^{-4}\text{Re}_b^{1.38}). \quad (4.23)$$

$\text{Re}_b = \frac{\rho_l |\mathbf{u} - \mathbf{u}_b| 2R}{\mu_l}$  is the bubble Reynolds number. When inertia forces, exerted from the carrier fluid onto the bubble, are smaller than gravity, e.g. for a bubble rising in a resting liquid, the drag force can be written as stated by Darmana et al. (2006):

$$\mathbf{F}_{\text{drag,grav}} = \frac{1}{2} c_{D,E\ddot{o}} \rho_l \pi R^2 |\mathbf{u} - \mathbf{u}_b| (\mathbf{u} - \mathbf{u}_b), \quad (4.24)$$

with the drag coefficient  $c_{D,E\ddot{o}} = \frac{8}{3} \frac{E\ddot{o}}{E\ddot{o}+4}$  and the Eötvös number  $E\ddot{o} = (\rho_l - \rho_b)\mathbf{g}(2R_b)^2/\sigma$ .  $\mathbf{g} = (0, 0, -9.81) \text{ m/s}^2$  is the gravitational acceleration vector, which is assumed to be constant.

Saffman (1965) showed that for a sphere in a parallel flow, a shear lift force perpendicular to the direction of the flow and in direction of higher parallel flow velocities acts on the bubble. Figure 4.1 sketches a bubble moving in the same direction as the parallel flow. Because the magnitude of flow velocities increases from bottom to top, an upwards directed shear lift force is generated on the bubble, which causes a bubble motion in direction of the higher parallel flow velocities.

#### 4.1 Modelling of Spherical Cavitation Bubbles

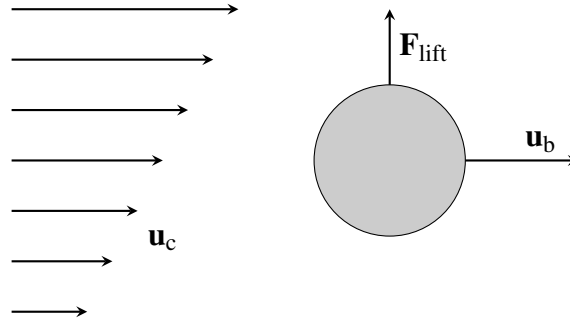


**Figure 4.1:** Saffman shear lift force generated on a bubble by the carrier fluid

The Saffman lift force depends on the relative velocity between the phases and the circulation in the flow and reads:

$$\mathbf{F}_{\text{lift}} = \frac{3}{8} c_L \rho_l V_b \frac{(\mathbf{u} - \mathbf{u}_b)}{\alpha_S} \times \boldsymbol{\omega}, \quad (4.25)$$

with the dimensionless shear rate:

$$\alpha_S = \frac{|\boldsymbol{\omega}|R}{|\mathbf{u} - \mathbf{u}_b|}. \quad (4.26)$$

$\boldsymbol{\omega} = \nabla \times \mathbf{u}$  is the vorticity of the carrier phase flow. The lift coefficient,  $c_L$ , depends on the values of bubble Reynolds number as well as dimensionless shear rate. For weak shear forces of  $\alpha_S \leq 5 \cdot 10^{-4}$  it is given by Auton (1987) and Auton et al. (1988):

$$c_L = \frac{4}{3} \alpha_S. \quad (4.27)$$

Furthermore, for Reynolds numbers less than 20, the lift coefficient is defined according to Saffman (1965):

$$c_L = 5.82 \sqrt{\frac{\alpha_S}{Re_b}}. \quad (4.28)$$

As shown in simulations of Dandy and Dwyer (1990) for  $5 \cdot 10^{-4} < \alpha_S \leq 0.4$  and  $Re_b > 20$  the lift coefficient can be approximated as:

$$c_L = 0.3 \alpha_S. \quad (4.29)$$

In all other cases, the coefficient is calculated from:

$$c_L = 0.59 \alpha_S^{0.25}, \quad (4.30)$$

which was experimentally determined by Sridhar and Katz (1999).

Finally, the buoyancy force exerted on a bubble originates from the difference in density between the two phases:

$$\mathbf{F}_{\text{grav}} = (\rho_b - \rho_l) \mathbf{g} V_b. \quad (4.31)$$

A gas bubble will, thereby, rise in a column of liquid without the presence of any liquid flow.

In the present approach, the virtual mass force (4.20) is decomposed into a part proportional to the acceleration of the carrier fluid,  $\frac{d\mathbf{u}}{dt}$ , and a part proportional to the acceleration of the bubble,  $\frac{d\mathbf{u}_b}{dt}$ . As explained by Ohl et al. (2003), when the Bjerknes force is expressed by the carrier fluid acceleration (see (4.19)), the pressure gradient force and the part of the added mass force, which is proportional to the carrier fluid acceleration, can be joined together as follows:

$$\mathbf{F}_{pg} + \mathbf{F}_{vm,c} = \frac{3}{2}\rho_l V_b \frac{d\mathbf{u}}{dt}. \quad (4.32)$$

The part of the virtual mass force, which is proportional to the bubble acceleration, is then moved to the left hand side of (4.16) to obtain:

$$m_{\text{eff}} \frac{d\mathbf{u}_b}{dt} = \sum_i \mathbf{F}_i. \quad (4.33)$$

Temporal integration of equation (4.33) is conducted using a semi-implicit scheme. Forces depending on the bubble velocity, i.e. parts of the volume variation and drag force, are treated implicitly (see (4.21), (4.22)) while all other forces are naturally treated explicitly. The bubble velocity is then calculated from the equation:

$$\mathbf{u}_b^{n+1} + \frac{\Delta t}{m_{\text{eff}}} \mathbf{F}^{n+1} = \mathbf{u}_b^n + \frac{\Delta t}{m_{\text{eff}}} \mathbf{F}^n. \quad (4.34)$$

$\mathbf{u}_b^{n+1}$  is the bubble velocity of the actual time step,  $(n+1)$ , for which the equation is solved.  $\mathbf{u}_b^n$  is the bubble velocity of the last time step,  $n$ . Implicit force terms are denoted  $\mathbf{F}^{n+1}$  and explicit ones  $\mathbf{F}^n$ .  $\Delta t$  is the time step of the Lagrangian time integration. The motions of bubbles take place in other time periods than motions of the carrier flow. If a Lagrangian bubble passes through multiple control volumes during one Eulerian time step, the Lagrangian time step is adapted and time integration is continued until the next Eulerian time instance is reached. Integration of the new bubble velocity over time yields the new bubble position,  $\mathbf{x}_b$ , from:

$$\frac{d\mathbf{x}_b}{dt} = \mathbf{u}_b. \quad (4.35)$$

## 4.2 Euler-Euler Approach

In this work, methods that treat both liquid and vapour phase of water as continua on an Eulerian grid, while solving one set of governing equations for the homogeneous mixture of the phases, are referred to as Euler-Euler methods. The VOF method is selected to capture the interface between the phases. Because a homogeneous mixture of liquid and vapour phases is considered, the quantities of the mixture vary according to the volume fractions of liquid and vapour in regarded control volumes. The vapour volume fraction is defined as  $\alpha_v = \frac{V_v}{V_{cv}}$  with the volume of vapour  $V_v$  in a certain control volume (CV) of total volume  $V_{cv} = V_v + V_l$ .  $V_l$  is the volume of liquid in the CV. For a two-phase flow, the liquid volume fraction is then defined as  $\alpha_l = 1 - \alpha_v$ . Using the volume fractions, density  $\rho$  and viscosity  $\mu$  of the mixture can be calculated according to (3.21). Considering the indices for vapour phase quantities, v, and liquid phase quantities, l, one obtains:

$$\rho = \alpha_v \rho_v + (1 - \alpha_v) \rho_l, \quad \mu = \alpha_v \mu_v + (1 - \alpha_v) \mu_l. \quad (4.36)$$

The vapour volume fraction needs to be obtained by solving a volume fraction equation. In light of the consideration of phase change, equation (3.23) is enhanced by adding source terms to the right hand side. This yields:

$$\frac{\partial}{\partial t} \int_V \alpha_v dV + \int_S \alpha_v \mathbf{u} \cdot d\mathbf{S} = \int_V (S_v - S_c) dV. \quad (4.37)$$

Using the calculated volume fraction, the equations of conservation are solved for the homogeneous mixture using the mixture quantities. The source terms  $S_v$  and  $S_c$  represent processes of vapourisation (index v) and condensation (index c), respectively, which are obtained from a cavitation model.

### 4.2.1 Sauer and Schnerr Cavitation Model

When considering the vapour phase as a continuum, information about single bubbles is limited because their individual behaviour is not directly calculated. To model the processes of vapourisation and condensation of cavitation structures reasonably, common cavitation models share the idea of using basic relations from bubble dynamics equations to derive the regarded source terms for the volume fraction equation (4.37) and pressure equation (3.63). These cavitation models need to account for growth and collapse of vapour structures. Convective transport of vapour volumes is naturally represented by the convection term in the volume fraction equation.

Singhal et al. (2002) developed the so-called *full cavitation model* taking into account growth and collapse of vapour volumes as well as their transport. Additionally, effects of turbulent pressure fluctuations on cavitation and the non-condensable gas content were considered. Zwart et al. (2004) as well as Merkle et al. (1998) used simplified bubble dynamics to find formulations for mass transfer rates between liquid and vapour phases during processes of

vapourisation and condensation. Another mass transfer approach was used by Kunz et al. (2000) incorporating the fraction of non-condensable gases. All of the mentioned models use a simplified Rayleigh-Plesset equation to yield the growth and collapse of vapour volumes.

Sauer (2000) and Sauer and Schnerr (2000) chose to model the processes of vapourisation and condensation based on the distribution of cavitation nuclei and the dynamics of single bubbles. In addition to aforementioned cavitation models, their approach considers the effect of the distribution of non-condensable gas nuclei on cavitation. The model is based on the fact that the vapour phase can be defined by an accumulated volume of a certain number of single vapour bubbles per volume of liquid. The vapour volume in a cell can be expressed as:

$$\alpha_v = \frac{V_v}{V_{cv}} = \frac{n_{\text{bub}}^{4/3} \pi R^3}{V_1 + V_v} . \quad (4.38)$$

Using the expression for the number of cavitation bubbles,  $n_{\text{bub}} = n_0 V_1$  ( $n_0$ : number of cavitation nuclei per volume of liquid), and  $V_{cv} = V_v + V_1$  the vapour volume fraction can be written as follows:

$$\alpha_v = \frac{n_0 V_1^{4/3} \pi R^3}{V_1 + n_0 V_1^{4/3} \pi R^3} = \frac{n_0^{4/3} \pi R^3}{1 + n_0^{4/3} \pi R^3} . \quad (4.39)$$

$R$  is the average radius of the bubbles in a regarded control volume. To simplify the derivation of the cavitation model, the vapour volume fraction equation is written for an infinitesimal small volume:

$$\frac{\partial \alpha_v}{\partial t} + \nabla \cdot (\mathbf{u} \alpha_v) = \frac{d \alpha_v}{dt} + \alpha_v \nabla \cdot \mathbf{u} . \quad (4.40)$$

Expressions need to be found for both the substantial derivative and the divergence of the velocity on the right hand side of (4.40). Substituting the homogeneous mixture expression (4.36) into continuity equation (3.2) yields:

$$\nabla \cdot \mathbf{u} = -\frac{1}{\rho} \frac{d \rho}{dt} = -\frac{1}{\alpha_v \rho_v + (1 - \alpha_v) \rho_l} \frac{d}{dt} (\alpha_v \rho_v + (1 - \alpha_v) \rho_l) , \quad (4.41)$$

after derivation one obtains:

$$\nabla \cdot \mathbf{u} = -\frac{1}{\alpha_v \rho_v + (1 - \alpha_v) \rho_l} \left( (\rho_v - \rho_l) \frac{d \alpha_v}{dt} + (1 - \alpha_v) \frac{d \rho_l}{dt} + \alpha_v \frac{d \rho_v}{dt} \right) . \quad (4.42)$$

Neglecting the derivatives of phase densities because of the incompressible flow assumption and assuming that  $(\rho_v \ll \rho_l)$  and  $(\alpha_v \rho_v \ll (1 - \alpha_v) \rho_l)$  it can further be simplified:

$$\nabla \cdot \mathbf{u} = -\frac{\rho_v - \rho_l}{\alpha_v \rho_v + (1 - \alpha_v) \rho_l} \frac{d \alpha_v}{dt} = \frac{1}{1 - \alpha_v} \frac{d \alpha_v}{dt} . \quad (4.43)$$

Substituting (4.43) into (4.40) yields:

$$\frac{\partial \alpha_v}{\partial t} + \nabla \cdot (\mathbf{u} \alpha_v) = \left( 1 + \frac{\alpha_v}{1 - \alpha_v} \right) \frac{d \alpha_v}{dt} . \quad (4.44)$$

## 4.2 Euler-Euler Approach

To find the substantial derivative of the volume fraction, the time derivative of vapour volume is stated as:

$$\begin{aligned}\frac{d}{dt}V_v &= \frac{d}{dt} \left( n_{\text{bub}} \frac{4}{3} \pi R^3 \right) = \frac{4}{3} \pi R^3 \frac{d}{dt} (n_0 V_{\text{cv}} (1 - \alpha_v)) + n_0 V_{\text{cv}} (1 - \alpha_v) \frac{d}{dt} \left( \frac{4}{3} \pi R^3 \right) \\ &= -n_0 \frac{4}{3} \pi R^3 V_{\text{cv}} \frac{d\alpha_v}{dt} + n_0 V_{\text{cv}} (1 - \alpha_v) \frac{d}{dt} \left( \frac{4}{3} \pi R^3 \right),\end{aligned}\quad (4.45)$$

from which the time derivative of the volume fraction can be obtained:

$$\begin{aligned}\frac{d\alpha_v}{dt} &= (1 - \alpha_v) \frac{n_0}{1 + \frac{4}{3} \pi R^3} \frac{d}{dt} \left( n_0 \frac{4}{3} \pi R^3 \right) \\ &= (1 - \alpha_v) \alpha_v \frac{3\dot{R}}{R}.\end{aligned}\quad (4.46)$$

The time derivative of the average bubble radius  $\dot{R}$  is still unknown. In hydrodynamic flows, it is assumed that the driving force to either cause bubble growth or bubble collapse is generated by the pressure difference between liquid pressure,  $p$ , and pressure in the bubble,  $p_b$ . A simplified formulation for  $\dot{R}$  is obtained from the Rayleigh-Plesset equation for bubble dynamics (4.8). It is further assumed that both liquid and vapour phases are incompressible, the bubble wall acceleration, surface tension, and viscous effects are negligible, and that  $p_b = p_v$  and  $p_\infty = p$ . When the liquid pressure,  $p$ , is lower than the vapour pressure,  $p_v$ , the bubble wall velocity,  $\dot{R} = \frac{dR}{dt}$ , also referred to as bubble growth rate, is calculated as:

$$\dot{R} = \sqrt{\frac{2}{3} \frac{(p_v - p)}{\rho_l}}, \quad \text{if } p < p_v. \quad (4.47)$$

On the other hand, the negative velocity of the bubble wall, referred to as bubble collapse rate, is calculated as follows:

$$\dot{R} = \sqrt{\frac{2(p - p_v)}{3\rho_l}}, \quad \text{if } p \geq p_v. \quad (4.48)$$

Using the relations (4.47), (4.48) and substituting (4.46) into (4.44) yields the volume fraction equation including cavitation source terms for the right hand side:

$$\frac{\partial \alpha_v}{\partial t} + \nabla \cdot (\mathbf{u} \alpha_v) = \pm \left( 1 + \frac{\alpha_v}{1 - \alpha_v} \right) (1 - \alpha_v) \alpha_v \left( \frac{4}{3} \pi n_0 \frac{\alpha_v}{1 - \alpha_v} \right)^{\frac{1}{3}} 3 \sqrt{\frac{2}{3} \frac{|p_v - p|}{\rho_l}}. \quad (4.49)$$

Here, the sign on the right hand side of the equation depends on the difference between the liquid and the vapour pressure to represent a process of condensation or vapourisation. In OpenFOAM a slightly different formulation for the source terms of condensation,  $S_c$ , and vapourisation,  $S_v$ , in (4.37) is used. The source terms are calculated as follows:

$$\begin{aligned}
 S_v &= \begin{cases} (-C_v) \frac{1}{R(\alpha_l)} \left[ \frac{1}{\rho_l} - \alpha_l \left( \frac{1}{\rho_l} - \frac{1}{\rho_v} \right) \right] \frac{3\rho_v \rho_l}{\rho} (1 + \alpha_{\text{nuc}} - \alpha_l) \sqrt{\frac{2}{3} \frac{(p_v - p)}{\rho_l}}, & \text{if } p < p_v \\ 0 & \text{else,} \end{cases} \\
 S_c &= \begin{cases} C_c \frac{1}{R(\alpha_l)} \left[ \frac{1}{\rho_l} - \alpha_l \left( \frac{1}{\rho_l} - \frac{1}{\rho_v} \right) \right] \frac{3\rho_v \rho_l}{\rho} \alpha_l \sqrt{\frac{2}{3} \frac{(p - p_v)}{\rho_l}}, & \text{if } p \geq p_v \\ 0 & \text{else.} \end{cases}
 \end{aligned} \quad (4.50)$$

Here, the reciprocal bubble radius is given by:

$$\frac{1}{R(\alpha_l)} = \left( \frac{4\pi n_0}{3} \frac{\alpha_l}{1 + \alpha_{\text{nuc}} - \alpha_l} \right)^{1/3}, \quad (4.51)$$

and the radius of the bubble is given by:

$$R = \sqrt[3]{\frac{3(1 - \alpha_l + \alpha_{\text{nuc}})}{\alpha_l 4\pi n_0}}. \quad (4.52)$$

where  $\alpha_{\text{nuc}}$  is the volume fraction related to the non-condensable gas and thus the equilibrium bubble radius,  $R_0$ . It is calculated analogously to the vapour volume fraction in 4.39 as:

$$\alpha_{\text{nuc}} = \frac{n_0 \frac{4}{3} \pi R_0^3}{1 + n_0 \frac{4}{3} \pi R_0^3}. \quad (4.53)$$

$C_v$  and  $C_c$  are constants of vapourisation and condensation. In this work, both constants were set to unity. Because cavitation has an influence on pressure as well, interaction between the phases takes place in terms of a source term on the right hand side of the pressure equation (3.63) (see section 3.3.2). The right hand side of this equation only vanishes for incompressible isothermal single-phase flows with a divergence free velocity field. For cavitating flows, the term on the right hand side needs to be considered. Sauer (2000) deduced an approach to handle the right hand side by source terms from the cavitation model. Depending on the local fluid pressure, a process of vapourisation or condensation starts, causing the vapour volume to either grow or shrink. The source terms in the pressure equation, which account for vapourisation,  $S_{p,v}$ , and condensation,  $S_{p,c}$ , are multiplied by the pressure difference between vapour pressure,  $p_v$ , and local fluid pressure,  $p$ . To increase the stability of this Poisson equation, the cavitation source terms are split into implicitly and explicitly treated parts. The fluid pressure is reduced by the hydrostatic pressure,  $p_{\text{rgh}} = p - \rho g_z h$ , and thus the pressure equation written as:

$$\nabla \cdot \left( \frac{\nabla p_{\text{rgh}}}{a_p} \right) + (S_{p,c} - S_{p,v}) p_{\text{rgh}} = \nabla \cdot \left( \frac{\mathbf{H}(\mathbf{u})}{a_p} \right) + (S_{p,c} - S_{p,v}) (p_v - \rho g_z h). \quad (4.54)$$

As a consequence of this conversion, the temporal derivative of the density is removed from (3.63). On the left hand side, the cavitation source terms proportional to  $p_{\text{rgh}}$  are handled

## 4.2 Euler-Euler Approach

implicitly in the same manner as the discretised gradient of  $p_{\text{rgh}}$  and are incorporated into the coefficient matrix. This procedure helps to stabilise the solution of the Poisson equation. Cavitation source terms on the right hand side are handled explicitly. The source terms for the pressure equation are defined as:

$$S_{p,v} = \begin{cases} (-C_v) \frac{1}{R(\alpha_1)} \left( \frac{1}{\rho_l} - \frac{1}{\rho_v} \right) (1 - \alpha_1) \alpha_1 \frac{3\rho_l \rho_v}{\rho} \sqrt{\frac{2}{3\rho_l |p - p_v|}} & \text{if } p < p_v \\ 0 & \text{else ,} \end{cases} \quad (4.55)$$

$$S_{p,c} = \begin{cases} C_c \frac{1}{R(\alpha_1)} \left( \frac{1}{\rho_l} - \frac{1}{\rho_v} \right) (1 - \alpha_1) \alpha_1 \frac{3\rho_l \rho_v}{\rho} \sqrt{\frac{2}{3\rho_l |p - p_v|}} & \text{if } p \geq p_v \\ 0 & \text{else .} \end{cases}$$

As these source terms depend on space and time, they have to be updated before the pressure equation is solved.

### 4.2.2 Turbulence Effects on Cavitation

Turbulence in a flow may have an essential influence on cavitation and vice versa. In experimental tests, Singhal et al. (2002) showed that turbulent pressure fluctuations have an effect on the local vapour pressure. More turbulence in a flow would therein lead to a higher theoretical value of the vapour pressure and thus earlier cavitation inception. This can be explained by the fact that the pressure computed in a RANS-based approach is the mean pressure of the flow; inside turbulent eddies, the actual pressure can be considerably lower. According to Singhal et al. (2002), this can be accounted for by calculating the turbulent pressure fluctuation as follows:

$$p'_{\text{turb}} = 0.39\rho k . \quad (4.56)$$

$k$  is the turbulent kinetic energy. The turbulent pressure fluctuation is added to the theoretical saturation pressure,  $p_{\text{sat}}$ , to obtain the local vapour pressure:

$$p_v = p_{\text{sat}} + \frac{p'_{\text{turb}}}{2} , \quad (4.57)$$

which is higher than the theoretical value of the saturation pressure.

Another challenge arises from the RANS-based approach of modelling turbulence for cavitating flows. Turbulence models for RANS-based flow solvers are often unable to predict a correct behaviour of cavitation. They fail to enable the re-entrant jet which is one of the main mechanisms to cause periodic shedding of cloud cavitation. Most of the time, using common two equation turbulence models will lead to a false prediction of the cavitation behaviour which may result in a steady sheet cavitation instead of periodic cloud cavitation, which was first noticed by Reboud et al. (1998).

Regions of liquid flow where vapour bubbles are present are characterised by high compressibility and a significant decrease of the local speed of sound. In fact, the speed of sound can

change considerably and may even be lower than the speed of sound in either pure liquid or pure vapour, as remarked by Kiefer (1977). Increased compressibility can influence the behaviour of turbulence and therefore play an important role in turbulence modelling. For that reason, it has to be dealt with highly compressible regions in cavitating flows.

Using Direct Numerical Simulation (DNS), Heinz (2006) showed that one result of growing compressibility is the reduction of turbulent kinetic energy,  $k$ , in the flow. Common two equation turbulence models for incompressible RANS methods do generally not account for these compressibility effects. As a consequence, these models overestimate the turbulent kinetic energy and thus the turbulent viscosity. Reboud et al. (1998) proposed a simple approach to correct the turbulent viscosity accounting for the aforementioned effects. The turbulent viscosity can be written as:

$$\mu_t = f(\rho) C_\mu k / \omega, \quad \text{with } f(\rho) = \rho \quad (\text{standard}). \quad (4.58)$$

$f(\rho)$  is a function of the density and substituted by the mixture density,  $\rho$ , in the standard form of the  $k$ - $\omega$ -SST turbulence model. To modify the turbulent viscosity, the authors proposed to use a different function:

$$f(\rho) = \rho_v + \frac{(\rho - \rho_v)^n}{(\rho_l - \rho_v)^{n-1}}, \quad \text{with } n = 10 \quad (\text{Reboud}). \quad (4.59)$$

$n$  is an exponential coefficient.

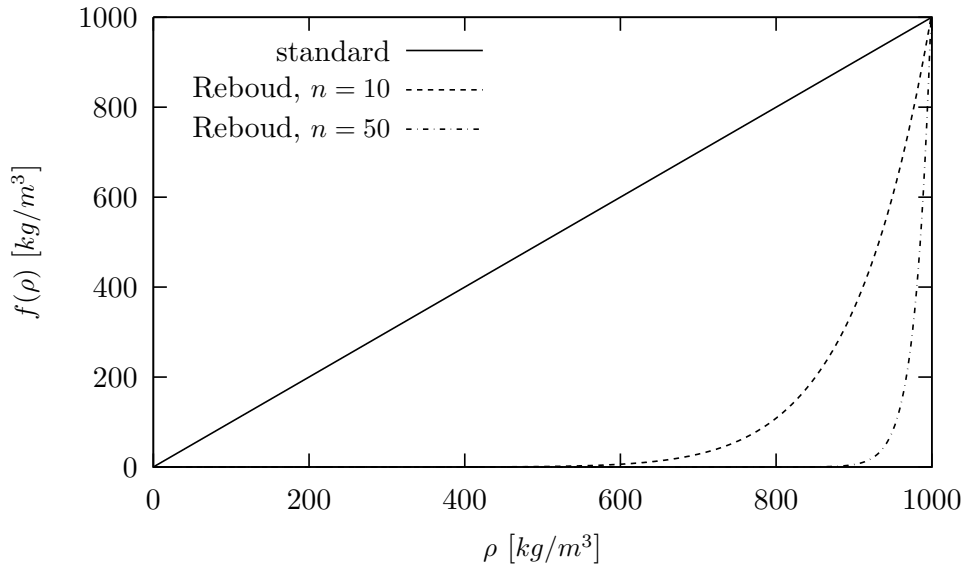


**Figure 4.2:** Comparison of density functions to calculate turbulent viscosity using no correction (solid line) and Reboud correction with  $n = 10$  (dashed line) and  $n = 50$  (dash-dotted line)

Figure 4.2 depicts these density functions for the standard turbulence model (solid line) and considering the correction by Reboud et al. (1998) using exponents of  $n = 10$  (dashed line),

### 4.3 Euler-Lagrange Approach

and 50 (dash-dotted line), respectively. It can be seen that the density functions that use the correction are much lower in the mixture region than the linear function, which leads to a reduction of the turbulent viscosity in the region considered. Higher values of  $n$  generate stronger damping of the turbulent viscosity in the mixture region. In this work, this correction of turbulent viscosity is applied with  $n = 10$  for all simulations of cavitating flows.

## 4.3 Euler-Lagrange Approach

Cavitation bubbles are mainly transported by the liquid flow. In presence of high gradients of flow quantities, however, their trajectories can deviate significantly from the streamlines of the carrier fluid. Cavitation bubbles and the liquid carrier flow can interact with each other in different ways. In contrast to an Euler-Euler approach, where the vapour phase is regarded as a continuum, in an Euler-Lagrange approach vapour volumes consist of accumulations of spherical Lagrangian bubbles. Euler-Lagrange approaches to deal with cavitation differ in complexity and computational effort, depending on the details of physics considered.

In case of a Lagrangian treatment of the vapour phase, effects of the liquid phase on the single Lagrangian bubbles are naturally included in the forces influencing transport and dynamics of a bubble (see section 4.1). Euler-Lagrange approaches where only influences of the liquid phase on the vapour bubbles are considered, but not vice versa, are characterised as *one-way coupling* approaches. With regard to cavitation simulations, this approach is usually not accurate enough and can only be used for low concentrations of small-size cavitation bubbles. For higher concentrations of bubbles or cavitation bubbles of larger sizes, effects of the bubbles on the carrier fluid may be implemented in form of a *two-way coupling*. Therein, analogous to Euler-Euler cavitation approaches (see section 3.1.3), density and viscosity of the carrier fluid are calculated using volume fractions of the liquid and vapour phase. Moreover, a two-way coupling approach incorporates the influence of bubble motions on momentum of the carrier fluid. For high concentrations of bubbles, which inevitably touch each other, *four-way coupling* approaches may be utilised. Interactions – coalescence and collision – of Lagrangian bubbles with each other are then evaluated. Complexity and computational time increase from a one-way coupling approach towards a four-way coupling approach while the regarded physics are more accurately described. Depending on the flow problem at hand, a reasonable compromise between accuracy and efficiency needs to be found choosing one of these approaches.

### 4.3.1 Bubble-Liquid Interactions

To obtain the quantities of a homogeneous mixture (see (4.36)), the vapour volume fraction is used to define the volume of vapour and liquid incorporated in a control volume. For vapour structures in the Eulerian frame, the vapour volume fraction is calculated from the vapour volume fraction equation (4.37). Processes of condensation and vapourisation are then modelled

by source terms of a cavitation model based on simplified bubble dynamics. In contrast to an Eulerian treatment of the vapour phase, a Lagrangian treatment does not require the solution of a volume fraction transport equation. The transport and dynamic behaviour of the vapour phase are obtained from the behaviour of single bubbles. The vapour volume fraction of the Lagrangian frame thus needs to be calculated based on the distribution of Lagrangian bubbles.

### Distribution of Vapour Volume

The basis of an Euler-Lagrange simulation of a cavitating flow is the distribution of cavitation nuclei in the simulation domain. Here, free-stream nuclei are stochastically inserted into the domain at pre-defined positions, randomly inside a pre-defined region, or at an inlet boundary. Moreover, the number of nuclei entering the domain per time is defined. The behaviour of cavitation therefore depends on the number of cavitation nuclei in the simulation domain. Interactions of the Lagrangian bubbles with the liquid carrier fluid require a projection of the vapour volume of these bubbles onto the Eulerian grid to calculate the vapour volume fraction of CVs overlapped by these bubbles. To evaluate the vapour volume contained in a bubble, the volume of non-condensable gas, corresponding to the equilibrium radius,  $R_0$ , is subtracted from the total volume of the bubble. The volume fraction is afterwards used to calculate the mixture quantities of the Eulerian flow. This process acts as an interaction between the phases because the updated mixture quantities are used in the equations of the flow. To distribute the bubble volume onto the numerical grid, different approaches exist which can be used depending on the density of bubbles per liquid volume.

**Indirect Distribution Using a Transport Equation** For large bubble densities, bubbles are expected to either overlap (two-way coupling) or touch each other (four-way coupling). In case of a two-way coupling approach, it is common for multiple bubbles to overlap each other. Therein, the vapour volume of cavitation bubbles can exceed the local volume of cells on the Eulerian grid significantly. An approach to efficiently distribute the bubble vapour volume onto the Eulerian grid is to transport the volume fraction by solving a convection-diffusion equation using pseudo time-stepping. The convection-diffusion equation is written as:

$$\frac{\partial}{\partial t} \int_V \alpha_{v,L} dV + \int_S \mathbf{u} \alpha_{v,L} \cdot d\mathbf{S} = \int_S \Gamma \nabla \alpha_{v,L} \cdot d\mathbf{S}. \quad (4.60)$$

$\alpha_{v,L}$  is the vapour volume fraction based on the Lagrangian bubble volume. Initially, all cells are filled with the vapour volume of all bubbles whose centres are located in them.  $\Gamma$  is the diffusion coefficient. Within every time step of Eulerian flow solution, a pseudo time-stepping is utilised to solve equation (4.60) until the vapour volume fraction in all CVs is decreased below unity.

### 4.3 Euler-Lagrange Approach

**Direct Distribution Into Neighbouring Cells** In cases of low concentrations of bubbles, their entire vapour content can be distributed onto the Eulerian grid directly. Control volumes incorporating bubbles, whose volumes are smaller than the volumes of the CVs, fill these CVs with vapour until the vapour volume fraction reaches unity. When the volume of a bubble exceeds the volume of the cell it is located in, the remaining vapour volume is distributed into neighbouring cells of the initial CV. This process is repeated until the complete vapour volume is distributed. This approach is used in regions of low bubble concentrations while conserving the complete volume of vapour.

#### Pressure Equation

Besides an interaction attributable to the change of mixture quantities of the flow by the Lagrangian bubbles, the pressure equation (4.54) is influenced by processes of condensation and vapourisation as well. In the Euler-Euler approach, the vapour volume fraction  $\alpha_v$  is used to calculate the source terms of condensation and vapourisation in the pressure equation (see (4.55)). The implicit treatment of the pressure in equation (3.63) yields a stable equation system. Although it is possible to choose a different substitution for the source terms on the right hand side of equation (3.63) based on bubble quantities and dynamics ( $R$  and  $\dot{R}$ ) these approaches can cause instabilities because, in contrast to the approach of Sauer (2000), the source terms cannot be handled implicitly. Accordingly, for the Euler-Lagrange approach used in this work, the cavitation source terms in the pressure equation are calculated using the approach of Sauer (2000) because of its numerical stability.

#### 4.3.2 Momentum of Lagrangian Bubbles Acting on Carrier Flow

Just as the momentum of the bubble depends on the carrier flow, bubbles can influence the momentum of the carrier flow in return. In case of Euler-Lagrange simulations with at least a two-way coupling, the momentum equation (3.29) is extended by a volume integral, which incorporates the source term  $\mathbf{s}_b$ :

$$\begin{aligned} \frac{\partial}{\partial t} \int_V \rho \mathbf{u} dV + \int_S \rho \mathbf{u} \mathbf{u} \cdot d\mathbf{S} = \int_S \mu (\nabla \mathbf{u} + (\nabla \mathbf{u})^T) \cdot d\mathbf{S} - \int_S p \mathbf{I} \cdot d\mathbf{S} \\ + \int_V \rho \mathbf{b} dV + \int_V \sigma \kappa_{\text{cur}} \frac{\nabla \alpha}{|\nabla \alpha|} dV + \int_V \mathbf{s}_b dV . \end{aligned} \quad (4.61)$$

$\mathbf{s}_b$  depends on the rate of change of the bubble velocities of all bubbles entering and leaving control volumes. When a Lagrangian bubble enters a new control volume, a new time step to calculate the bubble velocity is started. The rate of change of the bubble velocity is then calculated from equation (4.34). The source term in the momentum equation for a given cell  $j$  is then defined as, Vallier (2013), Lidtke (2017):

$$\mathbf{s}_{b,j} = -\frac{1}{V_j} \sum_i m_{\text{eff},i} \frac{\mathbf{u}_{b,i}^{n+1} - \mathbf{u}_{b,i}^n}{\Delta t}. \quad (4.62)$$

$i$  is the bubble index. This source term takes into account the momentum contribution from all bubbles the cell incorporates.  $n$  denotes the time step of Eulerian flow solution.

### 4.3.3 Bubble Collision and Coalescence

For two-way coupling approaches, only the aforementioned interactions between liquid and bubbles are considered. In addition to that, a four-way coupling approach considers also interactions between bubbles themselves. A Lagrangian bubble can then interact with all Lagrangian bubbles in its direct neighbourhood that are located within a distance of its own radius. Bubble-bubble interactions consist of two main processes, namely collision and coalescence. Prince and Blanch (1990) proposed a model to determine coalescence depending on the time two bubbles are in contact with each other. The approach was utilised in Euler-Lagrange methods by Sommerfeld et al. (2008) in a stochastic model and by Darmana et al. (2006) conducting direct collision calculations. Prince and Blanch (1990) supposed that two bubbles merge – coalesce – when they are in contact with each other for a sufficiently long time. Thereby, a thin liquid film between the bubbles emerges and starts to drain. Depending on the time of contact, the liquid film can decrease below a critical size and enable coalescence of the bubbles. It is assumed that the liquid contact area between two touching bubbles is a constant fraction of the bubble radius. The time needed for coalescence is then calculated from:

$$\tau_{c,12} = \sqrt{\frac{R_{12}^3 \rho_l}{16\sigma}} \ln \left( \frac{h_i}{h_f} \right). \quad (4.63)$$

$R_{12}$  is the equivalent bubble radius for a system of two bubbles of radii  $R_1$  and  $R_2$ . According to Chesters and Hofman (1982) it is defined as:

$$R_{12} = 2 \left( \frac{1}{R_1} + \frac{1}{R_2} \right)^{-1}. \quad (4.64)$$

The initial and critical film thickness are  $h_i = 0.1 \text{ mm}$  and  $h_f = 0.01 \mu\text{m}$ , respectively. The actual contact time between the two bubbles is calculated as, Sommerfeld et al. (2008):

$$t_{c,12} = \frac{C_c R_{12}}{|u_{b1,n} - u_{b2,n}|}, \quad (4.65)$$

which can be described as the ratio of a deformation distance and the relative normal velocity between the bubbles, Darmana et al. (2006). Here,  $u_{b1,n}$  and  $u_{b2,n}$  are the normal velocity components between the two bubble centres of bubble 1 and bubble 2, respectively.  $C_c$  is a variable to define the deformation distance as a fraction of the equivalent bubble radius. For  $t_{c,12} \geq \tau_{c,12}$ , when two bubbles are in contact long enough to break the liquid film, coalescence

### 4.3 Euler-Lagrange Approach

is supposed to occur. The two bubbles, therein, merge into one larger bubble whose velocity is calculated from:

$$\mathbf{u}_b^a = \frac{m_{b1}^b \mathbf{u}_{b1}^b + m_{b2}^b \mathbf{u}_{b2}^b}{m_b^a}, \quad (4.66)$$

and the position of the new bubble is given as:

$$\mathbf{x}_b^a = \frac{m_{b1}^b \mathbf{x}_{b1}^b + m_{b2}^b \mathbf{x}_{b2}^b}{m_b^a}. \quad (4.67)$$

The superscript  $a$  denotes the velocity components after collision and  $b$  the velocity components before collision.  $m_b^a = m_{b1}^b + m_{b2}^b$  is the mass of the bubble after coalescence consisting of the sum of the masses of the individual bubbles before coalescence,  $m_{b1}^b$  and  $m_{b2}^b$ .

For cases in which the contact time between two bubbles is smaller than the time needed for coalescence ( $t_{c,12} < \tau_{c,12}$ ), the interacting bubbles will collide. Their velocity components after collision are then in normal direction, “n”:

$$u_{b1,n}^a = -u_{b1,n}^b, \quad u_{b2,n}^a = -u_{b2,n}^b, \quad (4.68)$$

and in tangential direction, “ta”:

$$u_{b1,ta}^a = u_{b1,ta}^b, \quad u_{b2,ta}^a = u_{b2,ta}^b. \quad (4.69)$$

## 4.4 Hybrid Multi-Scale Cavitation Approach

Both Eulerian and Lagrangian approaches to treat the vapour phase have their advantages and disadvantages. Eulerian approaches are efficient for the simulation of macroscopic cavitation, but naturally contain numerical diffusion. Although the dynamics of single bubbles can be captured using Euler-Euler cavitation models, a high mesh resolution and therefore a high computational effort are needed. Accordingly, these simulations are usually limited to one single bubble or only very few bubbles. In technical flows, these single bubble dynamics are neglected in most cases and vapour structures are supposed to be continuous. In a Lagrangian approach, the dynamics and motions of single bubbles, which are assumed to be spherical, are calculated. This treatment allows to obtain detailed information about bubble behaviour in regions of high gradients of flow quantities or about collapse processes near walls, which are related to erosion. Depending on the number of nuclei in a cavitating flow, the computational time of an Euler-Lagrange simulation can be a multiple of the computational time of an Euler-Euler simulation.

The idea of a hybrid multi-scale approach is based on the simulation of macroscopic cavitation structures captured in an Eulerian frame, while handling small cavitation bubbles – resulting from shedding or collapsing of macroscopic cavitation volumes – as spherical in the Lagrangian frame. One of the major aims of this work was to give more accurate predictions of cavitation erosion by considering collapses of spherical single bubbles. Hybrid approaches to combine Euler-Euler and Euler-Lagrange cavitation models have recently been employed by different researchers and shown the potential to use the more accurate Lagrangian approach only in specific regions of interest. The multi-scale Euler-Lagrange method, implemented in this work, is similar to approaches used by Vallier (2013), Lidtke (2017), and Ma et al. (2017). A literature survey about hybrid multi-scale approaches to simulate cavitating flows is given in section 1.3. In the following, details about the present approach will be presented. The approach was used in Peters and el Moctar (2019) (paper under review).

### 4.4.1 Multi-Scale Treatment of Vapour Volumes

In the present multi-scale approach, the behaviour of liquid phase and large-scale vapour continua is simulated by solving the basic equations of conservation on an Eulerian grid (see chapter 3). As soon as the volume of an isolated vapour structure decreases below a certain size, considering the absolute size and the relative size related to the grid resolution, it is converted into a spherical cavitation bubble in the Lagrangian frame. Cavitation structures can, thereby, be transformed from the Eulerian into the Lagrangian frame and vice versa. The criteria for conversion can be set such that transformations depend on the absolute size of a vapour structure and/or its relative size compared to the resolution of the vapour structure on the Eulerian grid. In this section, the identification of isolated vapour volumes, the mechanisms to transform vapour volumes between the frameworks, the interactions between liquid and vapour phases, as well as specifics about the non-condensable gas content of Lagrangian bubbles are presented.

### Identification of Isolated Eulerian Vapour Volumes

To evaluate which vapour volumes on the Eulerian grid need to be transformed into Lagrangian bubbles, a procedure to identify isolated, connected vapour structures needs to be found. Vallier (2013) suggested an algorithm to identify isolated vapour volumes by collecting all control volumes containing a minimum threshold of vapour volume fraction,  $\alpha_{v,\text{limit}}$ , and assigning them to coherent vapour structures. The algorithm implemented in this work is shown in detail in section 7.1. It is based on the algorithm developed by Vallier (2013).

### Mechanisms of Transformation

After all coherent vapour bubbles are identified, the quantities of a coherent vapour bubble in the Eulerian frame need to be calculated to prepare the transformation into a spherical Lagrangian bubble. At first, the vapour volume of the bubble,  $V_{b,v}$ , is calculated from the sum of vapour volumes in the cells, which belong to the coherent bubble:

$$V_{b,v} = \sum_i^I (V_{cv} \alpha_{v,E})_i . \quad (4.70)$$

$i$  is the cell index and  $I$  the total number of cells contained in the coherent bubble.  $V_{cv}$  is the volume and  $\alpha_{v,E}$  the Eulerian vapour volume fraction of the regarded control volume, respectively. Since a Lagrangian bubble contains an amount of non-condensable gas as well, the volume of non-condensable gas needs to be added to the bubble. It is assumed that the non-condensable gas in the bubble is initially in equilibrium. The volume of non-condensable gas is calculated from:

$$V_{b,g} = \frac{4}{3} \pi R_0^3 , \quad (4.71)$$

with the equilibrium bubble radius,  $R_0$ . Finally, the complete volume of a bubble is obtained from:

$$V_b = V_{b,v} + V_{b,g} . \quad (4.72)$$

The reference bubble radius can then be calculated from the complete bubble volume as:

$$R_{\text{ref}} = \left( \frac{3V_b}{4\pi} \right)^{1/3} . \quad (4.73)$$

The new position of the bubble is obtained from the centre of vapour:

$$\mathbf{x}_b = \frac{\sum_i^I (\mathbf{x}_{cv} V_{cv} \alpha_{v,E})_i}{V_{b,v}} , \quad (4.74)$$

with  $\mathbf{x}_{cv}$  as the centre of a regarded control volume. The new velocity of the bubble is given by:

$$\mathbf{u}_b = \frac{\sum_i^I (\mathbf{u} V_{cv} \alpha_{v,E})_i}{V_{b,v}}. \quad (4.75)$$

Here,  $\mathbf{u}$  is the flow velocity in a regarded control volume. After calculation of the bubble quantities, the coherent Eulerian vapour bubble is examined for transformation into a spherical Lagrangian bubble according to the following algorithm:

---

**Algorithm 2:** Algorithm to transform Eulerian vapour volumes into Lagrangian bubbles

---

**for** all isolated vapour structures **do**

    Calculate volume,  $V_b$ , radius,  $R_{ref}$ , centre,  $\mathbf{x}_b$ , and velocity,  $\mathbf{u}_b$ , of Eulerian vapour bubble

**if**  $n_{cells} \geq n_{limit}$  **or**  $R_{ref} \geq R_{limit}$  **then**

        Continue to next bubble without transformation

**else**

        Transform coherent, Eulerian vapour bubble into spherical Lagrangian bubble of calculated quantities

        Remove vapour volume from the corresponding Eulerian control volumes

**end**

**end**

---

Here, the isolated vapour volumes are evaluated based on their absolute size and their size relative to the Eulerian grid. Transformations of vapour volumes into the Lagrangian frame are performed when an isolated vapour structure contains less than a threshold number of control volumes,  $n_{limit}$ , or when the representative radius related to the volume of the vapour structure,  $R_{ref}$ , is smaller than a threshold radius,  $R_{limit}$ . Transformations of Lagrangian vapour bubbles into the Eulerian frame take place, analogue, when vapour volumes exceed the aforementioned thresholds again. Furthermore, to prevent overlaps of single Lagrangian bubbles within Eulerian vapour structures, Lagrangian bubbles, which are in contact with larger Eulerian vapour structures, merge into the larger vapour structures and are transformed into the Eulerian frame. For all transformation mechanisms, it is assured that the complete volume of vapour is conserved while being transformed between the two frameworks. Hereinafter, the different mechanisms of transformation are explained.

First, we want to look at a conversion of a vapour structure from the Eulerian into the Lagrangian framework. This conversion occurs when a vapour structure is under-resolved by the numerical grid. Accordingly, for every isolated vapour structure, all cells that it comprises are counted,  $n_{cells}$ . As soon as this number is less than a limit number,  $n_{limit}$ , the vapour volume is transformed into a spherical Lagrangian bubble. Figure 4.3 shows an example of the evaluation of two vapour structures. The top part of the sketch shows the situation before transformation of vapour volumes and the bottom part after transformation. The left vapour volume is sufficiently resolved by the Eulerian grid ( $n_{cells} \geq n_{limit}$ ), whereas the right vapour volume is under-resolved ( $n_{cells} < n_{limit}$ ). Therefore, the right vapour volume is transformed into the Lagrangian frame and replaced by a spherical Lagrangian bubble of equivalent vapour volume.

#### 4.4 Hybrid Multi-Scale Cavitation Approach

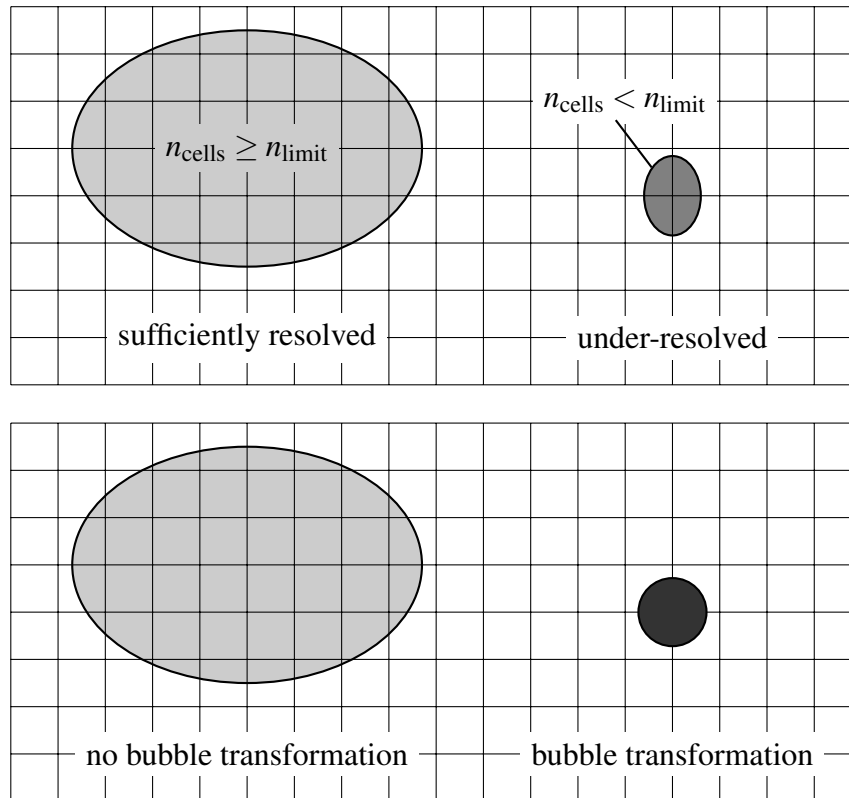


**Figure 4.3:** Evaluation of vapour structures in the Eulerian frame; under-resolved vapour volumes are replaced by spherical Lagrangian bubbles

Similarly, Lagrangian bubbles are transformed into vapour volumes on the Eulerian grid. When Lagrangian bubbles grow and exceed the limiting number of cells,  $n_{\text{limit}}$ , they are transformed into the Eulerian frame because the vapour volume is assumed to be sufficiently resolved by the numerical mesh. Figure 4.4 depicts the evaluation of transformations of Lagrangian bubbles. In the cases shown, the left bubble is too small to be transformed into the Eulerian framework because it overlaps too few cells. However, the right bubble overlaps enough cells to be sufficiently resolved by the numerical grid and is thus transformed into the Eulerian frame.

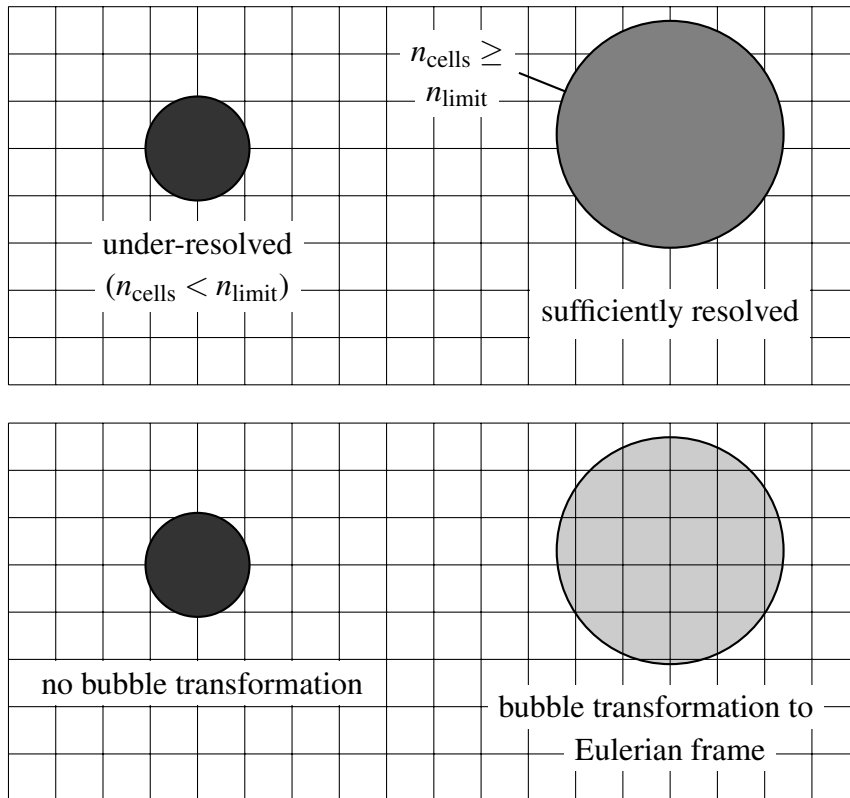


**Figure 4.4:** Evaluation of Lagrangian bubbles; bubbles are transformed when they can be resolved sufficiently by the Eulerian frame

Both aforementioned transformation mechanisms also apply when a criteria for the absolute radius of a vapour structure is used. Isolated vapour structures are then transformed from the Eulerian into the Lagrangian framework when the reference radius of the regarded vapour structure,  $R_{\text{ref}}$ , decreases below a limit radius,  $R_{\text{limit}}$ . On the other hand, the transformation of a Lagrangian bubble into the Eulerian framework is performed when its radius increases above the limit radius again.

A transformation of an Eulerian vapour volume into a spherical Lagrangian bubble can also be conducted for increasing vapour volume fractions in one single cell or just a few cells. As soon as the vapour volume fraction in a control volume of the Eulerian framework,  $\alpha_{v,E}$ , exceeds the limit value for identification of isolated vapour volumes,  $\alpha_{v,\text{limit}}$ , the vapour volume is replaced by a Lagrangian bubble, which contains the same vapour volume. Figure 4.5 (left) sketches an Eulerian grid in which some control volumes are partially filled with vapour ( $\alpha_{v,E} \geq \alpha_{v,\text{limit}}$ ). Contacting, vapour filled control volumes are detected as isolated vapour structures and transformed into the Lagrangian framework in form of spherical bubbles. Figure 4.5 (right) shows the spherical Lagrangian bubbles of equivalent vapour volume on the numerical grid.

#### 4.4 Hybrid Multi-Scale Cavitation Approach

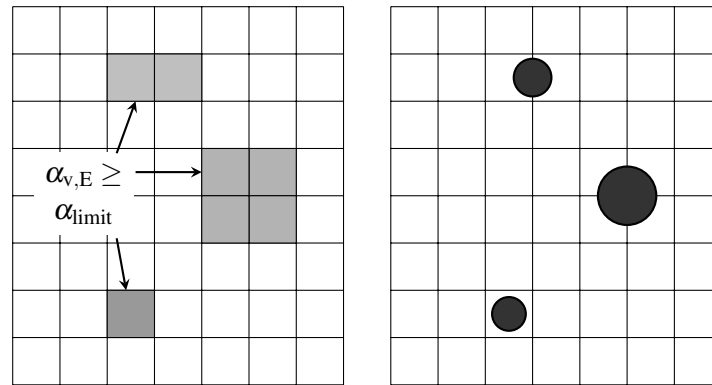


**Figure 4.5:** Small Eulerian vapour volumes in isolated cells are transformed into spherical Lagrangian bubbles

Another mechanism to transform a Lagrangian bubble into an Eulerian vapour volume takes place when a spherical Lagrangian bubble contacts with a vapour volume of the Eulerian frame. Figure 4.6 presents such a scenario with the situation before transformation shown on the left and after transformation shown on the right. The Lagrangian bubble touches the Eulerian vapour volume. Even though the isolated bubble is too small to be sufficiently resolved by the numerical grid individually, it is recognised touching the vapour cloud. Therefore, the bubble is transformed into the Eulerian frame and coalesces with the larger vapour structure.

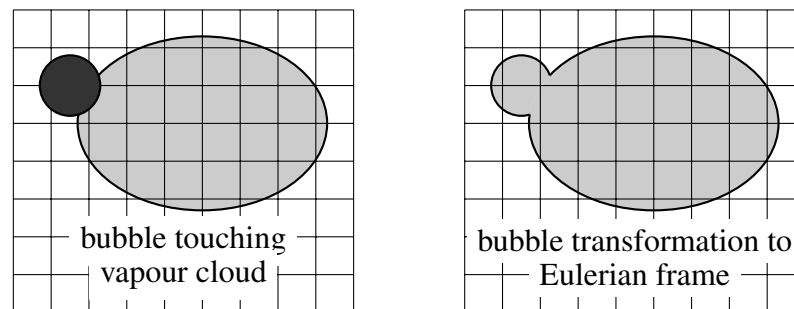


**Figure 4.6:** Lagrangian bubble transformed to the Eulerian frame as it is touching a vapour cloud

To prevent bubbles from being transformed back and forth between the frames, vapour volumes which have just been transformed into Lagrangian bubbles, cannot be transformed back within the same time step. The dynamics of Lagrangian bubbles can therefore evolve for longer periods of time.

#### Communication in Parallel Simulations

In parallel simulations, the aforementioned transformation processes deserve specific treatment. If transformations were just handled locally, vapour structures with small overlap over

processor boundaries could cause transformations from the Eulerian into the Lagrangian frame ascribable to a small vapour volume on the local processor. Thus, information about the sizes of the vapour structures needs to be exchanged across the processor interfaces in order to determine the global volume of a vapour structure in the domain. An algorithm to obtain full parallelization similar to Lidtke (2017) has been implemented to evaluate quantities of the global instead of processor-local vapour volumes.

In case of serial computations, the approach to transform vapour volumes between Eulerian and Lagrangian frame is straightforward to implement. For parallel simulations, problems arise at the boundaries between two processors. Although vapour structures are large in the complete domain, in a local processor domain, they would be identified as small enough in order to be transformed into a Lagrangian bubble. Figure 4.7 sketches such a case of a large, Eulerian vapour structure overlapping the processor boundary between processors 1 and 2. The entire coherent structure is large enough to be spatially resolved by the Eulerian grid. Nevertheless, if the vapour volume was treated solely locally on processors, the vapour volume of this structure on processor 2 could be analysed as just poorly resolved by the numerical grid, resulting in a transformation into a spherical Lagrangian bubble.

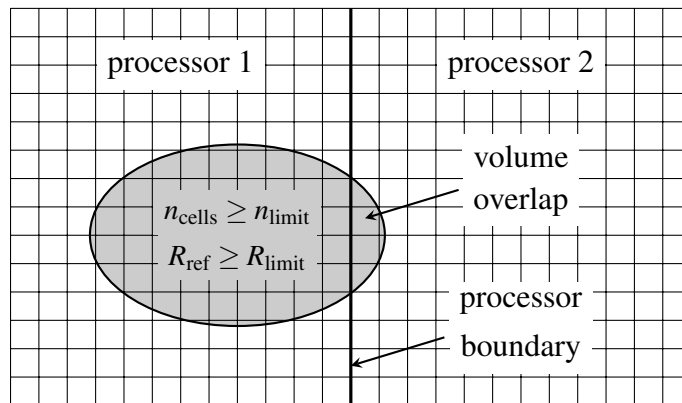


**Figure 4.7:** Treatment of a coherent, Eulerian vapour structure at a processor boundary in a parallel simulation

Accordingly, to prevent false transformations in parallel simulations, it is inevitable for processors to communicate information regarding coherent vapour bubbles, which are located directly at interfaces between two processors. The sizes of coherent vapour volumes then have to be calculated across multiple processor interfaces. Although this communication procedure is time-consuming, the advantage of simulating the behaviour of both the Eulerian flow and spherical Lagrangian bubbles in parallel on multiple processors outweighs. In this work, the algorithm used to organise parallel communication to connect the coherent vapour bubbles is shown in detail in section 7.2. The algorithm is similar to the algorithm described in Lidtke (2017) who also utilised a hybrid approach.

### 4.4.2 Calculation of Vapour Volume

To combine an Eulerian and Lagrangian treatment of the vapour phase, the vapour volume fractions calculated in both frameworks need to be added together. The vapour volume fraction from the Eulerian frame is calculated from the vapour volume fraction equation (see (4.37)). To obtain a volume fraction of vapour from the Lagrangian frame, the vapour volume fraction in control volumes occupied by Lagrangian bubbles,  $\alpha_{v,L}$ , is calculated by direct distribution of the entire vapour volume of the bubbles to the surrounding control volumes (see section 4.3.1). For two-way coupled Euler-Lagrange methods, a distribution can become problematic when the density of bubbles is large because bubbles overlap each other. For the hybrid approach used in this work, overlap of bubbles is unlikely to occur because bubble densities are small. In this hybrid approach, the vapour volume transferred between the frameworks is always conserved.

Adding the vapour volume fraction fields from the Eulerian and Lagrangian frame together yields the total vapour volume fraction in the domain:

$$\alpha_{v,\text{total}} = \alpha_{v,E} + \alpha_{v,L}. \quad (4.76)$$

Afterwards, the density and viscosity of the mixture fluid can be updated according to (4.36).

### 4.4.3 Non-Condensable Gas Content of Bubbles

Transformations of coherent, Eulerian vapour bubbles into spherical Lagrangian bubbles require, in addition to information about the volume of vapour inside the bubble, information about the non-condensable gas content inside it. Dynamics of a bubble depend significantly on the volume of non-condensable gas in it, related to its equilibrium radius,  $R_0$ . Nevertheless, the distribution of cavitation nuclei in forms of gas bubbles is rarely known from experiments. Hence, in Lagrangian methods to treat cavitation bubbles, nuclei sizes are often chosen to be bubbles of constant radius. More complex approaches consider a Gauss or Rayleigh distribution of non-condensable gas bubbles in a flow.

More reasonable nuclei distributions can be derived using optical measurement techniques. Reuter et al. (2018) performed measurements of bubble sizes in different structures of acoustically generated cavitation. Using high-speed observations of bubble sizes together with an equation for spherical bubble dynamics, the populations of equilibrium sizes of gas bubbles were determined. For different cavitation structures, they measured nuclei distributions and obtained equilibrium radii distributions for  $R_0 > 2.2\mu\text{m}$ . Reuter et al. (2018) found the best fit for the distributions by using the sum of an exponential decay and a Gaussian that reads:

$$F_1 = \exp\left(-\frac{R_0}{x_1}\right) + x_3 \frac{1}{\sqrt{2\pi x_2^2}} \exp\left(-\frac{R_0^2}{2x_2^2}\right), \quad (4.77)$$

with  $x_1 = 1.28 \mu\text{m}$ ,  $x_2 = 0.54 \mu\text{m}$ , and  $x_3 = 0.0838$  in the case of a measured cavitating jet. Bubbles of small equilibrium radii,  $R_0 < 2.2 \mu\text{m}$ , could not be measured because of the optical resolution limit. Owing to the high surface tension of bubbles below the Blake threshold, smaller bubbles did not oscillate to sizes large enough to be measured, Mettin et al. (1997). In this work, to obtain a measurement-based nuclei distribution, the distribution of Reuter et al. (2018) was normalised and combined with a simple quadratic polynomial as follows:

$$F(R_0) = \begin{cases} F_1 = \left( \exp\left(-\frac{R_0}{x_1}\right) + x_3 \frac{1}{\sqrt{2\pi x_2^2}} \exp\left(-\frac{R_0^2}{2x_2^2}\right) \right) / x_4 & \text{if } R_0 > 2.2 \mu\text{m} \\ F_2 = (a_1 R_0^2 + a_2 R_0) / a_3 & \text{else,} \end{cases} \quad (4.78)$$

with the constants  $x_4 = 1.328005544$ ,  $a_1 = -0.00883577$ ,  $a_2 = 0.03711025$ ,  $a_3 = 0.2879407$  and the aforementioned values of  $x_1$ ,  $x_2$ , and  $x_3$  in case of the cavitating jet. Figure 4.8 displays the combined distribution with the measured distribution by Reuter et al. (2018) on the right hand side of the dashed vertical line and the quadratic polynomial on the left hand side, respectively.

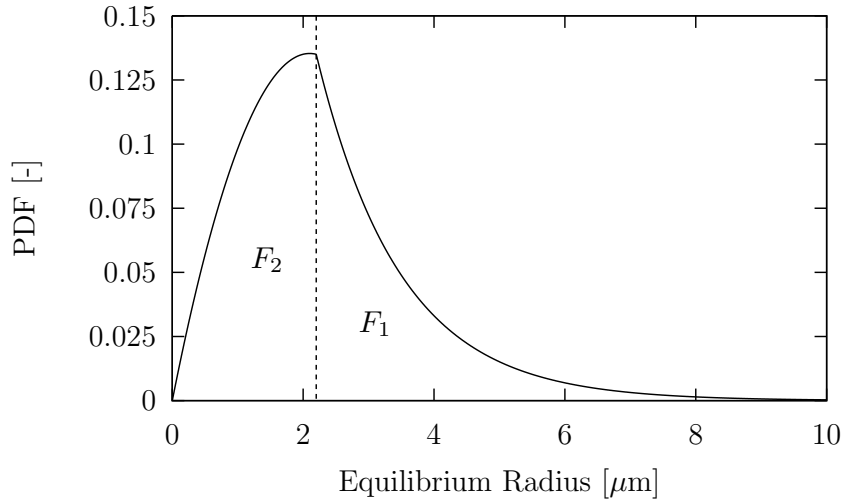


**Figure 4.8:** Probability density function of different bubble equilibrium radii,  $R_0$

#### 4.4.4 Solution Algorithm

The solution algorithm of the hybrid multi-scale approach combines the PIMPLE algorithm for Euler-Euler methods (see section 3.3.3) with the Lagrangian treatment of single spherical bubbles, and the mechanisms to transform vapour volumes between the two frameworks. Figure 4.9 presents the procedure of the solution algorithm. At the beginning of every Eulerian flow time step, Eulerian vapour structures, which meet the criteria described in section 4.4.1, are transformed into Lagrangian bubbles.

Afterwards, the Lagrangian equation of motion (4.34) is solved for each bubble to obtain its velocity, new position, and the bubble momentum source term for the Eulerian momentum

#### 4.4 Hybrid Multi-Scale Cavitation Approach

equation of the flow (4.62). The time step of the Eulerian flow solution is used as a basis for the Lagrangian equation of motion. In cases where a bubble would move through multiple cells within one time step, the Lagrangian time step would be reduced. Integration over sub-time steps is then conducted until the end of the Eulerian time step is reached. Depending on the size and bubble wall velocity of each bubble, its dynamics are calculated by solving equation (4.8), (4.9), or (4.11). Because the bubble dynamics take place within time periods multiple orders smaller than the time periods considered for the Eulerian flow solution, the time steps used to solve the equations for bubble dynamics are significantly smaller. Integration over the time interval used for the Eulerian flow solution is conducted in a large number of sub time steps using an implicit second order Trapezoidal scheme. In Figure 4.9, the time step for bubble dynamics is marked as *RPE time step* based on the Rayleigh-Plesset equation (RPE). Moreover, because collapse phases of a bubble take place within different time periods, an adaptive time-stepping technique is used. During computation of bubble dynamics, based on the change of sign of the radius growth rate of a bubble,  $\dot{R}$ , the beginning of a bubble collapse – change of sign of  $\dot{R}$  from positive to negative – or the end of a bubble collapse – change of sign of  $\dot{R}$  from negative to positive – is detected and stored. These collapse information can later be used to assess cavitation erosion in post-processing routines. As soon as the sizes and positions of the Lagrangian bubbles are determined, the vapour volume of Lagrangian bubbles is distributed into the control volumes of the Eulerian grid (see section 4.3.1).

The PIMPLE iteration is started after projection of the vapour volume of Lagrangian bubbles into the Eulerian frame. Figure 4.9 shows the PIMPLE iteration in a simplified way. It starts with the solution of the vapour volume fraction equation (4.37) to obtain the Eulerian vapour volume on the Eulerian grid. Adding both fields of vapour volume fraction – from Eulerian and Lagrangian frame – together yields the total vapour volume fraction according to (4.76). After updating the quantities of the homogeneous mixture using the vapour volume fraction, the momentum equation for the Eulerian flow (4.61) is solved taking into account the momentum of Lagrangian bubbles. Analogue to the description of the PIMPLE algorithm in section 3.3.3 the Poisson equation (3.66) is solved in a PISO loop and fluxes and velocities are corrected, hereinafter. These steps are omitted in Figure 4.9 for reasons of clarity and comprehensibility. Residual control is used for momentum and pressure equation. As long as the convergence criteria are not met, a new PIMPLE iteration is started. Once the criteria are fulfilled, turbulence equations are solved. If an Eulerian erosion prediction is selected along with the hybrid solver, the step of erosion prediction is conducted after obtaining the turbulence quantities. Finally, Lagrangian bubbles whose sizes meet the respective criteria, are transformed into the Eulerian frame (see section 4.4.1).

For spatial discretisation in the Eulerian flow simulation, all schemes used are of second order except for the turbulence equations, where first order upwind schemes are applied to increase stability. Time integration in the flow solver is conducted using the implicit Euler scheme.

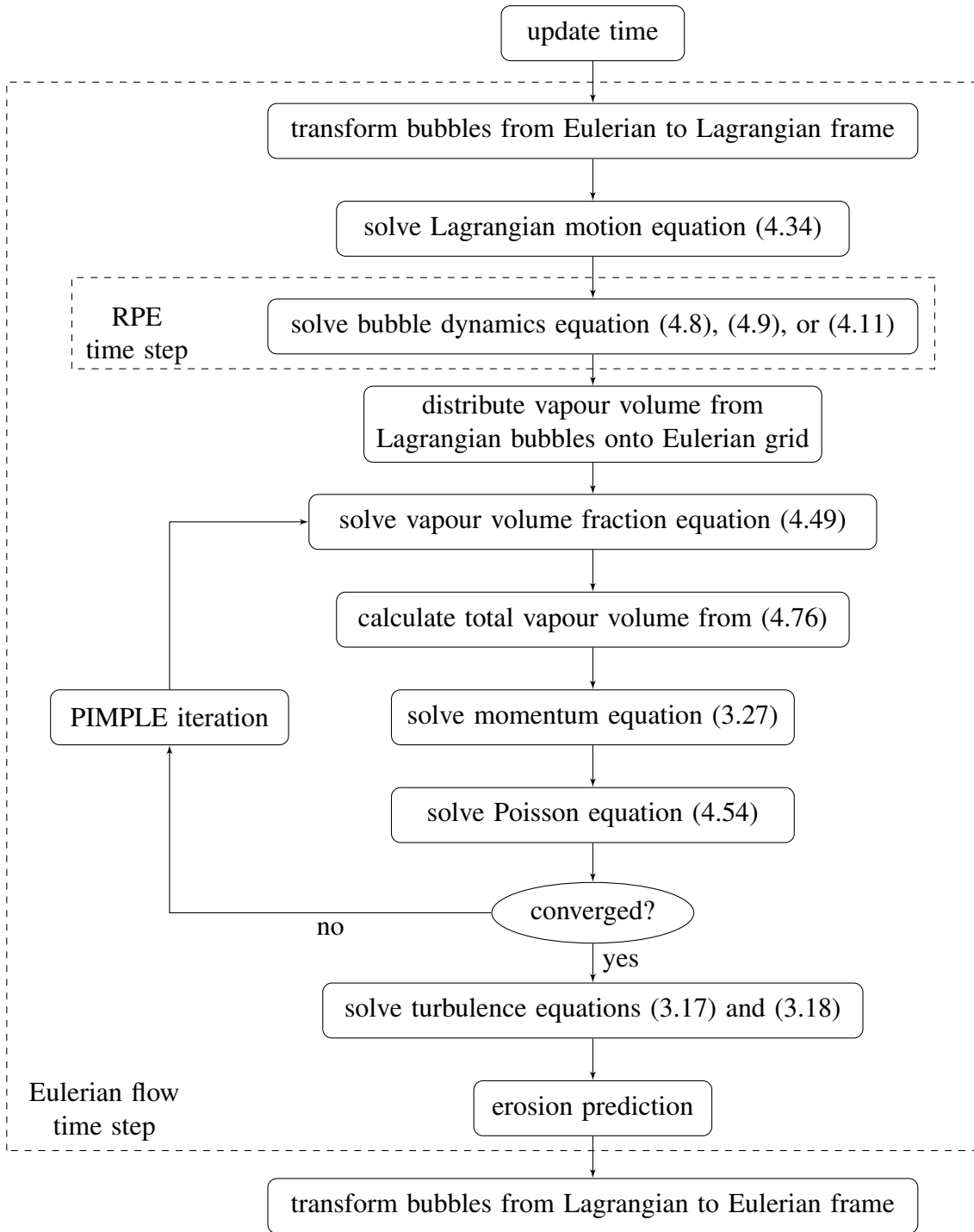


**Figure 4.9:** Solution algorithm of hybrid multi-scale method

## 4.5 Erosion Prediction

Approaches to numerically predict cavitation-induced erosion differ mainly in the complexity of the underlying numerical method as well as in the hypotheses stating the mechanisms responsible for erosion. While it is supposed that collapses of cavitation bubbles can only damage a surface in its direct vicinity (see section 2.2.2), the resolution of these processes in spatial and temporal scales is computationally too expensive for the simulation of macroscopic flows. Thus, vapour volumes are commonly treated as continua on an Eulerian grid while neglecting dynamics of single cavitation bubbles. To predict cavitation erosion applying an Eulerian treatment of the vapour phase, assumptions about collapses of single bubbles and their damage potential need to be made based on the simulation of dynamics of macroscopic cavitation volumes. More details about the erosive potential of single cavitation bubbles can be obtained using a Lagrangian approach. Therein, collapses of spherical Lagrangian bubbles are computed and their collapse positions and pressures are identified. Although bubbles are assumed spherical, cavitation behaviour is resolved to much lower spatial and temporal scales than in the Eulerian continuum approach. Based on these collapse information, more detailed predictions about cavitation erosion can be made. In this section, methods to predict erosion based on both an Eulerian and a Lagrangian treatment of the vapour phase are given. Details about physical considerations of cavitation erosion processes are given in section 2.2. State of the art approaches to predict cavitation erosion are reviewed in section 1.1.

### 4.5.1 Eulerian Approach

In the underlying work, two numerical models were used to predict cavitation erosion using an Eulerian approach to treat the vapour phase. Because spatial and temporal small scale processes of single bubble behaviour are not resolved, both models predict areas exposed to erosion based on information from the macroscopic flow solution in the vicinity of the surface considered. Faces and control volumes in the domain close to the surface are used to check conditions regarding the bubble behaviour that is assumed to lead to erosion.

#### Modelling of Microscopic Bubble Motion

Up to this point, the transport and dynamics of single cavitation bubbles in technical flows cannot be simulated reasonably using Euler-Euler approaches. Although the simulation of few bubbles can be simulated using suitable methods, small time steps and a high grid resolution are needed leading to a high computational effort. The method used considers the transport of vapour continua and incorporates numerical diffusion. The simulated behaviour of cavitation near surfaces can be such that vapour volumes vanish before reaching the vicinity of a surface. Hence, an approach was developed to predict the occurrence of cavitation bubbles close to a face of a boundary based on the flow quantities in the control volumes in its vicinity. Part of this approach was published in Peters et al. (2015a,c, 2018a). The neighbourhood of a surface

is evaluated for the presence of vapour, enabling the movement of single bubbles towards the surface. For each boundary face, spherical volumes are used to select cells around the face and collect them in a volumetric cell zone. Figure 4.10 depicts the procedure of cell selection with a boundary face marked red, the cell zone marked as a grey sphere, and a selected cell shown in white inside of the cell zone.

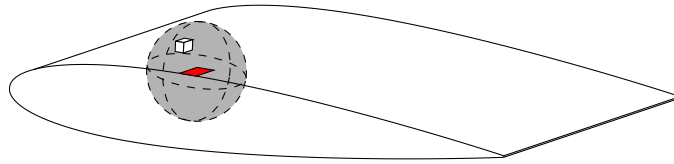


**Figure 4.10:** Cells around a face of a hydrofoil are collected in a cell zone using a spherical volume

In this approach, cell zones are generated during a pre-process to the flow simulation and exactly one cell zone is assigned to every face of a considered wall boundary. Figure 4.11 shows the cells (grey) which were collected for one face (red) using a half-sphere with cell zone radius,  $R_{cz}$ .

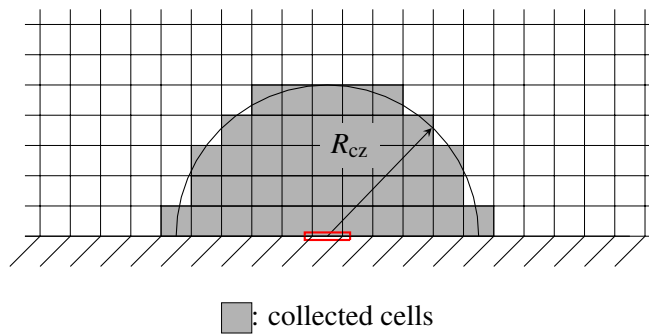


**Figure 4.11:** Cells located in a sphere are collected in a cell zone for the associated face

The erosion prediction is conducted after each time step of the flow solution. For each of the erosion models, two conditions need to be checked for every face of a regarded surface and its assigned cell zone in order to predict whether a numerical erosion impact occurs. The evaluation of the conditions is explained using the sketch in Figure 4.12. The conditions can be divided into two categories:

- **Vapour Condition:** It is examined if there is vapour present in the vicinity of the surface. This is done by evaluating if the vapour volume fraction,  $\alpha_v$ , is greater than a threshold value,  $\alpha_{\text{limit,ero}}$ , within any of the cells in the cell zone. In this work, a threshold value of 0.01 was chosen based on own simulation results. This value has shown to be large enough to prevent a fulfilment of the condition owing to numerical errors and small enough to fulfil the condition for fairly low vapour concentrations. When

## 4.5 Erosion Prediction

this condition is fulfilled, it is predicted that bubbles are able to move towards the solid surface and can be located in its direct vicinity.

- **Damage Condition:** Depending on the flow conditions in the vicinity of a face, the intensity of an impact on this face is predicted and compared to the yield strength of the considered material. The hypotheses for this condition are obtained from the erosion models presented in the following.

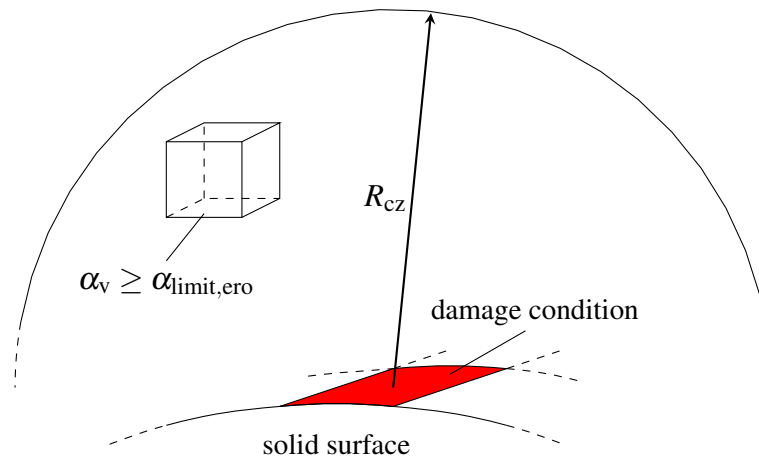


**Figure 4.12:** Erosion model conditions are examined for a face and an associated control volume in its cell zone

### Microjet Erosion Model

The microjet erosion model relies on the hypothesis that a liquid waterjet of high velocity is generated and impacts a solid wall when a cavitation bubble collapses in the wall's vicinity. The hypothesis supposes that pressure waves radiated from collapsing cloud cavitation cannot damage a surface directly, since their pressure amplitudes are attenuated as the waves travel through the water. It is rather supposed, that the pressure waves can cause cavitation bubbles to collapse and cause even higher pressures. Bubbles consequently causing other bubbles to collapse may even amplify the post-collapse pressures. When bubbles in the vicinity of a surface are initiated to oscillate and finally collapse, the collapse process is always asymmetrical. This is attributable to the fact that the flow towards the bubble is hindered by the presence of the wall surface. Because of the asymmetrical collapse process, the microjet is almost always pointing towards the material surface. The impact of the jet onto the wall leads to the generation of a shock wave radiated perpendicularly away from the wall. This phenomenon induces a very high pressure at the wall, the water hammer pressure, which can be higher than the yield strength of common materials used in technical flows.

Dular and Coutier-Delgosha (2009) and Dular et al. (2006) stated an erosion model, where it is assumed that the velocity of a microjet needs to exceed a certain velocity threshold to

cause erosion of a certain material. Both the number of pits on a surface, as well as the totally damaged surface are then calculated further on. The model was further developed by Peters et al. (2015c) to predict the areas most likely to be exposed to erosion as well as the qualitative intensity of erosive impacts during the incubation period – the erosion potential. Peters et al. (2015c,a) applied the model to predict cavitation erosion for an axisymmetrical nozzle and Peters et al. (2018a) applied it to predict cavitation erosion on a propeller. Therein, a favourable agreement compared to experimental erosion predictions was achieved.

According to Dular and Coutier-Delgosha (2009), the local velocity of the microjet is one of the critical quantities for the prediction of cavitation erosion. The most probable case for a microjet is selected at a dimensionless stand-off distance  $\gamma = 1.1$  based on former investigations by Dular and Coutier-Delgosha (2009) and Dular et al. (2006). This represents a typical collapse scenario of a bubble beginning to collapse while approaching a wall surface. As soon as the bubble is in the vicinity of the wall, it will start to deform quickly. A stand-off distance of  $\gamma = 1.1$  may lead to a microjet of high damaging potential, Philipp and Lauterborn (1998), Isselin et al. (1998), Dular et al. (2018). Considering the work of Lohrberg (2001), Dular and Coutier-Delgosha (2009), Dular et al. (2006), Chahine (2014a), and Supponen et al. (2016), the microjet velocity is defined as:

$$u_{\text{jet}} = c_{\gamma} \sqrt{\frac{p - p_b}{\rho_l}}, \quad (4.79)$$

which is inversely proportional to the Rayleigh collapse time of a bubble,  $t_{\text{coll}}$  (see (2.2)). It can be seen that the microjet velocity depends on the difference between liquid pressure,  $p$ , and inner bubble pressure,  $p_b$ , also referred to as the driving pressure, as well as on the parameter,  $c_{\gamma}$ . Chahine (2014a) found  $c_{\gamma} = 4.6$  from numerical simulations using different pressure differences,  $p - p_b$  for  $\gamma = 0.75$ . Supponen et al. (2016) derived a power law fit based on experimental and numerical investigations of single bubble collapses for different distances near a rigid surface to find  $c_{\gamma} = 4.615\gamma^2$ .

Based on a comparison of different jet velocities from literature by Lohrberg (2001), Peters et al. (2015c) found  $c_{\gamma} = 10.8$  to agree well with the measurements, assuming  $\gamma = 1.1$  to be the most probable collapse distance. Figure 4.13 shows the experimentally and theoretically obtained jet velocities by different researchers, taken from Lohrberg (2001). As can be seen, the microjet velocities deviated for stand-off distances higher than 1.2. Nevertheless, there were good agreements for stand-off distances  $0.8 \leq \gamma \leq 1.1$ . Assuming a typical scenario of water at 20°C, a liquid pressure of  $p = 100 \text{ kPa}$ , and  $c_{\gamma} = 10.8$ , a jet velocity of 107 m/s is obtained from equation (4.79). Figure 4.14 shows the impacting jet velocities on a solid surface measured by Philipp and Lauterborn (1998). Considering the observed deviations between the experiments shown in Figure 4.13 and the error bars for the experiments in Figure 4.14, the approximation using equation (4.79) with  $c_{\gamma} = 10.8$  shows fair agreement for a stand-off distance of  $\gamma = 1.1$ .

#### 4.5 Erosion Prediction

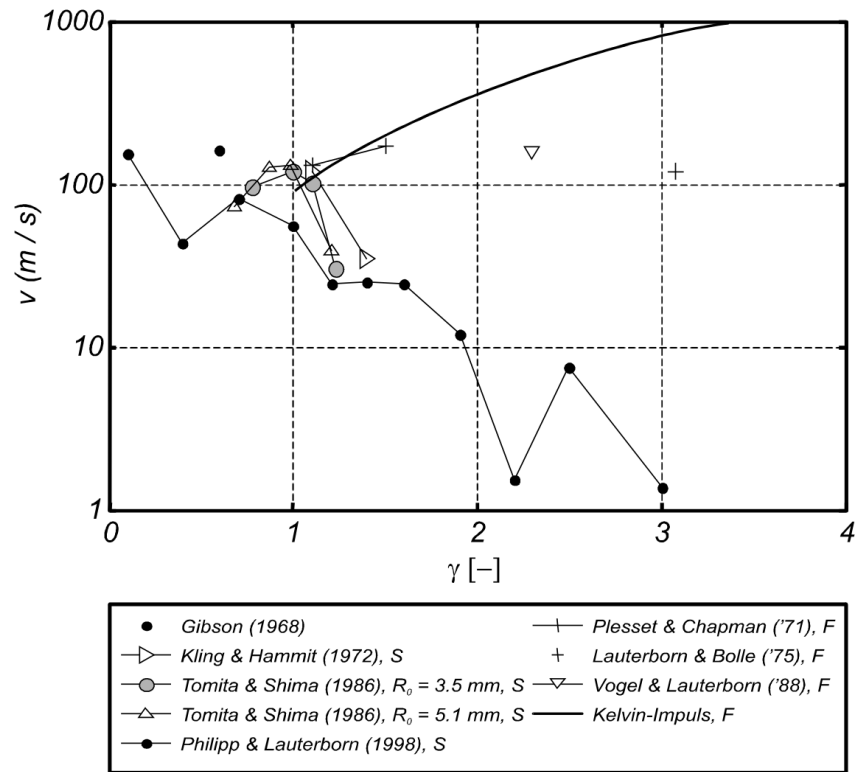


**Figure 4.13:** Comparison of microjet velocities from theoretical and experimental investigations taken from Lohrberg (2001)

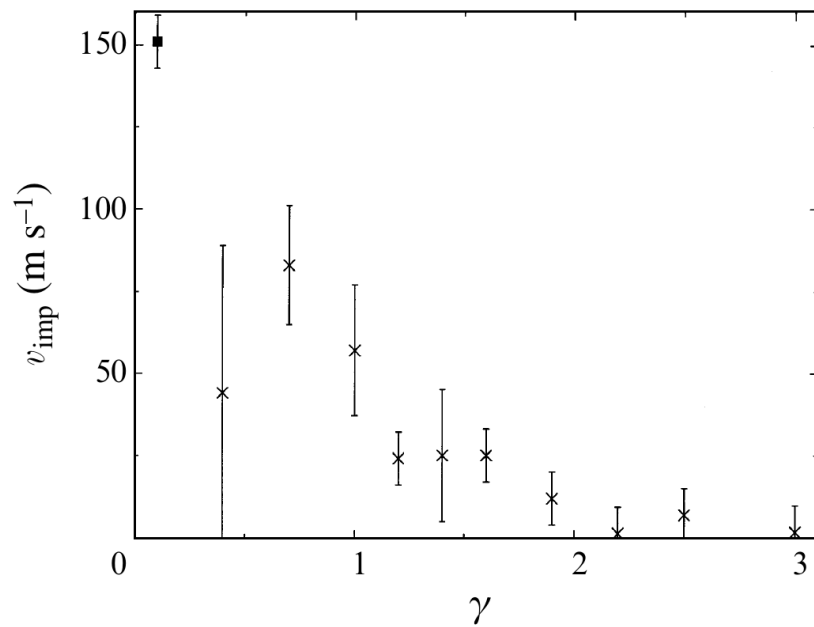


**Figure 4.14:** Impacting microjet velocities onto a solid surface taken from Philipp and Lauterborn (1998)

When a water column is stopped abruptly at a rigid wall, very high pressures are induced because the water is compressed at the wall and causes a shock impact. The induced pressure pulse at the wall is referred to as water hammer pressure,  $p_{wh}$ . When a valve in a pipe is suddenly closed, the water flow is stopped immediately in front of the valve generating high pressures at the valve itself, which are even able to damage it. Joukowsky (1898) was the first to state an equation for the water hammer pressure in pipe flows:

$$p_{wh} = \rho_1 c_1 \Delta u . \quad (4.80)$$

$c_1$  is the speed of sound in liquid water.  $\Delta u$  is the velocity difference between velocities before and after the deceleration. A similar process takes place when a high velocity microjet is brought to rest at a surface. Using the jet velocity and assuming that the velocity after impact is zero, the water hammer pressure can be approximated by substituting  $\Delta u = u_{jet}$ .

Lush (1983) derived a similar dependence between the velocity of a liquid mass and the pressure caused on a plastically behaving surface. Based on the equations of conservation of mass and momentum, the author considered a one-dimensional impact of the liquid mass onto a solid wall during which a shock wave is generated that travels perpendicularly away from the surface. Owing to the high pressure generated by a liquid mass impact, liquid water becomes compressible. The Tait equation of state, Tait (1889), was therefore used to relate pressure and density of compressible liquid water. Based on these assumptions, the author derived an equation for the liquid jet velocity, which causes a certain pressure on the solid surface. This approach is used to obtain the critical jet velocity,  $u_{crit}$ , which needs to be exceeded to plastically deform a surface of a material of yield strength  $\sigma_y$ . It is defined as:

$$u_{crit} = \sqrt{\frac{\sigma_y}{\rho_1} \left( 1 - \left( 1 + \frac{\sigma_y}{B} \right)^{-1/n} \right)} . \quad (4.81)$$

$B = 300\text{MPa}$  and  $n = 7$  are standard coefficients for liquid water in the Tait equation. If the velocity of a microjet,  $u_{jet}$ , is higher than the critical velocity,  $u_{crit}$ , it is assumed that the surface will be plastically deformed by the microjet. Using the microjet erosion model, the damage condition described above is then defined as:

$$u_{jet} > u_{crit} . \quad (4.82)$$

When vapour is present near the surface and the critical velocity is exceeded by the local jet velocity, a numerical erosion impact is predicted to occur. In each time step, exactly one numerical impact can be predicted on each face of a considered surface. To differentiate between the intensities of numerical erosion impacts, the ratio of microjet velocity to critical velocity is used to calculate the dimensionless intensity coefficient as:

$$c_{intensity, jet} = \frac{u_{jet}}{u_{crit}} . \quad (4.83)$$

## 4.5 Erosion Prediction

Using the Joukowsky relation (4.80), this ratio is approximately the ratio between the water hammer pressure caused by the microjet,  $p_{wh}$ , and the yield strength, which needs to be exceeded by the jet velocity to cause plastic flow. For non-impacted faces, the value of the intensity coefficient is equal to zero and for impacted faces the value is always greater than unity.

### Spherical Bubble Collapse Erosion Model

Another approach to numerically predict cavitation erosion using Euler-Euler solvers, relies on the hypothesis that erosion damage is caused by a pressure wave being radiated after the collapse of a single bubble within the vicinity of the surface. The bubble is assumed to be spherical and, during bubble collapse, effects caused by viscosity, initial gas, and surface tension are neglected. Despite the fact that some effects are not considered, Franc and Michel (2005) found that the general behaviour of a collapsing bubble can well be approximated with these assumptions even if the bubble is in motion. Therefore, the collapse of a spherical bubble can be calculated using a simplified form of the Rayleigh-Plesset equation. Under these conditions, a formula for the collapse induced pressure can be derived by integrating the Rayleigh-Plesset equation analytically. According to Franc and Michel (2005), the normalised collapse pressure is defined as:

$$\Pi_{\text{coll}} = \frac{p_{\text{coll}} - p}{p - p_v} \approx 0.157 \left( \frac{R_{\text{max}}}{R_{\text{min}}} \right)^3. \quad (4.84)$$

$p_{\text{coll}}$  is the pressure generated by the collapse. The main force causing the bubble to collapse comes from the liquid pressure,  $p$ , outside of the bubble. In the simulation,  $p$  is taken from the control volume neighbouring the regarded face.  $R_{\text{max}}$  is the radius at the start of the collapse and  $R_{\text{min}}$  the minimum radius, reached at the end of the collapse. Here, it is assumed that the final radius of the cavitation bubble is equal to the radius of the initial, non-condensable gas bubble,  $R_{\text{min}} = R_{\text{nuc}}$ . Equation (4.84) can be rewritten to approximate the collapse pressure:

$$p_{\text{coll}} = (p - p_v) \left( 0.157 \left( \frac{R_{\text{max}}}{R_{\text{min}}} \right)^3 \right) + p. \quad (4.85)$$

Unknown in this equation is the ratio of  $R_{\text{max}}/R_{\text{min}}$ . Although a bubble radius can be obtained from the cavitation model (see equation (4.52)), Sauer (2000) found that bubble radii can be rather large and grow to non-physical sizes according to the model. In the approach used in this work, a constant ratio of bubble radii during collapse is therefore chosen. In experiments of laser-induced bubbles near a solid boundary, Isselin et al. (1998) observed that the maximum and minimum radii during a collapse were linked depending on their distance to the wall. For bubbles, which were attached to the solid boundary, they observed a ratio of  $\frac{R_{\text{max}}}{R_{\text{min}}} = 10$ , while bubbles located in the vicinity of the wall without touching it, they observed a ratio of  $\frac{R_{\text{max}}}{R_{\text{min}}} = 20$ . In the present work, it is assumed that most bubble collapses occur before bubbles are actually attached to a solid boundary and a ratio of  $\frac{R_{\text{max}}}{R_{\text{min}}} = 20$  is used in equation (4.85). To

cause erosion of a material surface, it is supposed that the collapse pressure needs to exceed the yield strength of the considered material to cause plastic flow of the surface. Here, the damage condition is then written as:

$$p_{\text{coll}} > \sigma_y . \quad (4.86)$$

This condition implies that the collapse pressure is directly generated at the rigid surface and therefore a bubble is collapsing in the direct vicinity of it. Using this hypothesis, a surface is predicted to be eroded when a vapour bubble collapses rapidly in the vicinity of a surface and radiates a shock wave of high pressure magnitude, which is able to damage the surface. Analogue to the microjet erosion model, both the vapour and the damage condition need to be fulfilled to cause a numerical erosion impact. Following the approach used in equation (4.83), the numerical erosion impact for the spherical collapse model is calculated as:

$$c_{\text{intensity, coll}} = \frac{p_{\text{coll}}}{\sigma_y} . \quad (4.87)$$

### Normalised Erosion Potential

The numerical erosion prediction is supposed to be only qualitative because an Eulerian treatment of the vapour phase does not furnish information about single bubble behaviour and it is difficult to accurately predict the number of bubble collapses within a certain area and during a certain period of time. To still be able to differentiate between areas that are more or less endangered to erosion, a normalised erosion potential was derived. In general, erosion of a surface depends on the number of impacts within an area as well as the intensity of these impacts. To obtain a qualitative erosion prediction, all the erosion impacts of the entire temporal history and of the entire investigated surface are taken into account and used for normalisation. The erosion potential is presented as a measure of erosion aggressiveness for areas predicted to be eroded. It is calculated based on the accumulation of  $c_{\text{intensity}}$  (according to (4.83) or (4.87)) on each face explicitly over the temporal history and, afterwards, normalised with the total sum of  $c_{\text{intensity}}$  in the domain. The coefficient corresponding to the erosion potential for an Eulerian erosion prediction is introduced as:

$$c_{\text{ero,E}} = \frac{\sum_t^T c_{\text{intensity},t}}{\sum_n^N (\sum_t^T c_{\text{intensity},t})_n} . \quad (4.88)$$

$t$  is the time step index and  $T$  is the total time interval of the erosion prediction.  $n$  is the index of the face considered and  $N$  the total number of eroded faces. For clarification purposes, Figure 4.15 sketches a simple example of the calculation of  $c_{\text{ero,E}}$ . A surface of 9 faces is investigated regarding its erosion potential. In the first time step of erosion prediction, 3 faces are impacted and the intensities of these impacts are calculated using the intensity coefficient  $c_{\text{intensity}}$  for every face. Non-impacted faces are assigned with values of  $c_{\text{intensity}} = 0$ . In the second time step, 4 faces are predicted to be numerically impacted. This procedure is repeated for every time step within the time interval of erosion prediction and the values of  $c_{\text{intensity}}$

## 4.5 Erosion Prediction

are summed up for every face explicitly. According to equation (4.88), the sum of accumulated  $c_{\text{intensity}}$  values of all faces is then used for normalisation to obtain the dimensionless coefficient,  $c_{\text{ero,E}}$ , which represents the erosion potential of each face.  $c_{\text{ero,E}}$  is a measure for the percentage of predicted erosion on a single face compared to the total predicted erosion on all faces combined. On the right of Figure 4.15 the calculated  $c_{\text{ero,E}}$  values show that e.g. 29 % of the entire erosion is predicted to occur on the face in the centre of the grid and 8 % is predicted to occur on the face on the bottom right. In this case, the highest erosion potential is represented by the face in the centre of the numerical grid.

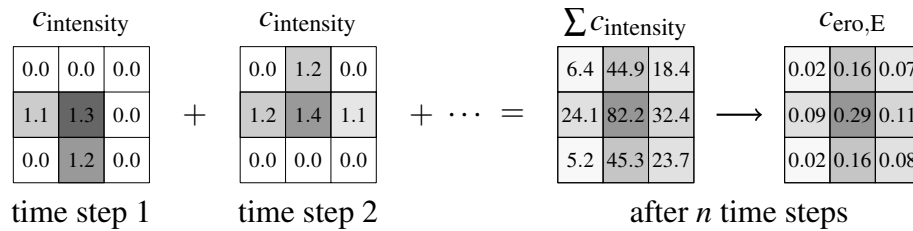


**Figure 4.15:** Exemplary calculation of the dimensionless coefficient  $c_{\text{ero,E}}$  to estimate erosion potential on a surface of 9 faces

The erosion coefficient,  $c_{\text{ero,E}}$ , combines both the intensity of a single impact (from equation (4.83) or equation (4.87)) with the number of impacts occurring on a face (sum of impacts). The erosion coefficient is limited between zero and unity because of normalisation so that the sum of  $c_{\text{ero,E}}$  of all faces equals unity. A value of zero represents a face on which no erosion is predicted to occur. Higher values correspond to higher erosion potentials for the regarded faces.

Both Eulerian-based erosion models are used as post-processing procedures which are executed at the end of every time step of flow solution. In this case, a one-way coupling is established because the calculated erosion potential does not influence the shape of the surface or the flow itself. This hypothesis is reasonable considering that these erosion predictions are conducted mainly for the incubation period in which material loss is negligible. During the incubation period, changes of a surface are supposed to be too small to influence the behaviour of the flow. The approach enables the comparison of the qualitative numerical erosion prediction with measured erosion patterns during the incubation period.

### 4.5.2 Lagrangian Approach

While an Eulerian approach to predict cavitation erosion requires hypotheses regarding bubble motion and dynamics and mostly neglects the spatial scales and time periods in which bubble collapses take place, a Lagrangian treatment offers far more information. Collapses of Lagrangian bubbles can be identified by a change of sign of the bubble wall velocity,  $\dot{R}$ . A change of  $\dot{R}$  from negative to positive denotes the time instance of the final stage of a bubble collapse, at which the bubble reaches its minimum radius during a bubble oscillation,  $R_{\text{min}}$ .

On the other hand, a change of sign of  $\dot{R}$  from positive to negative marks the moment of largest bubble radius during a bubble oscillation,  $R_{\max}$ . In these time instances, calculated quantities characterising a bubble collapse are stored in order to predict cavitation erosion. In the following, the approach to predict cavitation erosion based on these information is elaborated. First, theoretical considerations to model an asymmetric bubble collapse are presented.

Resolving shock wave radiation for asymmetric bubble collapses in a macroscopic flow simulation is almost impossible, because the computational effort would be excessive. To directly numerically simulate the multi-scale flow dynamics and the associated structural interaction may still be unrealistic. Here, erosion is therefore predicted based on spherical Lagrangian bubble collapses and mathematically modelled physics involved in an asymmetric near-wall bubble collapse. This physical modelling is based on well-recognised fundamental experiments and theoretical considerations that are not restricted to particular applications. The erosion model accounts for various phenomena during an asymmetric bubble collapse, such as (i) the motion of the bubble's centre towards the solid surface, (ii) the reduced collapse pressure attributed to the non-spherical collapse, and (iii) the pressure decay of the shock wave that travels towards the solid surface. Based on physical considerations from literature (see section 2.2.2) it is assumed that only bubbles within a normalised stand-off distance of  $\gamma \leq 3.0$  are able to damage a solid surface. The proposed model thus only considers bubbles that collapse within a distance of  $\gamma \leq 3.0$ .

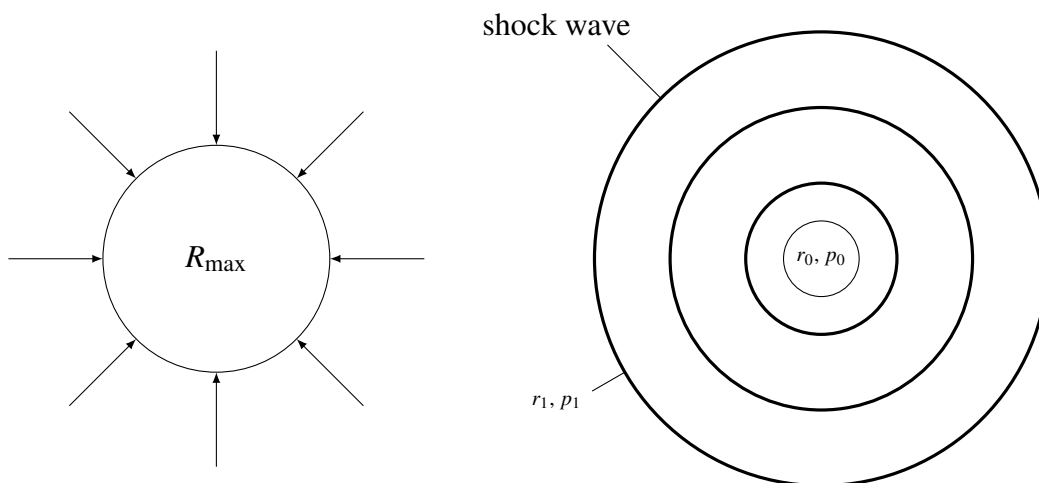


**Figure 4.16:** Simplified shock wave radiation during a spherical bubble collapse

During the collapse of a bubble, the bubble generates shock waves of high pressure amplitudes which are radiated spherically away from the bubble. While travelling through the liquid, the amplitudes of the shock waves decay. Figure 4.16 sketches a spherical bubble before (left) and after its collapse (right). Water flows from all directions towards the bubble, initiating a spherical collapse, resulting in the radiation of spherical shock waves. It is assumed that acoustic waves travel at velocities equal to the sound speed of the medium they permeate. Accordingly, acoustic waves in liquid water travel at velocities of about  $c_1 = 1450 \text{ m/s}$  corresponding to the

#### 4.5 Erosion Prediction

speed of sound in liquid water. The pressure after collapse,  $p_0$  is, thereby, assumed to decay linearly with the expansion of the acoustic wave. This yields:

$$\frac{p_1}{p_0} = \frac{r_0}{r_1}, \quad (4.89)$$

with the indices 0 and 1 indicating the initial and final positions of a spherically expanding acoustic wave, respectively.  $r_i$  is the radius of the spherically radiated, acoustic wave and  $p_i$  the pressure at the regarded radius.

In contrast to acoustic waves, shock waves usually travel at velocities much higher than the sound speed of the undisturbed permeated liquid. In these cases, a non-linear relation is used to account for pressure decay:

$$\frac{p_1}{p_0} = \left( \frac{r_0}{r_1} \right)^{n_{\text{shock}}}, \quad (4.90)$$

where  $n_{\text{shock}}$  depends on the expansion of the shock wave, the shock velocity, and the shock pressure (see section 2.2.2).

For bubbles collapsing near a rigid wall, the collapse process becomes asymmetric (see section 2.2.2). Thereby, shock waves are formed owing to the microjet impact onto the surface, the first collapse of the toroidal-shaped vapour structure, and rebounding collapses of vapour structures. Simultaneously, until the first collapse of the vapour torus completes, the bubble moves further towards the rigid surface and the impact concentrates in direction of the surface. Supponen et al. (2016) experimentally investigated collapses of laser-induced bubbles in a gravitational field, near a free surface, and near a rigid surface. They conducted experiments for different stand-off distances,  $\gamma$ , and found that the normalised bubble displacement,  $\Delta z/R_{\text{max}}$ , is related to a scalar anisotropy parameter,  $\zeta$ , as follows:

$$\Delta z/R_{\text{max}} = 2.5\zeta^{0.6}. \quad (4.91)$$

$\Delta z$  is the bubble displacement and  $\zeta \equiv -|\boldsymbol{\zeta}|$  is a scalar anisotropy parameter related to the Kelvin impulse, where  $\boldsymbol{\zeta}$  is the vector of the anisotropy parameter. In case of a bubble near a rigid surface,  $\boldsymbol{\zeta}$  is expressed as, Supponen et al. (2016):

$$\boldsymbol{\zeta} = -0.195\gamma^{-2}\mathbf{n}, \quad (4.92)$$

with  $\mathbf{n}$  as the unit normal vector of the surface pointing towards the centre of the bubble. Equating (4.91) and (4.92) yields a relation to calculate the motion of a collapsing bubble as a function of its normalised wall distance,  $\gamma$ , and the maximum bubble radius,  $R_{\text{max}}$ :

$$\Delta z = 2.5 \left( -|-0.195\gamma^{-2}\mathbf{n}| \right)^{0.6} R_{\text{max}}. \quad (4.93)$$

Accordingly, the distance from the bubble centre to the rigid boundary,  $H$ , is corrected to obtain  $H_{\text{corr}}$ :

$$H_{\text{corr}} = H + \Delta z. \quad (4.94)$$

Recall that, during collapse,  $\Delta z$  has a negative sign and a bubble will always move towards the boundary, i.e.  $H_{\text{corr}} < H$ .

Further considerations need to be made with regard to the conversion of the potential energy in the bubble, at the beginning of a collapse, into energy to generate shock waves. Supponen et al. (2017) investigated relations between the potential bubble energy and shock wave energy for laser-induced bubbles near rigid surfaces for  $\gamma > 4$ . Vogel et al. (1996) performed similar experiments for laser-induced bubbles near rigid walls for  $\gamma \leq 3$  and found that 60% – 70% of the energy initially stored in the bubble are converted into shock wave energy during the first and second collapse of a bubble. Using hydrophone measurements, they found dependencies of shock wave emission on the dimensionless wall distance,  $\gamma$ . Bubble collapses around  $\gamma = 0.9$  emitted a low part of shock wave energy during the first collapse, but an increased part during the second collapse of the bubble. For  $\gamma < 0.9$  the authors found an increase in sound emission during first collapse and a decrease in emission during second collapse.

As the shock wave emission is related to the collapse pressure of a bubble, the pressure generated after a bubble collapse is supposed to depend on  $\gamma$  as well. Accordingly, based on the experiments of Vogel and Lauterborn (1988) functions are found that take into account the asymmetric collapse with regard to shock wave emission. For  $\gamma \leq 3.0$ , these functions were fitted to the experiments to find the pressure generated during the first and second collapse of an asymmetric bubble collapse process,  $p_{\text{asym}}$ , compared to the pressure radiated during the first collapse of a spherically collapsing bubble,  $p_{\text{spher}}$ . For the first collapse, the pressure for an asymmetric collapse is approximated as:

$$p_{\text{asym},1} = p_{\text{spher}}[b_1(\gamma - 0.2)^4 + b_2(\gamma - 0.2)^3 + b_3(\gamma - 0.2)^2 + b_4(\gamma - 0.2) + b_5], \quad (4.95)$$

with the constants  $b_1 = 0.02788$ ,  $b_2 = -0.35725$ ,  $b_3 = 1.33158$ ,  $b_4 = -1.38117$ , and  $b_5 = 0.44444$ . The pressure radiated during second collapse is approximated according to:

$$p_{\text{asym},2} = \begin{cases} p_{\text{spher}}(c_1\gamma^5 + c_2\gamma^4 + c_3\gamma^3 + c_4\gamma^2 + c_5\gamma + c_6) & \text{if } \gamma \leq 2 \\ p_{\text{spher}}(d_1 + d_2e^{d_3\gamma}) & \text{else,} \end{cases} \quad (4.96)$$

with  $c_1 = 0.07680$ ,  $c_2 = -0.46386$ ,  $c_3 = 0.88197$ ,  $c_4 = -0.60657$ ,  $c_5 = 0.19778$ ,  $c_6 = 0.0006$ ,  $d_1 = 0.03802$ ,  $d_2 = 11.64971$ , and  $d_3 = -3.13128$ .

Because interactions and possibly amplifications of the pressure waves generated by the first and second collapse are likely, these two pressures are combined to predict erosion. The total radiated pressure during an asymmetric collapse is then approximated as the sum of both pressures as:

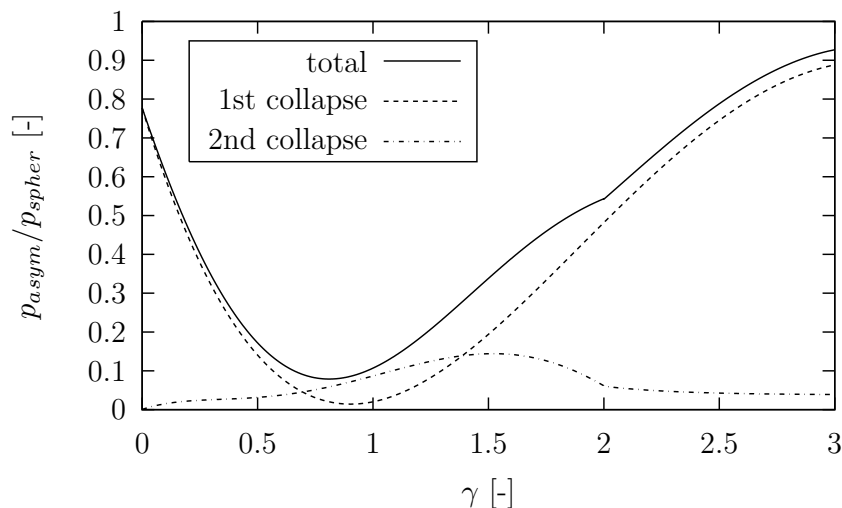
$$p_{\text{asym}} = p_{\text{asym},1} + p_{\text{asym},2} \cdot \quad (4.97)$$

Figure 4.17 illustrates the fitted functions, which represent the tendencies of shock wave behaviour with respect to normalised wall distance. The collapse pressure during an asymmetric collapse,  $p_{\text{asym}}$ , is normalised with the collapse pressure during a spherical collapse,  $p_{\text{spher}}$ ,

#### 4.5 Erosion Prediction

that is calculated for each bubble using the equations for bubble dynamics (4.8), (4.9), or (4.11).

Shock waves of higher pressure amplitudes and therefore higher collapse pressures are generated for  $\gamma < 0.3$  and  $\gamma > 1.0$  than in between. On the other hand, collapse pressures caused at larger distances from a wall do not necessarily generate higher impact pressures at the wall because the pressure waves decay over a longer distance (see equation (4.90)). Using this approach, bubble collapses of  $\gamma < 0.5$  and around  $\gamma \approx 1.0$  are assumed to be most aggressive because they take place in the immediate vicinity of a wall and generate high collapse pressures.



**Figure 4.17:** Normalised collapse pressure of an asymmetrical bubble collapse versus normalised wall distance fitted to experiments of Vogel and Lauterborn (1988)

In the present work, for simulations conducted with the multi-scale Euler-Lagrange approach, erosion was predicted using information of collapses of the spherical Lagrangian bubbles near regarded surfaces. For all identified collapses, the position, inner bubble pressure, maximum bubble radius, and minimum bubble radius after collapse are obtained and serve to predict erosion for a surface. Because only spherical collapses are calculated using the present method, two main effects of the asymmetric collapse behaviour and concentration of a collapse onto a surface are considered. Based on the above discussion, compared to a spherical collapse, during an asymmetric collapse:

1. the bubble moves towards the rigid surface, and
2. the conversion of potential bubble energy into shock wave energy decreases.

Figure 4.18 sketches the assumption of the underlying model for the collapse of a bubble close to a rigid wall. The asymmetric flow towards the bubble results in a motion of the bubble towards the rigid surface by the distance  $\Delta z$ .

For bubble collapses of  $\gamma \leq 1.0$ , it is assumed that after collapse the bubble is in contact with the rigid wall and the collapse pressure of the bubble is directly exerted on to the surface.

For  $\gamma > 1.0$ , the Kelvin impulse and (4.93) determine the bubble's motion towards the rigid surface.

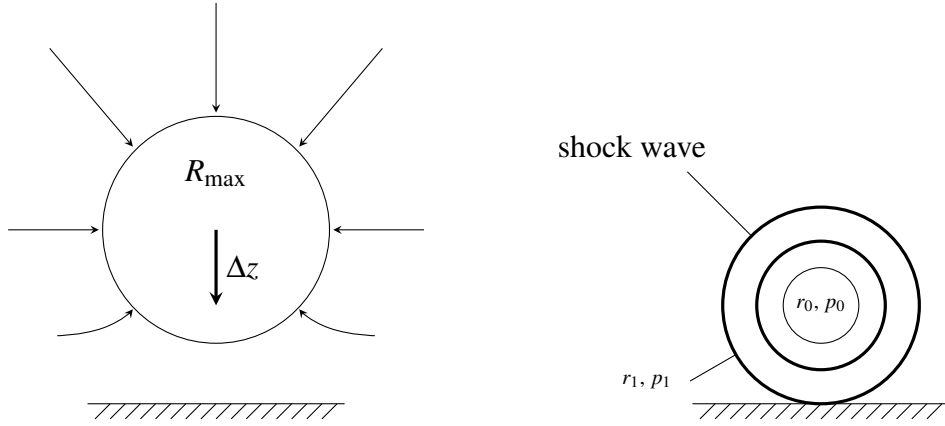


**Figure 4.18:** Assumed bubble motion and shock wave radiation during a near-wall bubble collapse

Depending on its displacement and radius after collapse, a bubble can be in contact with the surface in which case the impact pressure on the wall is calculated as follows:

$$p_{\text{imp}} = p_{\text{asym}} \cdot \quad (4.98)$$

The decreased collapse pressure of a bubble during an asymmetric collapse is determined from (4.95), (4.96), and (4.97). If liquid separates a bubble from the rigid surface, solving (4.90) with  $n_{\text{shock}} = 2$  obtains the pressure radiated by the bubble. This shock pressure is radiated over a distance until the shock wave reaches the considered face and causes an impact pressure expressed as follows:

$$p_{\text{imp}} = p_{\text{asym}} \left( \frac{R_{\text{min}}}{H_{\text{corr}}} \right)^2, \quad (4.99)$$

with  $H_{\text{corr}}$  obtained from (4.94). Although a microjet impact is not explicitly calculated, the influence of the microjet is incorporated also in the model. First, the motion of the bubble towards the wall is driven by the microjet and accounted for in (4.91) to (4.94). Second, the pressure decay functions from (4.95) to (4.97) take into account shock waves, which are radiated after the microjet impact. For different values of  $\gamma$ , the microjet impact on the surface occurs at different times, generates a shock wave, and influences the radiation of shock waves.

Analogous to (4.88), the Lagrangian erosion potential,  $c_{\text{ero,L}}$ , on the considered face is obtained by summing the individual impact pressures,  $p_{\text{imp}}$ , acting on one face and normalised against the sum of all impact pressures on the considered surface:

$$c_{\text{ero,L}} = \frac{\sum_i^I p_{\text{imp},i}}{\sum_n^N (\sum_i^I p_{\text{imp},i})_n}, \quad (4.100)$$

#### 4.5 Erosion Prediction

where index  $i$  refers to the impact itself and  $I$  is the total number of impacts on the regarded face. Similar to (4.88), (4.100) obtains the percentage of erosion in one face compared to all impacted faces of the considered surface.

Equation (4.100) assumes a linear relation between erosion and impact pressure,  $p_{\text{imp}}$ . On the contrary, experiments of Franc and Riondet (2006) indicated that incubation times and pit depths depend non-linearly on impact loads. They also stated that, for load stresses,  $\sigma$ , which exceed the yield strength,  $\sigma_y$ , of the considered material but not its ultimate strength,  $\sigma_u$ , the depth of an erosive pit,  $H_{\text{pit}}$ , depends non-linearly on load stress. For the material they considered (stainless steel 316L) and using a Ludwik type consolidation approach, they proposed the following relationship for the stress range of  $\sigma_y < \sigma < \sigma_u$ :

$$H_{\text{pit}} \propto (\sigma - \sigma_y)^{2.4} . \quad (4.101)$$

Although not all calculated impact pressures are assumed to exceed the yield strength of the regarded material, it is reasonable to assume, similar to (4.101), that the predicted erosion potential is proportional to impact pressure squared. Analogous to equation (4.100), the erosion potential is then calculated as being proportional to the impact pressure squared as follows:

$$c_{\text{ero,L2}} = \frac{\sum_i^I p_{\text{imp},i}^2}{\sum_n^N (\sum_i^I p_{\text{imp},i}^2)_n} , \quad (4.102)$$

which also yields the percentage of erosion on one face compared to all faces of the regarded surface. Here, influences of progressive erosion over different time periods were neglected.

In contrast to the Eulerian approach to predict erosion, the Lagrangian approach enables to find detailed information about bubble collapses leading to erosion. The approach not only enables to obtain information about spatial and temporal scales of bubble collapses but it allows to predict time instances of bubble collapses, collapse rates, collapse pressures, collapse positions as well as bubble sizes that can be correlated with erosive pits.

## **5 Numerical Prediction of Hydrodynamic Cavitation Erosion**

This chapter tackles the validation and application of different approaches to simulate cavitation behaviour and predict cavitation-induced erosion. Initially, using an Euler-Euler approach, numerical analyses of cavitation behaviour on hydrofoils, inside an axisymmetric nozzle, and around a propeller are presented. Results of numerical erosion predictions obtained using information from the Eulerian flow solution are given and compared against experimental measurements. Following the verification and validation of the main components of a Lagrangian-based solver, results for an internal nozzle flow, generated using an Euler-Lagrange approach, are shown. Combining advantages of Eulerian and Lagrangian approaches to treat the vapour phase, basic mechanisms of the multi-scale Euler-Lagrange approach are investigated. After comparison of numerical results from the multi-scale approach with Euler-Euler simulation results for the flow through an axisymmetric nozzle, erosion is predicted based on Lagrangian single bubble collapses. Finally, correlations between Lagrangian bubble collapses and measured erosion depths are revealed and the potential of the hybrid method to quantitatively predict cavitation erosion is introduced.

### **5.1 Euler-Euler Method**

This section presents verification and validation exercises and applications of an Euler-Euler method to simulate cavitating flows and predict cavitation erosion. The numerical method used to simulate cavitating flows utilises the finite volume method given in chapter 3 paired with the cavitation model presented in section 4.2.1. Approaches to numerically predict erosion use information from the Eulerian flow solution (see section 4.5.1). Numerical analyses of cavitating flows over hydrofoils, inside an axisymmetric nozzle, and around a propeller are compared to published experimental and numerical results to assess the accuracy of the method used. Numerical approaches to predict cavitation-induced erosion are compared to experimentally measured erosion patterns.

#### **5.1.1 NACA 0009 Modified Hydrofoil in Oblique Flow**

To validate the Euler-Euler approach concerning the simulation of transient cavitating flows, following the work of Peters et al. (2015c), the 3D cavitating flow over a modified NACA 0009

## 5.1 Euler-Euler Method

hydrofoil with a truncated trailing edge was simulated. Sufficient experimental results regarding pressure distributions, force coefficients, and the behaviour of cavitation were provided for this case by Dupont (1991). Based on a modified set of NACA equations, the geometry of the NACA profile was generated. For the considered symmetric profile, the first two digits of the NACA number defined the maximum camber and its position from the leading edge, respectively, and both equalled zero. The last two digits specified the maximum thickness of the foil given as a percentage of the foil's chord length. To obtain a symmetric geometry, modified NACA equations described the cross section according to Ausoni (2009) and read as follows:

$$\frac{y}{L_0} = \begin{cases} a_0 \left(\frac{x}{L_0}\right)^{\frac{1}{2}} + a_1 \left(\frac{x}{L_0}\right) + a_2 \left(\frac{x}{L_0}\right)^2 + a_3 \left(\frac{x}{L_0}\right)^3 & \text{for } 0 \leq \frac{y}{L_0} \leq 0.5, \\ b_0 + b_1 \left(1 - \frac{x}{L_0}\right) + b_2 \left(1 - \frac{x}{L_0}\right)^2 + b_3 \left(1 - \frac{x}{L_0}\right)^3 & \text{for } 0.5 < \frac{y}{L_0} \leq 1.0. \end{cases} \quad (5.1)$$

$L_0$  is the original chord length and  $y$  is the thickness of the foil corresponding to the longitudinal coordinate,  $x$ . For the geometry profile considered, the coefficients  $a_i$  and  $b_i$  with  $i = 0, 1, 2,$  and  $3$  were specified as:

$$\begin{aligned} a_0 = +0.1737, \quad a_1 = -0.2422, \quad a_2 = +0.3046, \quad a_3 = -0.2657 \quad \text{and} \\ b_0 = +0.0004, \quad b_1 = +0.1737, \quad b_2 = -0.1898, \quad b_3 = +0.0387 \end{aligned} \quad (5.2)$$

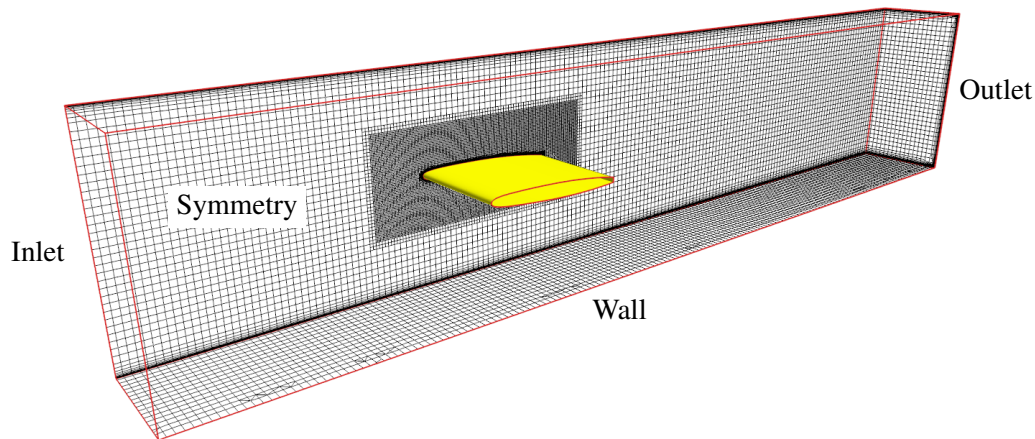
Originally, the chord length of the foil was 110 mm. In the investigations of Dupont (1991), the chord length of the geometry was truncated at 100 mm from the leading edge. The full description of the profile geometry is NACA 0009–7.8 45/1.93. According to Ausoni (2009), the first digits of the extension help to describe the radius of the leading edge, the second part describes the position of the maximum thickness and the third one is used to describe the slope at the trailing edge. In spanwise direction, the cross section extruded over the entire channel breadth of 150 mm. Table 5.1 lists particulars of the hydrofoil and the measurement section.

**Table 5.1:** Particulars of NACA 0009 and measurement section of the cavitation tunnel

property	symbol	
chord length (truncated trailing edge)	$c$ [mm]	100
thickness	$t_h$ [mm]	10
span width (channel breadth)	$s$ ( $B$ ) [mm]	150
channel height	$H_{ch}$ [mm]	150

For the numerical investigations, the geometry of the hydrofoil and the tunnel's measurement section of the experiments were geometrically modelled. In the experiments, the cross sectional area was of dimensions 150 mm × 150 mm. Figure 5.1 depicts the numerical domain together with the specified boundary conditions and the grid topology. The hydrofoil was inclined to the flow at an angle of attack of 2.5°. No-slip wall boundary conditions were specified for one side boundary, the top, the bottom, and the surface of the hydrofoil. A symmetry

boundary condition was defined for the other side boundary to enable the flow simulation in only one half of the experimental test section. An inlet boundary with a constant inflow velocity of 20 m/s was specified at the boundary, 200 mm upstream of the hydrofoil's leading edge. The pressure at an outlet boundary 450 mm downstream from the foil's trailing edge was specified to yield a cavitation number of 0.81. The total static pressure at the outlet was obtained by addition of the hydrostatic pressure.



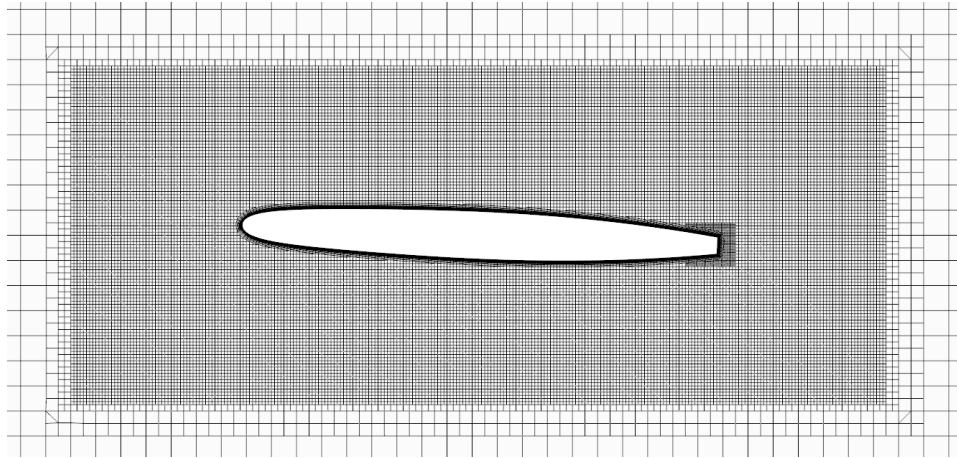
**Figure 5.1:** Numerical domain and grid topology around NACA 0009

Figure 5.2 displays the mesh around the NACA 0009 hydrofoil from a view normal to the spanwise direction. A grid containing hexahedral control volumes was generated and refined around the hydrofoil and around the trailing edge, where high gradients of flow quantities were expected. Trailing edge vortices were not fully resolved by the numerical grid because the cavitation structures behind the hydrofoil were not of interest with regard to cavitation erosion on the foil itself. Prism layers resolved the flow around the boundary layers at all wall boundaries. Resolving the boundary layer down to the viscous sub-layer requires a mesh refinement at the trailing edge involving a larger number of cells. Boundary layers were, therein, not fully resolved down to the viscous sub-layer, but to the logarithmic region where wall-functions were applied to model friction on all walls.

The cavitating flow around the hydrofoil was simulated using the cavitation model of Sauer and Schnerr (2000). Vapourisation and condensation coefficients of the cavitation model,  $C_v$  and  $C_c$ , equalled unity. In this case, the cavitation nuclei density (i.e. the number of bubbles per volume of liquid) equalled  $n_0 = 5 \cdot 10^8 \text{ m}^{-3}$  and the initial bubble radius equalled  $R_0 = 5 \cdot 10^{-6} \text{ m}$ . The influence of  $n_0$  on the behaviour of cavitation on a hydrofoil is presented in section 5.1.2. To model turbulence, the  $k$ - $\omega$ -SST model was employed together with the correction of turbulent kinetic energy of Reboud et al. (1998). The turbulence correction enabled the simulation of shedding of sheet and cloud cavitation. Spatial discretisation schemes and interpolation of variables for control volumes or faces were all of second-order, except for the turbulence equations of  $k$  and  $\omega$  where first order upwind schemes were used to increase stability. For time integration, the first-order implicit Euler scheme was employed

## 5.1 Euler-Euler Method

because time steps were sufficiently small and the scheme furnishes more stability than e.g. the second-order Crank-Nicolson scheme. During simulation, the average Courant number was about  $3 \cdot 10^{-3}$  and the maximum Courant number did not exceed 0.75.



**Figure 5.2:** Grid refinement regions around the NACA 0009

Figure 5.3 presents the formation of sheet cavitation and detachment of cloud cavitation on the NACA 0009 hydrofoil. The flow direction is from left bottom to right top. A light blue isosurface marks a vapour volume fraction of 10%. The pressure coefficient is defined as:

$$c_p = \frac{p - p_\infty}{\frac{1}{2}\rho_\infty u_\infty^2}, \quad (5.3)$$

with  $p_\infty$ ,  $\rho_\infty$ , and  $u_\infty$  as the pressure, liquid density, and velocity magnitude in the far field. The pressure coefficient is visualised on the symmetry boundary normal to the spanwise direction of the foil and on the wetted foil surface. Blue colours indicate low pressure regions; red colours, high pressure regions. Sheet cavitation was generated in the low pressure region on the suction side of the foil ranging from the leading edge further downstream. At time  $\Delta t = 0$  ms, the sheet cavitation was fully developed. A reversed flow developed under the end of the sheet – the re-entrant jet – owing to the flow circulation around the sheet cavitation and pierced the sheet cavitation at different positions. A cloud cavitation formed after a time of  $\Delta t = 0.95$  ms as the re-entrant jet shed a large part of the cavitation sheet from the foil. After time  $\Delta t = 1.95$  ms, the cloud cavitation detached from the surface of the foil and travelled further downstream, while a new sheet cavitation formed at the leading edge and elongated along the foil's surface. The collapse of the cloud cavitation occurred after a time of about  $\Delta t = 2.75$  ms and at about 30% of the foil's chord length downstream from the leading edge. High pressures were locally generated, as the cavitation cloud separated into small structures that collapsed consequently. Thereby, the sheet cavitation extended to almost its full length again. The periodic procedure of formation and collapse of cloud cavitation repeated itself with a frequency of about 155 Hz.

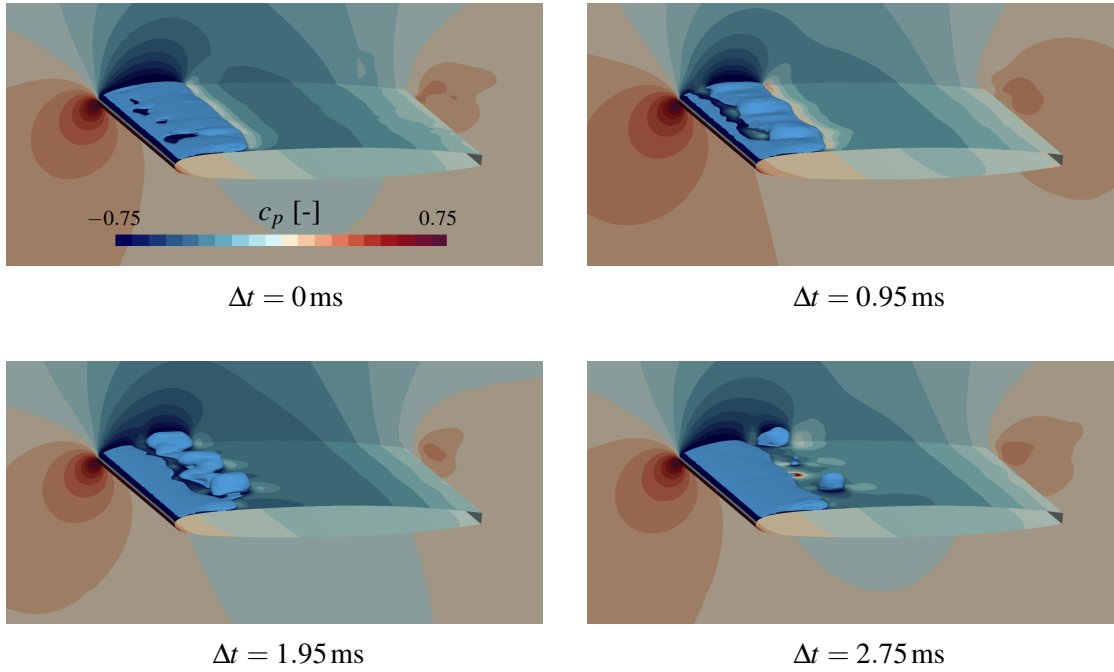


**Figure 5.3:** Cycle of generation of sheet cavitation and detachment of cloud cavitation around NACA 0009 at an angle of attack of  $2.5^\circ$

### Grid Dependence Study

Simulations were conducted using three different grids to identify convergence of spatial discretisation. The edge length of cells from one grid to another varied by a ratio of 1.53. Average force coefficients for drag and lift were calculated and the main frequencies of the harmonic cloud shedding were obtained from fast Fourier transforms (FFT) of the temporal progress of the normalised vapour volume in the computational domain,  $V_v^* = V_v/V_{\text{dom}}$ , with the total vapour volume in the domain,  $V_v$ , and the total volume of the domain,  $V_{\text{dom}}$ . Table 5.2 lists results of the three simulations. Time steps were specified as  $\Delta t = 1.0 \mu\text{s}$ ,  $0.654 \mu\text{s}$ , and  $0.427 \mu\text{s}$  to obtain the same ratio of temporal to spatial discretisation for simulations using grids of  $0.29 \cdot 10^6$ ,  $1.03 \cdot 10^6$ , and  $3.73 \cdot 10^6$  control volumes, respectively. For all simulations, these time steps yielded average Courant numbers of about  $3 \cdot 10^{-3}$ . Maximum Courant numbers for simulations using the two finer grids did not exceed 0.75, while maximum Courant numbers of the coarsest grid exceeded unity.

$c_D$  and  $c_L$  are the force coefficients of drag  $D$  and lift  $L$ , respectively, calculated from:

$$c_F = \frac{F}{1/2\rho_\infty u_\infty^2 A_{\text{ref}}}, \quad (5.4)$$

where  $F$  is the force of drag or lift,  $A_{\text{ref}}$  is the reference area of the hydrofoil, and  $f$  is the dominant frequency obtained from the temporal progress of the normalised vapour volume in the domain. In this case, the Strouhal number,  $St$ , is calculated using the frequency,  $f$ , related to

**Table 5.2:** Numerical results of the cavitating flow around a NACA 0009 at an angle of attack of  $2.5^\circ$  on different grids

grid	control volumes	$c_D$ [-]	$c_L$ [-]	$f$ [Hz]
G1	$0.29 \cdot 10^6$	0.0227	0.383	-
G2	$1.03 \cdot 10^6$	0.0189	0.348	154.45
G3	$3.73 \cdot 10^6$	0.0206	0.346	156.74

the normalised vapour volume. Drag coefficients obtained using grids G1 and G2 deviated by 10.2 % and 8.3 % from the drag coefficient obtained from simulation G3. The lift coefficient obtained using grid G1 deviated by 10.7 % from G3; for grid G2, deviated by 0.6 %. Because of the coarse resolution of the low pressure region near the leading edge, periodic shedding of the sheet cavitation could not be simulated using grid G1. Simulations on grids G2 and G3 showed a periodic behaviour of cavitation with similar characteristic frequencies obtained from the FFT. Frequencies were found by analysing the temporal progress of the lift forces. The frequency obtained from the simulation on grid G2 deviated by less than 1.5 % from the frequency obtained using grid G3. For grid G1, the spatial resolution was too low to capture the dynamic behaviour of cavitation for the present case. Except for a considerable difference in drag, grid G2 was sufficiently fine to capture the dynamics of cavitation behaviour.

### Validation of Cavitation Behaviour

Results of the numerical simulations were compared to experimental data. Table 5.3 lists results from different cases investigated experimentally and numerically.  $\sigma_{\text{cav}}$  is the cavitation number of the regarded case. Numerical results agreed favourably with experimental results. Forces acting on the hydrofoil were generally affected by length and form of cavitation structures as well as the frequency related to the shedding of cloud cavitation. The lift coefficient of the numerical simulation on grid G3 deviated by 4.5 % from the measured coefficient; the drag coefficient, by 1.9 %. The Strouhal number obtained from the simulation deviated by 9.4 % from the measured one.

**Table 5.3:** Comparable experimental and numerical results of the cavitating flow around a NACA 0009 at an angle of attack of  $2.5^\circ$ 

case	$u_\infty$ [m/s]	$\sigma_{\text{cav}}$ [-]	$c_D$ [-]	$c_L$ [-]	$f$ [Hz]	St [-]
experiment 1	20.00	0.82	0.0210	0.331	-	-
experiment 2	20.70	0.81	-	-	179.00	0.865
simulation G3	20.00	0.81	0.0206	0.346	156.74	0.784

Computed pressure distributions around the hydrofoil were compared to measured distributions. In advance, simulations without cavitation (deactivated cavitation model) were conducted. Figure 5.4 depicts instantaneous distributions of the calculated (solid line) and measured (triangles) pressure coefficient,  $c_p$ , over the chord length of the hydrofoil in non-cavitating (left) and cavitating condition (right). For the simulation of the cavitating condition, a time instance of maximum elongation of the sheet cavitation was chosen according to the time instance used in the experiments. In both non-cavitating and cavitating conditions, the instantaneous pressure distributions agreed well.

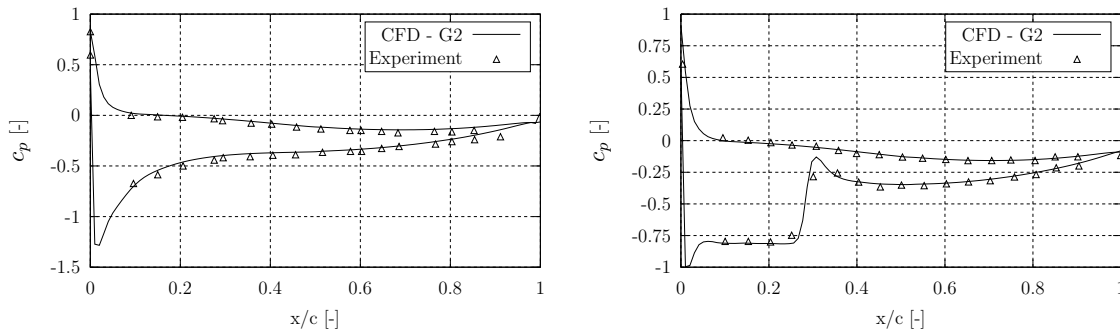


**Figure 5.4:** Calculated instantaneous pressure distributions compared to experimental data of Dupont (1991) on NACA 0009 hydrofoil at an angle of attack of  $2.5^\circ$

Simulation errors were particularly attributable to spatial discretisation and to modelling of cavitation and turbulence. Besides these errors, deviations in the obtained frequencies possibly stemmed from different approaches to obtain these. In the experiments, pressures and velocities were measured at different locations in the tunnel. Velocities were measured using laser Doppler anemometry. Characteristic frequencies of cavitation shedding were obtained from frequency analyses of the temporal progresses of these velocities. However, the measured velocities showed unsteady behaviour which was less harmonic than the oscillations of the calculated vapour volume in the simulations. Additionally, the presence of rotating components in front of the measurement section influenced the measurements such that frequencies related to the rotation rates could be found in the frequency analyses as well.

### 5.1.2 NACA 0015 Hydrofoil in Oblique Flow

In the joint project *KonKav III* approaches to predict cavitation erosion were developed and compared to experimental predictions. Reemts and Johannsen (2015) investigated the cavitation flow over a NACA 0015 hydrofoil in a cavitation tunnel and the aggressiveness related to cavitation-induced erosion. Experiments were performed in a cavitation tunnel of the Hamburgische Schiffbau-Versuchsanstalt GmbH (HSVA). To predict cavitation erosion, the surface of the hydrofoil was coated using the *Soft-Ink* method developed by the HSVA. Using this technique, a surface considered is coated with a electro-chemical technique and it is assumed that aggressive collapses of cavitation structures remove the coating on this surface. Table 5.4 lists particulars of the hydrofoil and the measurement section from the experiments of Reemts and Johannsen (2015). The span width equalled the channel breadth, as the foil was extended from one side wall of the channel to the other.

**Table 5.4:** Particulars of NACA 0015 and measurement section of the cavitation tunnel

property	symbol	
chord length	$c$ [mm]	200
thickness	$t$ [mm]	30
span width (channel breadth)	$s$ ( $B$ ) [mm]	570
channel height	$H_{ch}$ [mm]	570

Based on these experiments, the cavitating flow over a NACA 0015 hydrofoil was simulated. Simulated cavitation behaviour and numerically predicted erosion were compared to experimental data. To geometrically model the experimental test section, a numerical simulation domain was generated according to the same cross section. Angles of attack of  $5^\circ$  and  $8^\circ$  of the flow around the hydrofoil in the channel were numerically investigated. Figure 5.5 depicts the numerical domain with its boundary conditions and the grid topology, which was generated analogously to the topology used for the NACA 0009 hydrofoil (see section 5.1.1). Figure 5.6 displays the mesh around the NACA 0015 hydrofoil from a view normal to the spanwise direction. The grid was refined in a hexahedral block around the hydrofoil and further around the leading edge and the trailing edge of the foil. No-slip wall conditions were specified for the top, the bottom, one side boundary, and the surface of the hydrofoil. Only half of the tunnel geometry was modelled employing a symmetry boundary condition for one side boundary of the domain. Logarithmic wall functions were applied to all walls and near-wall cells were generated to yield dimensionless wall distances of  $n^+ \approx 30$ -300. Upstream of the hydrofoil, a boundary of constant inlet velocity was defined. Pressures at the outlet boundary downstream from the hydrofoil were specified to obtain different cavitation numbers. The model of Sauer and Schnerr (2000) was used to model cavitation with the constants for vapourisation and condensation that equalled unity. A nuclei density of  $n_0 = 1 \cdot 10^8 \text{ m}^{-3}$  and a nuclei radius of  $R_0 = 5 \cdot 10^{-6} \text{ m}$  were used. Later on, the nuclei density was varied to investigate its influence on cavitation behaviour. To resolve the shedding of cloud cavitation on the suction side of

the foil at higher angles of attack, the grid in this region and around the trailing edge of the hydrofoil was refined. As time steps were sufficiently small, for time integration, the implicit first-order Euler method was employed. Being of first order, the method is more stable to numerical oscillations than second order methods. For a characteristic case, sensitivity studies of temporal and spatial discretisation were performed. Second order schemes discretised all terms but convection terms for  $k$  and  $\omega$ , which were discretised by first order upwind schemes to maintain higher stability.

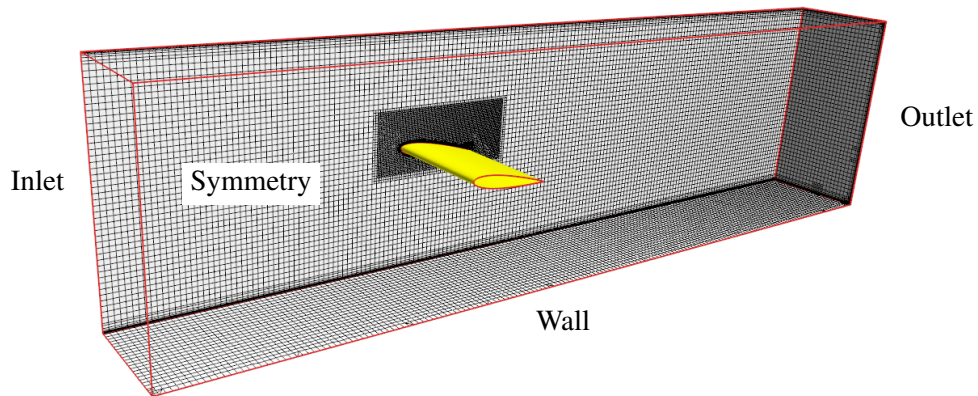


**Figure 5.5:** Numerical domain and grid topology around NACA 0015

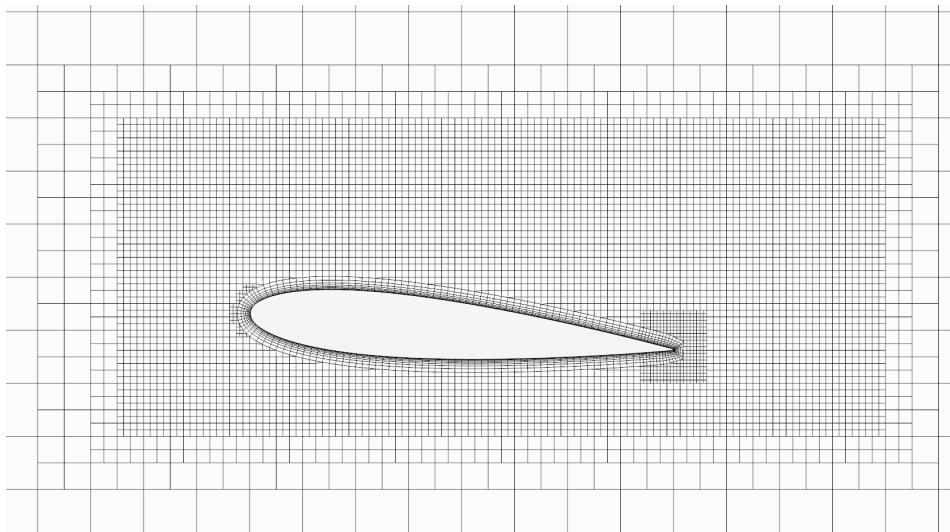


**Figure 5.6:** Grid refinement regions around the NACA 0015

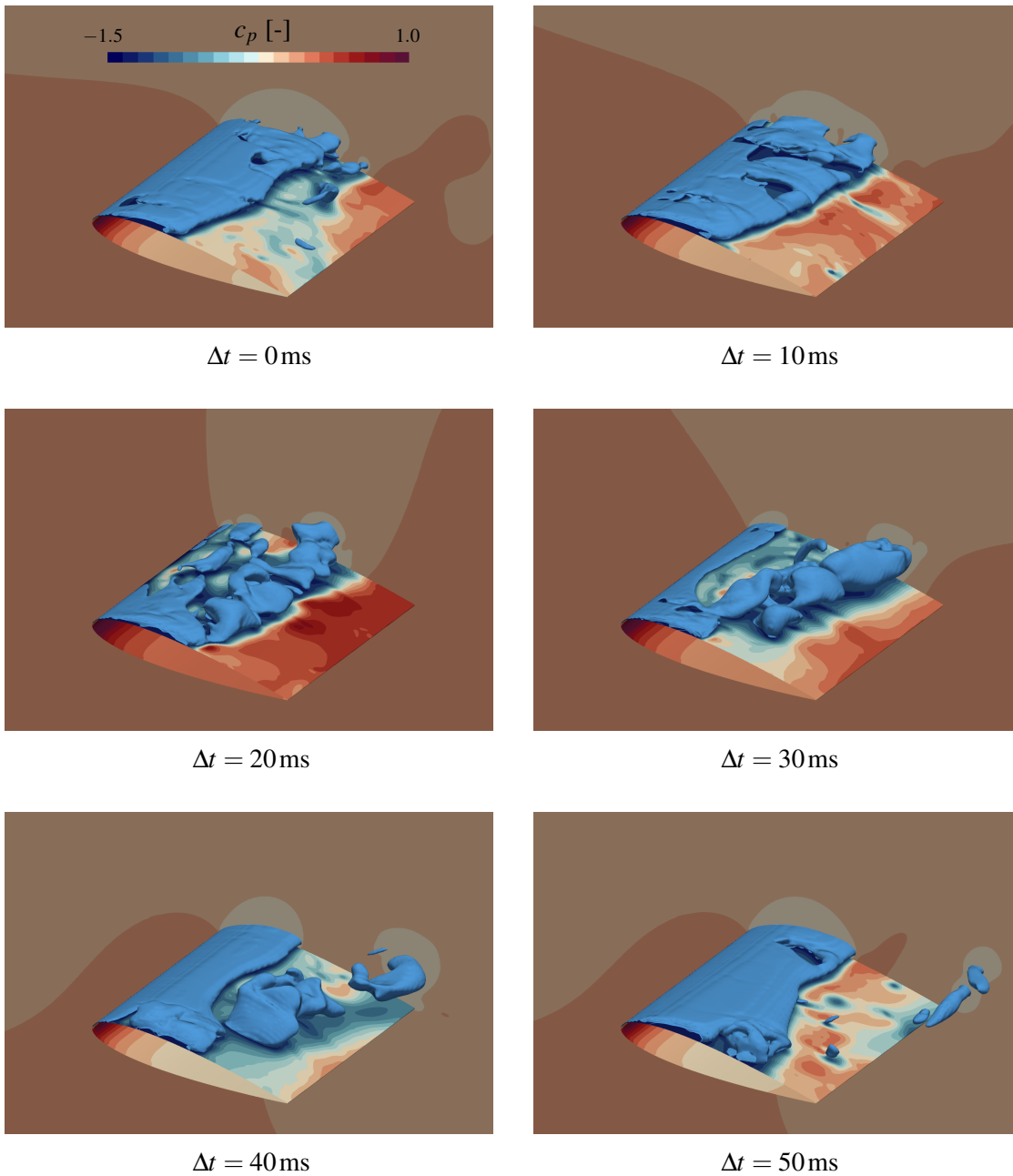
A case of  $8^\circ$  angle of attack with an inlet velocity of 8 m/s was considered. The pressure at the outlet was specified such that a cavitation number of  $\sigma_{\text{cav}} = 1.3$  was obtained. Figure 5.7 shows a cycle of the formation of sheet cavitation and shedding of cloud cavitation on the

## 5.1 Euler-Euler Method

NACA 0015 hydrofoil. Pressure regions are shown in terms of the pressure coefficient,  $c_p$ , plotted on the symmetry plane and the wetted hydrofoil surface. High values of pressure are shown in red and low values in blue. Liquid water flowed from top left to bottom right. Isosurfaces of 10 % vapour volume fraction are displayed in light blue. The side boundary at the lower end of the hydrofoil was defined as no-slip wall and the side boundary at the upper end of the span width was defined as symmetry. These boundary conditions influenced the cavitation behaviour as the flow decelerated at the spanwise end of the foil near the no-slip wall.

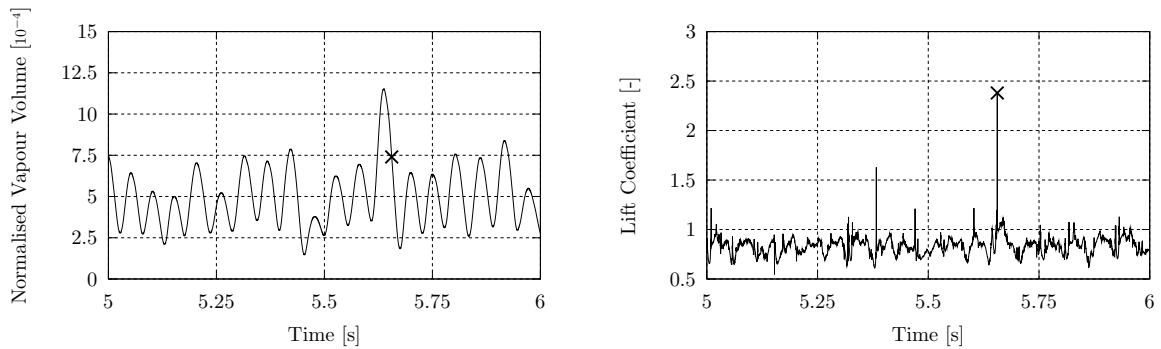
At the beginning, a sheet cavitation developed on the suction side of the foil in the region of lowest pressure. Small clouds shed from the sheet cavitation as re-entrant jets pierced holes in the attached sheet cavitation. At time  $\Delta t = 10$  ms, Figure 5.7 shows that the holes grew and cavitation clouds started to detach from the surface of the hydrofoil. After time  $\Delta t = 20$  ms cavitation clouds shed from the sheet cavitation, travelled further downstream, and grew to their maximum extents after a time of about  $\Delta t = 40$  ms. While the cloud cavitation was shed from the foil, the remaining sheet cavitation decreased to its minimum length and started to grow again between times  $\Delta t = 20$  ms and  $\Delta t = 30$  ms. From time  $\Delta t = 40$  ms to 50 ms, the clouds reached regions of higher pressure and collapsed near the surface of the hydrofoil. At time  $\Delta t = 50$  ms, some smaller clouds travelled further downstream behind the foil, while the attached sheet cavitation grew to its maximum length again and new re-entrant jets developed.

Figure 5.8 shows time histories of the normalised vapour volume in the domain,  $V_v^*$ , (left) and the lift coefficient of the hydrofoil (right) calculated from (5.4). The vapour volume oscillated periodically, which correlated with the shedding of cloud cavitation. Harmonic oscillations were not directly obvious from the temporal progress of the lift coefficient. The high peaks in lift were caused during collapses of large cavitation volumes near the surface of the hydrofoil. In Figure 5.8 a black cross marks the collapse of a cavitation volume at time 5.656 s. The cavitation structure collapsed close to the trailing edge of the foil. Figure 5.8 (right) shows that this collapse caused a high peak in lift force related to the pressure rise in the domain near the trailing edge after collapse of the cavitation cloud. It should be noted that high pressure peaks are overestimated when the liquid phase is considered incompressible and the propagation of pressure waves can not be accounted for. High pressures are, therein, instantly transported through the domain and the influence of cavitation collapses on the peaks in lift force is only of a qualitative nature.



**Figure 5.7:** Cycle of generation of sheet cavitation followed by shedding and collapse of cloud cavitation around NACA 0015 hydrofoil at an angle of attack of  $8^\circ$

## 5.1 Euler-Euler Method



**Figure 5.8:** Sequences of time series of the normalised vapour volume in the domain (left) and the lift coefficient on NACA 0015 (right)

### Grid Dependence Study

For the regarded case, a similar grid topology as for the NACA 0009 modified hydrofoil (see section 5.1.1) was used. To evaluate spatial discretisation, at the higher angle of attack of  $8^\circ$ , the cavitating flow over the hydrofoil was simulated on numerical grids of  $0.41 \cdot 10^6$  (G1),  $0.91 \cdot 10^6$  (G2), and  $2.17 \cdot 10^6$  (G3) employing a refinement factor of 1.31 between the base edge lengths from one grid to the next finer one. Refinement regions were generated around the hydrofoil surface and around the trailing edge.

**Table 5.5:** Numerical results for the cavitating flow around a NACA 0015 at an angle of attack of  $8^\circ$  on different grids

grid	control volumes	$c_L$ [-]	$\bar{V}_v^*$ [ $1 \cdot 10^{-4}$ ]	$f$ [Hz]
G1	$0.41 \cdot 10^6$	0.798 (-4.77%)	4.430 (-11.77%)	18.39
G2	$0.91 \cdot 10^6$	0.826 (-1.43%)	4.843 (-3.55%)	18.14
G3	$2.17 \cdot 10^6$	0.838	5.021	18.18

Table 5.5 lists results of the grid dependence study for the cavitating flow around the NACA 0015. The lift coefficient deviated by 4.8 % for simulation G1 compared to simulation G3; for simulation G2, by 1.4 %. The time-averaged normalised vapour volume,  $\bar{V}_v^*$ , obtained from simulation G1 compared to G3 deviated by 11.77 % and obtained from simulation G2 deviated by 3.55 %. The results of the lift coefficient and the time-averaged normalised vapour volume converged monotonically. Hence, grid independent values were Richardson extrapolated (see section 3.4.3).  $c_{L,RE} = 0.4295$  is the Richardson extrapolated lift coefficient and  $\bar{V}_{v,RE}^* = 5.334 \cdot 10^{-4}$  the extrapolated time-averaged normalised vapour volume.

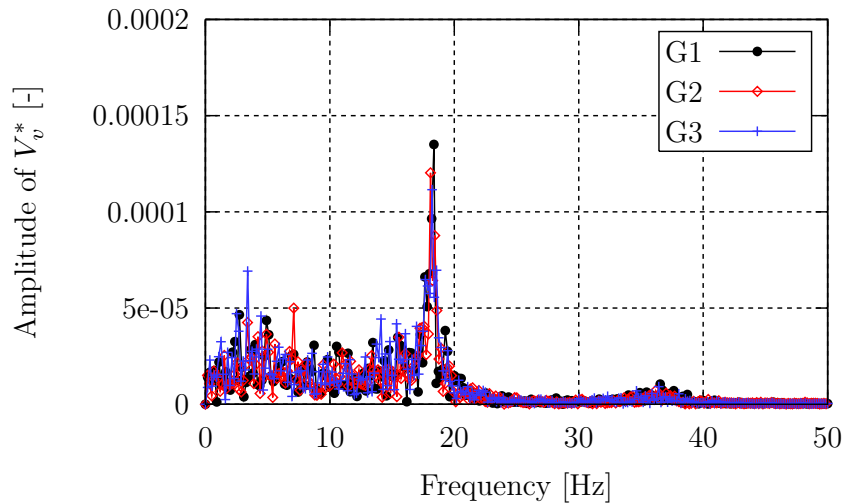


**Figure 5.9:** Fast Fourier transform of normalised vapour volume obtained from simulations using different grids

Figure 5.9 plots the FFTs of the normalised vapour volume from simulations using grids G1, G2, and G3. Frequencies smaller than 0.01 Hz were filtered out. For all simulations, characteristic frequencies of about 18 Hz were obtained which were related to the macroscopic shedding of cavitation clouds from the hydrofoil. A smaller peak was found close to 36 Hz. The Strouhal number corresponding to the shedding frequency of 18.18 Hz, obtained from case G3, is  $St = 0.455$  using the chord length of the foil as reference length.

### Time Step Dependence Study

Apart from the investigation of the dependence of the numerical solution on spatial discretisation, the dependence on temporal discretisation was investigated. Simulations on grid G2 were conducted for time steps of  $\Delta t = 40 \mu s$  (T1),  $\Delta t = 10 \mu s$  (T2), and  $\Delta t = 2.5 \mu s$  (T3). Table 5.6 summarises particulars and results from these simulations. The lift force was less sensitive to temporal than to spatial resolution. Related to simulation T3, the lift coefficient obtained from simulation T1 deviated by  $-1.47\%$ ; obtained from simulation T2, by  $+0.85\%$ . The time-averaged normalised vapour volume in the domain,  $\bar{V}_v^*$ , showed a larger influence of temporal discretisation. With regard to simulation T3,  $\bar{V}_v^*$  obtained from simulation T1 deviated by  $-12.97\%$  and from simulation T2 deviated by only  $+0.50\%$ . Although monotonic convergence was not achieved for the lift coefficient or the time-averaged normalised vapour volume, differences between results from simulations T2 and T3 were small. A time step of  $\Delta t = 10 \mu s$  was chosen for further flow simulations around the NACA 0015 hydrofoil.

### Variation of Nuclei Density

The cavitation model of Sauer and Schnerr (2000) contains different parameters that influence the behaviour of cavitation. Besides the constants for vapourisation,  $C_v$ , and condensation,  $C_c$ ,

**Table 5.6:** Numerical results of the cavitating flow around a NACA 0015 at an angle of attack of  $8^\circ$  for different time step sizes

case	$\Delta t$ [ $\mu\text{s}$ ]	$c_L$ [-]	$\bar{V}_v^*$ [ $1 \cdot 10^{-4}$ ]	$f$ [Hz]
T1	40	0.807 (-1.47%)	4.194 (-12.97%)	19.01
T2	10	0.826 (+0.85%)	4.843 (+0.50%)	18.14
T3	2.5	0.819	4.819	18.41

which equalled unity, the nuclei density,  $n_0$ , and the nuclei equilibrium radius,  $R_0$ , represent physically related parameters. Although Sauer (2000) showed that bubble radii calculated from this cavitation model may adopt unrealistic sizes,  $n_0$  and  $R_0$  can be configured to take into account effects attributable to water quality. To analyse the influence of the nuclei density on the computed behaviour of cavitation,  $n_0$  was varied for the previously described case using grid G2 and a time step of  $\Delta t = 10\mu\text{s}$ . An angle of attack of  $8^\circ$  and an inflow velocity of 8 m/s were specified. Table 5.7 lists results for three simulations using different values of  $n_0$ . Frequencies of the shedding of cavitation were identified from FFTs of time series of the normalised vapour volume in the domain. An increase of the nuclei density yielded higher lift coefficients. While the frequency of cavitation shedding decreased with increasing nuclei density, the vapour volume increased. For  $n_0 = 1 \cdot 10^6/\text{m}^3$  the time-averaged vapour volume equalled 46.7% compared to the case of  $n_0 = 1 \cdot 10^8/\text{m}^3$ . The time-averaged vapour volume was 10.9% larger for  $n_0 = 1 \cdot 10^{11}/\text{m}^3$  compared to  $n_0 = 1 \cdot 10^8/\text{m}^3$ . Thus, clear tendencies were identified for lift coefficient, time-averaged vapour volume, and shedding frequency of cavitation.

**Table 5.7:** Numerical results of the cavitating flow around a NACA 0015 at an angle of attack of  $8^\circ$  using different nuclei densities,  $n_0$

$n_0$ [ $1/\text{m}^3$ ]	$c_L$ [-]	$\bar{V}_v^*$ [ $1 \cdot 10^{-4}$ ]	$f$ [Hz]	St [-]
$10^6$	0.778	2.260	22.31	0.558
$10^8$	0.826	4.843	18.14	0.454
$10^{11}$	0.853	5.373	17.39	0.435

Arndt et al. (2000) investigated the NACA 0015 hydrofoil both experimentally and numerically. Therein, a dependence of the Strouhal number on  $\sigma_{\text{cav}}/2\alpha_{\text{AoA}}$  with  $\alpha_{\text{AoA}}$  as the angle of attack was found. At a condition of  $\sigma_{\text{cav}}/2\alpha_{\text{AoA}} \approx 4.6$ , similar to the present case, they obtained Strouhal numbers of  $\text{St} \approx 0.5$  to 0.65. Reemts and Johannsen (2015) conducted experiments of the present case and obtained a shedding frequency of approximately 21 Hz based on observations using high-speed video technique. This frequency agrees with the computed frequencies for different nuclei densities. In this case, the frequency for  $n_0 = 1 \cdot 10^6/\text{m}^3$  agreed best with the experimentally observed frequency of Reemts and Johannsen (2015) and frequencies obtained by Arndt et al. (2000). Results from simulation and experiment deviated

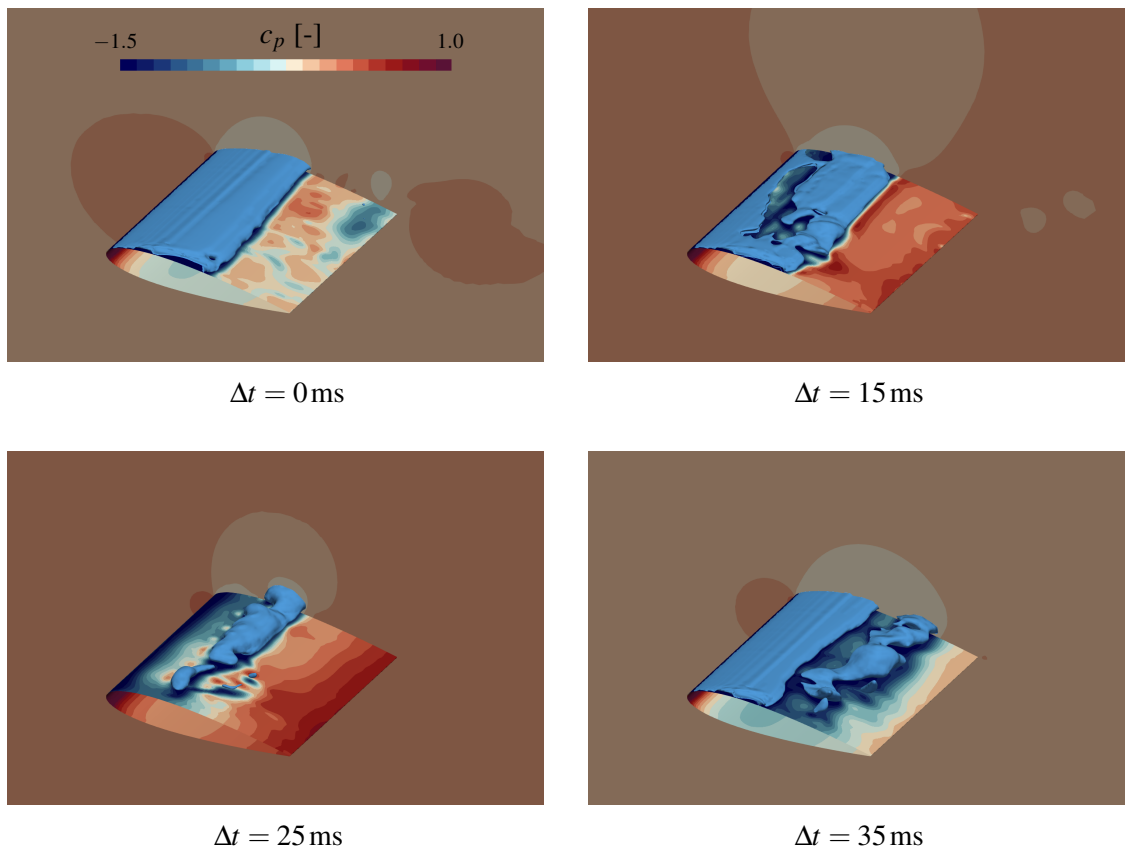
owing to different flow conditions and different techniques that were used to obtain these frequencies. It is noted that the influence of nuclei density differs depending on the flow problem considered.

### Cavitation Behaviour for Different Cavitation Numbers

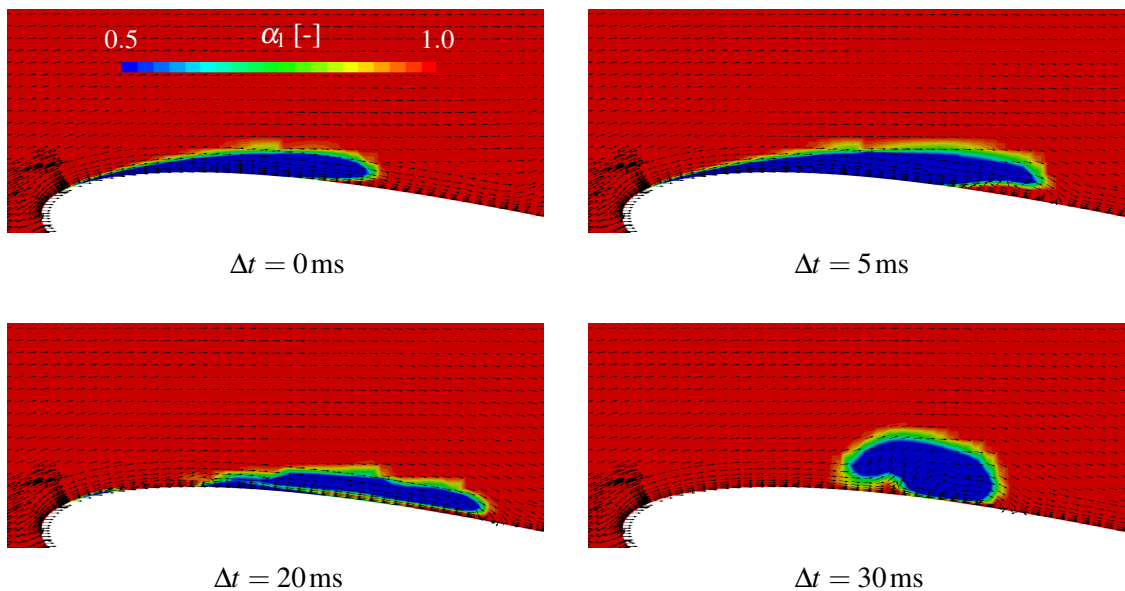
Reemts and Johannsen (2015) conducted experiments on the regarded NACA 0015 hydrofoil in a cavitation tunnel of the HSVA (see Table 5.4) to investigate cavitation and cavitation-induced erosion. Tests were performed at an angle of attack of  $5^\circ$ , an inflow velocity of 10 m/s, and a cavitation number of  $\sigma_{\text{cav}} \approx 1$ . Numerical simulations of flow around the NACA 0015 hydrofoil were conducted for three different cavitation numbers by specifying different pressures at the outlet of the computational domain and keeping the inflow velocity constant at 10 m/s. Depending on the cavitation number, a different cavitation behaviour was observed, which led to different predictions of erosion. Analogue to the topology of case G2 (see Table 5.5) a mesh was generated according to the measurement section of the experiments of Reemts and Johannsen (2015) for an angle of attack of  $5^\circ$ . For this case, Figure 5.10 illustrates the formation of sheet cavitation and shedding of cloud cavitation on the hydrofoil for a cavitation number of  $\sigma_{\text{cav}} = 0.95$ . At time  $\Delta t = 0$  ms, the sheet cavitation fully elongated over the suction side of the hydrofoil and reached a length of about 50% of the hydrofoil's chord length. Re-entrant jets formed at time  $\Delta t = 15$  ms, pierced the sheet cavitation at different locations, and enabled the shedding of a cloud cavitation. After 25 ms, a cloud cavitation started to detach from the hydrofoil's surface. The cloud formation was attributable to a vortex forming on the suction side of the hydrofoil that surrounded the cavitation cloud. A new sheet cavitation formed at time  $\Delta t = 35$  ms, at the leading edge of the hydrofoil, while the cloud cavitation travelled further downstream and collapsed vertically above the trailing edge of the hydrofoil.

Figure 5.11 visualises the formation of a re-entrant jet and a cavitation cloud on the suction side of the NACA 0015 hydrofoil. The liquid volume fraction is plotted on a plane normal to the span width around the hydrofoil. Black arrows represent velocity vectors on this plane. From time  $\Delta t = 0$  ms to 5 ms, a sheet cavitation formed at the leading edge of the hydrofoil. A vortex generated after 5 ms at the downstream end of the sheet cavitation, grew, and travelled further upstream resulting in the generation of a re-entrant jet. The re-entrant jet flow between cloud cavitation and hydrofoil surface became apparent at time  $\Delta t = 20$  ms. As the vortex-induced flow around the cloud cavitation increased in extent, more vapour volumes connected to the cloud. After time  $\Delta t = 30$  ms, the vortex and the cavitation cloud moved vertically upwards and further downstream. Thereby, the cavitation cloud detached from the foil and travelled further downstream as well.

### 5.1 Euler-Euler Method



**Figure 5.10:** Cycle of generation of sheet cavitation followed by shedding and collapse of cloud cavitation around NACA 0015 at an angle of attack of  $5^\circ$  and a cavitation number of  $\sigma_{\text{cav}} = 0.95$



**Figure 5.11:** Formation of re-entrant jet and cloud cavitation around NACA 0015 at an angle of attack of  $5^\circ$  and a cavitation number of  $\sigma_{\text{cav}} = 0.95$

Figure 5.12 presents the generation of sheet cavitation and shedding of cloud cavitation on the NACA 0015 at an angle of attack of  $5^\circ$  and a cavitation number of  $\sigma_{\text{cav}} = 1.07$ . The overall behaviour of cavitation for this case was qualitatively similar compared to the case of  $\sigma_{\text{cav}} = 0.95$  (see Figure 5.10). Although, for  $\sigma_{\text{cav}} = 1.07$ , the maximum length of sheet cavitation and average volume of vapour were smaller. Moreover, cavitation clouds were not transported as far downstream as for  $\sigma_{\text{cav}} = 0.95$ .

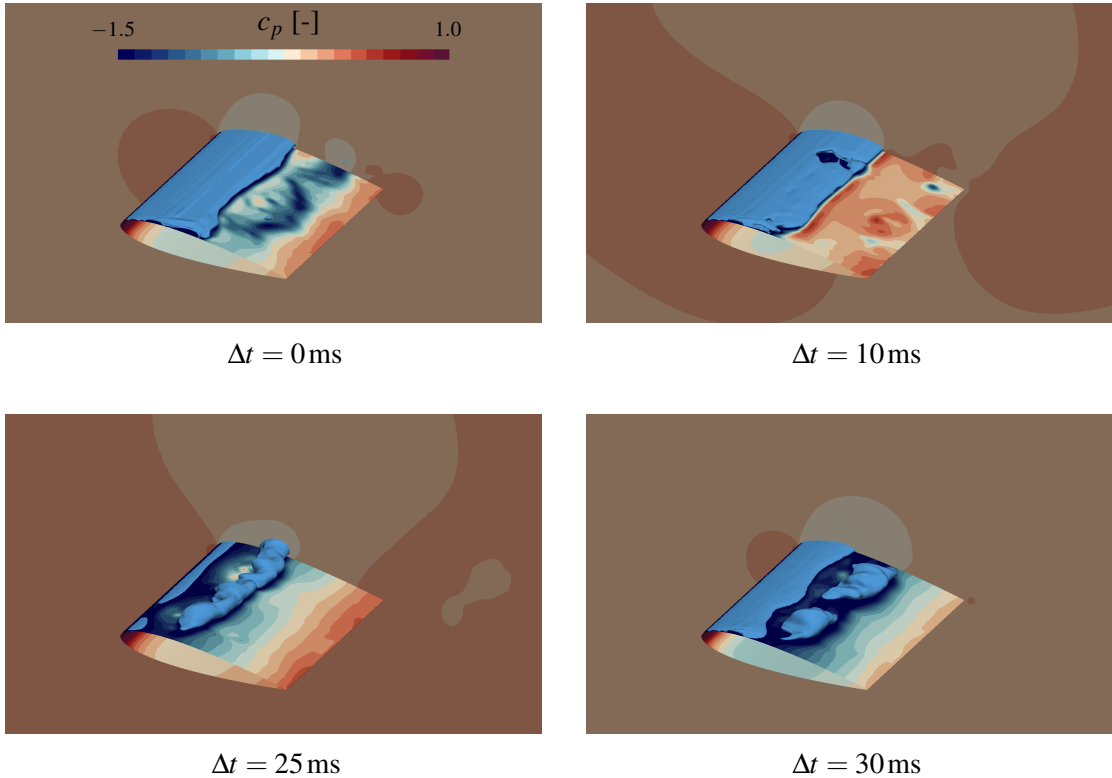


**Figure 5.12:** Cycle of generation of sheet cavitation followed by shedding and collapse of cloud cavitation around NACA 0015 hydrofoil at an angle of attack of  $5^\circ$  and a cavitation number of  $\sigma_{\text{cav}} = 1.07$

Figure 5.13 presents the cavitation behaviour on the hydrofoil at an angle of attack of  $5^\circ$  and  $\sigma_{\text{cav}} = 1.19$ . Contrary to the two smaller cavitation numbers, the average length of sheet cavitation and the time-averaged vapour volume were significantly smaller. Although cavitation clouds were formed, they were not transported as far downstream as for the smaller cavitation numbers. A cavitation cloud was formed after time  $\Delta t = 10$  ms and transported further downstream by the flow. Residuals of the cloud cavitation collapsed after time  $\Delta t = 12.5$  ms. In this case, the cloud cavitation collapsed near the hydrofoil surface before reaching about 50% of the hydrofoil's chord length.

## 5.1 Euler-Euler Method

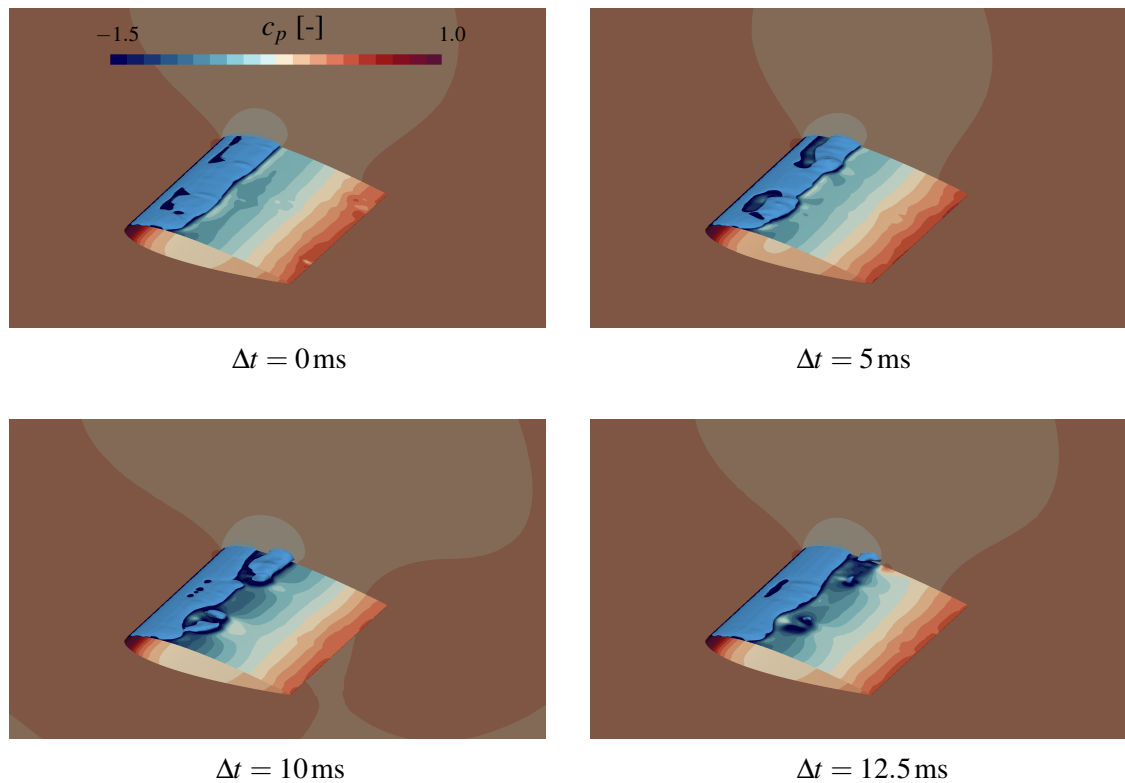


**Figure 5.13:** Cycle of generation of sheet cavitation followed by shedding and collapse of cloud cavitation around NACA 0015 at an angle of attack of  $5^\circ$  and a cavitation number of  $\sigma_{\text{cav}} = 1.19$

Figure 5.14 shows time histories of the lift coefficient on the NACA 0015 hydrofoil for cavitation numbers of 0.95, 1.07, and 1.19. All time sequences revealed a harmonic behaviour of the lift force attributable to the shedding of cloud cavitation. For the two higher cavitation numbers, a negative peak in lift force appeared owing to the collapse of cavitation structures on the suction side of the foil. Peaks in the lift force appeared less regularly for  $\sigma_{\text{cav}} = 0.95$ . In this case, collapses of cloud cavitation appeared further downstream, behind the trailing edge of the hydrofoil. Thereby, the pressure on the pressure side of the foil increased owing to cloud cavitation collapses. For  $\sigma_{\text{cav}} = 0.95$ , the comparison of frequency analyses of vapour volume and lift force shows that the most dominant frequency in the temporal progress of lift was 43.89 Hz. With low deviation, this frequency was close to twice the frequency of the vapour volume of 21.72 Hz. Further oscillations in lift appeared owing to the formation of sheet cavitation and re-entrant jets, which caused the detachment of sheet cavitation from the hydrofoil. In the numerical method used, high peaks in lift force can only be considered of a qualitative nature because the liquid phase was assumed to be incompressible and pressure decay during shock wave radiation was therefore not taken into account. For  $\sigma_{\text{cav}} = 1.07$  and 1.19, frequency analyses of lift force and vapour volume revealed similar frequencies to be characteristic.

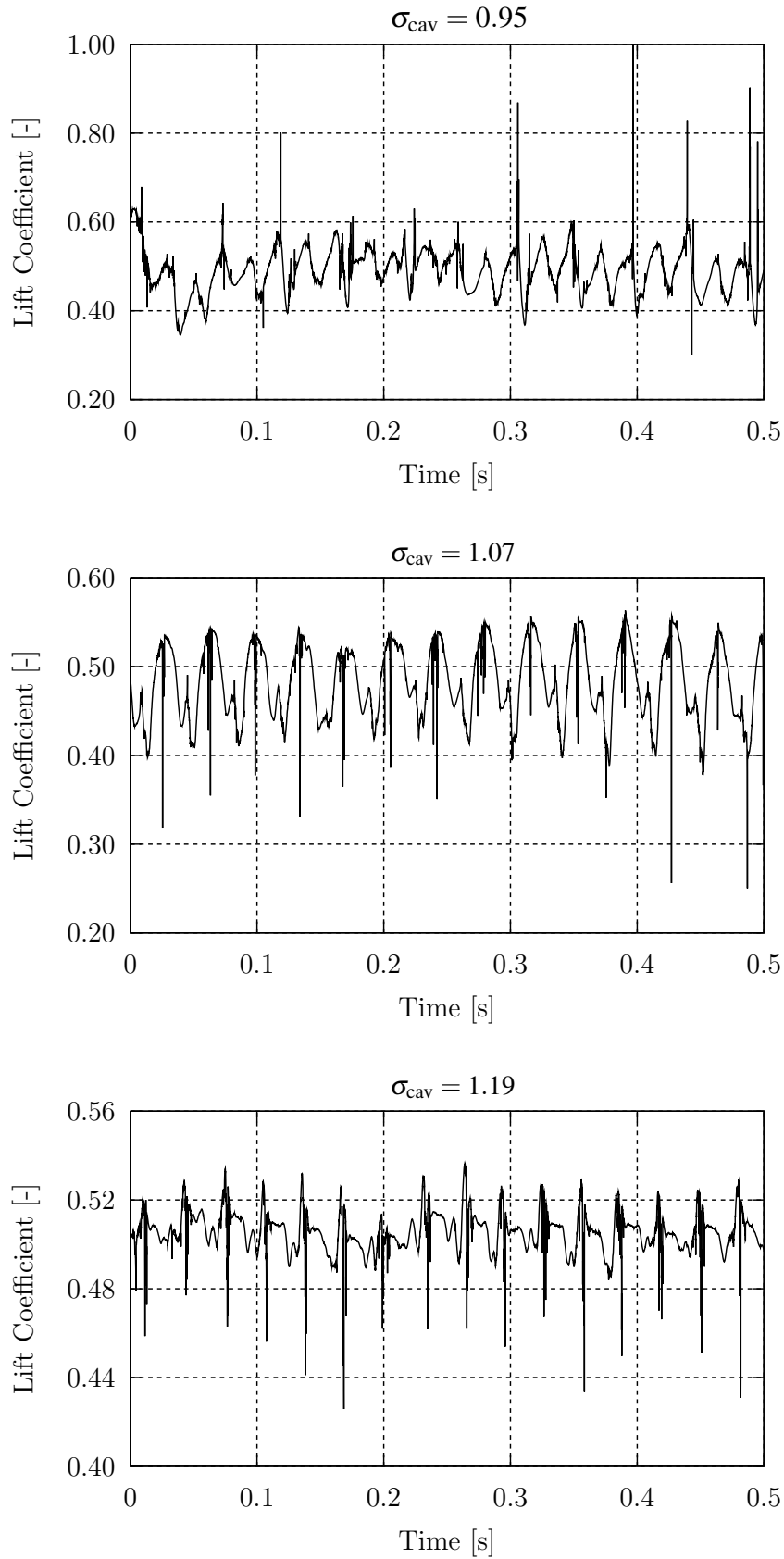


**Figure 5.14:** Sequences of time series of the lift coefficient on NACA 0015 for different cavitation numbers

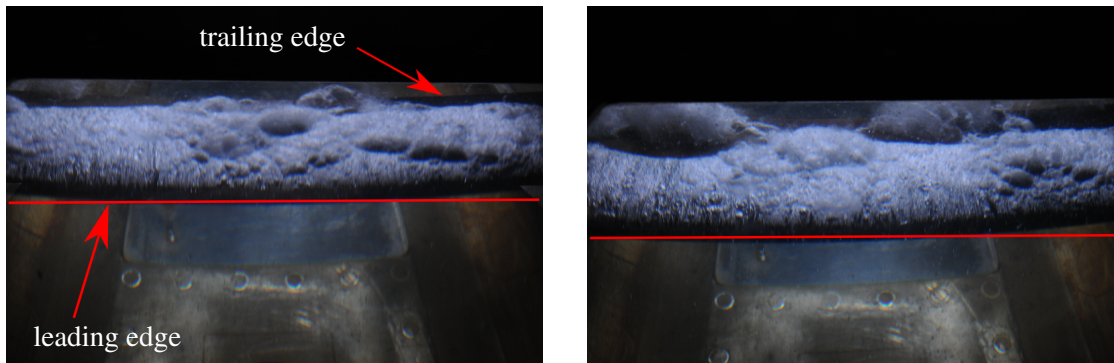
## 5.1 Euler-Euler Method

Table 5.8 lists numerical results for the cavitating flow around the NACA 0015 hydrofoil for the cavitation numbers 0.95, 1.07, and 1.19. For all three cavitation numbers, average lift coefficients deviated by less than 5%. On the other hand, the time-averaged normalised vapour volume deviated significantly between the three simulations. With decreasing cavitation number, more vapour volume was generated on average owing to the lower far field pressure. Frequencies related to the shedding of cloud cavitation increased for greater cavitation numbers. In case of  $\sigma_{\text{cav}} = 1.07$  and  $\sigma_{\text{cav}} = 1.19$ , the frequencies obtained from lift,  $f_L$ , and from vapour volume,  $f_v$ , agreed well. For a cavitation number of 0.95, the characteristic frequency of lift was twice the characteristic frequency of the vapour volume. For all three cavitation numbers, the FFT of the lift force furnished multiple characteristic frequencies. In case of  $\sigma = 0.95$ , the higher frequency at around 44 Hz was more pronounced than the frequency at around 22 Hz and amplitudes of force peaks were larger than for the higher cavitation numbers (see Figure 5.14). The Strouhal number,  $St_v$ , was calculated for the three cases using  $f_v$ , the chord length of the hydrofoil as characteristic length, and the inflow velocity as characteristic velocity.

**Table 5.8:** Numerical results related to lift and vapour volume for the flow around a NACA 0015 at an angle of attack of  $5^\circ$  for different cavitation numbers

$\sigma_{\text{cav}}$ [-]	$c_L$ [-]	$\bar{V}_v^*$ [ $10^{-4}$ ]	$f_L$ [Hz]	$f_v$ [Hz]	$St_v$ [-]
0.95	0.496	3.249	43.89	21.72	0.434
1.07	0.484	1.564	27.54	26.89	0.538
1.19	0.505	0.476	32.04	32.04	0.641

A similar dynamical behaviour of cavitation was observed in the experiments of Reemts and Johannsen (2015). Figure 5.15 displays sheet and cloud cavitation on the NACA 0015 hydrofoil in the cavitation tunnel of the HSVA. A perspective view onto the suction side of the hydrofoil's leading edge is presented. Here, the flow was from bottom to top such that sheet cavitation generated on the leading edge of the foil (see Figure 5.15). A red line marks the hydrofoil's leading edge. It should be noted that the leading edge is curved further upwards on the sides of Figure 5.15. This curved view is owing to the camera angle and the camera's lens. Sheet and cloud cavitation covered a large part of the trailing edge and the area upstream from it. Figure 5.15 (right) shows cavitation clouds detaching and travelling further downstream. The cavitation clouds were of significant volume and collapsed further downstream behind the hydrofoil. Accordingly, the overall behaviour of cavitation was similar to the simulated cavitation case of  $\sigma_{\text{cav}} = 0.95$ . Generation and extent of sheet cavitation and shedding of cloud cavitation agreed favourably with experimental observations.



**Figure 5.15:** Sheet and cloud cavitation around NACA 0015 in the cavitation tunnel of the HSVA, Reemts and Johannsen (2015)

### Erosion Prediction for Different Cavitation Numbers

To predict cavitation erosion, experimental methods involve coatings that are applied to a considered surface and it is assumed that erosion appears within regions where the coating is fully removed by collapses of single cavitation bubbles in the vicinity of the surface. Reemts and Johannsen (2015) developed a Soft-Ink coating technique to predict erosion. Contrary to other coating techniques, when exposed to cavitation, the coating was not removed but deformed in form of small pits in the coating surface.

The previous investigations showed the dependence of cavitation behaviour on the free stream pressure and therefore cavitation number. Although collapses of large cavitation structures may cause erosion on material surfaces, an increase of the time-averaged vapour volume does not necessarily lead to a higher risk of erosion. Cavitation structures will only cause erosion if bubble collapses take place repeatedly within the vicinity of a material surface.

For the NACA 0015 hydrofoil, numerical predictions of cavitation erosion were conducted using the microjet approach (see section 4.5.1). For the experimental erosion prediction, the Soft-Ink technique was used. Compared to erosion of a material, impact loads required to damage the Soft-Ink coating are supposedly smaller. First, to compare the numerical erosion prediction with the experimental prediction, a low yield strength of  $100 \text{ N/mm}^2$  was used in the microjet erosion model.

Figure 5.16 plots the coefficient of erosion prediction,  $c_{\text{ero,E}}$ , on the suction side of the hydrofoil for cavitation numbers of 0.95, 1.07, and 1.19 from top to bottom. For the two lower cavitation numbers, a region just downstream from the leading edge was predicted to be eroded. In both cases, during the shedding of cloud cavitation, the entire sheet cavitation detached from the leading edge and led to an erosion prediction in this area. At the moment of detachment of the cavitation cloud, cavitation bubbles are able to collapse owing to the abrupt increase of static pressure when re-entrant jets pierce the sheet cavitation. While for  $\sigma_{\text{cav}} = 0.95$  the prediction of erosion was mostly concentrated on the area downstream from the leading edge, for  $\sigma_{\text{cav}} = 1.07$  a second characteristic area of erosion was predicted at about 40 % to 50 % of

## 5.1 Euler-Euler Method

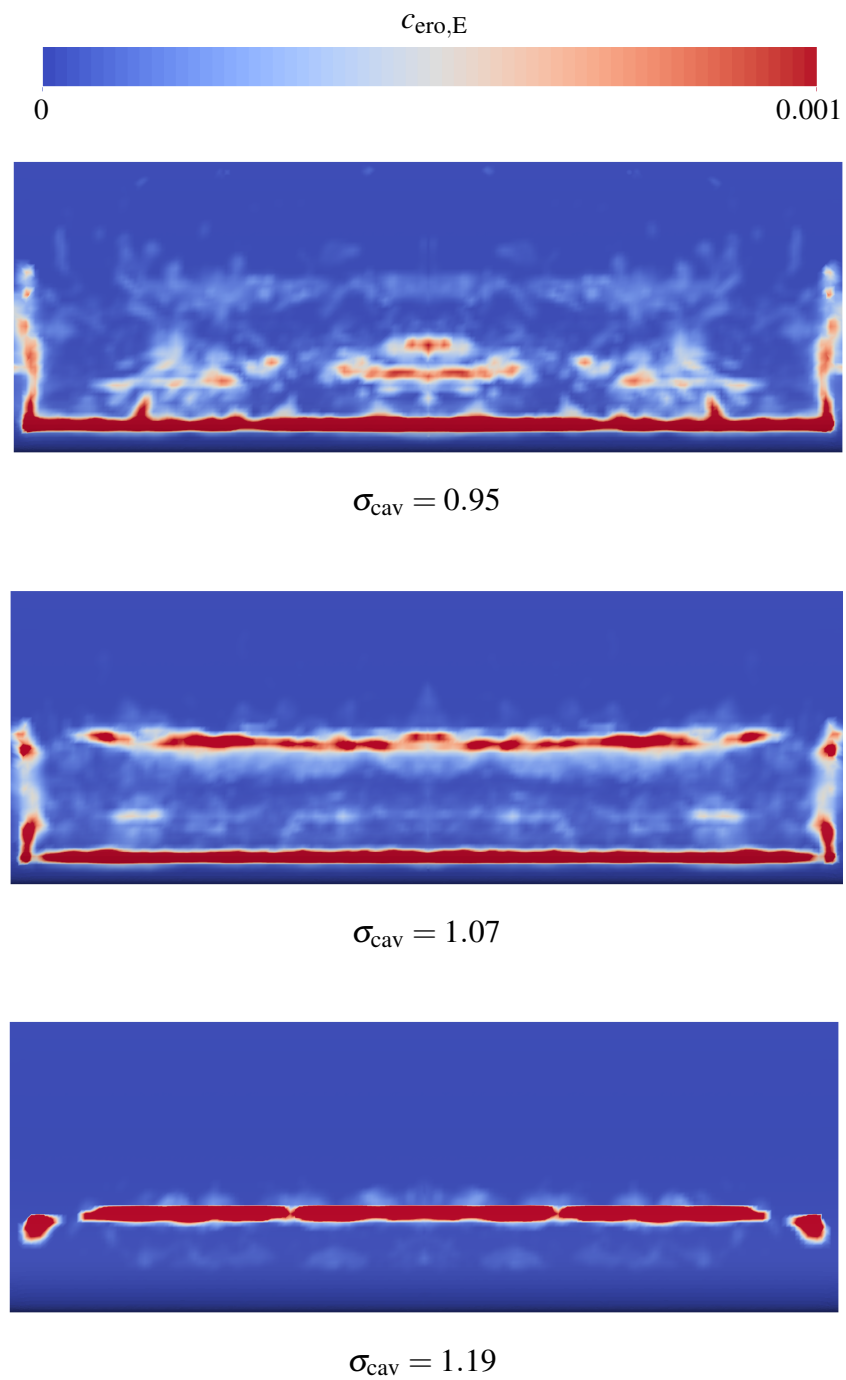


**Figure 5.16:** Numerical erosion prediction on the NACA 0015 for different cavitation numbers

chord length from the leading edge. In case of  $\sigma_{\text{cav}} = 1.19$ , the area behind the leading edge was predicted to be free of cavitation damage because the sheet cavitation was never fully shed from the foil. Here, a single region of high erosion potential was predicted at 30 % of chord length from the leading edge. In this case, the area predicted to be eroded was similar compared to the case of a cavitation number of 1.07. The predicted erosion potential for  $\sigma_{\text{cav}} = 1.19$  was in agreement with the positions of cloud cavitation collapses in the vicinity of the hydrofoil surface (see Figure 5.13 (c) and (d)). Because the overall volume of cavitation was smaller in this case and cloud cavitation did not travel further downstream, the predicted region of erosion was well circumscribed.

Reemts and Johannsen (2015) predicted cavitation erosion for an angle of attack of  $5^\circ$  and a cavitation number of  $\sigma_{\text{cav}} \approx 1.0$ . Figure 5.17 presents the experimentally obtained erosion pattern on the suction side of the hydrofoil. Figure 5.17 (left) shows the hydrofoil from top view with the leading edge at the bottom. During cavitation tests, circular pits formed on the hydrofoil surface. Most of these pits appeared in the red marked area in Figure 5.17 (left) between 20 % and 40 % of chord length downstream from the leading edge. Figure 5.17 (right) shows the NACA 0015 from detailed perspective view. A red circle marks a black isolated pit. The experimental erosion predictions agreed favourably with the numerical prediction for cavitation numbers of  $\sigma_{\text{cav}} = 1.07$  and 1.19 (see Figure 5.16). For these cavitation numbers, predicted erosion concentrated in the same area.

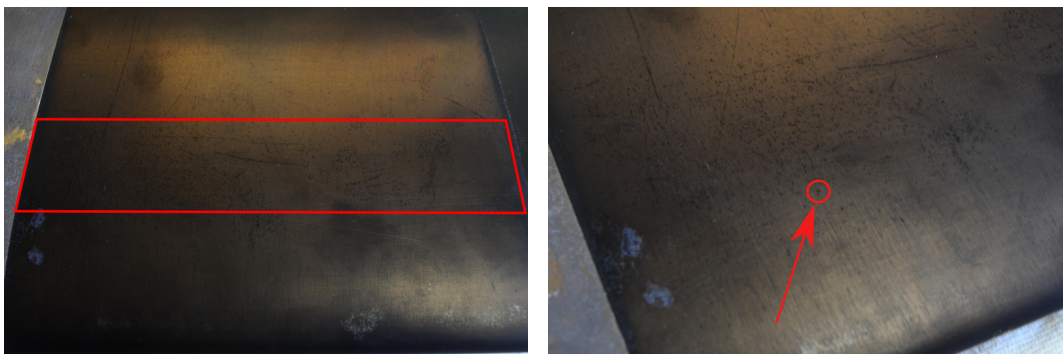


**Figure 5.17:** Circular pits in the coating of the NACA 0015 from top view (left) and detail view (right) provided by the HSVA, Reemts and Johannsen (2015)

The microjet erosion model enables erosion predictions for different materials. The yield strength of a considered material is, thereby, used to calculate the critical jet velocity (see (4.81)). Numerical predictions of erosion were conducted for  $\sigma_{\text{cav}} = 0.95$  with the previously used yield strength of  $100 \text{ N/mm}^2$  and a yield strength of  $400 \text{ N/mm}^2$  related to a material of high strength such as steel. Figure 5.18 depicts erosion predictions on the suction side of the NACA 0015 hydrofoil for the two different yield strengths. Results agreed well with the hypotheses of the microjet erosion model. Accordingly, less erosion impacts were predicted

### 5.1 Euler-Euler Method

for the higher yield strength. Furthermore, the predicted area exposed to erosion was more defined for the higher yield strength and concentrated mostly within a region close to the hydrofoil's leading edge. Presumably, materials of lower yield strengths can be exposed to multiple and larger areas of erosion.

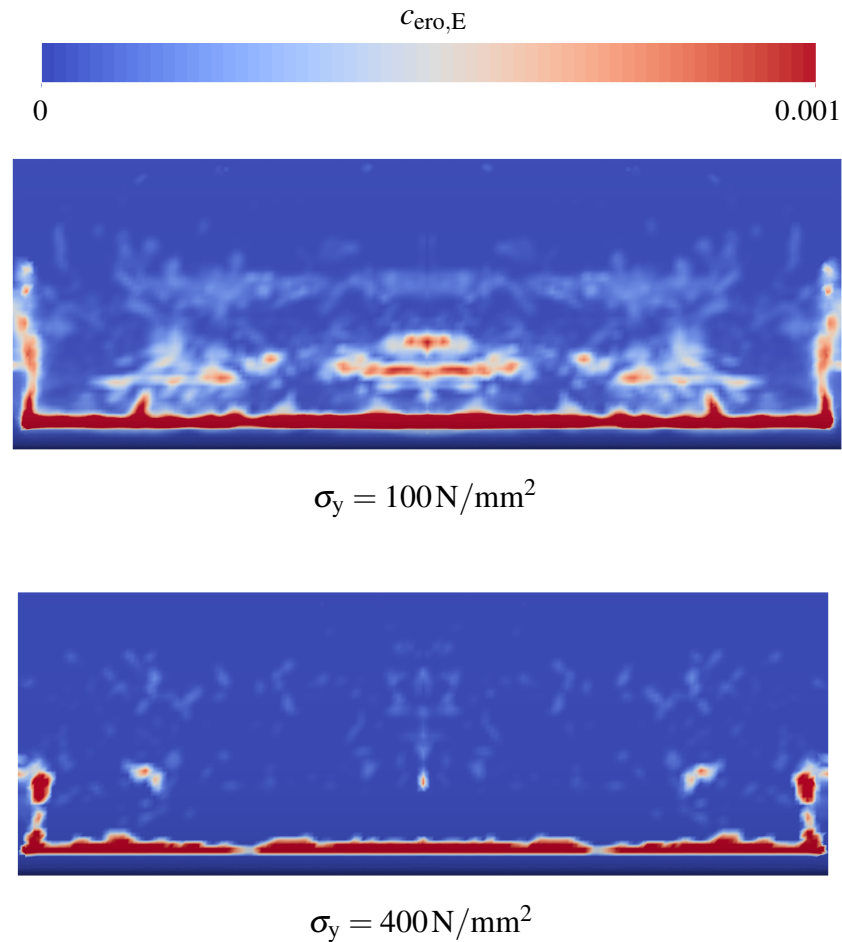


**Figure 5.18:** Numerical erosion prediction on the NACA 0015 for  $\sigma_{cav} = 0.95$  and two different yield strengths

### 5.1.3 Internal Nozzle Flow

To study quantitative aspects of cavitation-induced erosion, such as incubation times and erosion rates, simulations of the flow passing through an axisymmetric vertical nozzle as it subjects a target plate to cavitation erosion were carried out. Franc and Riondet (2006), Franc et al. (2011), and Franc et al. (2012) investigated the internal nozzle flow experimentally and analysed the erosion damage caused by collapses of unsteady cavitation structures. The experiment serves as a benchmark to investigate cavitation erosion because of the characteristic axisymmetric erosion caused on the bottom plate of the test section. Figure 5.19 sketches the nozzle geometry. The nozzle consisted of a 16 mm diameter vertical cylinder and a horizontal target plate, which formed the bottom of a 2.5 mm high radial channel. With an average velocity of 31 m/s the flow passed through the vertical cylinder and, at the connection with the channel, the small radius of  $R_{\text{con}} = 1.0$  mm ensured that flow separated and radially accelerated. Periodic sheet and cloud cavitation generated at the radius, travelled further downstream, and collapsed in regions of higher liquid pressure. The pressure at the outlet of the test section of 10.1 bar caused aggressive cavitation collapses leading to erosion on the target plate. In the experiments of Franc and Riondet (2006), Franc et al. (2011), and Franc et al. (2012) bubble collapses caused erosion pits on the bottom surface, which was used as an erosion sensor. The area of highest erosion concentrated within a radial distance of about 21 to 22 mm from the centre axis. Mihatsch et al. (2011, 2012, 2015), Mihatsch (2017), Koukouvinis et al. (2014), Mottyll (2017), and Mouvanal et al. (2018) numerically investigated the flow passing through the nozzle under different operating conditions. Part of the present work was published in Peters et al. (2015a,c).

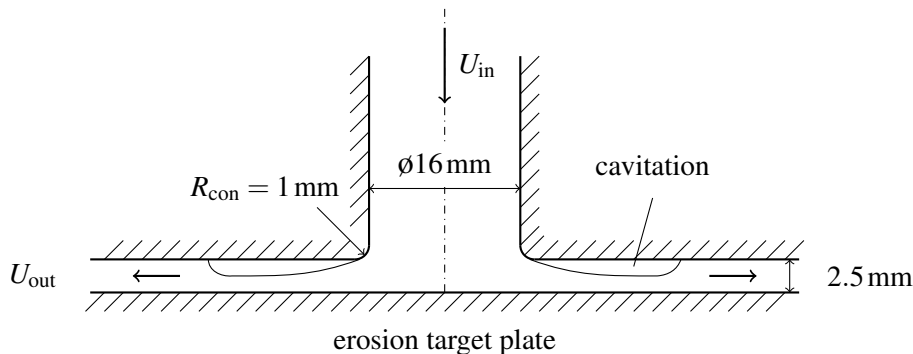
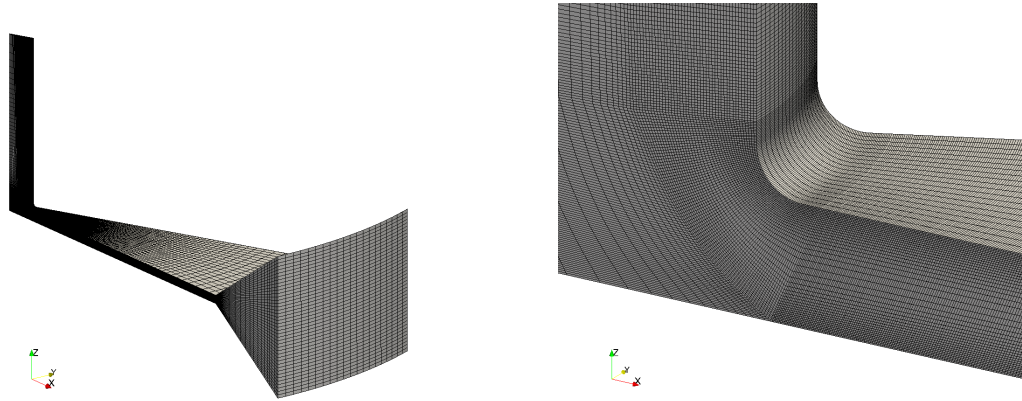


**Figure 5.19:** Sketch of axisymmetric nozzle geometry and flow conditions

To validate the Eulerian-based erosion models with respect to predict areas exposed to erosion, the cavitating flow through the nozzle was simulated. The computational effort was reduced by modelling only a  $17.45^\circ$  part of the full  $360^\circ$  geometry of the nozzle. Periodic boundary conditions were specified for the side boundaries of the domain yielding periodicity in circumferential direction. An inlet velocity of 31 m/s was defined at the top of the domain. At the end of the outlet part, a pressure reservoir was attached in a radial distance of 100 mm from

## 5.1 Euler-Euler Method

the centre axis. The pressure at the outlet was set to 10.1 bar according to the downstream pressure in the experiments of Franc and Riondet (2006). The top and bottom boundaries of the domain were specified as no-slip wall boundaries.



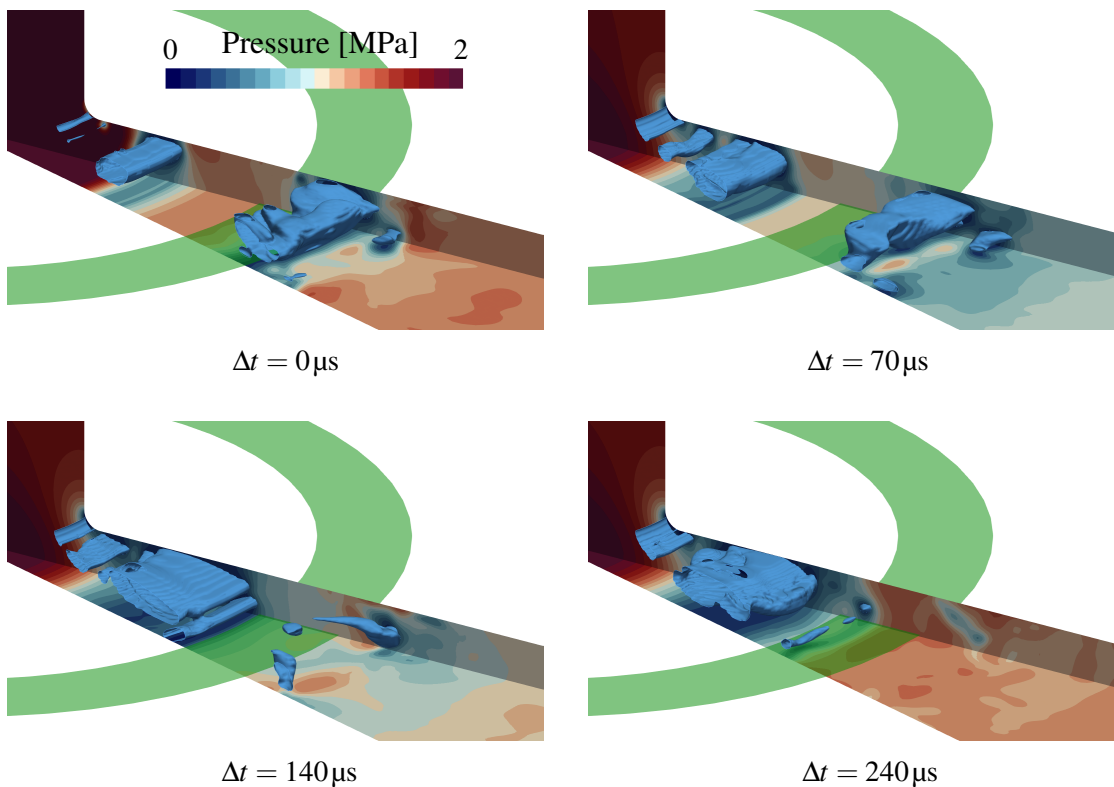
**Figure 5.20:** Perspective view of the entire solution domain (left) and detail view of the region around the connecting radius (right) for grid G3 of  $2.09 \cdot 10^6$  cells

Figure 5.20 (left) presents the mesh of the entire simulation domain. In the previous work of Peters et al. (2015a,c) a Cartesian mesh was generated to discretise the nozzle's geometry. In this work, a cylindrical mesh was generated around the rotation axis of the nozzle geometry, which is symmetric in circumferential direction. In contrast to a Cartesian grid, influences of the grid on the flow in circumferential direction were minimised. For the present case, cell sizes increased in radial direction and towards the centre of the outlet channel. Figure 5.20 (right) displays the mesh around the connecting radius. To predict cavitation inception, a high spatial resolution of the radius was applied. Near wall cells on top and bottom wall boundaries were generated with respect to dimensionless wall distances of  $n^+ \approx 30$  to 300 to enable the use of logarithmic wall functions. Maximum CFL numbers were below 2 for all cases with average CFL numbers of about  $2.5 \cdot 10^{-3}$ . The cavitation model of Sauer and Schnerr (2000) modelled processes of vapourisation and condensation. For the present simulations, in preparation to compare with a case using an Euler-Lagrange approach, where a nuclei density of  $n_0 = 1 \cdot 10^{11} \text{ m}^{-3}$  and nuclei of radius  $R_0 = 1 \cdot 10^{-5} \text{ m}$  were used, the same parameters were specified in the cavitation model of Sauer and Schnerr (2000).



**Figure 5.21:** Circumferential cross section of the nozzle domain showing the velocity magnitude on the left half and the pressure on the right half for grid G2 of  $0.723 \cdot 10^6$  cells

Figure 5.21 shows a time instance of the axial cross section of the rotationally symmetric nozzle geometry. The left half plots the velocity magnitude and the right half plots the pressure in the domain. Although only pressures between 0 and 2 bar are depicted, minimum and maximum pressures were outside of this range. Pressures below zero occurred at the connection between top cylinder and radial channel. A stagnation point flow developed owing to the flow from top onto the bottom boundary. In the stagnation point, the pressure was of about 20 bar. Around the 1 mm radius, the flow accelerated into the channel and vortices generated in the flow. Thereby, in the vicinity of the radius, the pressure decreased to values lower than the vapour pressure, which caused the growth of cavitation structures that travelled radially outwards. Further downstream, the static pressure increased again, leading to collapses of these cavitation structures.



**Figure 5.22:** Formation, shedding, and collapse of cavitation structures in the nozzle from perspective view for grid G2 of  $0.723 \cdot 10^6$  cells

Figure 5.22 displays the formation, shedding, and collapse of cavitation structures in the nozzle from a perspective view. The pressure is plotted on the bottom and a cyclic side boundary of the domain. Light blue isosurfaces mark a vapour volume fraction of 10% and a light green ring marks the area of highest measured erosion in a radial distance from 19 to 25 mm from the centre axis. From times  $\Delta t = 0 \mu\text{s}$  to  $\Delta t = 70 \mu\text{s}$ , cavitation structures are shown to be transported through the green marked area and collapsing just behind it at roughly the half of the channel height. At the same time, a new cloud cavitation formed downstream from the

## 5.1 Euler-Euler Method

connecting radius and grew to its maximum size at a time of about  $\Delta t = 140\mu\text{s}$ . Small vapour clouds detached from the larger structure, travelled into the region above the green marked area, and collapsed in the vicinity of the surface at time  $\Delta t = 240\mu\text{s}$ . Although different cavitation structures collapsed further downstream from the green marked area, as shown below, they were not responsible for erosion because their collapse distances from the bottom wall were too large. The simulated behaviour of cloud cavitation agreed with experimental observations of Franc and Riondet (2006) who reported a mean cavity length of about 25 mm. In the simulations, the cavitation structures seemed chaotic and unsteady. However, frequency analyses identified harmonic processes.

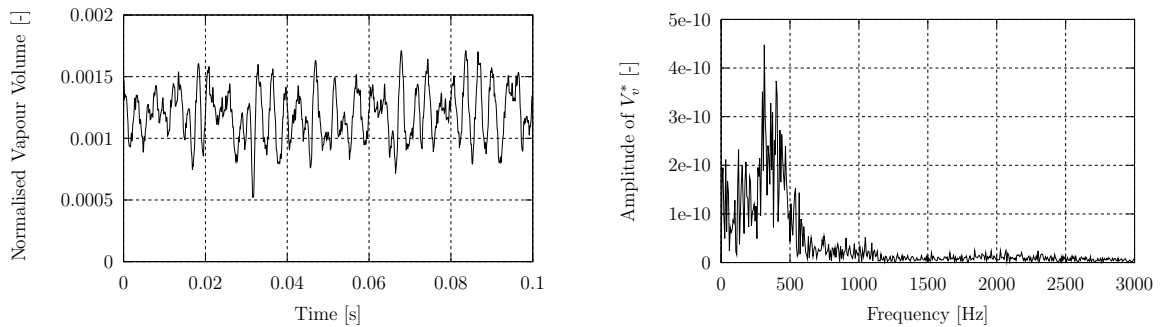


**Figure 5.23:** Sequence of time series (left) and FFT (right) of normalised vapour volume in the domain

Figure 5.23 plots a sequence of the time series of the normalised vapour volume in the domain,  $V_v^*$ , (left) and its FFT (right). The behaviour of cavitation in the nozzle was less harmonic than for the flow around the NACA 0015 hydrofoil (see Figure 5.8 (left)). Low frequency oscillations of the vapour volume were superposed by high frequency oscillations. Multiple characteristic frequencies were identified, because the time series was not purely harmonic. The lowest characteristic frequency was found between 300 and 400 Hz (see Figure 5.23 (right)). Because of the high amplitude in the FFT, this frequency was related to the shedding and collapse of the largest cavitation structures. In addition, higher dominant frequencies of lower amplitudes appeared at just over 1000 Hz and its first superharmonic at over 2000 Hz. These lower amplitudes denoted the growth and collapse of smaller vapour structures.

To further examine the sources of different frequencies, the average pressure in a virtual sensor was analysed. Analogue to Franc et al. (2011), a virtual circular sensor of 3.2 mm diameter was positioned on the bottom of the geometry with its centre at a radial distance of 24.5 mm from the centre axis of the nozzle. The average pressure taking into account all numerical faces on the bottom boundary, whose face centres were located within the sensor area, was evaluated for each time step. Figure 5.24 shows a sequence of the time series of the averaged pressure in the numerical sensor (left) and its FFT (right). Collapses of cavitation structures generated high impact pressure peaks at high frequencies. Figure 5.24 (right) reveals the characteristic frequencies related to time series of the pressure. In contrast to the FFT of the vapour volume

(see Figure 5.23 (right)) the frequency of just over 1000 Hz and its first superharmonic at over 2000 Hz were more pronounced for the virtual pressure sensor. Presumably, the high pressure peaks were related to collapses of smaller cavitation structures that were repeated at high frequencies.

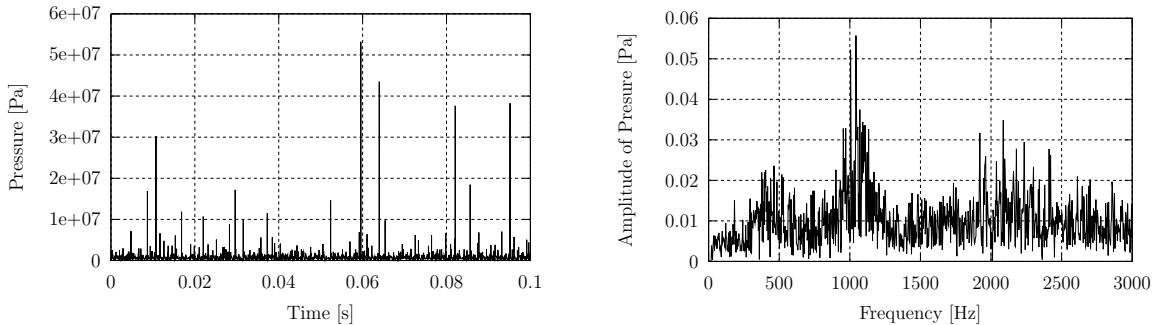


**Figure 5.24:** Sequence of time series (left) and FFT (right) of average pressure in numerical pressure sensor

Mihatsch et al. (2011) investigated the present case numerically using a compressible density-based solver with a barotropic cavitation model. They identified characteristic frequencies of cavitation shedding of 408 Hz and two well defined frequencies at 1139 and 1182 Hz. Mihatsch et al. (2015) obtained four dominant frequencies for the same case (denoted as '20 bar case' owing to the stagnation pressure of the incoming flow). They reported the lowest frequency at 350 Hz, a second characteristic frequency at 1100 Hz, and the first harmonic mode of the second characteristic frequency at about 2200 Hz. Mottyll (2017) simulated the present case using a similar density-based solver and identified frequencies of 450, 1550, 2920, and 8800 Hz. Especially the frequencies identified by Mihatsch et al. (2011, 2015) agreed favourably with the cavitation shedding frequencies obtained in this work (see Figure 5.23 (right), Figure 5.24 (right)).

The microjet erosion model was used to predict erosion potential on the bottom surface of the nozzle geometry. To calculate the critical velocity  $u_{\text{crit}}$  (see equation (4.81)), a yield strength of  $\sigma_y = 400 \text{ MPa}$  was specified according to the yield strength of stainless steel 316 L that was used in the experiments of Franc and Riondet (2006). To verify the mechanisms of the numerical erosion prediction, correlations between cavitation dynamics and erosion impacts were analysed. Figure 5.25 displays the numerical domain from perspective lateral view. A reflection of the bottom boundary with respect to the cyclic side boundary was generated. The upper part of the domain shows the pressure on the cyclic side boundary and on the bottom boundary. The black colour on the reflected bottom boundary identifies the numerically predicted erosion impacts that take place within the respective time step, while the grey colour identifies non-impacted regions. At time  $\Delta t = 0 \mu\text{s}$ , a large cavitation structure, surrounded by a low pressure region, touched the bottom boundary. Because the pressure near the vapour structure was low, no erosion impacts were predicted. As the cloud started to compress and

## 5.1 Euler-Euler Method

the pressures at its outer extents, especially upstream, increased, erosion impacts were predicted (Figure 5.25  $\Delta t = 35\mu\text{s}$  to  $\Delta t = 70\mu\text{s}$ ). According to the hypotheses of the microjet erosion model, it is assumed that cavitation bubbles on the outer extents of the cloud started to collapse in the vicinity of the bottom boundary. Afterwards, pressures around the cavitation cloud decreased again, which led to a reduction of the number of predicted impacts. Note that, even though the regarded cavitation structures collapsed further downstream, collapses only resulted in predictions of erosion impacts when these collapses took place close enough to the bottom surface.

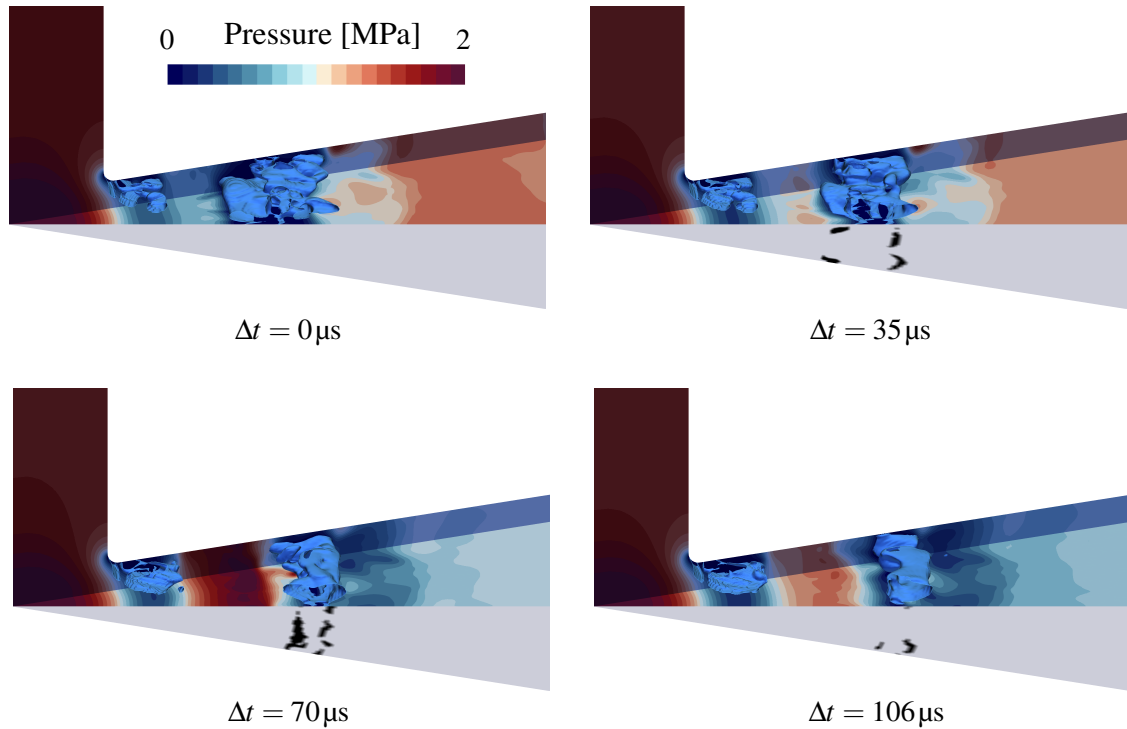


**Figure 5.25:** Correlations between cavitation behaviour and numerical erosion prediction on the bottom boundary of the nozzle from perspective view

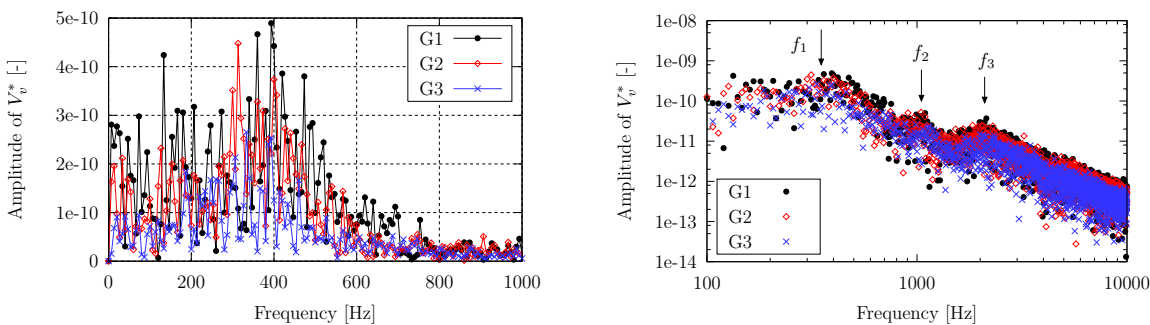
### Grid Dependence Study

For the present case, a systematic grid dependence study for the entire mesh was performed using a refinement ratio of  $r_k = \sqrt{2}$ , resulting in meshes of  $2.6 \cdot 10^5$  (G1),  $7.23 \cdot 10^5$  (G2), and  $2.090 \cdot 10^6$  (G3) control volumes. Table 5.9 lists general data of the numerical meshes and the calculated time-averaged vapour volume in the domain for each case. Time steps,  $\Delta t$ , were adjusted for each mesh to obtain the same CFL number. The time-averaged vapour volume in the domain for the coarsest grid, G1, deviated by over 20 % from the time-averaged vapour volume calculated using grid G3; for a simulation using grid G2, deviated by only 0.7 %. Although monotonic convergence was not achieved, deviations between simulations on grids G2 and G3 were small.

**Table 5.9:** Numerical results of the cavitating flow in the axisymmetric nozzle on different grids

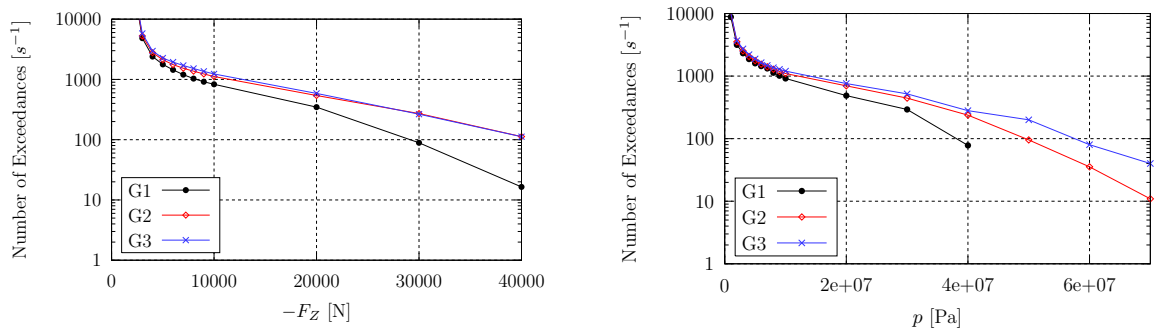
grid	control volumes [-]	$\Delta t$ [ns]	$\bar{V}_v$ [ $1 \cdot 10^{-8} \text{ m}^3$ ]
G1	$0.260 \cdot 10^6$	500	2.656 (-20.1%)
G2	$0.723 \cdot 10^6$	354	3.345 (+0.7%)
G3	$2.090 \cdot 10^6$	250	3.322

Figure 5.26 shows FFTs of the normalised vapour volume in the domain for the simulations on grids G1, G2, and G3. Although the temporal progress of vapour volume seemed chaotic, in each simulation, three characteristic frequencies were identified. In Figure 5.26 (left) a characteristic frequency between 300 and 400 Hz can be seen while in Figure 5.26 (right) characteristic frequencies at just over 1000 and 2000 Hz are found.

**Figure 5.26:** Frequency analysis of normalised vapour volume in the domain calculated on different grids plotted on a linear scale (left) and on a double logarithmic scale (right)

Collapses of cloud cavitation caused high amplitude pressures. In the present case, vertical forces on the bottom boundary and pressures in the numerical pressure sensor were studied for different grids. Figure 5.27 (left) plots the number of exceedances of vertical forces on the bottom boundary of the domain. Forces exceeding 10000 N deviated considerably between simulation G1 and the other two simulations. Simulations using grids G2 and G3 agreed favourably over the entire range of forces. Figure 5.27 (right) plots the number of exceedances of averaged pressures in the numerical pressure sensor. Pressures calculated using grid G1 deviated significantly from the other two simulations for the entire range of pressures larger than  $1 \cdot 10^7$  Pa. Furthermore, using this grid no pressure peaks higher than  $4 \cdot 10^7$  Pa were calculated. Computed pressures for G2 and G3 agreed favourably for values up to  $4 \cdot 10^7$  Pa. Pressures larger than  $4 \cdot 10^7$  Pa appeared more frequently in the simulation using the finest grid, G3.

## 5.1 Euler-Euler Method



**Figure 5.27:** Exceedances of values of vertical force on the bottom boundary (left) and of pressure in numerical sensors (right)

A more quantitative statistical erosion prediction is obtained by evaluating the erosion impacts in circumferential direction of the nozzle at different radial intervals. Franc and Riondet (2006) measured the depth of erosion in terms of mass loss on this area of the target plate. Based on an interval length of 1 mm, their moving averaging technique obtained the distribution of penetration depth over the radial distance from the centre axis of the nozzle. For comparison purposes, an interval length of the same size was chosen to sum the erosion coefficient,  $c_{\text{ero},E}$ , for all faces on the bottom surface. Figure 5.28 plots the erosion coefficient,  $c_{\text{ero},E}$ , calculated on the bottom boundary versus the radial distance from the centre axis of the domain,  $r$ , for simulations using grids G1, G2, and G3. All three distributions identified the highest erosion potential in a radial distance between 20 mm and 22 mm distance from the centre axis. Distributions of erosion potential for simulations G2 and G3 agreed well for all radial intervals, while the distribution for G1 showed larger deviations.

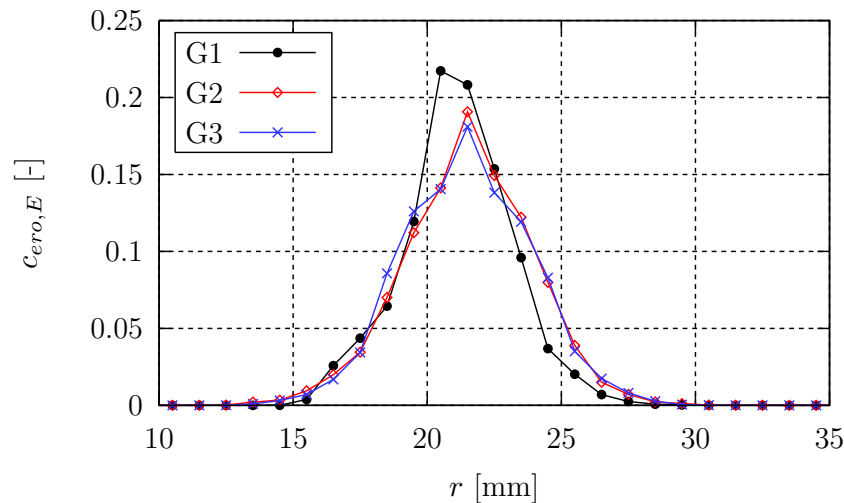


**Figure 5.28:** Numerical erosion prediction using the microjet model for simulations on three different grids

Besides the exceedance of high pressures, simulations using grids G2 and G3 agreed well regarding time-averaged vapour volume and frequencies related to the dynamics of vapour volume in the domain, the force on the bottom boundary, and the radial distribution of erosion

prediction. For further investigations, grid G2 was chosen to simulate cavitation and predict erosion using other methods.

### Comparison of Numerically Predicted Erosion with Pit Measurements

For Euler-Euler simulations, erosion was numerically predicted using two different hypotheses based on (i) a microjet impact and (ii) the pressure caused by a spherical bubble collapse (see section 4.5.1). To assess erosion, both models require that the computational domain near the surface is evaluated for the presence of vapour within cell zones of radius  $R_{CZ}$  that are generated for every face of the regarded surface, Peters et al. (2015a,c). The influence of the size of these cell zones was investigated with regard to the numerical erosion prediction using the microjet erosion model. Figure 5.29 depicts the prediction of normalised erosion potential,  $c_{ero,E}^* = c_{ero,E}/c_{ero,E,max}$ , using different  $R_{CZ}$ .  $c_{ero,E,max}$  is the maximum value of the erosion coefficient  $c_{ero,E}$  over all radial intervals. Only simulations using larger cell zone sizes of  $R_{CZ} = 1$  mm and  $R_{CZ} = 2$  mm predicted erosion distributions that deviated considerably from the other ones. These false predictions were results of the large cell zones taking into account vapour volumes far away from the regarded surface. For all simulations using cell zones of  $R_{CZ} \leq 0.5$  mm, the area of predicted erosion was smaller, narrower, and qualitatively similar. For  $R_{CZ} \leq 0.5$  mm, all predictions found the area of maximum erosion between  $r = 21$  mm and  $r = 23$  mm radial distance from the centre axis of the nozzle geometry.

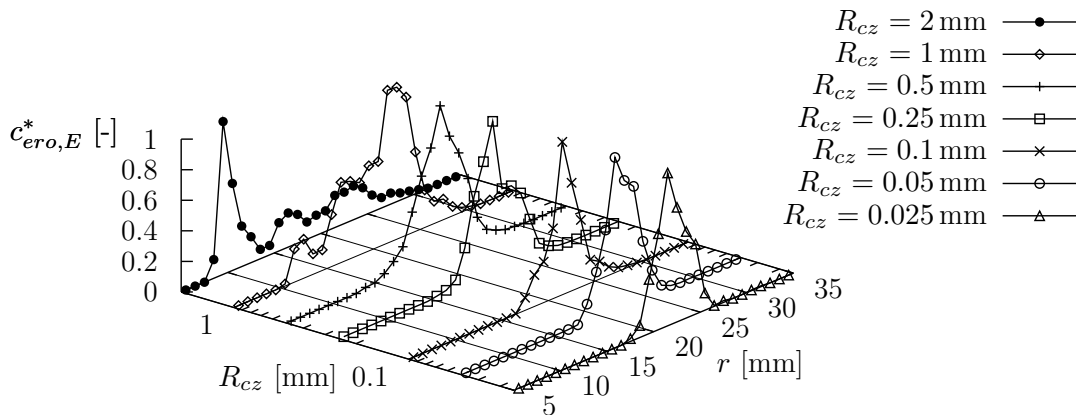


**Figure 5.29:** Radial distribution of normalised erosion coefficient,  $c_{ero,E}^*$ , applying the microjet model and using different cell zone radii,  $R_{CZ}$ , in a 3D plot

Figure 5.30 shows the predictions of erosion potential,  $c_{ero,E}$ , for cell zones of radii  $R_{CZ} = 0.5$  mm and  $R_{CZ} = 0.025$  mm. Both predictions are qualitatively similar, but the erosion prediction using the smaller cell zone predicts a narrower area to be eroded from about 17 to 26 mm radial distance from the centre axis. In the simulations, the boundary layer thickness of the non-cavitating, fully developed, turbulent flow was about  $\delta_{BL} \approx 0.2$  mm in the area of highest erosion potential. In the present case, choosing a cell zone radius,  $R_{CZ}$ , equal to the boundary layer thickness led to a reasonable erosion prediction. Although the prediction of

## 5.1 Euler-Euler Method

eroded areas was fairly similar, a considerably higher number of impacts was predicted for larger cell zones because the probability of a predicted impact was increased. Using a cell zone radius of  $R_{cz} = 0.5$  mm, approximately  $1 \cdot 10^8$  numerical impacts were calculated per second, while for  $R_{cz} = 0.025$  mm,  $4 \cdot 10^5$  impacts per second were obtained.

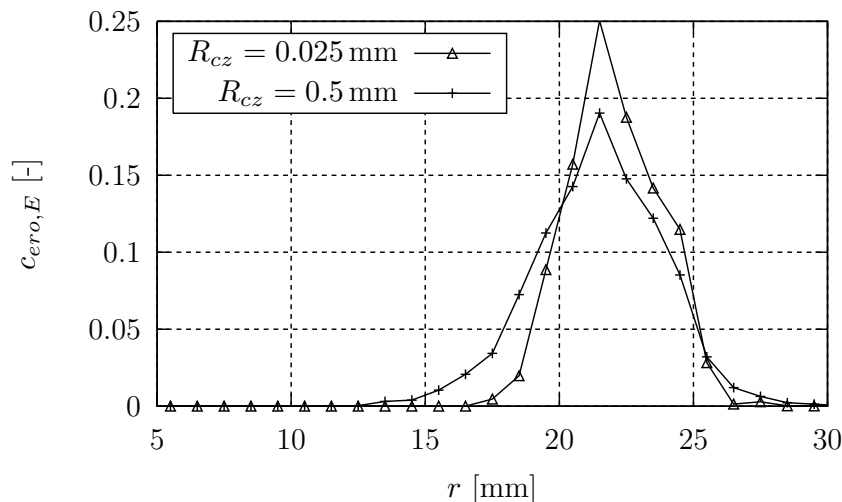


**Figure 5.30:** Radial distribution of erosion coefficient,  $c_{ero,E}$ , applying the microjet model and using two different cell zone radii,  $R_{cz}$ , in a 2D plot

Radial distributions of erosion predictions using the two Eulerian approaches – the microjet model and the spherical collapse model (see section 4.5.1) – were compared to measured erosion depths of Franc and Riondet (2006). While more impacts per time were predicted when using larger cell zone sizes, the erosion predictions for smaller cell zones agreed better with measured erosion patterns. As a compromise between a faster convergence and a more accurate prediction, cell zone sizes of a radius of  $R_{cz} = 0.05$  mm were used for both numerical erosion models. Figure 5.31 plots distributions of normalised erosion potential,  $c_{ero,E}^*$ , using the two Eulerian approaches to predict erosion and measured erosion depths of Franc and Riondet (2006). Within the accuracy of the radial averaging process, both numerical approaches predict the location of highest erosion fairly well. Both approaches predict a larger area to be eroded than the area measured by Franc and Riondet (2006). The main reason for this is that impact intensities in both models were only linearly superposed to obtain the distributions of erosion potential. However, it may be expected that erosion depends non-linearly on impact pressures. For the spherical collapse model, the number of impacts per second was more than two orders of magnitude higher than for the microjet model because the impact pressures calculated from (see equation (4.85)) were on average much larger.

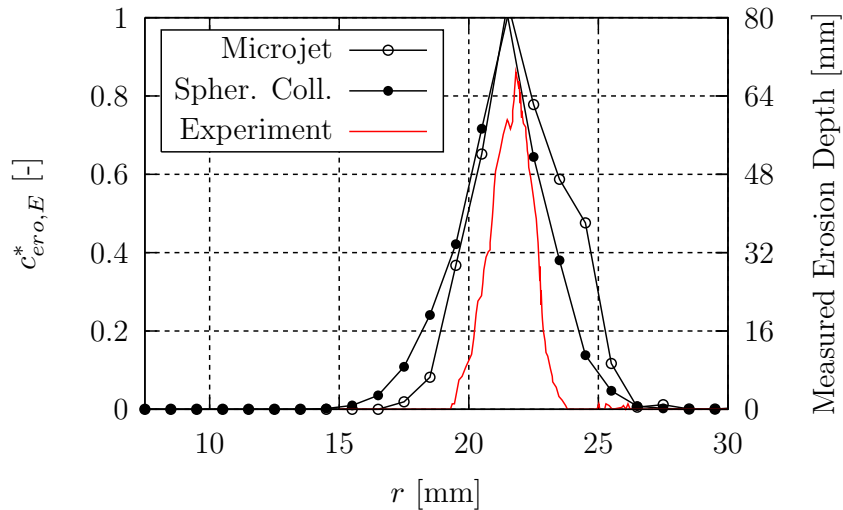


**Figure 5.31:** Numerical erosion prediction using microjet model and spherical collapse model compared to measured erosion depths of Franc and Riondet (2006)

Figure 5.32 depicts the eroded bottom plate from the experiment of Franc et al. (2011) (left) and the numerical prediction of areas exposed to erosion (right). To visualise the erosion potential on a larger area, the numerical domain was reflected multiple times in circumferential direction around the centre axis because only  $17.45^\circ$  of the entire nozzle geometry were modelled for the simulation. A red circle marks the area of highest erosion in the experiment. The numerical prediction agreed favourably with the erosion pattern in the experiments and the main area of erosion was adequately predicted in the simulation.

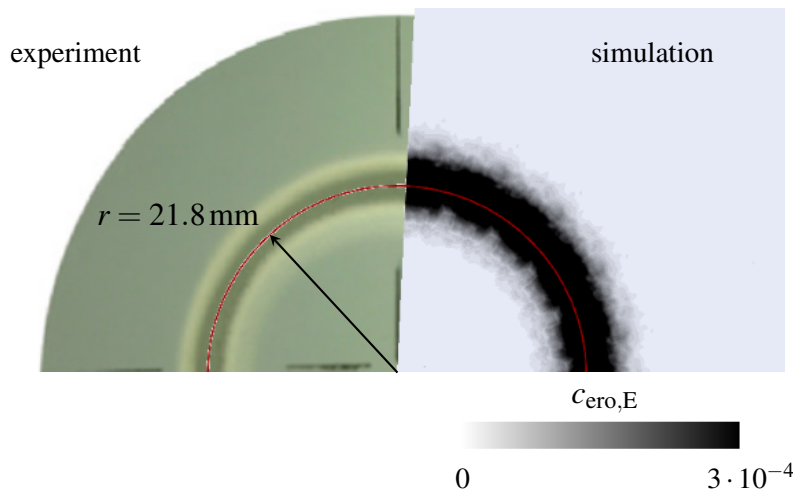


**Figure 5.32:** Top view of erosion on bottom plate from experiment of Franc and Riondet (2006) (left) and numerical prediction of erosion potential on bottom boundary (right)

### 5.1.4 Propeller in Oblique Flow

Ship propellers are exposed to inhomogeneous flow because of the ship's wake, manoeuvres driven by the ship, changes of current, and waves. Under these permanently changing operating conditions, correlating cavitation and cavitation damage is rather difficult. Model tests serve to study these correlations under simplified conditions but introduce scale effects and are, furthermore, expensive. Therefore, numerical predictions of cavitation behaviour and the assessment of cavitation erosion are demanded. In model tests, a simplified case of inhomogeneous flow is obtained by positioning a propeller at an inclined angle of attack towards the flow. This oblique flow scenario serves to compare experimental and numerical results. This section deals with the numerical prediction of the flow around a ship propeller in oblique cavitating flow and of the cavitation-induced erosion on the propeller's blades. The propeller P1225 was not designed to be applied for a ship but as a benchmark propeller for model tests to experimentally investigate cavitation and cavitation-induced erosion on the propeller's blades. Both axial and oblique flow around the propeller, under non-cavitating and cavitating conditions, were simulated to address effects of incidence angle and cavitation. Propeller open water simulations were compared to model tests carried out by Bernitt and Heinke (1983). For oblique flow cases, flow quantities, cavitation and erosion predictions were compared to measured results of Heinke et al. (2013). Part of the results shown in this section originate from the work of Peters et al. (2018a).

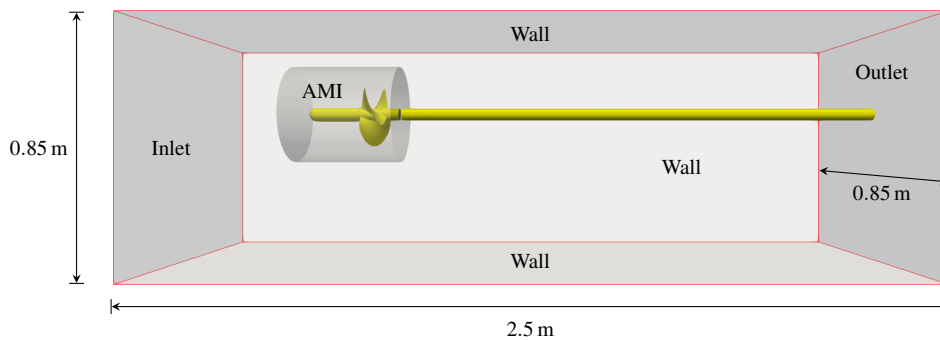
#### Propeller in Axial Homogeneous Flow

Prior to investigations of cavitation and erosion on the propeller P1225 in oblique flow, a validation of the simulation of the propeller in open water was carried out. Table 5.10 lists particulars of the SVA cavitation tunnel and properties of the propeller. Bernitt and Heinke (1983) used a propeller diameter of 0.25 m, while Heinke et al. (2013) used a diameter of 0.24 m.

The simulation domain was modelled according to the measurement section of the cavitation tunnel in which the cavitation experiments were carried out, Heinke et al. (2013). Figure 5.33 shows the simulation domain of the propeller for the simulations in axial homogeneous flow. An Arbitrary Mesh Interface (AMI), also known as sliding interface, between a stationary region (stator) and a rotating region (rotor) realised the rotation of the propeller. The stator comprised the far field simulation domain including all non-rotating parts outside of the AMI; the rotor of a cylinder around the propeller, part of the shaft, and the hub inside the AMI. All parts in the rotor region rotated according to the propeller's revolution rate of the considered case. For the hub inside the rotor, a counter-clockwise velocity boundary condition was specified to counteract the rotation of rotor. Between rotor and stator, a permeable interface was introduced at the surface of the cylinder. Rotation of the propeller was performed at the beginning of every time step. Flow variables were interpolated at the AMI in every outer iteration of the flow solution.

**Table 5.10:** Particulars of the SVA cavitation tunnel and properties of the P1225 propeller

property	symbol	
propeller diameter	$D$ [m]	0.24, 0.25
pitch ratio at $0.7R$	$P_{0.7}/D$ [-]	1.0595
blade area ratio	$A_E/A_0$ [m]	0.95
blade chord length at $0.7R$	$c_{0.7}$ [m]	0.1854
hub diameter ratio	$d_h/D$ [-]	0.1857
number of blades	$Z$ [-]	3
scale	$\lambda$ [-]	5.25
direction of rotation		clockwise
channel breadth	$B$ [m]	0.85
channel height	$H_{ch}$ [m]	0.85

**Figure 5.33:** Perspective view of the simulation domain for the P1225 propeller in axial homogeneous flow

Walls with no-slip boundary conditions were defined around the propeller according to the walls of the cavitation tunnel. An inlet boundary was defined 0.7 m upstream from the propeller plane. The pressure was defined at the outlet boundary, 1.8 m downstream from the propeller plane. To avoid additional flow separation, the propeller shaft was extruded until reaching the outlet boundary of the domain. In contrast to the experimental setup, the gearbox behind the propeller was not modelled because its influence on the flow towards the propeller was supposed to be negligible. At sides, top, and bottom walls, no-slip boundary conditions were defined. The propeller shaft was positioned in the centre between the side walls, at a distance of 0.3 m from the top. A smooth interpolation between rotor and stator region was assured by applying refinements and using similar grid topologies on both sides of the AMI. At all hub, propeller, and shaft surfaces no-slip wall boundary condition were fulfilled.

Figure 5.34 shows the mesh in the propeller plane normal to the propeller's rotation axis and a cross sectional view of the grid around a single blade. Refinements at the blades and

## 5.1 Euler-Euler Method

the connection of blade roots to the rotating shaft part were applied. The mesh was also refined to some extent at the interface between outer and inner region. Here, control volumes were generated orthogonally to the AMI surfaces at the inner and outer region to ensure good interpolation between the two AMI boundaries.

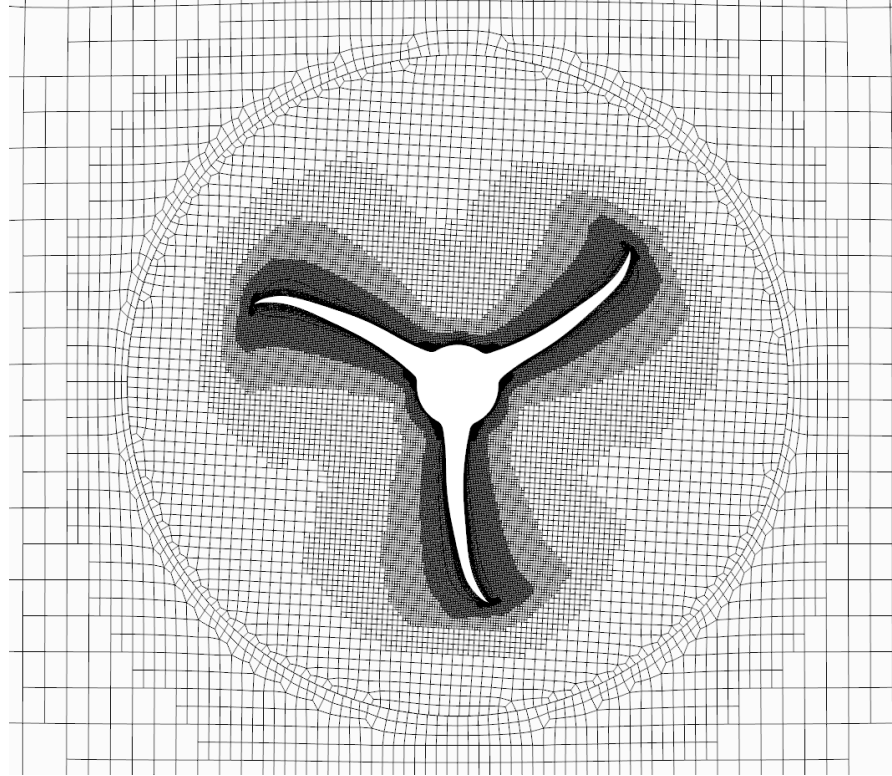


**Figure 5.34:** Front view of grid topology and refinement regions at the rotor-stator interface and around the propeller in the propeller plane

An important aspect of the numerical grid is the generation of near-wall control volumes. Whether fully resolving the boundary layer or using a logarithmic wall function, specific cell sizes need to be generated in the normal direction to the wall. For a propeller, Vaz et al. (2015) investigated the effects of a resolution of the boundary layer by generating near-wall cells with dimensionless wall distances of  $n^+ < 1$  compared to using logarithmic wall functions with  $n^+ > 30$ . They showed that with different codes the prediction of cavitation differed significantly only when using different cavitation models or different parameters in the cavitation models. Using the same cavitation models but different approaches for the wall (full resolution or logarithmic wall function) results agreed favourably. It is assumed that the influence of the wall-approach on the macroscopic cavitation behaviour for a propeller is small. Owing to difficulties in the generation of near-wall cells according to  $n^+ < 1$  at the blade tips, cells near the walls were generated yielding  $n^+ \approx 70 - 100$  on all blade surfaces in order to use logarithmic wall functions. Figure 5.35 shows the mesh around the propeller blade in overall view (left) and detail view of the root (right). Refinements were generated at the blades and around the roots of the blades. Prism layers were generated around all blades.

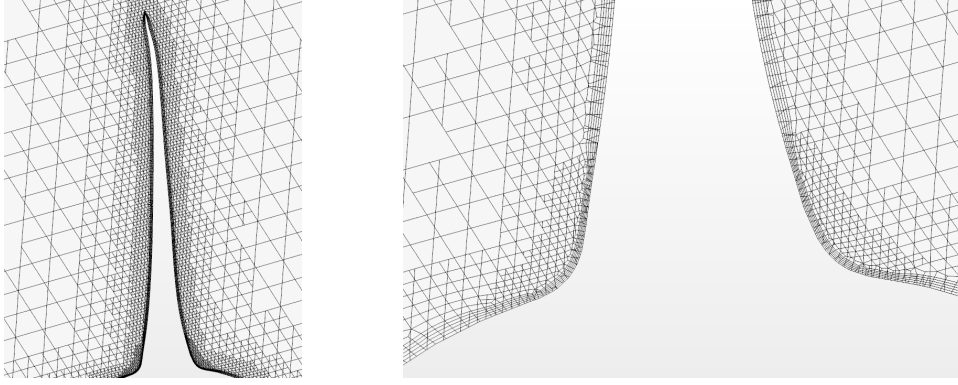


**Figure 5.35:** Grid around a propeller blade (left) and prism layer grid near the root of the blade (right); taken from Peters et al. (2018a)

Spatial discretisation schemes and interpolation of variables at control volumes or faces were of second-order. For time integration, the Crank-Nicolson scheme was used which is implicit and of second-order. Time steps were set corresponding to an average Courant number of  $CFL \approx 1.5 \cdot 10^{-3}$  and a maximum Courant number of  $CFL < 2$ . Table 5.11 lists the investigated cases of homogeneous flow.

**Table 5.11:** Parameters for open water conditions of P1225

$\alpha_{AoA}$	$J$ [-]	$u_\infty$ [m]	$n_p$ [ $s^{-1}$ ]	$\sigma_{cav}$ [-]
$0^\circ$	0.7813	5.62	29.97	11.27
	0.7989	6.23	32.47	9.17

The advance ratio is defined as:

$$J = \frac{u_\infty}{n_p D}. \quad (5.5)$$

$u_\infty$  is the velocity in the far field.  $n_p$  is the propeller's revolution rate and  $D$  the propeller diameter. To prevent cavitation, the far field pressure at the outlet was increased to  $p_\infty = 180.3$  kPa, corresponding to the tunnel pressure of the experiments and resulting in high cavitation numbers.

Figure 5.36 shows the axial flow around the propeller. The flow decelerated in front of the hub and accelerated behind the propeller owing to the propeller rotation. High gradients of pressure and velocity were generated at the tips of the blades caused by pressure differences between suction side and pressure side. Flows at no-slip boundaries decelerated owing to friction effects and evolved into boundary layer flows.

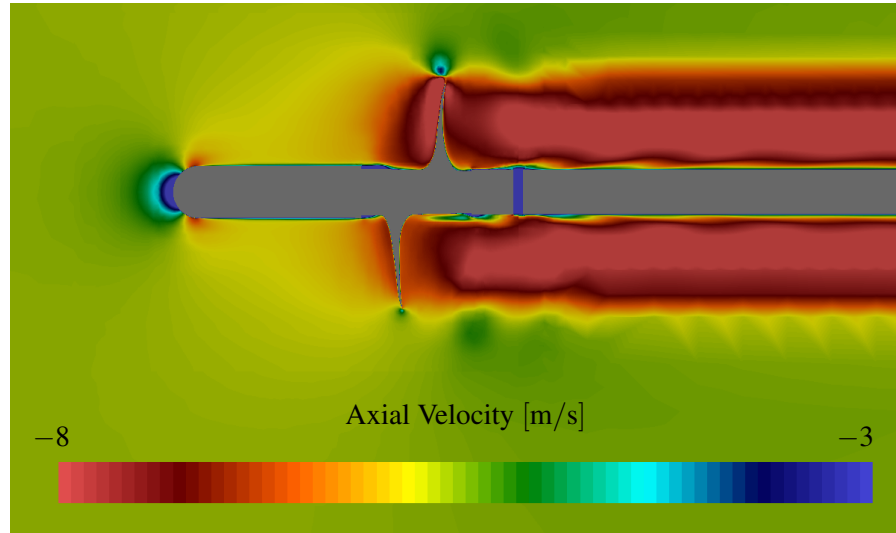


**Figure 5.36:** Axial velocity field around the P1225 propeller for  $J = 0.7813$  in homogeneous flow

Figure 5.37 shows start sequences of the converging time series of thrust coefficient,  $K_T$ , (left) and torque coefficient,  $K_Q$ , (right) of the propeller. The thrust coefficient is defined as:

$$K_T = \frac{T}{\rho n_p^2 D^4}, \quad (5.6)$$

and the torque coefficient as:

$$K_Q = \frac{Q}{\rho n_p^2 D^5}. \quad (5.7)$$

$T$  is the thrust and  $Q$  the torque on all blades of the propeller, the rotating part of the shaft, and the hub. Oscillations of thrust and torque were small compared to the averages.

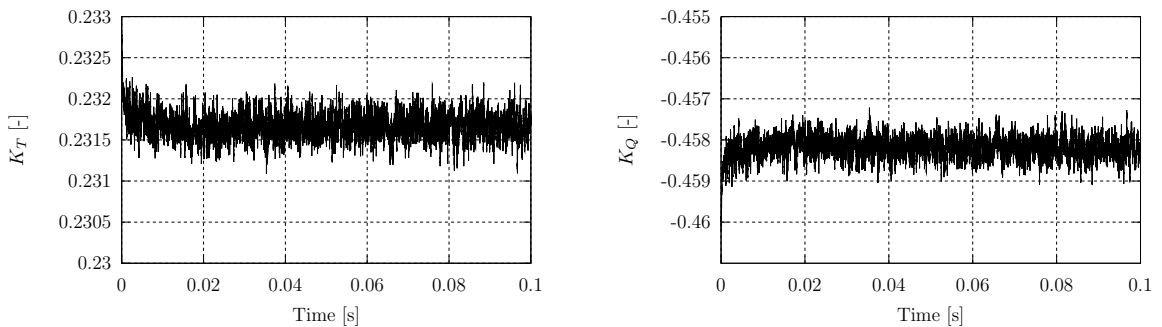


**Figure 5.37:** Start sequence of time series of thrust coefficient (left) and torque coefficient (right) for  $J = 0.7813$

The case of  $J = 0.7813$  was simulated on three different numerical meshes. A grid convergence study was conducted for thrust and torque of the propeller to estimate the influence of

spatial discretisation in preparation for the simulations of cavitating flow. The grid topology in the stator region was similar for all three grids. At the interface between rotor and stator regions, a good transition from coarser to finer cells was assured for all meshes. Refinements in the rotor region were applied consistently on all surfaces of the propeller, the hub, and parts of the shaft.

**Table 5.12:** Results from grid dependence study for P1225 propeller in axial homogeneous flow

grid	control volumes	$K_T$ [-]	$10K_Q$ [-]
G1	$0.84 \cdot 10^6$	0.2442 (+3.52 %)	0.4814 (+3.19 %)
G2	$1.89 \cdot 10^6$	0.2317 (-1.78 %)	0.4582 (-1.78 %)
G3	$5.07 \cdot 10^6$	0.2359	0.4665

Table 5.12 lists grid properties and results from these simulations. Relative differences  $\varepsilon_\phi$  with  $\phi$  as either  $K_T$  or  $K_Q$  were calculated for simulations on grid G2 and G1 compared to those obtained on grid G3, which comprised the largest number of control volumes. The differences are listed in parentheses in Table 5.12. Results from these simulations were close to each other, and deviations were well below 4 % for grid G1 and below 2 % for grid G2.

The open water cases from Table 5.11 were compared to experimental results of Bernitt and Heinke (1983). Table 5.13 lists comparable experimental and numerical results. Experimental results were obtained from open water tests using a propeller with a diameter of  $D = 0.25$  m operating at a revolution rate of  $n_p = 30$  1/s. Note that the propeller diameter in these tests deviated from the one in the tests conducted by Heinke et al. (2013). The inlet velocity of the simulation was configured to obtain the same advance ratios as in the experiment. For an advance ratio of  $J = 0.7813$ , values of  $K_T$  and  $K_Q$  between simulation and experiment deviated less for the simulation on grid G3 than for the simulation on grid G2. For the simulation on grid G1,  $K_T$  deviated more than for the other two simulations, while  $K_Q$  deviated less. The larger deviations of  $K_Q$  may be attributable to the transition of laminar to turbulent flow in the tunnel, which could not be properly predicted with the turbulence models used in the simulations. This influenced the calculation of friction, which has a larger effect on torque than on thrust.

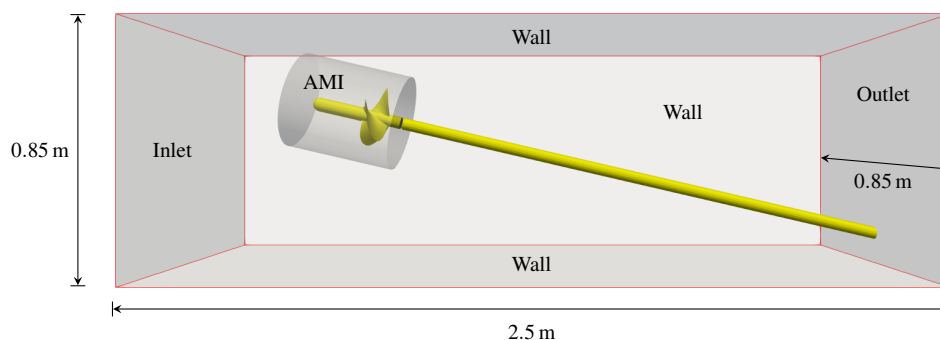
### Propeller in Oblique Homogeneous Flow Without Cavitation at $\alpha_{AoA} = 13^\circ$

The propeller was investigated in oblique flow under non-cavitating and cavitating conditions. In the numerical domain, the propeller was positioned in the same way as in the experimental tests of Heinke et al. (2013), at an angle of attack of  $\alpha_{AoA} = 13^\circ$ . Figure 5.38 depicts the simulation domain of the propeller in oblique flow. The appendage driving the propeller and containing the gearbox was not modelled because its influence on the flow surrounding the

**Table 5.13:** Results of thrust and torque for P1225 in axial homogeneous flow

$J$ [-]	case	$K_T$ [-]	$10K_Q$ [-]
0.7813	simulation G1	0.2442 (+3.73 %)	0.4814 (-1.21 %)
	simulation G2	0.2317 (-2.61 %)	0.4582 (-5.37 %)
	simulation G3	0.2359 (+0.84 %)	0.4665 (-3.66 %)
	experiment	0.2354	0.4873
0.7989	simulation G2	0.2220 (-3.10 %)	0.4433 (-5.82 %)
	experiment	0.2268	0.4742

propeller was assumed to be negligibly small. The same rotor meshes were used as for homogeneous flow. The stator mesh was adjusted with regard to the oblique flow. Grid lines were, therein, aligned with the dominant flow direction to minimise numerical diffusion.

**Figure 5.38:** Perspective view of simulation domain for the P1225 propeller in oblique flow at  $\alpha_{AoA} = 13^\circ$ 

To estimate effects caused by oblique flow and by cavitation, two cavitating cases and one non-cavitating case were investigated at an angle of attack  $\alpha_{AoA} = 13^\circ$  as listed in Table 5.14.

**Table 5.14:** Parameters for P1225 in oblique flow conditions

$\alpha_{AoA}$	$J$ [-]	$u_\infty$ [m]	$n_p$ [ $s^{-1}$ ]	$\sigma_{cav}$ [-]
$13^\circ$	0.8009	5.760	29.97	10.994
	0.8009	5.760	29.97	1.464
	0.8208	6.396	32.47	0.963

In an axial homogeneous flow, forces on a propeller blade do generally not oscillate over one revolution. However, in a cavitation tunnel, the flow is generally not absolutely homogeneous.

Amongst others, disturbances are mainly caused by the tunnel walls, the propeller's position, asymmetries in front of the test section, and gravity. In an oblique flow, the blade's angle of attack continuously changes over one revolution. This results in large oscillations of the axial and the lateral forces on the blades and affects the propeller's thrust and torque.

For a propeller in oblique flow, the propeller's thrust is understood as the force in direction of the propeller's rotation axis. Figure 5.39 plots sequences of time series of the thrust generated by a single propeller blade for angles of attack of  $\alpha_{AoA} = 0^\circ$  (black) and  $\alpha_{AoA} = 13^\circ$  (red) at comparable advance ratio.  $t$  is the time and  $T$  is the period of one propeller revolution. In both cases, the average thrust was similar, but the amplitudes of force oscillations differed significantly. The thrust oscillations for  $\alpha_{AoA} = 0^\circ$  were attributable to the change of distance of the propeller blade to the tunnel walls and the changing influence of gravity within one revolution. The amplitude was smaller than 1% compared to the average thrust. For an angle of attack of  $\alpha_{AoA} = 13^\circ$ , the amplitude of the thrust oscillations was close to 50% of the average thrust. These high amplitudes were a consequence of the change in the effective angle of attack during one propeller revolution.

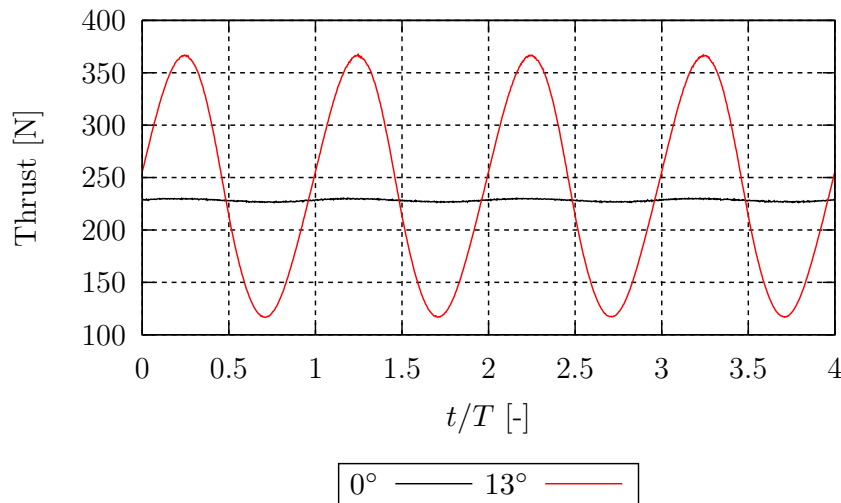


**Figure 5.39:** Comparison of thrust generated by one propeller blade for  $\alpha_{AoA} = 0^\circ$  and  $\alpha_{AoA} = 13^\circ$

### Propeller in Oblique Homogeneous Flow With Cavitation at $\alpha_{AoA} = 13^\circ$

For cavitating flows around propellers, even more attention has to be given to spatial and temporal discretisation. Regions of cavitation appearance have to be refined further to better predict cavitation extent and especially cavitation inception. Mesh regions which are too coarse may either lead to earlier inception because of sharpened geometrical edges or to later inception by damping high gradients of flow quantities because of numerical diffusion. In contrast to non-cavitating flows around propellers, temporal discretisation cannot solely be

## 5.1 Euler-Euler Method

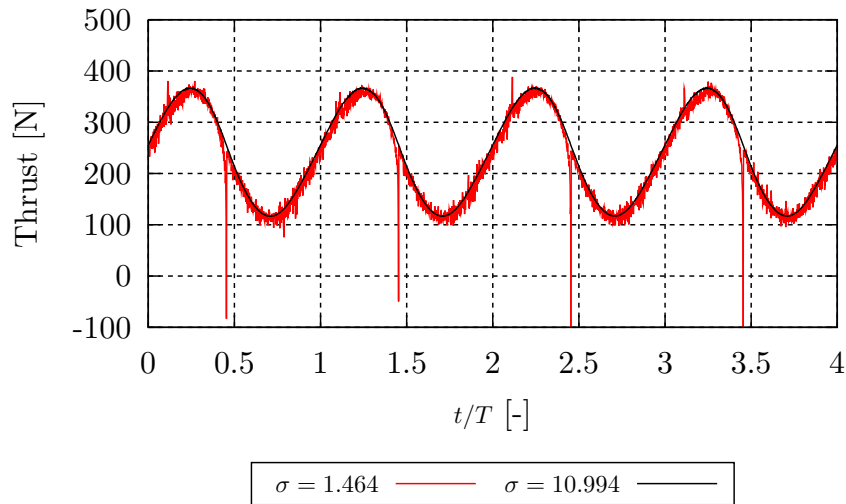
defined by the blade rotation angle per time step, but with regard to the resolution of the behaviour of macroscopic cavitation. At first, the implicit Crank-Nicolson scheme was used for time integration.

As a first estimation, Peters et al. (2018a) used the numerical grids from Table 5.12 to simulate the oblique, cavitating flow around the propeller at an angle of attack of  $13^\circ$ . Table 5.15 lists results of the grid dependence study for  $\sigma_{\text{cav}} = 1.464$  and  $J = 0.8009$  from Peters et al. (2018a). Here, three grids without additional refinements at blade tips or roots were used. Values of forces, torque, and time-averaged normalised vapour volume converged monotonically. As the propeller was operating in oblique flow, the axial force generated in direction of the flow is then calculated as  $F_X = T \sin(\alpha_{\text{AoA}}) - F_L \cos(\alpha_{\text{AoA}})$ , where  $\alpha_{\text{AoA}}$  is the angle of attack and  $F_L$  is the lateral force on the propeller referred to its body-fixed coordinate system.  $K_X$  is the axial force coefficient related to the force in flow direction,  $F_X$ . Force and torque values obtained on grids G1 and G2 were compared to results obtained on grid G3. Axial force and torque deviated by less than 2.1 % for grid G1 and by less than 1 % for grid G2. Although monotonic convergence was achieved, the time-averaged normalised vapour volume obtained from different grids deviated rather largely. It is concluded that axial force and torque were only slightly affected by further refinements, while cavitation behaviour was influenced more significantly.

**Table 5.15:** Results from grid dependence study for P1225 propeller in cavitating flow without additional refinements for  $\sigma_{\text{cav}} = 1.464$ ,  $J = 0.8009$

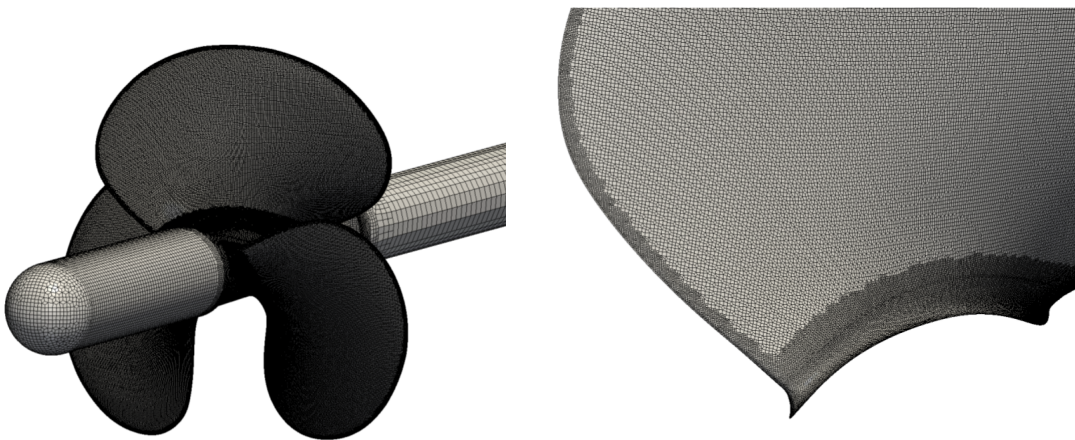
grid	control volumes	$K_X$ [-]	$10K_Q$ [-]	$\bar{V}_v^*$ [ $10^{-6}$ ]
G1	$0.84 \cdot 10^6$	0.2165 (-2.04 %)	0.4558 (-1.28 %)	5.929 (-25.02 %)
G2	$1.89 \cdot 10^6$	0.2189 (-0.95 %)	0.4605 (-0.26 %)	7.218 (-8.71 %)
G3	$5.07 \cdot 10^6$	0.2210	0.4617	7.907

Figure 5.40 plots the thrust on a single blade in cavitating (red) and non-cavitating (black) oblique flow. Their average values were similar, and ensemble averaging yielded even more similar time histories. However, the influence of cavitation was obvious. In cavitating flow, the thrust oscillated at a high frequency. This was partly attributed to numerical oscillations using the Crank-Nicolson scheme for time integration. Therefore, further on, the implicit Euler scheme was used for time integration yielding less numerical oscillations. In addition, strong negative peaks are seen to occur periodically, which were related to collapses of cloud cavitation on the blade surface.



**Figure 5.40:** Comparison of thrust on one propeller blade at  $\alpha_{AoA} = 13^\circ$  with and without cavitation

Based on preliminary findings, further refinements at blade tips and roots were needed to better resolve cavitation near the blades. Figure 5.41 (left) shows a mesh on the surface of the entire propeller, the hub, and the shaft. Figure 5.41 (right) displays a detail view of the additional refinements on a blade. Additional refinements were applied on the tips and the roots of the propeller blades.



**Figure 5.41:** Perspective view of grid on entire propeller (left) and detail view of refinements at root and leading edge of a blade (right); taken from Peters et al. (2018a)

To examine the influence of additional blade refinements, Table 5.16 lists axial force and torque coefficients and the average vapour in the domain obtained from different simulations. Except for additional refinements at blade roots and blade tips, the numerical mesh of case

## 5.1 Euler-Euler Method

G3-R is similar to the mesh G3. For case G4-R, the numerical mesh of G3-R was systematically refined in the entire rotor region. Force and torque coefficients of simulations G3 and G3-R with respect to G4-R deviated by less than 1.5 %. While the influence of the additional spatial discretisation on forces and moments was small, its influence on cavitation behaviour was more significant. For case G3, the time-averaged normalised vapour volume,  $\bar{V}_v^*$ , deviated by 20.64 % related to case G4-R; for case G3-R, by 11.57 %. Because further grid refinement leads to more tip vortex cavitation, convergence of  $\bar{V}_v^*$  in the entire domain can not be expected.

**Table 5.16:** Results for cavitating flow obtained from different grids with and without additional refinements for  $\sigma_{\text{cav}} = 1.464$ ,  $J = 0.8009$

grid	control volumes	$K_X$ [-]	$10K_Q$ [-]	$\bar{V}_v^*$ [ $10^{-6}$ ]
G3	$5.07 \cdot 10^6$	0.2210 (+1.42 %)	0.4617 (+0.85 %)	7.907 (−20.64 %)
G3-R	$7.78 \cdot 10^6$	0.2176 (−0.14 %)	0.4613 (+0.76 %)	8.811 (−11.57 %)
G4-R	$12.44 \cdot 10^6$	0.2179	0.4578	9.964

Table 5.17 lists comparable numerical and experimental results of propeller forces for an uncorrected advance ratio of  $J = 0.8009$  and a cavitation number of  $\sigma_{\text{cav}} = 1.464$ . It is noted that the revolution rate in the experiment was  $n_p = 29.989 \text{ s}^{-1}$  and in the simulations  $n_p = 29.965 \text{ s}^{-1}$ . Although further grid refinements resulted in a better resolution of vapour structures, the influence on the calculation of force coefficients was negligible. The axial force coefficients obtained using grids G2 and G4-R deviated by 8 % to 9 % compared to the force coefficient obtained from the experiment; the torque coefficient, by 5 % to 6 % from the measured result. As simulations using both grids yielded similar results of propeller forces, the influence of further spatial discretisation on these forces is supposedly small. Therefore, deviations between numerically and experimentally obtained forces were mostly attributed to differences in the flow conditions such as inflow velocity and tunnel pressure. Further differences stem especially from errors owing to turbulence and cavitation modelling as well as their interactions.

**Table 5.17:** Comparison of propeller forces obtained from experiments, Heinke et al. (2013), and simulations for  $\sigma_{\text{cav}} = 1.464$ ,  $J = 0.8009$

case	$K_X$ [-]	$10K_Q$ [-]	$\eta_0$ [-]
simulation G2	0.2189 (−8.41 %)	0.4605 (−5.13 %)	0.599 (−3.39 %)
simulation G4-R	0.2179 (−8.83 %)	0.4578 (−5.69 %)	0.600 (−3.23 %)
experiment	0.2390	0.4854	0.620

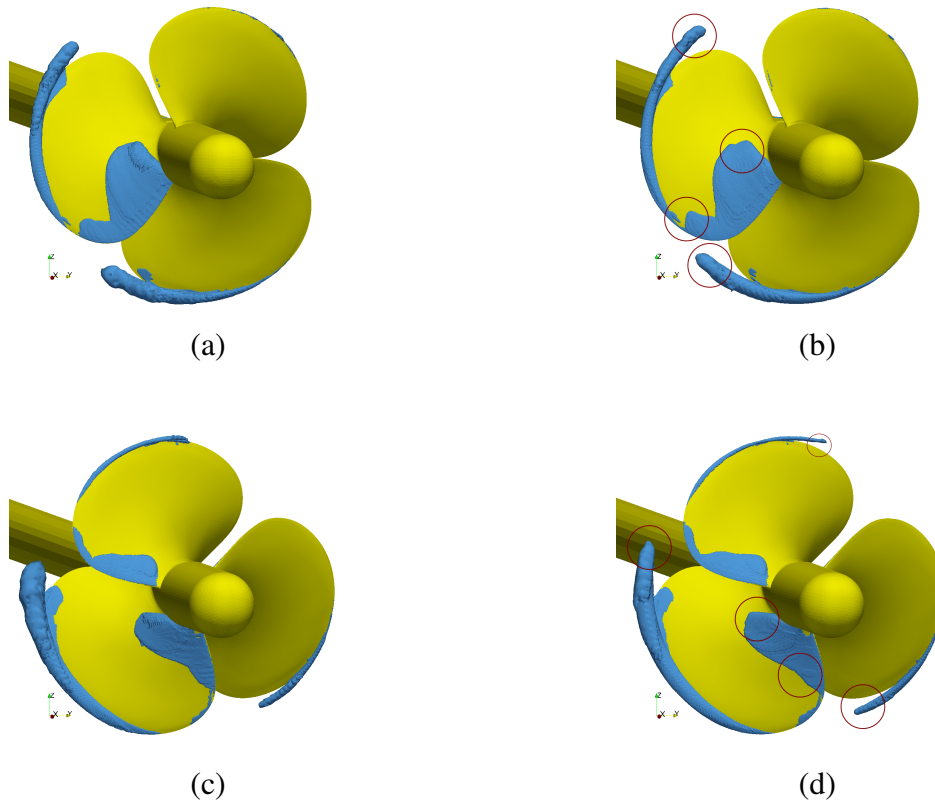


**Figure 5.42:** Images from the simulations of cavitation for  $\sigma_{\text{cav}} = 1.464$  at different blade positions on a grid without (left) and a grid with grid refinements at blade roots and blade tips (right); taken from Peters et al. (2018a)

Red circles in Figure 5.42 mark differences between simulations without (left) and with grid refinements (right). In graphs (a) and (b) of Figure 5.42 the left propeller blade is at its  $90^\circ$  position. These graphs demonstrate that the additional refinements generated more cavitation in the tip vortex, at the connection between sheet and tip vortex cavitation, and at the end of the sheet cavitation. In Figures 5.42 (c) and (d), although the blades are in a different position, it is seen that the resulting effect on cavitation was similar. More cavitation was generated in the root region of the sheet cavitation, and on the leading edge, as well as on all tip vortex cavitation structures. The majority of additional cavitation seems to be generated in the tip vortex cavitation, which did not affect the prediction of cavitation erosion for the propeller itself, because these structures collapsed further downstream. It could be concluded, that further leading edge and root refinements on the blades are necessary to better resolve the cavitation structures.

To demonstrate that flow quantities were correctly interpolated between rotor and stator region, Figure 5.43 depicts the pressure coefficient distribution around the propeller and the AMI of case G3-R. The flow direction is from right bottom to left top. The pressure coefficient is plotted on planes normal to the flow direction and normal to the transverse direction, the propeller geometry, and the slightly transparent AMI cylinder. Pressure values along the AMI and on both sides of the AMI were similar and were smoothly distributed.

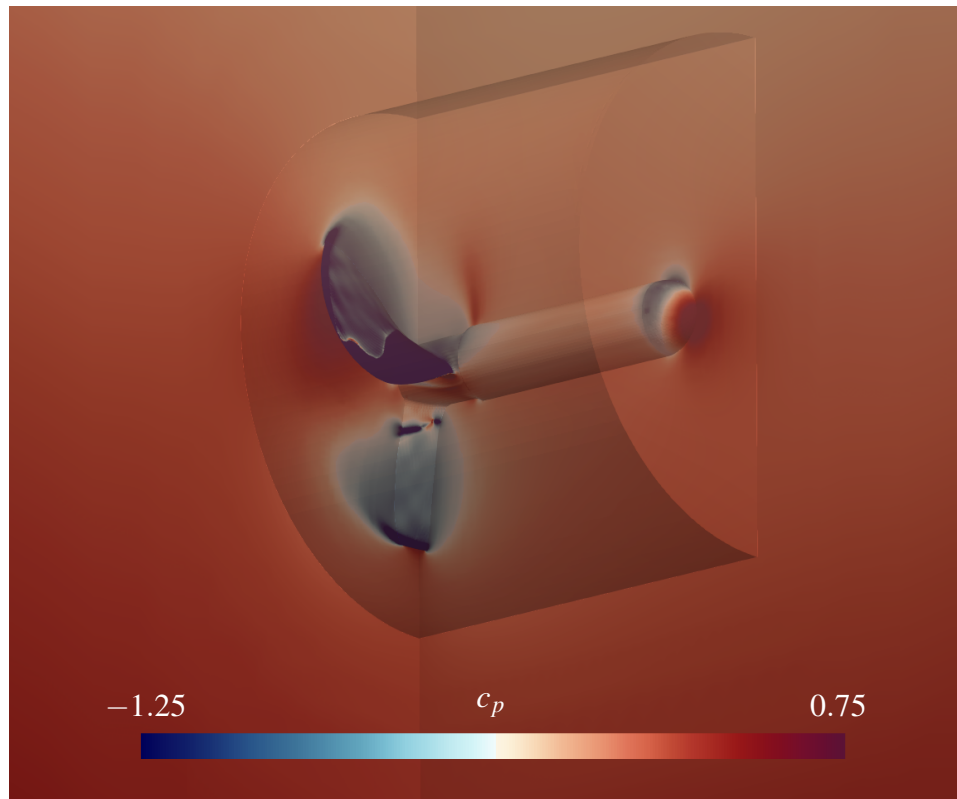


**Figure 5.43:** Distribution of pressure coefficient around the propeller and the AMI

For case G3-R, Figure 5.44 shows correlations between pressure distribution and cavitation behaviour for different blade positions. Dark blue regions on the left mark areas of low pressure, while dark red areas mark regions of high pressure. Light blue isosurfaces on the right mark a vapour volume fraction of 10 %. Figure 5.44 (a) illustrates the growth of sheet cavitation on a blade in the  $0^\circ$  position. The sheet cavitation reached its full length at a blade position of approximately  $120^\circ$ . Vortex cavitation appeared mostly between blade angles of  $45^\circ$  to  $225^\circ$ . As expected, low pressure regions coincided with regions of high vapour content. Figure 5.44 (b) depicts the collapse of a cavitation cloud on the blade positioned at  $180^\circ$ . High pressures surrounding the loosely-connected vapour structure caused its continuous collapse.

The behaviour of cavitation around the P1225 propeller in simulation and experiment was investigated for the two cases of  $\sigma_{\text{cav}} = 0.963$  and  $\sigma_{\text{cav}} = 1.464$ . Figure 5.45 displays the case of  $J = 0.8208$  and  $\sigma_{\text{cav}} = 0.963$ . The numerical simulation (left) and the experiment (right) both show a similar behaviour of cavitation. Tip vortex cavitation was permanently present during one propeller revolution. Its growth started near the  $0^\circ$  position and increased until reaching the  $180^\circ$  position, where the cavitation volume decreased again. A rotationally dependent growth and shedding of the sheet cavitation on the blade is seen. Regions of sheet cavitation started to form on the leading edge and on the surface of the blade for blade positions near  $0^\circ$ . Figure 5.45 (c) shows that these regions grew until the blade reached the  $90^\circ$  position and fused to form a large sheet cavitation covering a considerable area of the blade's

suction side. The sheet cavitation was shed from the leading edge and collapsed, while the blade approached  $180^\circ$ . The vapour volume collapsed at a propeller radius of 20 % to 50 %. Figures 5.45 (b) and (d) show that a qualitatively similar behaviour occurred in the experimental tests. Figure 5.45 (b) shows a right-sided blade in the  $0^\circ$  position; Figure 5.45 (d) shows a left-sided blade in the  $90^\circ$  position, where the blade was almost fully covered by sheet cavitation. Besides details such as single cavitation bubbles and small cavitation structures that were not be resolved by the numerical grid, the overall predicted cavitation behaviour compared favourably to the observations made during experiments.

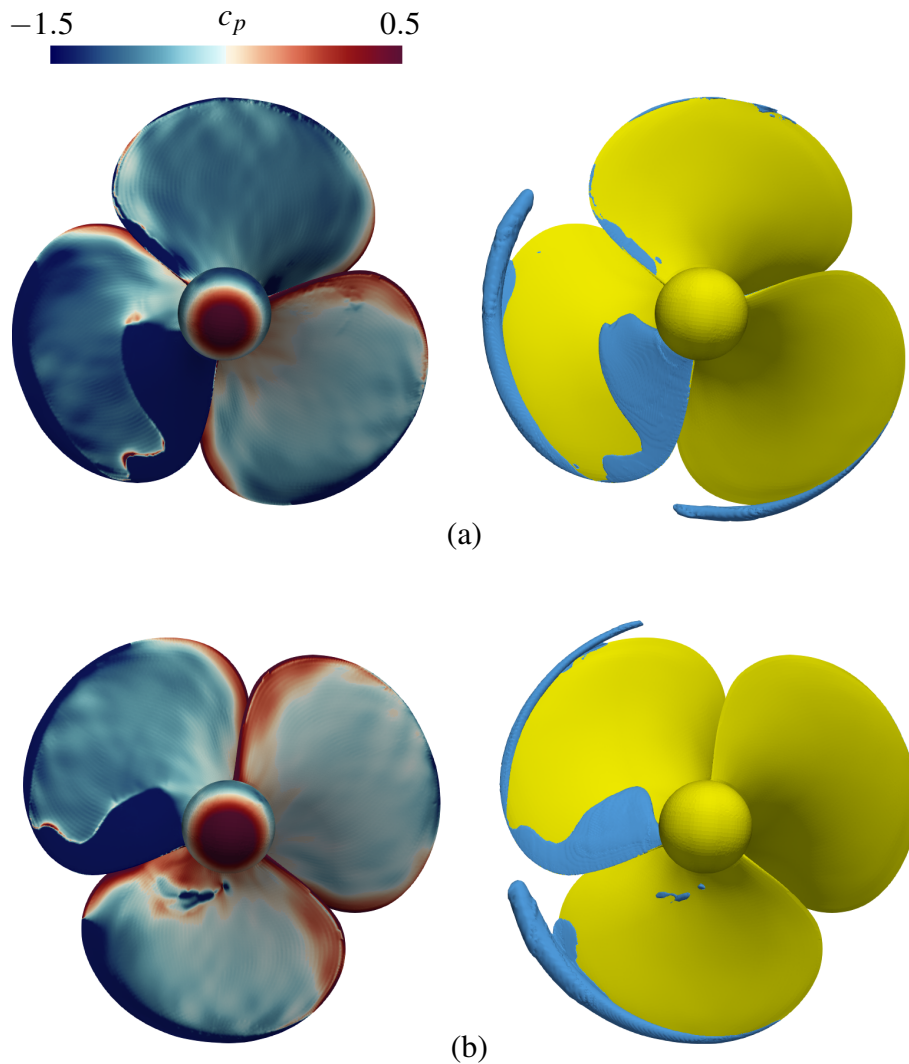


**Figure 5.44:** Correlations between distribution of pressure coefficient (left) and vapour volumes (right) at the propeller blades' suction sides

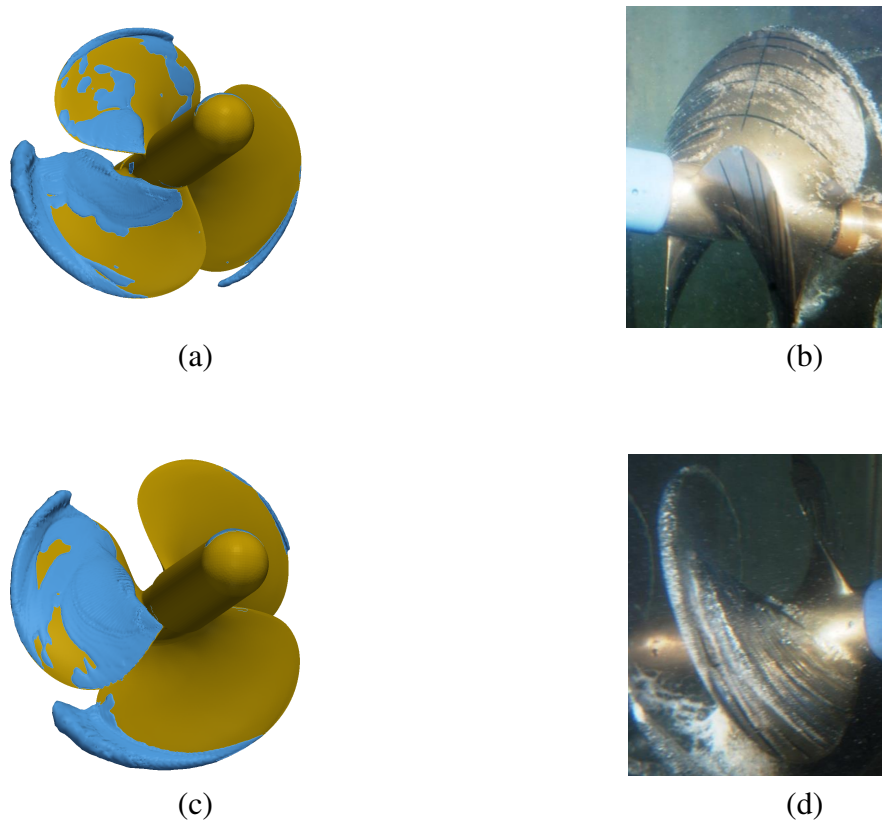


**Figure 5.45:** Images from the simulation of cavitation for  $\sigma_{\text{cav}} = 0.963$  at different blade positions (left) and from experiments of Heinke et al. (2013) (right) for a blade position of  $0^\circ$  (b) and  $90^\circ$  (d); taken from Peters et al. (2018a)

Cavitation-induced erosion was predicted using the microjet erosion model described in section 4.5.1. Numerical results were compared to measurements of Heinke et al. (2013). In the experimental tests the propeller blades were coated with a special erosion coating. The coating technique was validated with regard to predict cavitation erosion in Heinke (2001). Supposedly erosion appears in these regions when the coating is partially to fully removed from the blade's surface. This procedure was used for decades and was proven valid for the prediction of areas exposed to erosion. A considered material cannot be specified for the experimental erosion prediction which uses an erosive coating. However, the experimental prediction has shown to be a valid method to qualitatively predict erosion on surfaces for propellers usually made of copper alloys such as bronze. According to Germanischer Lloyd (2009), the minimum yield strength for any standard cast copper alloy for a propeller is  $175 \text{ N/mm}^2$ . To be able to compare experimental and numerical prediction methods and to reasonably predict erosion, a yield strength of  $200 \text{ N/mm}^2$  was chosen. This yield strength is at the lower end of these commonly used copper alloys but still fulfills the rules of Germanischer Lloyd (2009) and was used to define the critical velocity,  $u_{\text{crit}}$  (see (4.81)). Figure 5.46 shows the comparative numerical erosion prediction using grid G2 of  $1.89 \cdot 10^6$  control volumes (left) and the experimental erosion prediction using an erosive coating technique, Heinke et al. (2013) (right) for the case of  $\sigma_{\text{cav}} = 0.963$ . The erosion coefficient,  $c_{\text{ero,E}}$ , is plotted using a logarithmic colour

scale. The suction sides of the blades are shown from front view where the propeller rotation would be counter-clockwise. The leading edge of the blades is on the left side and the trailing edge on the right side. Erosion was predicted at an area above the root of the blade. In the experiment the predicted area extended from about mid-chord to the trailing edge of the blade, with a higher erosion potential at the trailing edge. The numerical model predicted erosion above the root of the blade. Nevertheless, the erosion potential spread discontinuously from the leading edge to the trailing edge. In the simulation, the region near the trailing edge was predicted to be less endangered to erosion compared to the experimental prediction. Taking into account that the experimental prediction was not clearly circumscribed, an overall agreement was found concerning the behaviour of cavitation and prediction of erosion.

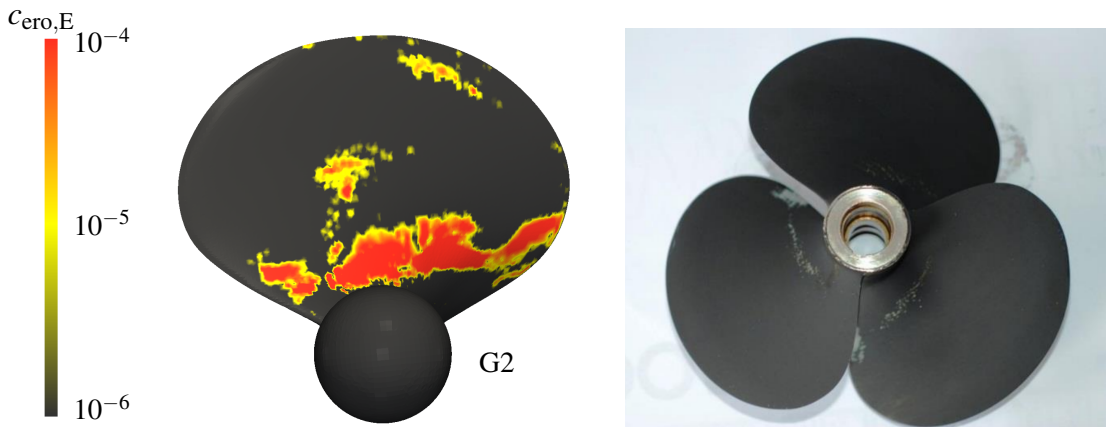


**Figure 5.46:** Erosion predictions on a propeller blade for  $\sigma_{cav} = 0.963$  obtained from a simulation on grid G2 (left) and from the experiment of Heinke et al. (2013) (right)

The second operating point was chosen to represent a higher cavitation number, where less cavitation volume was generated and erosion supposedly occurred at more confined areas. Figure 5.47 presents images for the cases of  $J = 0.8009$  and  $\sigma_{cav} = 1.464$ . The simulated tip vortex cavitation and processes of generation and collapse of cloud cavitation on the blade are depicted. Figures 5.47 (a) and (c) show that tip vortex cavitation was present over the entire revolution of the propeller, reaching its maximum extent at about  $150^\circ$ . Sheet cavitation started to develop from the leading edge of the blade when it was near the  $0^\circ$  position. The sheet elongated and reached its maximum length around the  $90^\circ$  position. Afterwards, it detached from the leading edge and travelled further downstream forming a cloud. When the blade was near the  $180^\circ$  position, the vapour volume collapsed at medium chord length, just above the root of the blade. These collapses were the main cause for the peaks in the blade force plotted in Figure 5.40. The similarities between simulation and experiment are apparent. However, the Euler-Euler method was unable to resolve single bubbles and finely scattered cavitation volumes seen in the experiments.

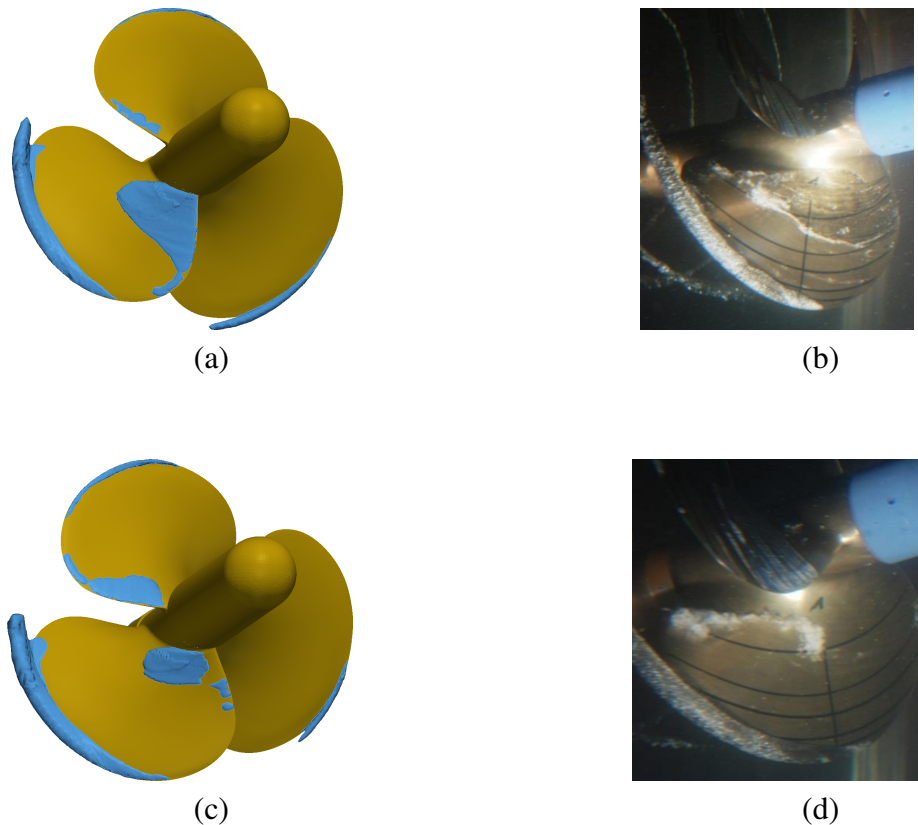


**Figure 5.47:** Images from the simulation of cavitation for  $\sigma_{\text{cav}} = 1.464$  at different blade positions (left) and from experiments of Heinke et al. (2013) (right) for blade positions of  $150^\circ$  (b) and  $180^\circ$  (d); taken from Peters et al. (2018a)

Figure 5.48 shows the numerical erosion prediction obtained using grids G2 of  $1.89 \cdot 10^6$  CVs, grid G3-R of  $7.78 \cdot 10^6$  CVs, grid G4-R of  $12.44 \cdot 10^6$  CVs, and from the comparable experimental prediction. As described for Figure 5.46, the suction sides of the blades are shown from front view where the propeller rotation would be counter-clockwise. The leading edge of each blade from the simulation is on the left side and the trailing edge on the right side. The erosion coefficient,  $c_{\text{ero,E}}$ , is plotted using a logarithmic scale. Generally, all methods predicted erosion close to the region where the cloud cavitation collapsed on the blade. The experiments show the removal of the erosion coating in an area that lies between leading edge and mid-chord and near the root of the blade. Some coating was removed more discontinuously when moving further to the leading edge or away from it. The experimental erosion prediction for both coated blades agreed well within the area where most of the coating was removed, but deviated somewhat in areas where coating was removed more discontinuously. Agreement of the numerical predictions on all grids with the experimental results can be seen. The simulations on grid G3-R and G4-R were able to predict a more confined area to be eroded. Deviations were mainly attributed to a poorer resolution of cavitation structures collapsing on the blade. Despite grid G2 being rather coarse compared to grids G3-R and G4-R, the predicted area of erosion agreed positively.

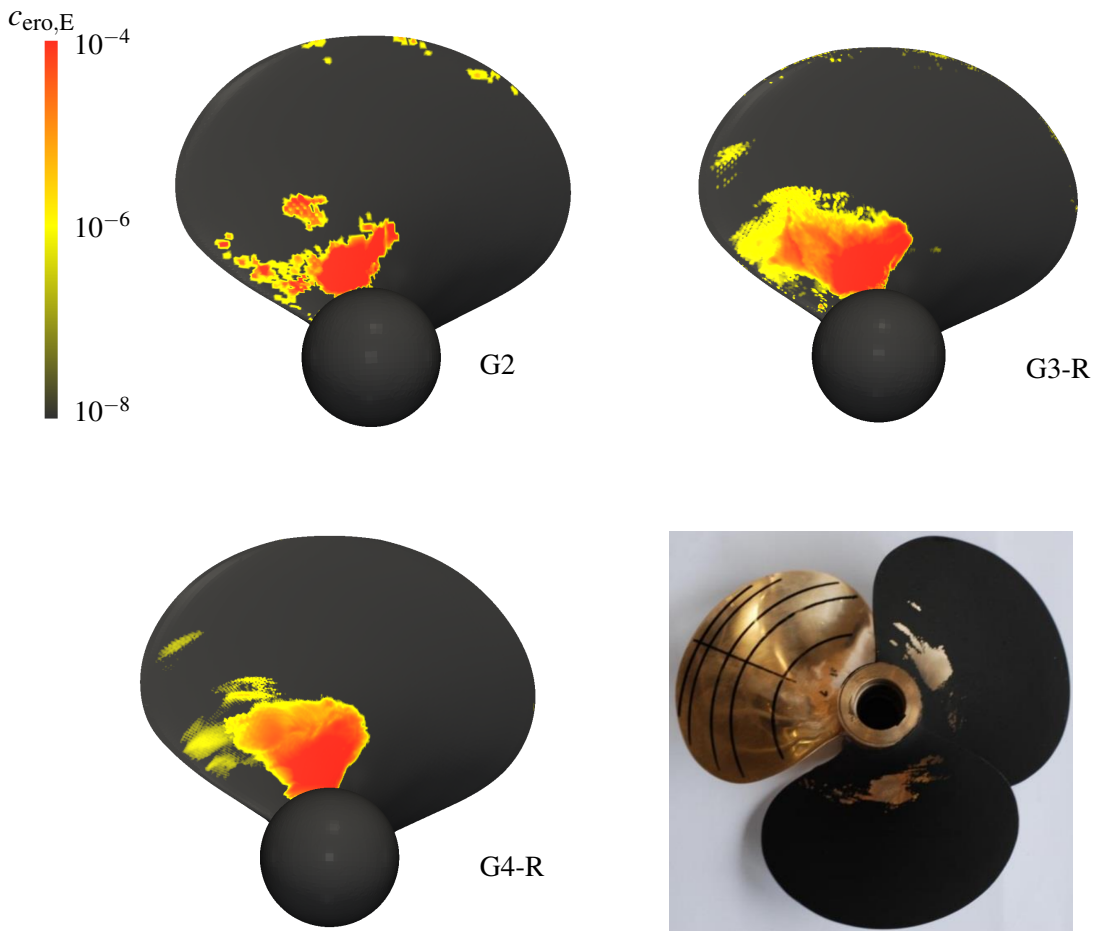


**Figure 5.48:** Erosion predictions on a propeller blade for  $\sigma_{\text{cav}} = 1.464$  obtained from simulations on different grids and from the experiment of Heinke et al. (2013)

### Scale Effects on Cavitation and Cavitation Erosion

Scale effects are apparent in different types of flows. For cavitating flows, it is difficult to predict the behaviour of a full-scale flow from model-scale tests because only a part of the scaling laws can be fulfilled at the same time. Propeller tests are usually conducted by fulfilling kinematic similarity by using the same advance ratio (see equation (5.5)) for both scales. The scale factor  $\lambda = D_S/D_M$  is the ratio of the diameter  $D$  of the full-scale propeller (“S”) to the model-scale propeller (“M”). To investigate scale effects related to erosion, the cavitating flow around the P1225 propeller was additionally simulated in full-scale. Here, the inlet velocity was scaled with  $\sqrt{\lambda} = v_S/v_M$  and the propeller’s rate of revolution with  $\sqrt{\lambda} = n_{p,M}/n_{p,S}$  to achieve kinematic similarity.

Similarity of cavitation was obtained by setting the same cavitation number,  $\sigma_{\text{cav}}$ , (see equation 2.5) for the model test compared to full-scale. Generally, cavitation tests are performed

## 5.1 Euler-Euler Method

by fulfilling this requirement, supposing that the behaviour of cavitation is qualitatively similar. However, cavitation behaviour can additionally depend on nuclei distribution, size of the cavitator, Reynolds number, Mach number, surface roughness, or the larger influence of hydrostatic pressure in full-scale (see section 2.3.2). In model-tests, usually only the advance ratio and the cavitation number can be kept the same. As seen from literature, it is therefore possible, that differences in cavitation behaviour may result from the aforementioned scale effects.

For the same cavitation number, cavitation erosion rates have shown to depend on nuclei distribution, geometric scale, and especially velocity (see section 2.3.2). While an increase of gas content has shown to lower the aggressiveness of cavitation erosion, erosion rates have shown to be proportional to a higher power of the size of the cavitator and of the magnitude of flow velocity. It is therefore assumed that the higher velocity and the larger full-scale propeller diameter would result in a higher erosion rate.

Scale effects were investigated by comparing simulations performed at full-scale and at model-scale for the case of  $\sigma_{\text{cav}} = 1.464$  and  $J = 0.8009$ . Both simulations were carried out on the same grid topology with the same number of faces on the blades. The grid in wall normal direction was not changed so that cell zones for the numerical erosion prediction comprised the same number of cells. Changing the number of cells in wall normal direction would result in a change of the prediction of the area exposed to erosion (see section 5.1.3 and Figure 5.29). Nevertheless, this resulted in higher values of the dimensionless wall distance of  $n^+ \approx 700 - 1000$  for the full-scale case. Koopmann et al. (2015) showed that values of  $n^+ > 1000$  can be used for simulations of ships in full-scale. Although this was not validated for the regarded case, the grid was scaled, taking into account that there may be small influences owing to different  $n^+$  values. The approach for the walls is the logarithmic wall function in both cases.

Here, at a scale of  $\lambda = 5.25$ , an inflow velocity of  $u_S = 13.2 \text{ m/s}$  and a propeller revolution rate of  $n_{p,S} = 13.07 \text{ s}^{-1}$  were specified. Generally, the local flow on a propeller depends on the inflow velocity and on the rotational velocity of the revolving blades. A reference velocity of  $u_{\text{ref}} = \sqrt{v^2 + (0.7D\pi n_p)^2}$  was specified to compare flow conditions at the two scales. To obtain the same cavitation number of  $\sigma_{\text{cav}} = 1.464$ , the outlet pressure in the full-scale simulation was set to  $p_{\text{outlet,S}} = 130 \text{ kPa}$ . The time step size was adapted in order to achieve the same rotation per time step as for model-scale.

**Table 5.18:** Comparison of full-scale and model-scale simulations of the propeller in cavitating flow at  $\sigma_{\text{cav}} = 1.464$  and  $J = 0.8009$

case	$u_{\text{ref}}$ [m/s]	$K_T$ [-]	$10K_Q$ [-]	$\bar{V}_v^*$ [ $10^{-6}$ ]	$n_{\text{pit}}^{\text{rev}}$ [-]
model-scale	16.823	0.2331	0.4621	7.218	25388
full-scale	38.546	0.2391	0.4541	7.747	375450

At both scales, no obvious qualitative differences of cavitation behaviour were found. Vortex cavitation and cloud shedding occurred also at full-scale. Nevertheless, a detailed comparison of different flow quantities revealed quantitative differences. Table 5.18 lists the associated reference velocity, the thrust and torque coefficients, the time-averaged normalised vapour volume,  $\bar{V}_v^*$ , and the sum of the number of predicted erosion impacts in one propeller revolution,  $n_{\text{pit}}^{\text{rev}}$ . Thrust and torque coefficients differed slightly. The reference velocity was higher at full-scale, which led to a higher Reynolds number. Thus, viscosity most likely had a smaller influence on the flow at full-scale. This led to less friction in full-scale and therefore a reduction of propeller torque by 1.7%. The thrust coefficient increased from model-scale to full-scale by 2.6%. The generated vapour volume was on average 7.3% larger at full-scale. This is in agreement with Pelz et al. (2017), Keil et al. (2011), Ganesh et al. (2016), and Keller et al. (1999) (see section 2.3.2). More vapour is supposedly generated because reference velocity and scale, and therefore the Reynolds number, were higher.

Comparing the sum of the number of numerically predicted impacts during one propeller revolution,  $n_{\text{pit}}^{\text{rev}}$ , almost 15 times as many impacts were predicted at full-scale. This was expected because of the larger propeller diameter and the higher reference velocity at full-scale. It is not surprising that this behaviour was reflected by the numerical erosion prediction. The average pressure difference between the pressure in the flow and the vapour pressure was higher at full-scale because the pressure in the tunnel was higher. Theoretically, higher driving pressures cause more rapid bubble collapses. Therefore, the numerically predicted erosion is in accordance with physical considerations. As stated in the literature, the large increase of the predicted erosion rate at model-scale confirmed the dependence of this erosion rate on power laws of flow velocity and also on power laws of the scale. However, since both velocity and scale of the investigated cases differed, it was not possible to explicitly derive appropriate power laws for each scale effect.

### 5.1.5 Conclusion

Using an Euler-Euler approach, different hydrodynamic cavitating flows were investigated. For a NACA 0009 modified hydrofoil, the computed lift coefficient and the Strouhal number related to the shedding frequency of cavitation agreed favourably with comparable measured results of Dupont (1991). Instantaneous pressure distributions for non-cavitating and cavitating conditions obtained from simulation and experiment agreed well. Simulations of the cavitating flow around a NACA 0015 hydrofoil revealed that increasing cavitation numbers lead to smaller vapour volumes and higher cavitation shedding frequencies. An increase of the nuclei density,  $n_0$ , as a parameter of the cavitation model of Sauer and Schnerr (2000), resulted in greater vapour volumes and lower shedding frequencies. The simulated cavitation behaviour agreed favourably to experimental observations, and numerical erosion predictions, based on the number of impacts and their intensities, agreed favourably with experimental erosion predictions of Reemts and Johannsen (2015). Simulation results of the unsteady cavitating flow through an axisymmetric vertical nozzle agreed favourably with numerical results of Mihatsch

### *5.1 Euler-Euler Method*

et al. (2011, 2015), and Mottyll (2017) concerning cavitation shedding frequencies. Predictions of areas exposed to erosion and erosion intensities from two different Eulerian-based erosion models agreed favourably with measured pit depths of Franc and Riondet (2006). Cavitation erosion on a propeller in transient oblique flow was numerically investigated employing a sliding interface technique. In model-scale, the simulated cavitation behaviour was compared to experimental observations of Heinke et al. (2013) and agreed favourably in terms of cavitation generation at the leading edge and cloud cavitation collapses close to the roots of the propeller blades. Numerically predicted erosion on the propeller blades agreed favourably with experimentally predicted erosion of Heinke et al. (2013). Scale effects on cavitation and erosion published in the literature were confirmed by simulating the cavitating flow around the propeller at model- and full-scale. While the time-averaged vapour volume was only slightly larger in the full-scale simulation compared to the model-scale simulation, it was found that numerically predicted erosion impacts depend on higher powers of geometric scale and flow velocity which is in accordance with literature.

## 5.2 Euler-Lagrange Method

Main components of the Euler-Lagrange method – bubble dynamics and motions – presented in section 4.3 are verified and validated for simple test cases. Bubble dynamics are validated against experimental data for a single bubble in an acoustic field. Dynamics and motions of a bubble are verified for a bubble travelling in a vortex-induced flow. Velocities of a bubble rising in a liquid column obtained from an analytical solution, a one-way coupled Euler-Lagrange simulation, and a two-way coupled Euler-Lagrange simulation are compared. Mechanisms of coalescence and collision of Lagrangian bubbles are addressed. Simulations of the cavitating flow inside an axisymmetric nozzle are conducted for various nuclei densities using a two-way coupled Euler-Lagrange approach.

### 5.2.1 Spherical Bubble Dynamics in an Acoustic Field

Pressure changes in the surrounding liquid are the main driving mechanism for growth and decay of cavitation bubbles. Before investigating agglomerations of multiple moving bubbles in a flow, bubble dynamics of a single static bubble were examined based on measurements of Ohl et al. (1999). A bubble in equilibrium at a radius of  $R_0 = 8 \mu\text{m}$  and at atmospheric pressure of  $p_0 = 100 \text{ kPa}$  was considered. An acoustic wave of frequency  $f_{ac} = 21.4 \text{ kHz}$  and acoustic pressure  $p_{ac} = 132 \text{ kPa}$  prescribed the surrounding liquid pressure field.

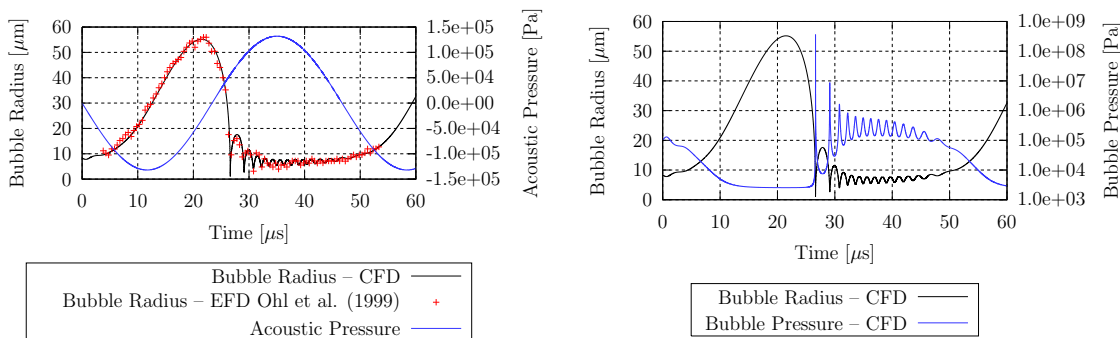


**Figure 5.49:** Time histories of measured and calculated radius of a spherical cavitation bubble exposed to an acoustic wave in an infinite liquid (left) and time histories of calculated radius and inner pressure of the same bubble (right)

To illustrate the numerical predictions of bubble dynamics, Figure 5.49 presents time histories of bubble radius, acoustic pressure, and bubble pressure for a spherical cavitation bubble. The left graph in Figure 5.49 plots the calculated bubble radius (black line) together with the comparative experimentally measured radius (red crosses), and the prescribed acoustic pressure (blue line) on the right ordinate over time. Figure 5.49 (right) plots the calculated bubble radius (black) on the left ordinate, and the inner bubble pressure,  $p_b$ , (blue) on the right ordinate over time. Time sequences shown were shifted to visualise the instance when liquid and atmospheric pressure were equal. At the beginning, the bubble radius started to grow because liquid

## 5.2 Euler-Lagrange Method

pressure decreased below atmospheric pressure, at which the bubble was initially in equilibrium. The bubble growth rate reached its maximum approximately when the acoustic pressure was minimal. When the liquid pressure increased again, the acceleration of the bubble wall became negative and caused the bubble's growth rate to decrease. Further bubble growth led to a decrease of the bubble's inner pressure, and this inner pressure approached the vapour pressure until the bubble attained its maximum radius. When the liquid pressure exceeded the atmospheric pressure again, it initiated the first bubble collapse. As the non-condensable gas inside the bubble was compressed, the bubble's radius decreased well below its equilibrium radius.

At the end of the collapse, the pressure inside the bubble increased by multiple orders of magnitude above the equilibrium pressure. The peak of the blue line in the right graph of Figure 5.49 visualises the process, which is in accordance with an adiabatic change of state of an ideal gas. During collapse, the largest part of the potential energy, which was stored in the bubble at maximum size, was converted into energy to form shock waves that were radiated into the liquid. Viscous effects dissipated additional energy. Compression and expansion of the non-condensable gas caused multiple bubble radius and pressure oscillations of decreasing amplitude. The entire process was repeated periodically according to the frequency of the acoustic pressure oscillation. Calculated and measured radii compared well.

### 5.2.2 Behaviour of a Spherical Single Bubble in a Vortex

To ensure that a single bubble's motion and the associated dynamics were computed correctly and interact reasonably with each other, the behaviour of a bubble was simulated in a Lamb-Oseen based vortex-flox modified from the work of Oweis et al. (2005). Generally, vortex flows can be modelled as Rankine vortices, consisting of the combination of the following two vortex parts:

1. a *rotational vortex* (with:  $\nabla \times \mathbf{u} \neq 0$ ; rigid body vortex) on the *inside* and
2. an *irrotational vortex* (with:  $\nabla \times \mathbf{u} = 0$ ) on the *outside*.

The two parts of the vortex are joined together at the core radius,  $r_{\text{core}}$ , measured from the centre of its rotational axis. At the vortex core, the tangential velocity is greatest and is calculated as follows:

$$u_{\text{core}} = \gamma_1 \frac{\Gamma_0}{2\pi r_{\text{core}}} . \quad (5.8)$$

The corresponding core pressure is then defined as:

$$p_{\text{core}} = p_{\infty} - \frac{\rho_l}{2} u_{\text{core}}^2 . \quad (5.9)$$

$\Gamma_0 = 0.29 \text{ m}^2/\text{s}$  is the circulation of the vortex and  $\gamma_1 = 0.715$ .  $p_{\infty}$  is the pressure in the undisturbed far field. The tangential velocity measured from the centre of the vortex's axis of rotation reads as follows:

$$u_{\theta} = \gamma_1 \frac{\Gamma_0}{2\pi r_{\text{core}}} \frac{r}{r_{\text{core}}} . \quad (5.10)$$

It increases with increasing radius,  $r$ , from 0 m/s at the vortex centre to its maximum value,  $u_{\text{core}}$ , at the vortex core. The pressure inside the inner rotational vortex region is defined as

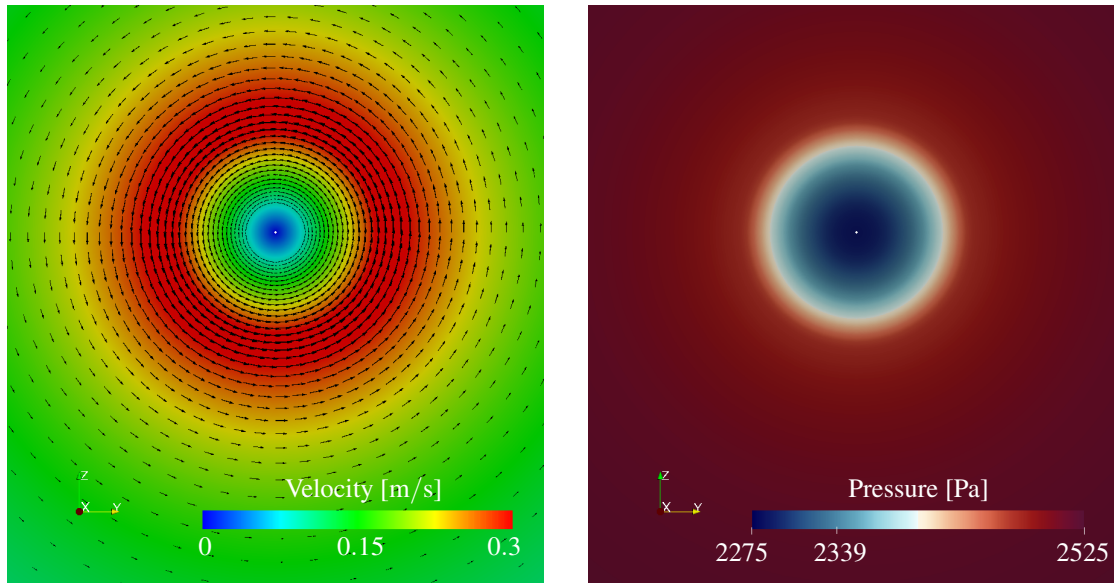
$$p = p_{\text{core}} + \gamma_2 \rho_1 \left( \frac{\Gamma_0}{2\pi r_{\text{core}}} \right)^2 \frac{(r^2 - r_{\text{core}}^2)}{r_{\text{core}}^2} , \quad (5.11)$$

with  $\gamma_2 = 0.87$ . Outside the vortex core ( $r \geq r_{\text{core}}$ ), the flow velocity decreases with increasing distance from the vortex core:

$$u_{\theta} = \frac{\Gamma_0}{2\pi r_{\text{core}}} \left( 1 - e^{-\gamma_3 (r/r_{\text{core}})^2} \right) , \quad (5.12)$$

with  $\gamma_3 = 1.255$ . The pressure,  $p$ , increases with increasing distance from the centre of the vortex's axis of rotation. It is calculated by substituting equation (5.12) into the following expression:

$$p = p_{\infty} - \frac{\rho_1}{2} u_{\theta}^2 . \quad (5.13)$$



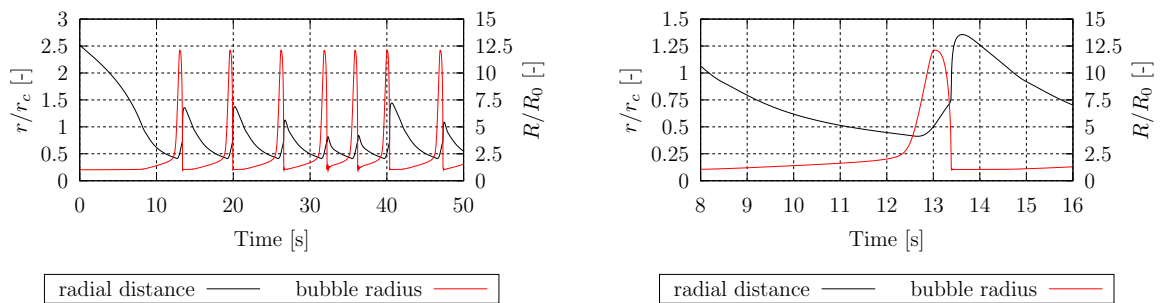
**Figure 5.50:** Radial distributions of velocity magnitude in the vortex with velocity vectors (left) and of pressure in the vortex (right)

Figure 5.50 depicts the velocity magnitude (left) and pressure in the vortex (right). Arrows in the left graph of Figure 5.50 identify magnitude and direction of the counter-clockwise flow. Flow velocities were highest near the vortex core and decreased with increasing distance away from the vortex core. Varying colours in the right graph of Figure 5.50 mark the corresponding

## 5.2 Euler-Lagrange Method

pressure. They are seen to increase from a value of 2275 Pa on the inside to a value of 2525 Pa on the outside. The vapour pressure was specified as  $p_v = 2339$  Pa.

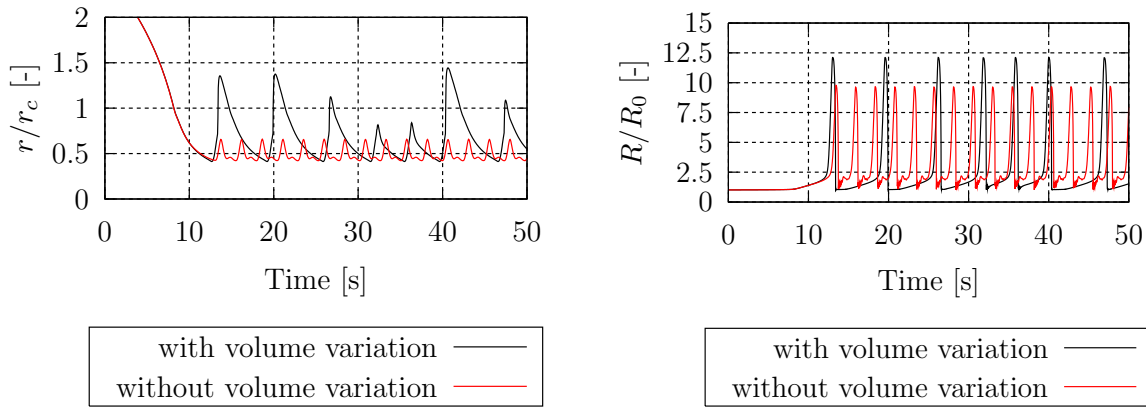
A bubble of radius  $R = 2$  mm was initially placed in the outer region of the vortex at a radial distance of 0.25 m from its rotation axis. At first, the bubble was in equilibrium at a pressure of 2525 Pa and its velocity equalled the carrier fluid velocity, causing it to move in a rotational counter-clockwise direction along the streamlines of the flow. Thereafter, the bubble trajectory deviated from the carrier flow streamlines as multiple forces influenced its motions.



**Figure 5.51:** Bubble motion in terms of radial distance to the vortex centre and bubble dynamics for the entire time series (left) and in detailed view (right)

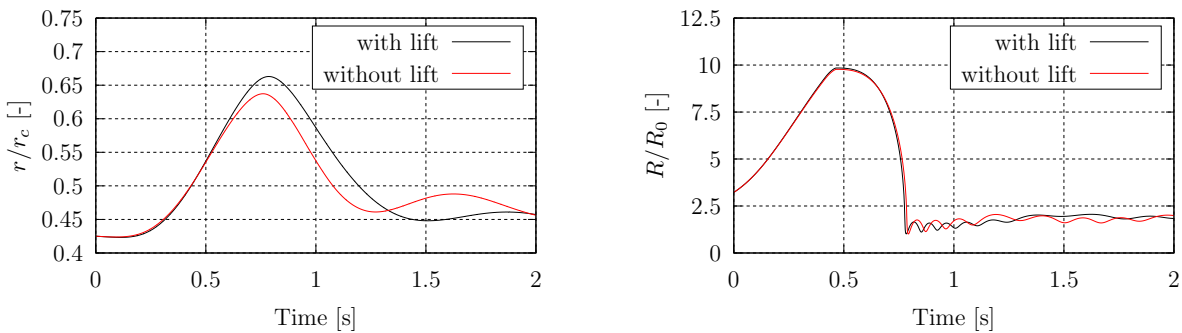
Figure 5.51 (left) plots the normalised radial distance ( $r$  is the absolute radial distance) of the bubble centre from the rotation axis of the vortex on the left ordinate and the normalised bubble radius on the right ordinate versus time. The bubble travelled consecutively towards the vortex centre and away from it owing to its growth and collapse behaviour. At the beginning, the pressure gradient force led to an attraction of the bubble towards the vortex centre where the pressure was lowest. The first growth and collapse are depicted in Figure 5.51 (right). The growth of the bubble started as it moved into the low pressure regions close to the vortex centre. During its growth, the cavitation bubble moved outwards again because forces which were proportional to bubble size and bubble growth raised in magnitude. Moreover, for larger bubble sizes, the liquid pressure, acting on the bubble, was averaged from multiple locations at the bubble wall to prevent it from being trapped in the vortex centre. Once the bubble had reached its initial size, it was again attracted by the low pressure region in the centre. The processes of bubble growth and decay as well as of motion towards the centre and away from it were repeated consecutively.

Figure 5.52 displays the normalised distance of the bubble to the vortex centre on the left and the normalised bubble radius on the right, respectively. A rapid bubble growth or collapse (large  $|\dot{R}|$ ) caused the bubble to accelerate in the same or the opposite direction of the relative velocity between bubble and carrier fluid. When considering the volume variation force (black line), during growth, the bubble moved closer to the vortex centre and was afterwards transported further away from it (see Figure 5.52 (left)). Not accounting for the volume variation force (red line) caused the bubble to move closer to the centre and, also, not attain the same size had the volume variation force been considered (see Figure 5.52 (right)).



**Figure 5.52:** Influence of the volume variation force on the bubble motion (left) and the bubble dynamics (right)

To demonstrate the influence of the lift force on the bubble’s motion, two cases considering different forces were compared. In both cases, the bubble started at the same position under equal conditions and the influence of the volume variation force was deactivated to heighten the influence of the lift force. The first case considered all other bubble forces, whereas, the second case deactivated the lift force. Figure 5.53 shows the bubble motion (left) and its dynamics (right) for both cases. Black lines mark calculated values accounted for the lift force; red lines, values that were determined without considering the lift force. The lift force transported the bubble further away from the vortex centre and closer to the maximum flow velocity in the vortex core (located at  $r_{\text{core}} = 0.1$  m). The deviating bubble trajectories led to different bubble dynamics after its first collapse. Although the lift force did influence the bubble’s motion, its effect was relatively small.



**Figure 5.53:** Influence of the lift force on the bubble motion (left) and the bubble dynamics (right)

In hydrodynamic flows, two dominant forces mostly define a bubble’s motion, namely the drag force and the pressure gradient force. To visualise their effect, Figure 5.54 shows three simulated trajectories of the bubble’s motion. All three simulations started with a bubble of the same size located at the same position. At the start, the bubble’s velocity equalled the carrier fluid velocity of the control volume incorporating the bubble initially. The black line

## 5.2 Euler-Lagrange Method

identifies the bubble's trajectory considering all forces; the green line, the bubble's trajectory considering all forces except the drag force; the pink line, the bubble's trajectory considering all forces except the pressure gradient force. The pressure gradient force mainly caused the bubble to move to low pressure regions, i.e. towards the vortex centre, where the fluid pressure was lowest. By neglecting this force, the bubble mostly followed streamlines of the carrier fluid flow (pink line in Figure 5.54). The importance of the drag force is clearly obvious, too. By neglecting the drag force, the bubble deviated from streamlines of the carrier fluid as its motion was then dominated by the pressure gradient force, causing it to move towards the centre of the vortex (green line in Figure 5.54). This oscillatory behaviour was additionally influenced by forces that depend on bubble dynamics. Considering both the drag and the pressure gradient force, the bubble approached the vortex centre following a spiral-shaped path (black line in Figure 5.54).

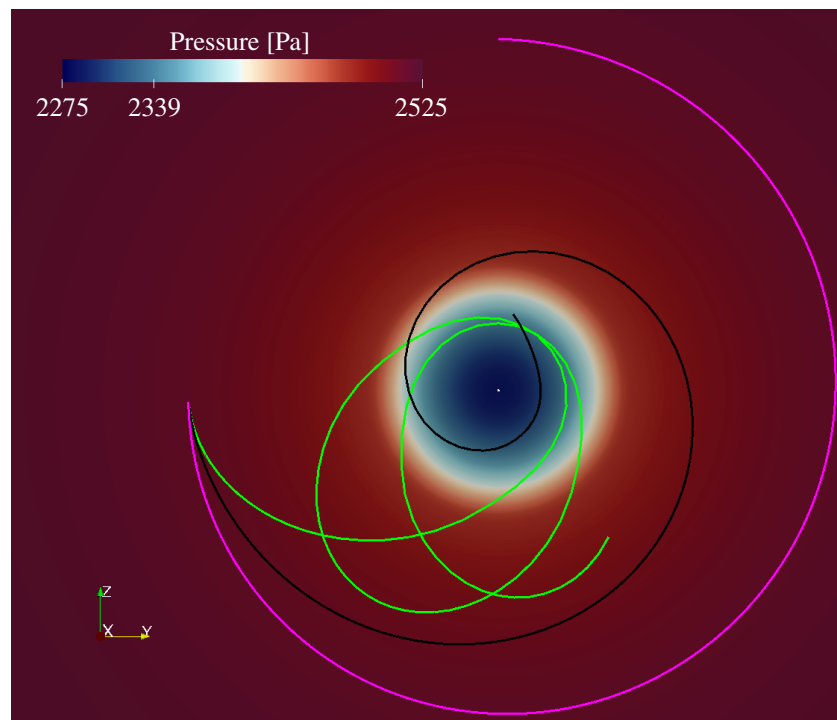


**Figure 5.54:** Bubble trajectories calculated using all forces (black line), without drag force (green line), and without pressure gradient force (pink line)

### 5.2.3 Bubble Rising in a Liquid Column

Gas bubbles rise in resting liquids owing to the gravity or buoyancy force generated by the density difference between the gas inside a bubble and the liquid surrounding this bubble. After an initial acceleration, a rising bubble reaches its final rise velocity because an equilibrium between buoyancy force and drag force is achieved. An analytical solution yields the final rise velocity of the bubble.

Based on a bubble's interaction with the liquid phase, a one-way and a two-way coupling technique were employed to simulate a bubble rising in a liquid medium initially at rest ( $u_z = 0$  m/s). A gas bubble was considered, positioned at the bottom of a water column, having an initial radius of  $R_0 = 2$  mm and an initial velocity of  $u_{b,z} = 0$  m/s. Densities of gas (i.e. air) and liquid water were assumed to be  $\rho_{\text{air}} = 1$  kg/m<sup>3</sup> and  $\rho_l = 1000$  kg/m<sup>3</sup>, respectively. Surface tension of water was set at  $\sigma = 0.073$  N/m. For the calculation of bubble motions from the Lagrangian equation, forces owing to gravity, pressure gradient, virtual mass, Saffman lift, and drag attributable to gravity were considered.

Assuming that buoyancy and gravity forces are in equilibrium and that no other forces influence the bubble's motion, Darmana et al. (2006) derived the following analytical formula for the bubble's final rise velocity:

$$u_{b,z} = u_z + \sqrt{\frac{\sigma}{R\rho_c} + \frac{(\rho_c - \rho_b)|g_z|R}{\rho_c}}. \quad (5.14)$$

Under initial conditions and fluid quantities mentioned above, a final rise velocity of  $u_{b,z} = 0.23686$  m/s is obtained.

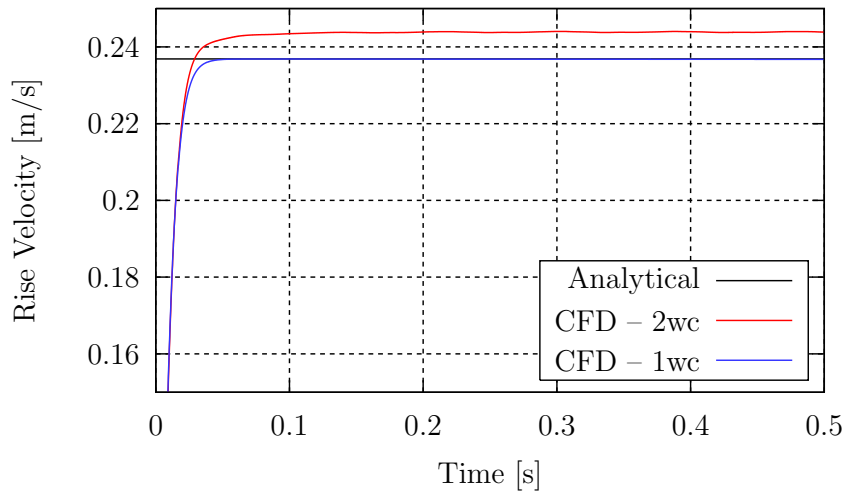


**Figure 5.55:** Rise velocity of the bubble from an analytical calculation and from simulations employing one-way (CFD – 1wc) and two-way coupling techniques (CFD – 2wc)

Figure 5.55 depicts the rise velocities for the analytical solution, as well as for simulations applying one-way and two-way coupling. The rise velocities on the ordinate are limited to the range of interest. For both simulations, the initially resting bubble was accelerated. In case of the one-way coupling, the rise velocity approached the analytical solution which verifies the correct numerical solution of the Lagrangian equation of motion. In the simulation applying two-way coupling, the bubble reached a velocity, about 3% higher than the analytically calculated velocity. Here, owing to the upward motion of the bubble and its interaction with the liquid phase, momentum was transferred to the liquid surrounding the bubble. As a consequence, the liquid was accelerated with the bubble, decreasing the relative velocity between the phases and reducing the drag force acting on the bubble.

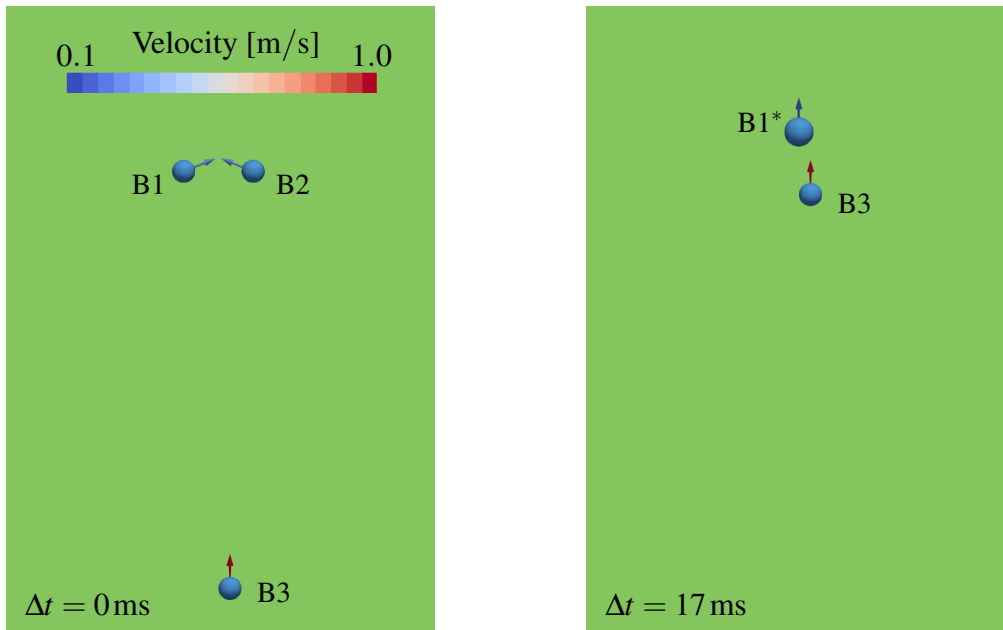
### 5.2.4 Lagrangian Bubble-Bubble Interaction

Large agglomerations of bubbles involve bubbles touching each other. Depending on their contact time, two bubbles may either coalesce or collide (see section 4.3.3). In a four-way coupled Euler-Lagrange approach, bubble-bubble interactions such as coalescence and collision are considered. The mechanisms, responsible for these interactions, were verified for a simple test case. Figure 5.56 shows the initial positions and velocity vectors of three bubbles of initial radius  $R = 0.5$  mm prior to two bubble contact situations at different times. Table 5.19 lists initial positions,  $\mathbf{x}_b$ , and velocities,  $\mathbf{u}_b$  of the three bubbles. To prescribe the bubble velocities, forces affecting the bubble motion were neglected. Figure 5.56 (left) shows the bubbles B1 and B2 approaching each other at  $\Delta t = 0$  ms. Figure 5.56 (right) shows a later time instance with rising bubble B1\*, resulting from the coalescence of bubbles B1 and B2, as well as bubble B3 rising at a higher velocity.

**Table 5.19:** Initial positions and velocities of Lagrangian bubbles

bubble	$\mathbf{x}_b$ [m]	$\mathbf{u}_b$ [m/s]
B1	(0, -0.0015, 0.02)	(0, 0.25, 0.1)
B2	(0, 0.0015, 0.02)	(0, -0.25, 0.1)
B3	(0, 0.0005, 0.002)	(0, 0, 1)

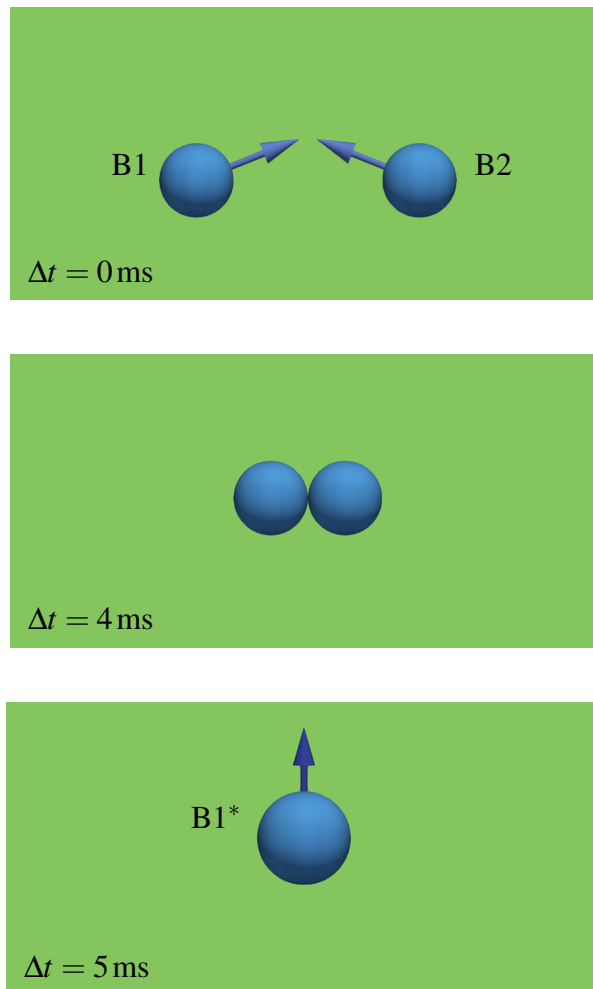
Figure 5.57 depicts the process of coalescence of two Lagrangian bubbles (see Figure 5.56 (left)). The two bubbles approach each other and touch after  $\Delta t = 4$  ms. The time needed for the two bubbles to coalesce is  $\tau_{12} = 3.04$  ms. To identify, whether the bubbles coalesce or collide, their collision is evolved, calculating new velocities and positions. Therein, multiple steps of collision are tested until the time of coalescence is exceeded or the bubbles move away from each other. In this case, the two bubbles cannot separate each other within  $\tau_{12}$  and coalesce into a larger bubble, B1\*, containing the sum of the volumes of bubbles B1 and B2. The velocity of the new bubble B1\* is  $\mathbf{u}_b = (0, 0, 0.1)$ .



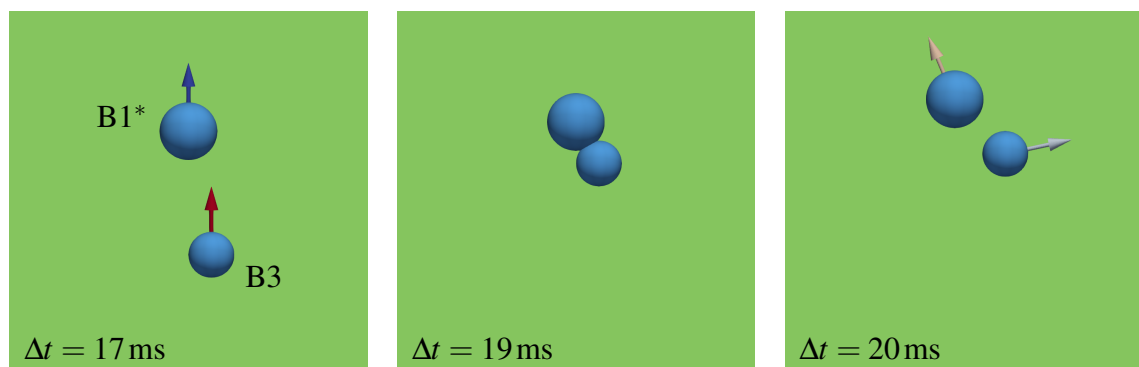
**Figure 5.56:** Lagrangian bubble positions and directions of motion prior to a process of coalescence (left) and prior to a process of collision (right) for a simulation utilising bubble-bubble interaction

Figure 5.58 shows the collision of two Lagrangian bubbles. The initial situation is equal to the situation depicted in Figure 5.56 (right). Bubble B3 rises at a higher velocity than bubble B1\*. After  $\Delta t = 19 \text{ ms}$ , the bubbles collide. For the bubbles to coalesce, their time of collision needed to be longer than  $\tau_{12} = 3.58 \text{ ms}$ . Owing to the high bubble velocity of bubble B3, the contact time of the two bubbles is smaller than  $t_{c,12} < 1.5 \text{ ms}$  resulting in bubble collision. The new velocities of bubble B1\* and B3 were  $(0, -0.231, 0.551)$  and  $(0, 0.462, 0.099)$ , respectively.

## 5.2 Euler-Lagrange Method



**Figure 5.57:** Coalescence of two Lagrangian bubbles into one larger bubble of new velocity



**Figure 5.58:** Collision of two Lagrangian bubbles of different sizes; after collision, both bubbles change their velocities

### 5.2.5 Internal Nozzle Flow

On the basis of simulations conducted with the Euler-Euler approach (see section 5.1.3), the Euler-Lagrange approach was used to numerically investigate the flow passing through an axisymmetric nozzle. Here, simulations were conducted using a two-way coupling approach because simulations based on a four-way coupling approach would have led to a severe increase of computational time. The present numerical investigations pursue the analyses of cavitation erosion for an axisymmetric nozzle of Peters et al. (2018b). The converged flow field from an Euler-Euler simulation obtained using grid G2, comprising of  $0.723 \cdot 10^6$  CVs (see Table 5.9), generated the initialisation for the Euler-Lagrange simulations. A time step of  $\Delta t = 250$  ns was used to obtain average Courant numbers of less than  $2 \cdot 10^{-3}$  and maximum Courant numbers of less than 0.7. In an Euler-Lagrange simulation, each Lagrangian bubble represents a cavitation nucleus. In all simulations, an initial radius of  $R_0 = 10 \mu\text{m}$  was chosen for all Lagrangian bubbles. The nuclei density was defined by setting the rate of nuclei per second through a cross-sectional area in the inlet cylinder. Simulations of nuclei densities from  $n_0 = 1 \cdot 10^9/\text{m}^3$  to  $1 \cdot 10^{11}/\text{m}^3$  were conducted. To calculate density and viscosity of the homogeneous mixture, the vapour volume fraction was obtained by indirectly distributing the vapour volume from Lagrangian bubbles onto the numerical grid using a transport equation (see section 4.3.1).

Table 5.20 lists numerical results obtained using different nuclei densities,  $n_0$ .  $\bar{V}_{v,L}^*$  is the time-averaged normalised vapour volume in the domain obtained after distribution of the Lagrangian vapour volume. The behaviour of cavitation was considerably influenced by  $n_0$ . A shedding frequency was identified for all but the simulation using  $n_0 = 1 \cdot 10^9 \text{m}^{-3}$ , where oscillations did not show a harmonic behaviour. Increasing the nuclei density by two orders of magnitude from  $1 \cdot 10^9 \text{m}^{-3}$  to  $1 \cdot 10^{11} \text{m}^{-3}$  resulted in an increase of the time-averaged normalised vapour volume of more than three orders of magnitude. On the contrary, a variation of  $n_0$  in the Sauer and Schnerr (2000) cavitation model by five orders of magnitude resulted in a change of time-averaged vapour volume by a factor of about two (see section 5.1.2, Table 5.7). For the Euler-Lagrange simulations, an increase of  $n_0$  further resulted in a reduction of the shedding frequency. A simultaneous increase of vapour volume and decrease of shedding frequency is in accordance with numerical results presented in section 5.1.2, Table 5.7 and Table 5.8. Further analyses focused on simulations using  $n_0 = 5 \cdot 10^{10} \text{m}^{-3}$  and  $n_0 = 1 \cdot 10^{11} \text{m}^{-3}$  of reasonable equivalent vapour volume.

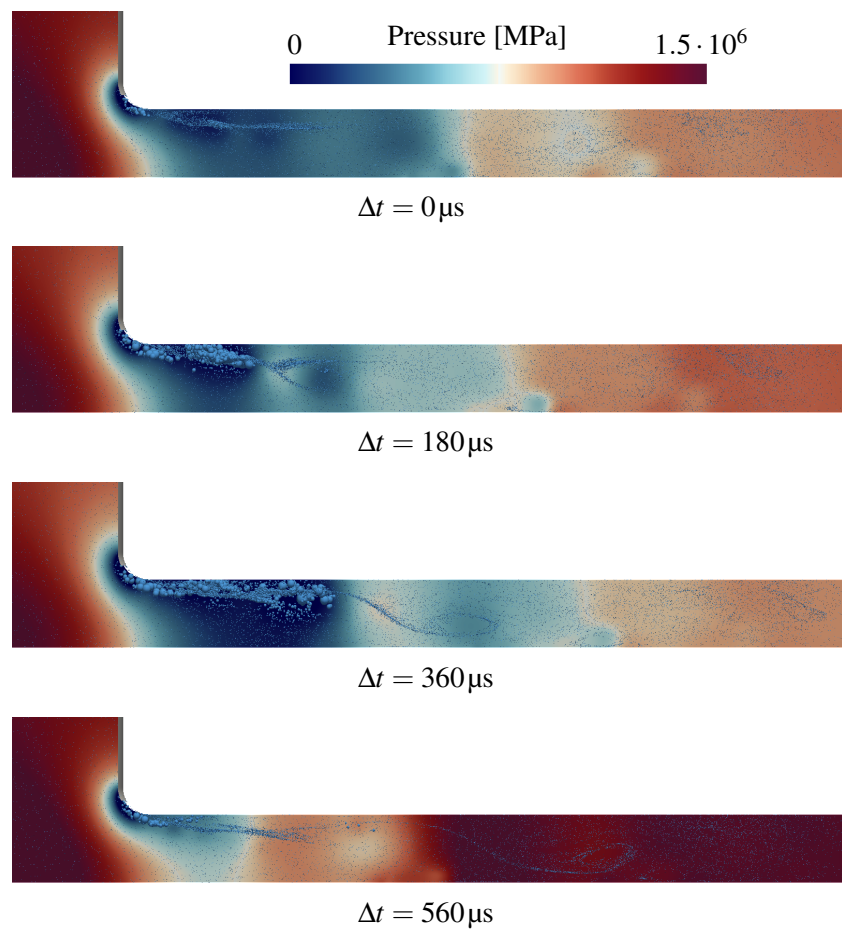
Figure 5.59 displays the generation and collapse of cloud cavitation for  $n_0 = 5 \cdot 10^{10} \text{m}^{-3}$  from side view into the nozzle. The pressure is plotted on a plane normal to the circumference. Cavitation bubbles started to grow at the connecting radius between inlet cylinder and outlet channel. In this region, the lowest pressures in the domain were reached. Between  $\Delta t = 180 \mu\text{s}$  and  $360 \mu\text{s}$ , vortices generated from the connecting radius further downstream leading to agglomerations of cavitation bubbles inside them. At about  $\Delta t = 360 \mu\text{s}$ , the cavitation region elongated to its largest size. After about  $\Delta t = 560 \mu\text{s}$ , cavitation bubbles started to collapse consecutively, from positions further downstream to positions close to the connecting

## 5.2 Euler-Lagrange Method

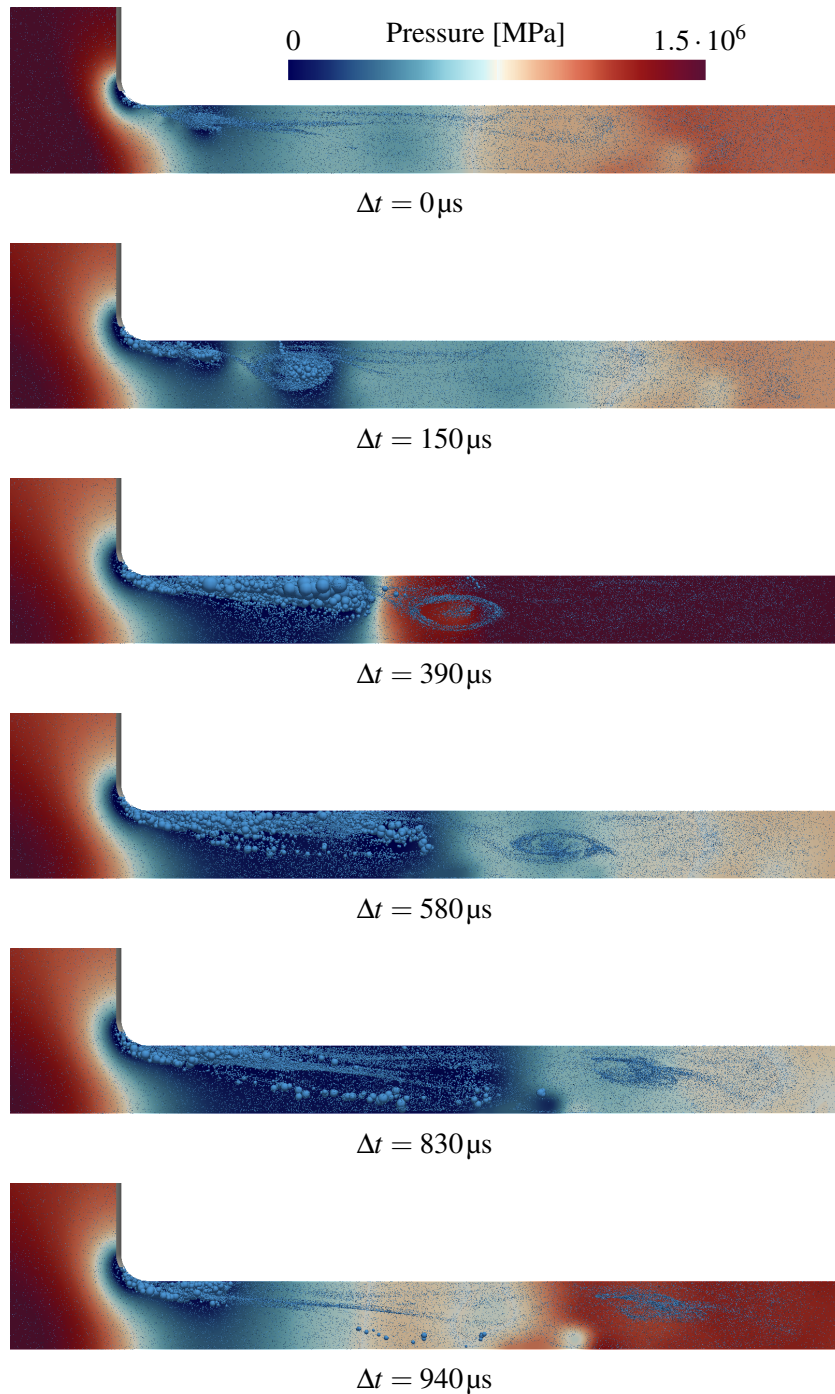
radius. Bubble collapses took place only close to the top boundary but not near the bottom boundary.

**Table 5.20:** Numerical results of cavitation behaviour for different nuclei densities

$n_0$ [1/m <sup>3</sup> ]	$\bar{V}_{v,L}^*$ [-]	$f_v$ [Hz]
$1.0 \cdot 10^9$	$4.5 \cdot 10^{-9}$	-
$1.0 \cdot 10^{10}$	$4.5 \cdot 10^{-8}$	8391
$2.5 \cdot 10^{10}$	$1.5 \cdot 10^{-7}$	4630
$5.0 \cdot 10^{10}$	$2.9 \cdot 10^{-6}$	1684
$1.0 \cdot 10^{11}$	$1.7 \cdot 10^{-5}$	1043



**Figure 5.59:** Generation of cavitation clouds and vortices, collapse of cavitation cloud near the top surface from side view for  $n_0 = 5 \cdot 10^{10} \text{ m}^{-3}$



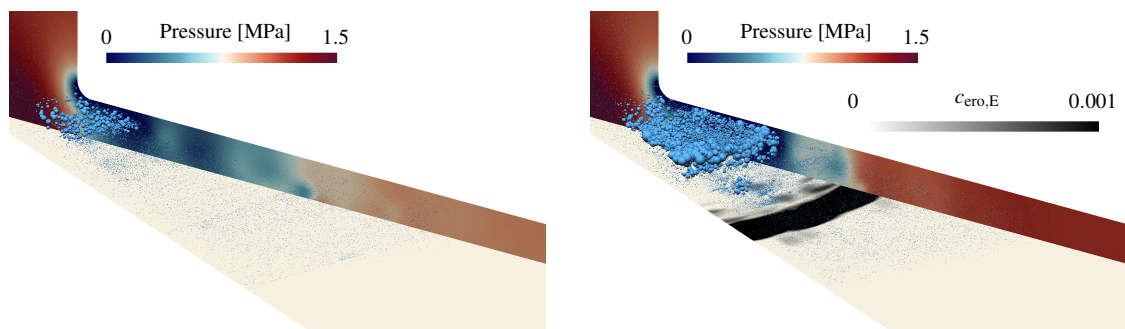
**Figure 5.60:** Generation of cavitation clouds and vortices, collapse of cavitation bubbles near the bottom surface from side view for  $n_0 = 1 \cdot 10^{11} \text{ m}^{-3}$

Figure 5.60 shows the generation of clouds and vortices as well as bubble collapses for  $n_0 = 1 \cdot 10^{11} \text{ m}^{-3}$  from side view into the nozzle. From  $\Delta t = 0 \mu\text{s}$  to  $150 \mu\text{s}$ , a vortex formed downstream from the connecting radius. Cavitation bubbles accumulated in the low pressure region of the vortex, travelling further downstream with it. The cloud collapsed after about

## 5.2 Euler-Lagrange Method

390  $\mu\text{s}$ . Thereby, from  $\Delta t = 150 \mu\text{s}$  to  $\Delta t = 390 \mu\text{s}$ , a second circulation region formed at the connecting radius, without detaching from it. Single cavitation bubbles were transported to the bottom surface at  $\Delta t = 830 \mu\text{s}$ . In the second circulation region, bubbles did not accumulate in form of a dense cloud. After  $\Delta t = 940 \mu\text{s}$ , similar to the simulation with  $n_0 = 5 \cdot 10^{10} \text{ m}^{-3}$ , bubbles started to collapse consecutively, from locations further downstream towards the connecting radius. In this case, bubbles collapsed in the vicinity of the bottom surface representing potential candidates for erosion impacts.

Figure 5.61 depicts the bubble distribution for cases of  $n_0 = 5 \cdot 10^{10} \text{ m}^{-3}$  (left) and  $n_0 = 1 \cdot 10^{11} \text{ m}^{-3}$  (right) from perspective view into the nozzle. Using the microjet erosion model, Erosion was predicted from the distributed vapour volume fraction,  $\alpha_{v,L}$ , but not from information of Lagrangian bubble collapses. The erosion potential is plotted on the bottom boundary. For both simulations, time instances corresponding to a large vapour volume in the domain are shown. Bubbles overlapped in both cases owing to the two-way coupling approach. The vapour volume for the lower nuclei density was smaller by a factor of more than five compared to the higher nuclei density. For  $n_0 = 5 \cdot 10^{10} \text{ m}^{-3}$ , no characteristic erosion was predicted to occur on the bottom boundary because Lagrangian bubbles collapsed too far away from it. In the case of  $n_0 = 1 \cdot 10^{11} \text{ m}^{-3}$ , erosion was predicted in a region of 19 mm to 26 mm radial distance from the centre axis. This is in favourable agreement with the measured erosion of Franc and Riondet (2006).



**Figure 5.61:** Formation, shedding, and collapse of cavitation structures in the nozzle for  $n_0 = 5 \cdot 10^{10} \text{ m}^{-3}$  (left) and  $n_0 = 1 \cdot 10^{11} \text{ m}^{-3}$  (right) from perspective view

Although results of the simulation using an Euler-Lagrange method for  $n_0 = 1 \cdot 10^{11} \text{ m}^{-3}$  seemed promising with respect to erosion prediction, multiple problems were encountered:

- *Computational effort:* Computational times were almost two orders of magnitude larger using the Euler-Lagrange approach. For the regarded simulation, using the Euler-Lagrange method, 0.55 time steps were computed per hour and CPU core. In contrast, for a simulation using the Euler-Euler method, 36.87 time steps were calculated per hour and CPU core. Despite the possibility to decompose a large number of Lagrangian

bubbles into multiple CPU cores, the simulation times for the Euler-Lagrange approach could not be further enhanced.

- *Nuclei density*: The nuclei density largely influenced cavitation behaviour. Without information about nuclei sizes and distributions, a validation of the method is difficult.
- *Vapour volume distribution*: Vapour volumes in the domain obtained from the Euler-Lagrange simulations were significantly lower than those obtained from the Euler-Euler simulations. The two main causes of this discrepancy are the influence of nuclei density on the cavitation behaviour as well as the difficulty to distribute the vapour volume, contained in the Lagrangian bubbles, onto the Eulerian mesh. Especially in regions where large numbers of bubbles overlapped, non-physical behaviour may have resulted from the distribution of the vapour volume into the Eulerian frame.

These reasons lead to different suggestions of possible solutions. Using an Euler-Lagrange method incorporating a four-way coupling, bubbles would interact with each other – collide or coalesce – instead of overlapping. A higher nuclei density would therefore not necessarily lead to a larger vapour volume in the domain because of the ability of bubbles to coalesce or collide. The distribution of the vapour volume, contained in the Lagrangian bubbles, into the Eulerian framework, would be trivial. For the regarded case, a four-way coupling approach was found to be computationally too expensive.

With regard to these reasons, to benefit from the more accurate simulation of bubble behaviour using a Lagrangian approach, while maintaining computational efficiency, a combination of an Eulerian and Lagrangian treatment of the vapour phase seemed encouraging.

### 5.2.6 Conclusion

Dynamics of a bubble exposed to a surrounding acoustic field were examined. Calculated radii agreed well with radii obtained from measurements of Ohl et al. (1999). Bubble motions and dynamics were verified for a bubble in a vortex-induced flow considering different forces affecting the bubble's momentum. For a bubble rising in a liquid column, its motions were verified by comparison with an analytical solution. Employing a two-way coupling, the bubble interacted with the flow and, as expected, the bubble's rise velocity increased. Bubble-bubble interactions were verified for different cases of touching bubbles enabling simulations using a four-way coupled Euler-Lagrange approach. For different Lagrangian nuclei densities,  $n_0$ , two-way coupled Euler-Lagrange simulations of the flow passing through an axisymmetric nozzle were performed. With increasing nuclei density, the time-averaged vapour volume increased and the cavitation shedding frequency decreased significantly. For a nuclei density of  $n_0 = 1 \cdot 10^{11}$ , erosion was numerically predicted using the Eulerian-based microjet approach and agreed favourably with measurements of Franc and Riondet (2006). Remarkably greater computational times paired with a strong dependence of the cavitation behaviour on nuclei density led to the development of a hybrid multi-scale approach combining an Eulerian with a Lagrangian treatment of the vapour phase.

## 5.3 Hybrid Multi-Scale Method

Results obtained from the hybrid multi-scale method (see section 4.4) are presented. Initially, mechanisms to transform vapour volumes between the Eulerian and Lagrangian frameworks are verified for a simple test case. Using the hybrid method, the flow through an axisymmetric nozzle is simulated and compared to results obtained from Euler-Euler and Euler-Lagrange simulations. The influence of model parameters is analysed concerning cavitation behaviour. Finally, an erosion prediction based on collapses of Lagrangian bubbles, according to the approach proposed in section 4.5.2, is compared to erosion measurements. Part of the work presented in this section can be found in Peters and el Moctar (2019) (paper under review).

### 5.3.1 Coalescence of a Lagrangian and an Eulerian Vapour Volume

To demonstrate the ability of the developed hybrid approach to transform a vapour volume from the Lagrangian to the Eulerian framework and vice versa (see section 4.4.1), the process to merge a small Lagrangian bubble with a larger almost spherical vapour structure in the Eulerian framework was simulated. To visualise this transformation between frames, the solution of the equations of bubble motion and bubble dynamics for the Lagrangian bubbles was deactivated. The velocity of the Lagrangian bubble was predefined, such that it moved with constant velocity in the direction of the Eulerian vapour structure.

Figure 5.62 illustrates the coalescence of a spherical Lagrangian bubble (identified by a small blue coloured sphere) with an Eulerian vapour volume (distinguished by a gray coloured shape) followed by the collapse of this Eulerian vapour volume and its subsequent transformation into a Lagrangian bubble. At time  $\Delta t = 0\mu\text{s}$ , the Lagrangian bubble approached the Eulerian vapour structure and coalesced with it at time  $\Delta t = 20\mu\text{s}$ . Then, the complete vapour volume of the Lagrangian bubble was transformed into the Eulerian frame. The influence of the coalesced Lagrangian bubble on the shape of the vapour volume remained until, at time  $\Delta t = 50\mu\text{s}$ , the Eulerian vapour structure began to collapse because the pressure surrounding the bubble greatly exceeded the vapour pressure. Furthermore, the action of gravity caused the bubble to deform asymmetrically in the vertical direction. Between times  $\Delta t = 130\mu\text{s}$  and  $\Delta t = 160\mu\text{s}$ , the Eulerian volume was transformed into a spherical Lagrangian bubble because the vapour volume decreased below the threshold volume related to the predefined bubble's limit radius of  $R_{\text{limit}} = 50\mu\text{m}$ .

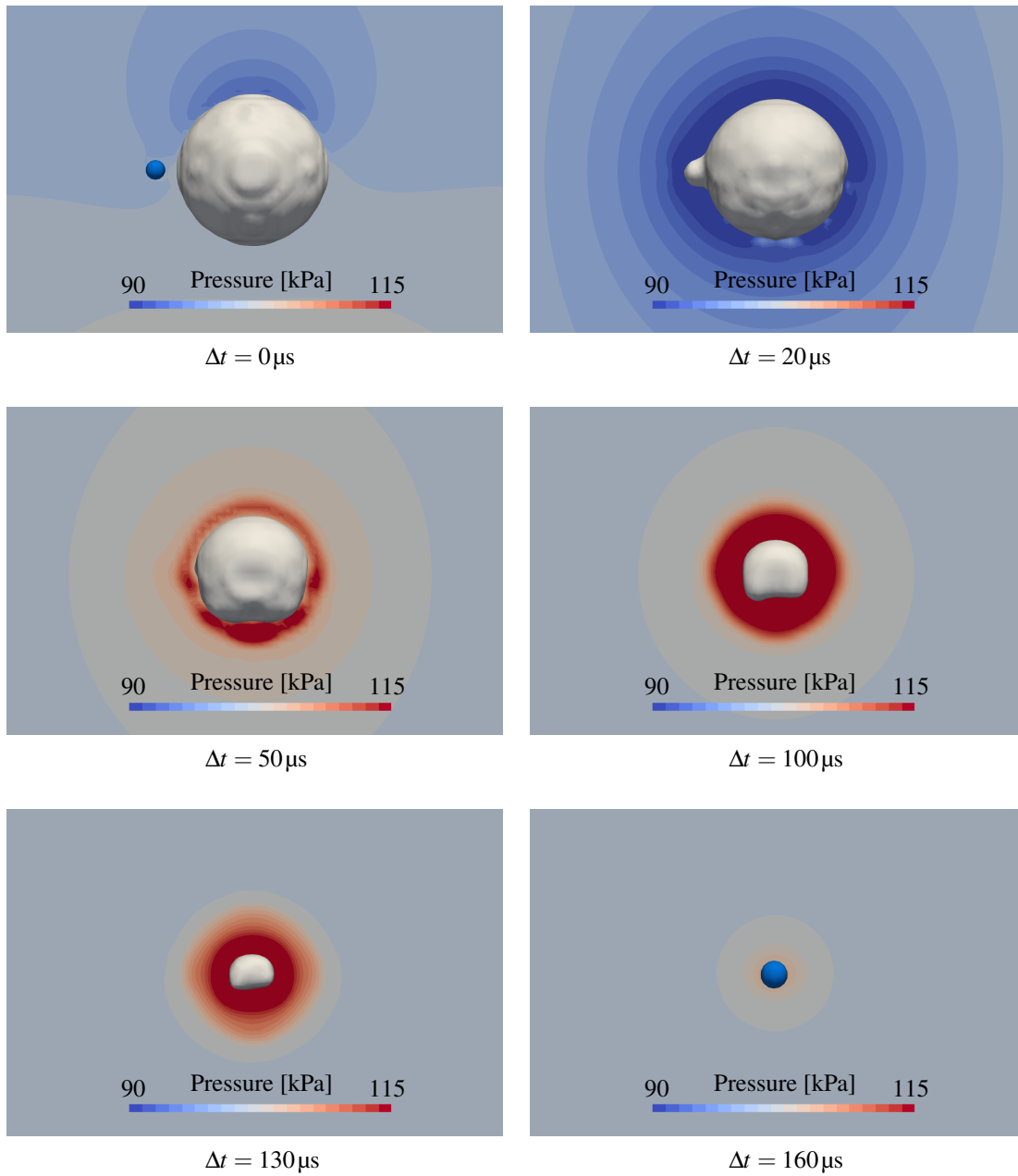


**Figure 5.62:** Coalescence of a single Lagrangian bubble with an Eulerian vapour volume, the collapse of the Eulerian vapour volume, and the vapour volume's subsequent transformation into a Lagrangian bubble

#### 5.3.2 Internal Nozzle Flow

The hybrid method used in this work unites an efficient Eulerian treatment of large vapour structures with a more accurate Lagrangian approach to simulate the behaviour of single spherical bubbles. Transformations of vapour volumes between the two frameworks are performed when the regarded predefined conditions are met (see section 4.4.1). Vapour structures are transformed into Lagrangian bubbles when their resolution by the mesh is not sufficient. Lagrangian bubbles are transformed into vapour volumes in the Eulerian framework conversely, when they grow to a sufficient size or merge with other Eulerian vapour structures.

#### Cavitation Prediction

The internal flow through an axisymmetric nozzle was simulated, enabling comparisons to results obtained from pure Euler-Euler and Euler-Lagrange simulations. All simulations using the hybrid multi-scale method were started from a previously converged Euler-Euler simulation on grid G2 of  $7.23 \cdot 10^5$  control volumes (see section 5.1.3, Figure 5.20). To obtain a maximum Courant number of less than two and an average Courant number of about  $2.5 \cdot 10^3$ , a time step of  $\Delta t = 3.54 \cdot 10^{-7}$  s was specified. Figure 5.63 displays larger cavitation structures (blue) as well as Lagrangian bubbles (pink) in the domain at one time instance. Although the domain contained many Lagrangian bubbles, most of them were small until reaching regions of low pressure. At the time instance presented, single Lagrangian bubbles were introduced into the domain owing to vapour structures collapsing, splitting into smaller parts, or from the growth of small isolated vapour volumes. Afterwards, bubbles accumulated and started to form a larger vapour structure again. Figure 5.64 shows a time instance of Eulerian vapour structures detaching from a cavitation cloud in the Eulerian frame, collapsing afterwards, and transforming into a Lagrangian bubble.

Figure 5.65 shows the generation of a large scale vapour structure from individual bubbles (*View 1* from Figure 5.63). From time  $\Delta t = 0 \mu\text{s}$  to  $10.62 \mu\text{s}$ , bubbles moved to a low pressure region and grew, while other bubbles followed into this region. At time  $\Delta t = 3.54 \mu\text{s}$ , bubbles were already large enough to be transformed into the Eulerian framework. From time  $\Delta t = 3.54 \mu\text{s}$  to  $\Delta t = 31.86 \mu\text{s}$ , Lagrangian bubbles that were contacting the Eulerian vapour structure were consecutively transformed into the Eulerian framework and merged into the larger vapour structure.

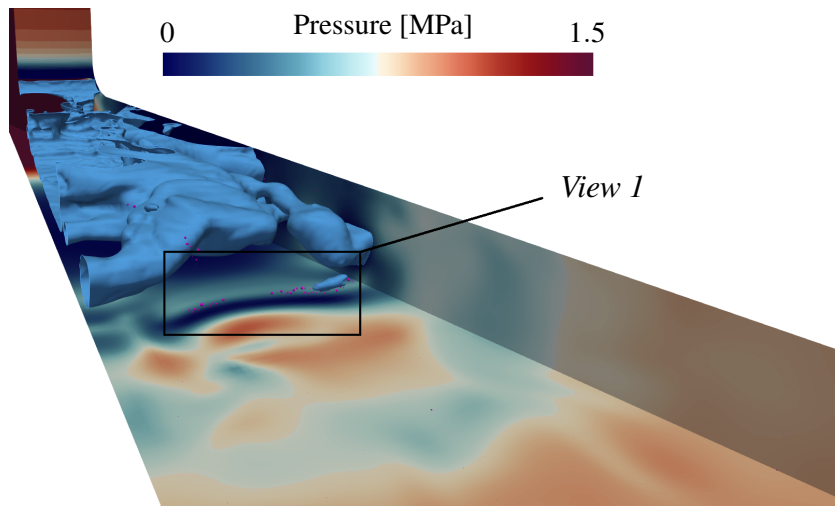


**Figure 5.63:** Perspective front view of Eulerian cavitation structures and Lagrangian bubbles inside the nozzle

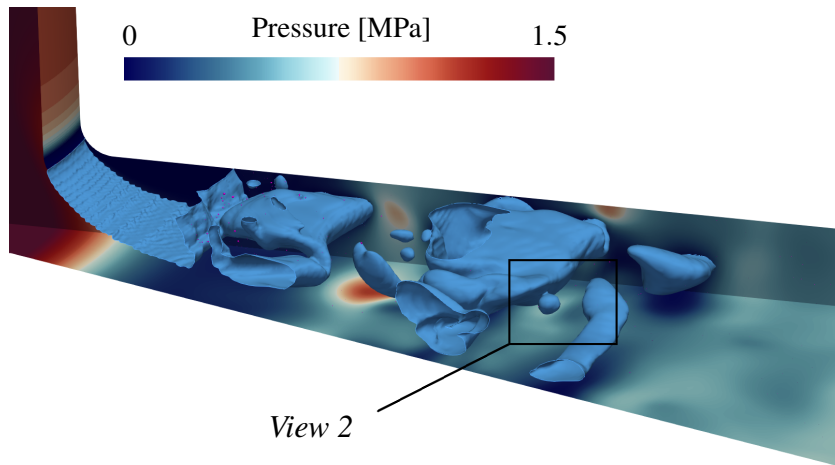


**Figure 5.64:** Perspective side view of Eulerian cavitation structures and Lagrangian bubbles inside the nozzle

### 5.3 Hybrid Multi-Scale Method

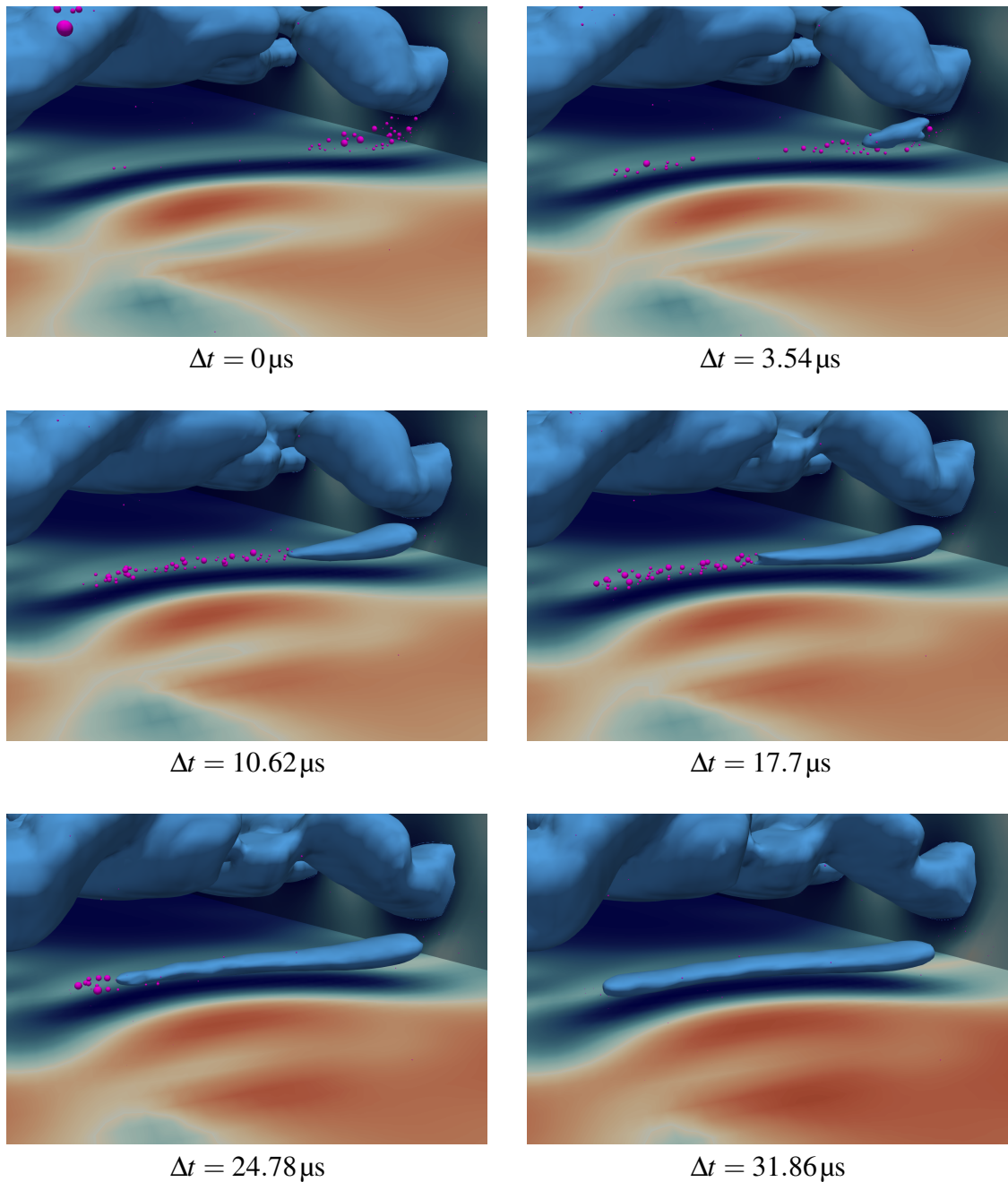


**Figure 5.65:** Lagrangian bubbles growing and forming a larger Eulerian vapour structure

Figure 5.66 illustrates the conversion of a vapour volume from the Eulerian into the Lagrangian framework (*View 2* from Figure 5.64). Between times  $\Delta t = 0\mu\text{s}$  and  $\Delta t = 7.02\mu\text{s}$ , a nearly spherical cavitation structure detached from a larger cavitation cloud. From  $\Delta t = 3.54\mu\text{s}$  to  $\Delta t = 10.62\mu\text{s}$ , the smaller structure detached from the larger cloud and collapsed. After a time of  $\Delta t = 7.02\mu\text{s}$ , the bubble achieved a size for which a sufficient grid resolution could not be maintained. As a result, the vapour volume was transformed into a spherical Lagrangian bubble of equivalent vapour volume.

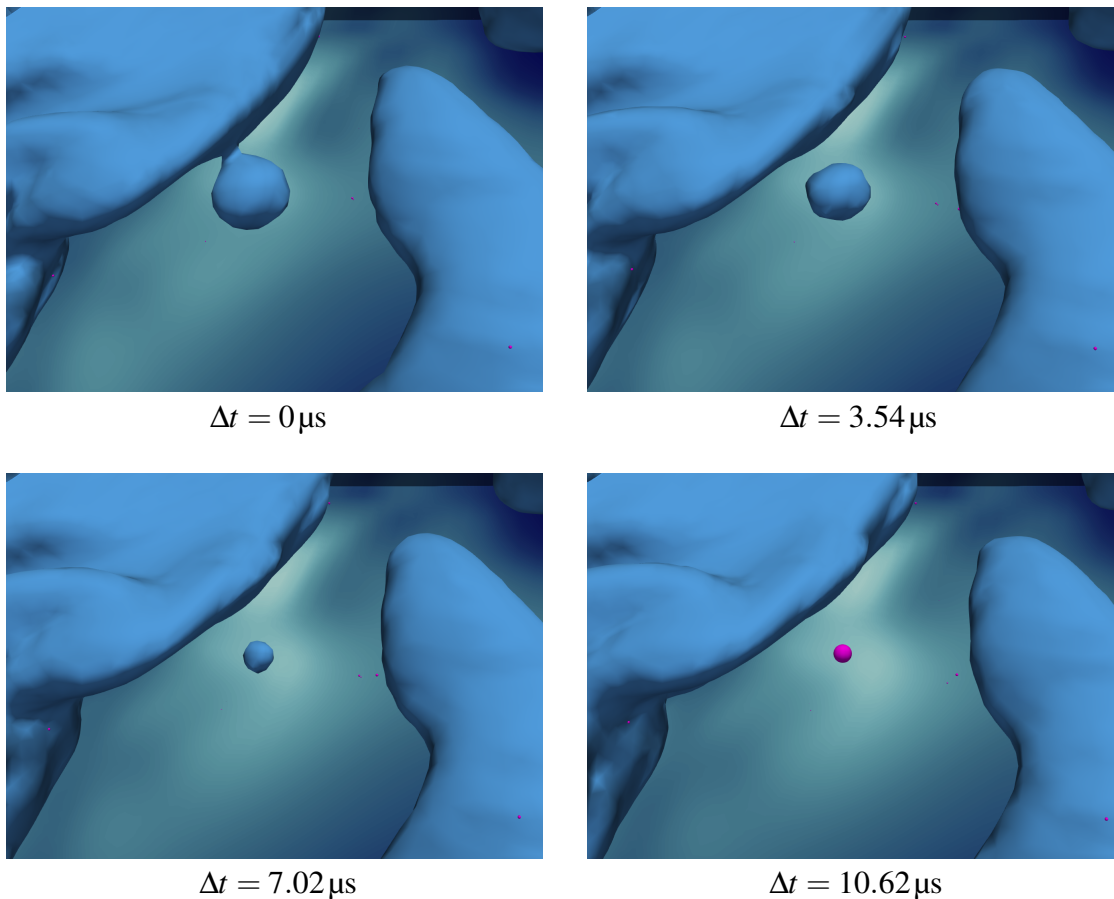


**Figure 5.66:** An Eulerian vapour volume detaching from a larger cloud, collapsing, and being transformed into a Lagrangian bubble

Recall that  $\alpha_{v,\text{limit}}$  is the limit value for identification of isolated vapour volumes and  $n_{\text{limit}}$  and  $R_{\text{limit}}$  are the limit number of cells and the limit radius for vapour transformation between frames, respectively (see section 4.4.1). The influence of these thresholds on the transformation processes was investigated. Lagrangian bubbles were transformed into the Eulerian frame, not only by growing above a specified threshold ( $n_{\text{limit}}$  or  $R_{\text{limit}}$ ), but also by merging into present Eulerian vapour structures. Table 5.21 lists the results of simulations conducted using the hybrid approach, specifically, the number of transformations into the Lagrangian frame per time step,  $n_{\text{EtoL}}/\Delta t$ , the number of transformations into the Eulerian frame per time step,  $n_{\text{LtoE}}/\Delta t$ , and the net number of bubbles added into the Lagrangian frame per time step,  $\Delta n/\Delta t = (n_{\text{EtoL}} - n_{\text{LtoE}})/\Delta t$ . For simulations H1, H2, and H3, only the threshold  $\alpha_{v,\text{limit}}$  varied. Although no clear dependence of the number of transformations on  $\alpha_{v,\text{limit}}$  was found, its increase yielded a greater net number of bubbles added into the Lagrangian frame per time step,  $\Delta n/\Delta t$ . Simulated cases H2, H4, and H5, differed only in the specified values of threshold  $n_{\text{limit}}$ . With a higher threshold related to the grid resolution,  $n_{\text{limit}}$ , more vapour volumes were transformed from the Eulerian to the Lagrangian frame and vice versa. Nevertheless, the net number of bubbles added into the Lagrangian frame did not clearly depend on  $n_{\text{limit}}$ . In contrast to the other simulations, case H7 used an absolute threshold radius of  $R_{\text{limit}} = 25 \mu\text{m}$  to

### 5.3 Hybrid Multi-Scale Method

evaluate transformations of vapour volumes. Compared to maximum radii achieved in other simulations, this threshold radius was about one order smaller. Fewer Eulerian vapour volumes were therefore transformed into the Lagrangian frame and a considerably smaller net number of Lagrangian bubbles was introduced. Cases H2, H6, and H8 differed only in the equilibrium radius specified. For simulation H8, the average equilibrium radius was larger than for simulation H2 and it was even larger for simulation H6. Increasing the equilibrium radius yielded a larger number of transformations between the frames in both directions, but decreased their difference per time step,  $\Delta n/\Delta t$ .

**Table 5.21:** Results of simulations using the hybrid multi-scale Euler-Lagrange method with different transformation thresholds (symbols defined above)

case	$\alpha_{v,\text{limit}}$	$n_{\text{limit}}$	$R_{\text{limit}}$	$R_0$	$n_{\text{EtoL}}/\Delta t$	$n_{\text{LtoE}}/\Delta t$	$\Delta n/\Delta t$
H1	0.01	8	–	1 $\mu\text{m}$	2.105	2.018	0.087
H2	0.05	8	–	1 $\mu\text{m}$	1.912	1.806	0.106
H3	0.10	8	–	1 $\mu\text{m}$	2.257	2.132	0.125
H4	0.05	14	–	1 $\mu\text{m}$	3.586	3.482	0.104
H5	0.05	22	–	1 $\mu\text{m}$	4.331	4.220	0.111
H6	0.05	8	–	10 $\mu\text{m}$	2.789	2.721	0.068
H7	0.05	–	25 $\mu\text{m}$	1 $\mu\text{m}$	0.346	0.324	0.022
H8	0.05	8	–	Spectra	2.148	2.065	0.083

Figure 5.67 presents the start of the time histories of the total number of Lagrangian bubbles inside the domain for cases H1, H2, and H3. Simulations started from a converged solution of an Euler-Euler simulation. In the beginning, for all cases, the number of Lagrangian bubbles increased until reaching an average number of bubbles at a time of about 0.03 s. This figure shows that the number of Lagrangian bubbles transformed between the two frames and the bubbles moving out of the outlet of the domain approached a value that, depending on the temporal behaviour of cavitation, varied only slightly.

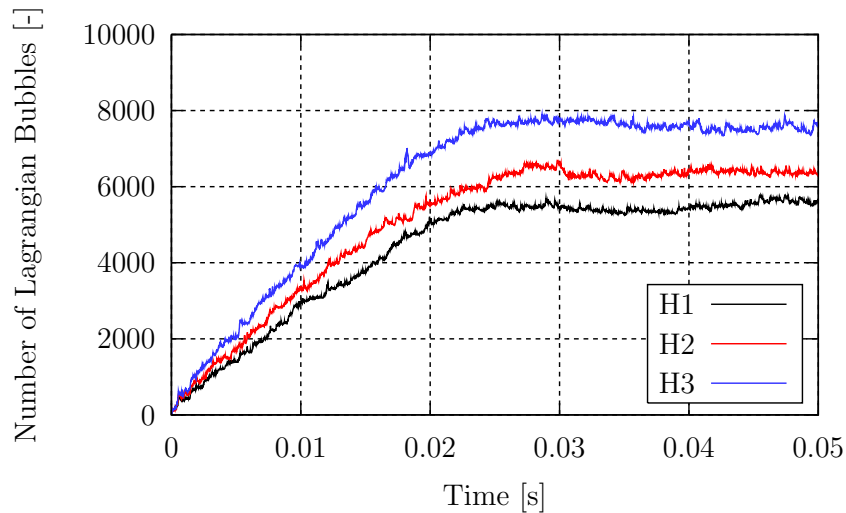


**Figure 5.67:** Time history of the total number of Lagrangian bubbles inside the simulation domain for different simulations

With the exception of simulation H6, for all hybrid simulations, the macroscopic cavitation behaved similarly compared to an Euler-Euler simulation with regard to the average cavitation volume, its temporal progress, and its characteristic frequencies. Accordingly, transformations of vapour volumes between the Eulerian and Lagrangian frames influenced the cavitation behaviour only on a microscopic scale. For simulation H6, a much larger equilibrium bubble radius and, thereby, a greater non-condensable gas content in the bubbles was specified. As a result, the vapour volume in the domain increased and augmented amplitudes of oscillations of the vapour volume occurred. Figure 5.68 plots time histories of vapour volumes in the domain for the Euler-Euler simulation and simulations H2 and H6 performed using the hybrid approach. Although the equilibrium radius of the Lagrangian bubbles differed, cases H2 and H6 used the same parameters for the hybrid model (see Table 5.21). The behaviour of macroscopic cavitation was similar for the Euler-Euler simulation and the hybrid simulation H2. For case H6, owing to the high gas content in the bubbles, large oscillations of vapour volume occurred and the average vapour volume increased significantly. For simulation H8, although the gas content and, thereby, the equilibrium radius was spectrally distributed, the macroscopic cavitation behaviour resembled not only the Euler-Euler simulation, but also all other hybrid simulations. The only exception was simulation H6.

### 5.3 Hybrid Multi-Scale Method

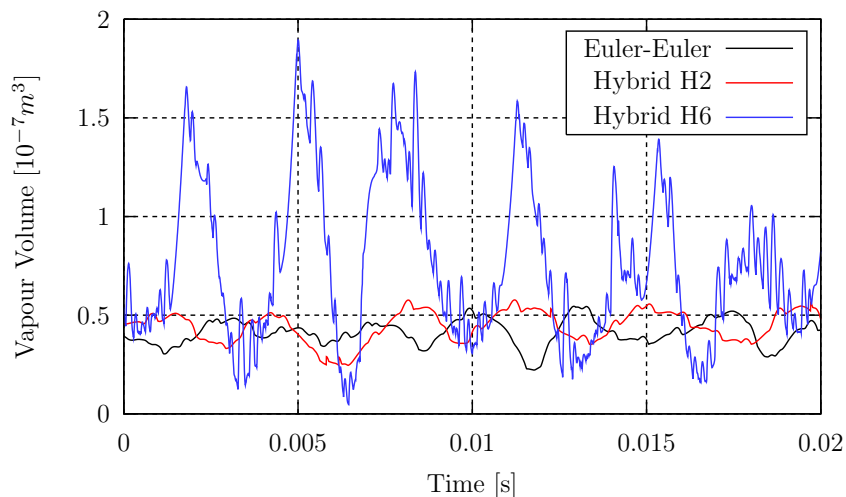


**Figure 5.68:** Temporal progress of vapour volume for simulations using an Euler-Euler approach and the hybrid multi-scale approach for cases H2 and H6

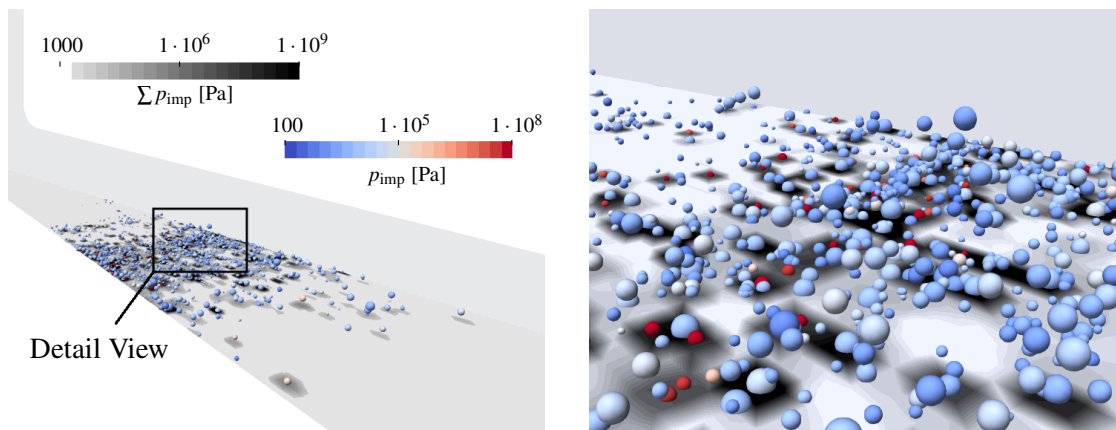
Simulations of the flow through an axisymmetric nozzle were conducted using a pure Euler-Euler, a pure Euler-Lagrange, and the developed hybrid approach. By limiting the Lagrangian treatment of the vapour phase to specific vapour volumes, the fully parallel hybrid approach efficiently employs the simulation of single Lagrangian bubbles. For the pure Euler-Lagrange simulation, Lagrangian bubbles were distributed with a nuclei density of  $n_0 = 5 \cdot 10^{10}$  and  $n_0 = 1 \cdot 10^{11}$ , while simulations performed using the Euler-Euler and the hybrid approach used the latter nuclei density in the cavitation model of Sauer and Schnerr (2000). Table 5.22 lists the number of processor cores,  $n_{\text{proc}}$ , and simulation times obtained from the different approaches, specifically, the number of flow time steps calculated per computational time,  $n_{\Delta t}/t_{\text{cpu,total}}$ , and the number of flow time steps calculated per computational time and per processor core,  $n_{\Delta t}/(t_{\text{cpu,total}} n_{\text{proc}})$ . As expected, the computational effort was lowest for the simulation performed using the pure Euler-Euler approach and highest for simulations conducted using the pure Euler-Lagrange approach. Although the computational time for simulations using the hybrid method were higher compared to a simulation using the pure Euler-Euler approach, its computational efficiency per processor core,  $n_{\Delta t}/(t_{\text{cpu,total}} n_{\text{proc}})$ , is more than one order of magnitude higher than for the Euler-Lagrange simulations. For the Euler-Lagrange simulations, the computational time increased with an increasing nuclei density,  $n_0$ . For the hybrid simulations, the computational time increased with increasing numbers of transformations between the Eulerian and Lagrangian frames. For simulation H4, during one time step of flow solution, more time was needed to perform transformations between the frames compared to simulation H8. Moreover, for all hybrid simulations, the algorithms that identified isolated vapour volumes and transformed these between the Eulerian and Lagrangian frames occupied the longest time during one time step. Further decomposition of a computational domain to use more than 24 processor cores was limited because it produced more vapour volumes overlapping processor boundaries (see Figure 4.7) and, thereby, decreased parallel efficiency.

**Table 5.22:** Processor times for simulations using a pure Euler-Euler, a pure Euler-Lagrange, and the hybrid multi-scale approach

approach	$n_{\text{proc}}$	$n_{\Delta t}/t_{\text{cpu,total}}$ [1/min]	$n_{\Delta t}/(t_{\text{cpu,total}} n_{\text{proc}})$ [1/h]
Euler-Euler	48	29.50	36.87
Euler-Lagrange, $n_0 = 5 \cdot 10^{10}$	240	3.16	0.79
Euler-Lagrange, $n_0 = 1 \cdot 10^{11}$	240	2.20	0.55
Hybrid H4	24	4.27	10.69
Hybrid H8	24	5.26	13.15

## Erosion Prediction

To predict erosion caused by the flow through the axisymmetric nozzle, bubbles collapsing in the fluid domain were identified and their quantities, such as collapse pressure, initial and final radii during collapse, and bubble position, were stored. The procedure then consisted of calculating pressures impacting the rigid target plate. For case H4, considering dimensionless stand-off distances of  $\gamma \leq 3.0$ , Figure 5.69 visualises Lagrangian bubble collapses impacting on the target plate using their initial radii at the beginning of the associated collapses. The blue to red colouring and a logarithmic scale identify impact pressures,  $p_{\text{imp}}$ , associated with bubble collapses; different shades of grey and another logarithmic scale, the sum of impact pressures on the bottom boundary,  $\sum p_{\text{imp}}$ . A circumscribed region of the target plate was covered by impacts of Lagrangian bubble collapses. In the close-up view, shown in the right graph of Figure 5.69, darker gray colours on the bottom target plate identify areas of the target plate subject to erosion. Faces neighbouring collapses of high impact pressures and/or multiple collapses were predicted to have the highest damage potential. Moreover, bubbles collapsing in larger distances from the bottom boundary ( $\gamma \geq 1.5$ ) seldom caused high impact pressures.

**Figure 5.69:** Lagrangian bubble collapses displayed as spherical bubbles using their maximum radii prior to collapse in far view (left) and detail view (right)

### 5.3 Hybrid Multi-Scale Method

A more quantitative statistical erosion prediction is obtained by evaluation of collapse impacts in circumferential direction of the nozzle at different radial intervals. Franc and Riondet (2006) measured the depth of erosion in terms of mass loss on this area of the target plate. Based on an interval length of 1 mm, their moving averaging technique obtained the distribution of penetration depth over the radial distance from the central axis of the nozzle. For comparison purposes, radial intervals were chosen to be of the same length to evaluate Lagrangian collapse impacts. Here, all faces which were multiply impacted were considered. For case H4, Figure 5.70 exemplarily plots the number of impacts (normalised against the maximum number of collapse impacts),  $n_{\text{imp}}/n_{\text{imp,max}}$ , versus the radial distance from the nozzle's central axis,  $r$ , obtained for different thresholds of dimensionless collapse distances of  $\gamma \leq 1$ ,  $\gamma \leq 3$ , and  $\gamma \leq 5$ . The legend in this figure lists the maximum number of collapse impacts associated with each simulation. Bubbles collapsed mostly between radial distances of 15 to 30 mm. For larger collapse distances, the distribution of predicted impacts turned out to be broader banded and, also, a greater number of impacts were predicted.

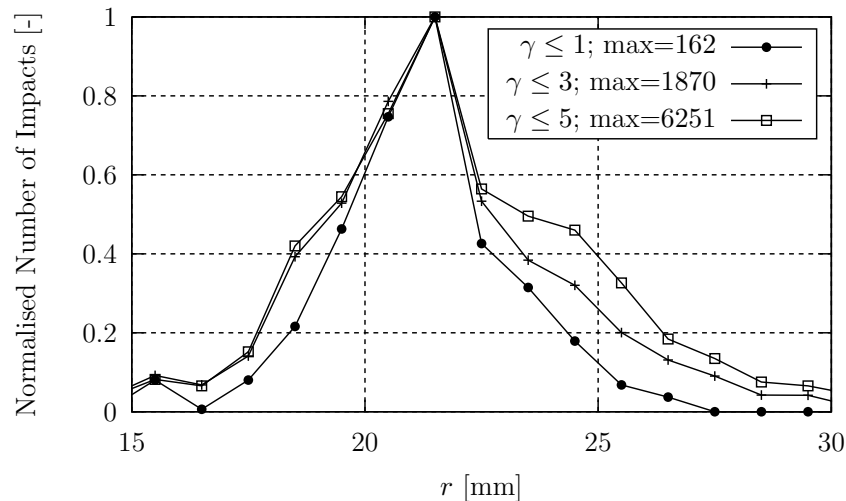


**Figure 5.70:** Normalised number of impacts for different collapse distance thresholds versus radial distance from the nozzle's centre axis for case H4

To investigate the influence of the parameters listed in Table 5.21 on the simulation of Lagrangian bubble collapses, Figure 5.71 exemplarily plots distributions of the number of impacts per time versus the radial distance from the nozzle's central axis for  $\gamma \leq 3$  and for cases H1 to H4, case H7, and case H8. Despite small deviations in the distributions' shapes, in all cases the highest number of impacts was predicted between radial distances of 21 to 22 mm. The number of impacts per unit time increased as  $\alpha_{v,\text{limit}}$  and  $n_{\text{limit}}$  increased and as the average equilibrium radii decreased. Comparing the parameters listed in Table 5.21, it seemed obvious that the number of impacts per unit time increased as  $\alpha_{v,\text{limit}}$  from simulation H1 to H2 and from simulation H2 to H3 increased and as  $n_{\text{limit}}$  from simulation H2 to H4 increased. For simulation H7, the lowest number of calculated impacts correlated well with the fact that,

for this case, the number of transformations from Eulerian to Lagrangian vapour volumes,  $n_{\text{EtoL}}/\Delta t$ , was smallest.

Franc and Riondet (2006) reported that they did not consider pits with diameters smaller than  $20\ \mu\text{m}$ , because their contribution to overall erosion was too low. The largest pit they found had a diameter of  $220\ \mu\text{m}$  and the characteristic pit diameter leading to most surface erosion was between  $80$  and  $100\ \mu\text{m}$ . In numerical simulations of single bubbles near a solid wall considering fluid-structure interaction, Chahine (2014a) investigated the dependence of pit radius on the maximum bubble radius at the beginning of a collapse. They found that the radius of a generated pit is similar to the bubble radius at the beginning of a collapse.

More than 95 % of the calculated bubble collapses occurred at maximum diameters between  $20$  and  $180\ \mu\text{m}$  for simulations H1, H2, and H3; for simulation H4, between  $20$  and  $400\ \mu\text{m}$ ; for simulation H7, between  $20$  and  $50\ \mu\text{m}$ ; for simulation H8, between  $20\ \mu\text{m}$  and  $1\ \text{mm}$ . Maximum collapse radii were smaller for simulation H7 because the maximum Lagrangian bubble size was limited by the transformation threshold  $R_{\text{limit}}$  and were larger for simulation H8 because the average equilibrium radii were larger compared to other cases. Presumably pit diameters are similar to initial bubble diameters. The calculated maximum bubble diameters agreed favourably with observations from Franc and Riondet (2006) and Chahine (2014a). For further comparisons, simulation H4 was considered because it comprised a large number of collapses and was considered to be statistically most reliable. Moreover, the maximum bubble diameters of this case correlated favourably with measured pit diameters.

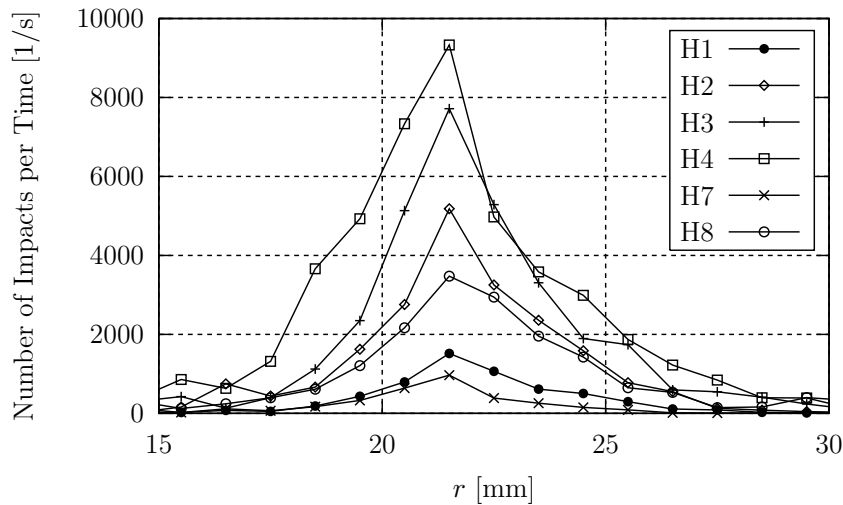


**Figure 5.71:** Number of impacts per time for different simulated cases versus radial distance from the nozzle's centre axis

For collapses of  $\gamma \leq 3$ , the erosion potential for Lagrangian bubbles,  $c_{\text{ero,L}}$ , (see (4.100), section 4.5.2) was calculated. Additionally, the erosion potential from an Euler-Euler simulation,  $c_{\text{ero,E}}$ , (see (4.88), section 4.5.1) was calculated for the same case based on the microjet model. Summing the erosion potentials,  $c_{\text{ero}}$ , of all faces in each radial interval yielded the erosion as

### 5.3 Hybrid Multi-Scale Method

a function of the radial distance,  $r$ , from the nozzle's centre axis. Figure 5.72 plots, as functions of  $r$ , the erosion potential,  $c_{\text{ero},E}$ , obtained from a pure Euler-Euler simulation (using the Eulerian erosion model), the erosion potential,  $c_{\text{ero},L}$ , obtained from a simulation based on the multi-scale approach (using the Lagrangian erosion model), and the experimentally measured erosion depths of Franc and Riondet (2006). Maximum values of potentials obtained from the multi-scale method and from the Euler-Euler simulation compared favourably to maximum values of measured erosion depths (Exp.); however, the overall distribution of erosion potential from the Lagrangian prediction was narrower and agreed more closely with measured erosion depths. For collapse distances of  $\gamma < 1$ , far lesser impacts occurred than for collapse distances of  $1 \leq \gamma \leq 3$ . However, only collapses of  $\gamma < 1$  were able to exceed the yield strength of the stainless steel 316L target plate of  $\sigma_y = 400\text{MPa}$ , i.e. the material Franc and Riondet (2006) used in their experiments. It is concluded that the calculated collapses close to the surface were most aggressive. This is in agreement with experimental investigations on near-wall cavitation bubble collapses of Vogel and Lauterborn (1988), Isselin et al. (1998), Philipp and Lauterborn (1998), and Dular et al. (2018) who found that near-wall collapses are most aggressive and that, for bubble collapses occurring at distances of  $\gamma > 2$ , almost no erosion takes place.

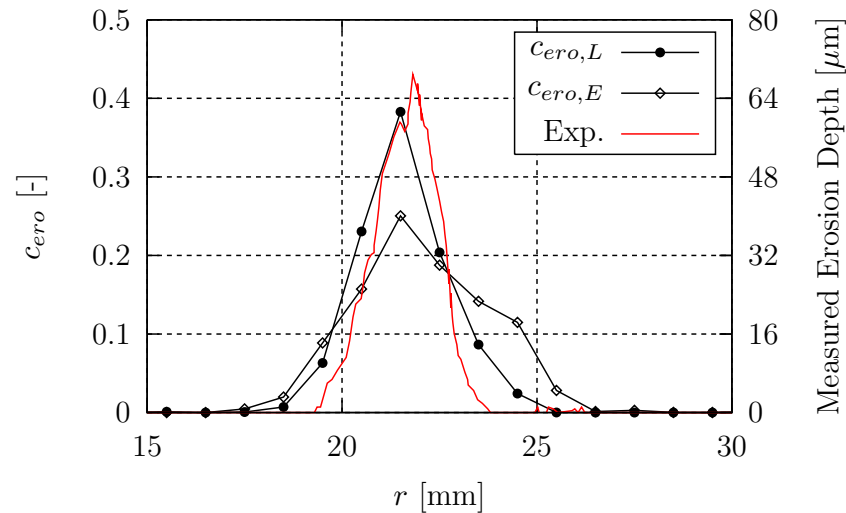


**Figure 5.72:** Numerical erosion predictions obtained from case H4 using the multi-scale method with a Lagrangian erosion model ( $c_{\text{ero},L}$ ) and using an Eulerian erosion model ( $c_{\text{ero},E}$ ) and comparative measured erosion depths of Franc and Riondet (2006) (Exp.) plotted against radial distance from the nozzle's central axis

Recall that mass loss of material from an impacted surface depends non-linearly on impact loads (see (4.101), section 4.5.2). Thus, an erosion coefficient proportional to the impact pressure squared was proposed (see (4.102)). Although most of the predicted impact pressures did not necessarily exceed the yield strength of  $\sigma_y = 400\text{MPa}$  for stainless steel 316 L, it was assumed that all collapses within  $\gamma \leq 3$  impacted the surface of the target plate. To compare, the coefficient,  $c_{\text{ero},L2}$ , was calculated by summing the coefficients from all other faces within

radial intervals of 1 mm. Figure 5.73 plots, as functions of  $r$ , these coefficients, assuming a linear dependence,  $c_{ero,L}$ , and a non-linear dependence of erosion on impact pressure,  $c_{ero,L2}$ , together with measured erosion depths of Franc and Riondet (2006). Although the assumption of a quadratic proportionality in (4.102) is rough, the erosion prediction was improved and agreed more favourably with measured erosion depths, demonstrating that the non-linear dependence of erosion on impact pressures is valid. Considering this non-linear pressure dependence, the area of erosion was predicted to be narrower because not only most impacts, but also the impacts of highest pressures occurred at radial distances between 21 to 22 mm from the nozzle's central axis.

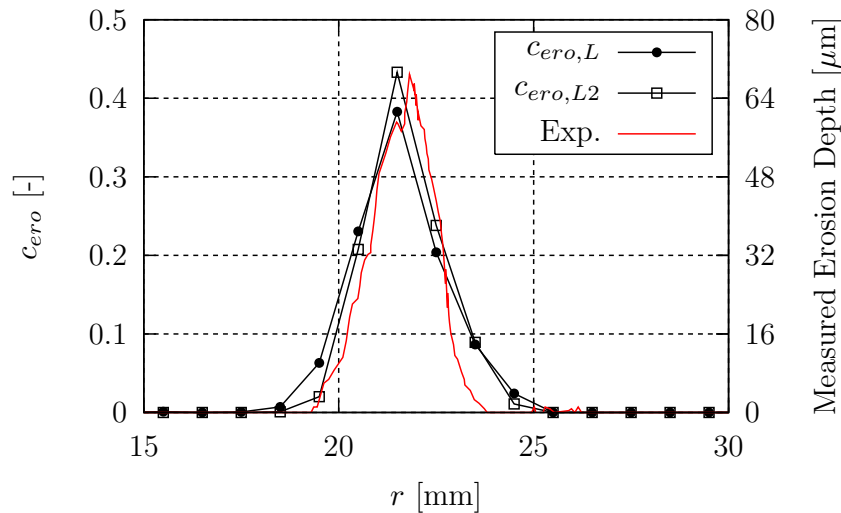


**Figure 5.73:** Numerical erosion predictions obtained from case H4 using the multi-scale method with a Lagrangian erosion model assuming a linear dependence ( $c_{ero,L}$ ) and assuming a non-linear dependence on impact pressure ( $c_{ero,L2}$ ) and comparable measured erosion depths of Franc and Riondet (2006) (Exp.) plotted against radial distance from the nozzle's central axis

### 5.3.3 Conclusion

Cavitating flow was numerically simulated using a multi-scale Euler-Lagrange approach to predict cavitation erosion based on Lagrangian bubble collapses. The multi-scale approach treated large vapour volumes on an Eulerian grid; small vapour volumes, as spherical Lagrangian bubbles. To gain insight into bubble behaviour, the dynamics and motions of each Lagrangian bubble were solved individually. For one simple case and for the flow through an axisymmetric nozzle, the transformation mechanisms demonstrated the conversion of Eulerian vapour volumes into Lagrangian bubbles and vice versa. To simulate the cavitating flow through an axisymmetric nozzle, various characteristic parameters of the multi-scale solver were considered and their influence on cavitation behaviour and erosion prediction was identified. Although the average number of Lagrangian bubbles differed in all cases, these bubbles

### *5.3 Hybrid Multi-Scale Method*

did not influence the macroscopic behaviour of cavitation. With the exception of a constant nucleus diameter of 10  $\mu\text{m}$ , all simulations showed that the behaviour of macroscopic cavitation was alike and compared favourably to cavitation from a pure Euler-Euler simulation. As the distribution of cavitation nuclei can largely influence cavitation behaviour, a measurement-based distribution of nuclei based on experiments of Reuter et al. (2018) was used to provide the gas content of Lagrangian bubbles without considering additional assumptions. Erosion predictions obtained from Lagrangian bubble collapses agreed favourably with measured erosion depths of Franc and Riondet (2006). Moreover, maximum collapse radii correlated well with pit diameters considering investigations of Franc and Riondet (2006) and Chahine (2014a). Assuming a non-linear dependence of the erosion prediction on impact pressures of Lagrangian bubble collapses yielded an even better agreement with measured erosion pits.

## 6 Conclusions and Outlook

For hydrodynamic flows, numerical predictions of cavitation-induced erosion were performed using Euler-Euler and multi-scale Euler-Lagrange methods. Cavitation erosion leads to lower efficiencies of damaged components and results in higher energy consumption and higher repair and maintenance costs. To improve designs of technical applications exposed to cavitation erosion, more accurate numerical predictions are called for. Despite the occurrence of cavitation erosion for almost all materials in engineering flows, the developed methods give accurate predictions of cavitation erosion beyond the state of the art.

In this thesis, numerical approaches to simulate cavitation and predict erosion were reviewed and promising approaches were chosen for further development and applied to hydrodynamic flow problems. To model cavitation, Eulerian approaches to treat the vapour phase as a continuum and Lagrangian approaches to treat the vapour phase as an accumulation of discrete spherical bubbles were used. For an Euler-Euler approach, a microjet model and a spherical collapse model were developed that predict erosion based on pressure and vapour content in the flow. The erosion potential on a solid surface is, therein, calculated from the number of impacts and their intensities. Using these Eulerian-based approaches, cavitation erosion was numerically predicted for flows around a hydrofoil, inside an axisymmetric nozzle, and around a propeller. Numerical erosion predictions agreed favourably with experimental predictions for the flow around the hydrofoil and the propeller and with the measured erosion patterns for the axisymmetric nozzle case. After validation of the main components of an Euler-Lagrange approach to simulate bubble dynamics and motions, the method was applied to simulate the flow through an axisymmetric nozzle using different nuclei densities. A multi-scale Euler-Lagrange approach combined the advantages of an efficient Eulerian and an accurate Lagrangian treatment of the vapour phase and was implemented for the finite volume method used. Based on collapse dynamics of spherical Lagrangian bubbles, a more accurate approach to predict erosion impacts was developed that yielded locations, time instances, radii, and pressures during a bubble collapse. Compared to the Eulerian erosion prediction, for the cavitating flow through an axisymmetric nozzle, the impacts predicted based on Lagrangian bubble collapses agreed even better with measured erosion depths. Computed maximum bubble radii during collapse correlated fairly with measured pit diameters. A non-linear dependence of erosion on impact pressures was confirmed and, in comparison to measured erosion patterns, further improved the numerical erosion prediction. Paired with an erosion prediction based on Lagrangian bubble collapses, the multi-scale approach establishes a connection between the behaviour of macroscopic cavitation structures and near-wall bubble collapses that lead to erosion.

## 6.1 Conclusions

With special attention paid to phenomena related to hydrodynamic cavitation, background information about processes involved in cavitation and cavitation-induced erosion was given. Besides basic principles of cavitation inception and cavitation generation, cavitation structures that induce erosion were reviewed and mechanisms that lead to erosion during a near-wall cavitation bubble collapse were analysed. Scale effects of cavitation and erosion and dependencies of erosion processes on material properties were summarised. Appearances of cavitation and cavitation-induced erosion in maritime environments were highlighted.

A FVM flow solver for a continuous liquid phase builds the basis for the approaches used in the underlying work. Cavitation is modelled by treating the vapour phase as continuous in an Eulerian frame or as single bubbles in a Lagrangian frame, including a hybrid multi-scale method that combines the Eulerian with the Lagrangian approach for the vapour phase. In the Euler-Euler method, growth and decay of vapour volumes are modelled by source terms based on a simplified equation for bubble dynamics. For this approach, models were derived that predict cavitation erosion based on the flow quantities in the control volumes near a solid surface. Erosion potential is, therein, defined as a combination of the number of impacts in an area and the impact intensities. For the Euler-Lagrange method, dynamics and motions of each single Lagrangian bubble are calculated using forces exerted by the liquid phase. For a two-way coupled approach, interactions of cavitation bubbles with the liquid carrier fluid are accounted for by exchanging momentum and considering the flow properties of the homogeneous mixture. The implementation of bubble-bubble interaction in terms of coalescence and collision yields a four-way coupled Euler-Lagrange approach. Eulerian and Lagrangian approaches for the vapour phase were efficiently combined in a multi-scale method that, based on their absolute and relative sizes, transforms vapour volumes between the frames. In this method, to obtain the non-condensable gas content for the Lagrangian bubbles, a measurement-based distribution of cavitation nuclei was derived. To predict erosion, Lagrangian bubble dynamics are used to identify the exact locations and time instances, bubble radii, and bubble pressures during a bubble collapse. Motion and shock wave radiation during an asymmetric near-wall bubble collapse are accounted for by modelling these processes according to experimental investigations. Similar to the Eulerian erosion prediction, the number of collapse impacts and the collapse pressures are used to calculate erosion potential.

Various hydrodynamic flow problems were numerically investigated using a pure Euler-Euler, a pure Euler-Lagrange, and a multi-scale Euler-Lagrange method. An Euler-Euler approach yielded results of cavitating flows around differently shaped hydrofoils, inside an axisymmetric nozzle, and around a propeller. The numerical method was validated for the flow around a NACA 0009 modified hydrofoil. Numerically obtained cavitation shedding frequency, force coefficients, and pressure distributions agreed well with results from measurements. For the flow around a NACA 0015 hydrofoil, when decreasing the cavitation number or increasing the nuclei density of the Eulerian cavitation model, the average vapour volume in the domain increased, while the shedding frequency decreased. Comparisons of numerical erosion predictions with measurements using a coating technique to predict erosion showed fair agreements.

For the flow through an axisymmetric nozzle, sensitivities of the erosion model were studied. The numerical erosion prediction agreed well with measured erosion patterns. Simulations of the model-scale propeller P1225 were performed in accordance with experiments. For the propeller in cavitating oblique flow, a fair agreement of calculated and measured forces was achieved. Areas predicted to be eroded agreed fairly with measurements for a cavitation number of  $\sigma_{\text{cav}} = 0.963$  and agreed well for a cavitation number of  $\sigma_{\text{cav}} = 1.464$ . Assumptions from literature that erosion rates depend on higher powers of geometric scale and on velocity were confirmed by numerically predicting erosion for the same propeller in full-scale. Overall, erosion predictions conducted using the Euler-Euler method agreed favourably with experimental observations.

To validate and verify the main components of the Euler-Lagrange approach, namely bubble dynamics and bubble motions, numerical exercises were performed for simple simulation cases. As part of a four-way coupling, the numerical solver was verified concerning collision and coalescence of Lagrangian bubbles. Considering different nuclei densities, a two-way coupled Euler-Lagrange approach was used to simulate the cavitating flow through an axisymmetric nozzle. With increasing nuclei density, both the frequency of cavitation shedding decreased and the average vapour volume increased significantly. The computational effort of the two-way coupled pure Euler-Lagrange method was remarkably higher than for either the pure Euler-Euler or the multi-scale Euler-Lagrange method. As a result, four-way coupled Euler-Lagrange simulations of the flow through the axisymmetric nozzle could not be conducted within reasonable time.

For the multi-scale Euler-Lagrange method, transformation mechanisms were analysed for a simplified case and for the flow through an axisymmetric nozzle. Parameters influencing these transformations were studied for the nozzle flow with respect to the number and the sizes of Lagrangian bubbles in the numerical domain. With the exception of a constant nucleus diameter of  $10\ \mu\text{m}$ , simulations using a nucleus diameter of  $1\ \mu\text{m}$  and using the measurement-based nuclei distribution showed that the behaviour of macroscopic cavitation compared favourably to the cavitation behaviour obtained from a pure Euler-Euler simulation. The measurement-based nuclei distribution enables to perform multi-scale simulations without further assumptions regarding the initial gas content in cavitation bubbles. Based on Lagrangian bubble collapses, erosion was predicted on a target surface of the nozzle for different transformation thresholds. The distribution of numerically predicted impacts agreed well with measured erosion patterns. Computed maximum bubble radii during collapse correlated fairly with measured pit diameters. The hypothesis of a non-linear dependence of erosion pits on impact pressures was confirmed for the numerical erosion prediction and yielded a better agreement with the measured erosion pattern.

### 6.1.1 Summary of Author's Contributions

A summary of the author's own contributions within this thesis is given below:

- Implementation:
  - Equations for bubble dynamics (4.8), (4.9),(4.11) and of an iterative solver using adaptive time-stepping (see section 4.1.1)
  - Volume variation force (4.21) for Lagrangian bubbles and drag force for rising Lagrangian bubbles (4.24) (see section 4.1.2)
  - Correction of turbulent viscosity according to Reboud et al. (1998) and correction of vapour pressure according to Singhal et al. (2002) (see section 4.2.2)
  - Different approaches to distribute the vapour volume of Lagrangian bubbles to the Eulerian grid (direct or indirect) to calculate the homogeneous mixture quantities (see section 4.3.1)
  - Exchange of momentum between Lagrangian bubbles and carrier fluid (see section 4.3.2)
  - Coalescence of Lagrangian bubbles for four-way coupled Euler-Lagrange simulations (see section 4.3.3)
  - Hybrid multi-scale method that captures large vapour volumes on an Eulerian frame and small vapour volumes as spherical Lagrangian bubbles, similar to Vallier (2013), Lidtke (2017), and Ma et al. (2017) (see sections 4.4 and 7.1). The method was fully parallelised (see section 7.2).
  - Measurement-based nuclei distribution to specify the non-condensable gas content of Lagrangian bubbles (see section 4.4.3)
- Development:
  - Eulerian erosion models based on the microjet hypothesis, Dular and Coutier-Delgosha (2009) and Dular et al. (2006), and based on a spherical bubble collapse, Franc and Michel (2005), were further developed and implemented (see section 4.5.1)
  - Lagrangian erosion model based on spherical Lagrangian bubble collapses was developed and implemented (see section 4.5.2)
- Simulation: All simulations presented in chapter 5

## 6.2 Outlook

Design improvements to prevent cavitation-induced erosion require an accurate quantitative prediction in terms of incubation periods and material removal rates. Besides the lower accuracy of the Eulerian-based erosion prediction compared to the Lagrangian-based prediction, information about the number of bubble collapses and the spatial and temporal resolution of these collapses is missing as well. A quantitative prediction, therefore, relies on information gained from more accurate approaches, such as the presented multi-scale Euler-Lagrange method that predicts erosion impacts based on Lagrangian bubble collapses. Con-

necting collapse-rates of Lagrangian bubbles to measured erosion-rates would pave the way to a quantitative prediction. In this regard, the Eulerian-based erosion prediction could be improved to estimate the number of bubble collapses per area and time. Furthermore, the efficient Eulerian-based erosion models can be combined with any pressure-based cavitating flow solver.

After the identification of basic influences of the transformation parameters in the multi-scale Euler-Lagrange method, further investigations should aim to study dependences of cavitation behaviour and Lagrangian collapses on spatial and temporal discretisation. To improve the proposed Lagrangian erosion model, future numerical and experimental work is needed to gather additional information about single bubble collapses and to identify dependences of erosion patterns on absolute bubble size, stand-off distance, driving pressure, and material properties. Moreover, the developed multi-scale method enables specifying input data for simulations of isolated asymmetric bubble collapses. Further plans call for applying the developed multi-scale approach to predict cavitation behaviour and erosion for more complex flow problems, such as ship propellers.

## 7 Appendix

### 7.1 Algorithm for Identification of Isolated Eulerian Vapour Volumes

---

**Algorithm 3:** Algorithm to identify coherent vapour bubbles

---

```
Create hash table bubble-IDs (key: cell-ID; value: bubble-ID)
Create hash table bubble-cells (key: bubble-ID; value: list(cell-ID))
Create list vapour-cells with cell-ID of all cells with  $\alpha_{v,E} \geq \alpha_{v,limit}$ 
Create maximum-bubble-ID = 0
for all vapour-cells do
    Create list connected-cells
    Create minimum-bubble-ID = maximum-bubble-ID
    for all neighbours of cell-ID do
        if found neighbour-ID in bubble-IDs then
            Append neighbour-ID to list connected-cells
            Update minimum-bubble-ID
        end
    end
    if size(connected-cells) = 0 then
        Create key for cell-ID in bubble-IDs with value maximum-bubble-ID
        Create key for maximum-bubble-ID in bubble-cells with value cell-ID
        Increase maximum-bubble-ID by 1
    else if size(connected-cells) = 1 then
        Create key for cell-ID in bubble-IDs with value bubble-ID of connected-cell
        Append cell-ID to key of connected-cell in bubble-cells
    else if size(connected-cells) > 1 then
        Update entries of connected-cells in bubble-IDs to minimum-bubble-ID
        Append all connected-cells to key minimum-bubble-ID in bubble-cells
        Remove former entries of all connected-cells in bubble-cells
        Create key for cell-ID in bubble-IDs with value minimum-bubble-ID
        Append cell-ID to key minimum-bubble-ID in bubble-cells
    end
end
```

---

The algorithm to identify coherent vapour volumes, implemented in the present work, is based on the algorithm developed by Vallier (2013). In this algorithm, *hash tables* are used to organise the identification of coherent vapour bubbles. Hash tables are characterised by couples

of keys and values. The advantage of a hash table lies in the quick access to data through any given string which is transformed into a key using a *hash function*. At the beginning of the algorithm, the hash tables `bubble-IDs` and `bubble-cells` are defined. Here, all coherent vapour structures are referred to as bubbles because they are candidates for transformations into spherical Lagrangian bubbles. `bubble-IDs` stores the indices of cells (`cell-ID`) as a key and the indices of bubbles (`bubble-ID`) as an integer value. Using this hash table, it can be identified whether a cell has already been added to a coherent vapour bubble and, if so, which index belongs to this bubble. `bubble-cells` stores the `bubble-ID` as a key and the list of cell indices connected within this coherent vapour bubble as a value. This hash table serves to quickly access all cells incorporated in a coherent vapour bubble. The list `vapour-cells` is initialised, storing the IDs of all cells containing a minimum vapour volume fraction ( $\alpha_{v,E} \geq \alpha_{\text{limit}}$ ). A for-loop over all elements in `vapour-cells` is started to find all connected vapour-filled cells and, thereby, all coherent vapour bubbles which are candidates for transformation into Lagrangian bubbles. For every cell in `vapour-cells`, all neighbouring cells are examined whether they have already been registered within a coherent vapour bubble and, thereby, added to `bubble-IDs`. `minimum-bubble-ID` is updated whenever a neighbouring cell belongs to a vapour bubble of lower `bubble-ID`. Depending on how many neighbouring cells are already part of other bubbles, different commands are executed. If no other neighbouring cell is part of a vapour bubble, a new key according to the current `cell-ID` is added in `bubble-IDs` with the `maximum-bubble-ID` as a value. In `bubble-cells` a key for the `maximum-bubble-ID` is created with the current `cell-ID` as a value. In case exactly one neighbouring cell is part of a bubble, a key of the current `cell-ID` is generated in `bubble-IDs` using the same `bubble-ID` as a value as for the neighbour cell. In the hash table `bubble-cells`, the current `cell-ID` is appended to the list of cells corresponding to the `bubble-ID` key. For more than one neighbouring cell being part of a coherent vapour bubble, all keys of these `cell-IDs` in the hash table `bubble-IDs` are updated with the `minimum-bubble-ID` and an entry for the current `cell-ID` is made. The indices of all neighbouring cells and the current cell are moved to the same list corresponding to the `minimum-bubble-ID` key in `bubble-cells`.

## 7.2 Algorithm to Organise Communication in Parallel Simulations

---

### Algorithm 4: Algorithm to organise parallel communication for bubble identification

---

Make lists of local interface bubbles on each processor

Gather data of interface bubbles from all processors to master processor

On master processor, create a list for global indexing of interface bubbles from all processors

From master processor, go through all processors and execute:

```

for all interface bubbles on the source processor do
  for all interface bubbles on neighbouring slave processors do
    if interface bubbles on source and slave processor are connected then
      if one interface bubble is found in global index list then
        Update other interface bubble with same global ID
        Update ID of interface bubble on local processor
      else
        Create new entry in global index list with information from local interface bubbles
        Update IDs of interface bubbles on local processors
      end
    else
      Continue with next interface bubble on slave processor
    end
  end
end

```

---

At the start of the algorithm, all bubbles in contact with a processor boundary/processor interface, referred to as interface bubbles, are identified on each processor. Thereby, the IDs of faces and cells located at the processor interface, and of the local interface bubble are stored. Afterwards, from the master processor which organises communication over processor interfaces, all information corresponding to the local interface bubbles is gathered and a list is created to organise the global connection and indexing of interface bubbles. Because all information needs to be gathered to and scattered from the master processor, a loop over all processors is started from the master processor. For all interface bubbles on a *source processor* – first processor from which an interface bubble is chosen – the connections to interface bubbles on a neighbouring *slave processor* – second processor from which a bubble is chosen – are examined based on the positions of faces on the shared processor boundary. If two interface bubbles on different processors are connected, they are registered as one global interface bubble. In the case that one local interface bubble was already globally registered because it is connected to another vapour structure through another processor interface, all global indices of the coherent vapour bubble are updated as well as the IDs of the interface bubbles on the local processors. If no geometric connectivity between two interface bubbles exists, the next interface bubble on a neighbouring slave processor is examined.



## Bibliography

- Abdel-Maksoud, M., Hänel, D., and Lantermann, U. Modeling and Computation of Cavitation in Vortical Flow. *International Journal of Heat and Fluid Flow*, 31:1065–1074, 2010.
- Achkinadze, A. S. Supercavitating Propellers. In *RTO AVT Lecture Series on “Supercavitating Flows”*, Brussels, Belgium, 2001.
- Alyanak, E., Grandhi, R., and Penmetsa, R. Optimum Design of a Supercavitating Torpedo Considering Overall Size, Shape, and Structural Configuration. *International Journal of Solids and Structures*, 43(3-4):642–657, 2006. ISSN 00207683. doi: 10.1016/j.ijsolstr.2005.05.040.
- Apte, S. V., Shams, E., and Finn, J. a Hybrid Lagrangian-Eulerian Approach for Simulation of Bubble Dynamics. In *Proceedings of the 7th International Symposium on Cavitation*, number 74, 2009.
- Arndt, R. E. A., Arakeri, V. H., and Higuchi, H. Some observations of tip-vortex cavitation. *Journal of Fluid Mechanics*, 229:269–289, 1991. doi: 10.1017/S0022112091003026.
- Arndt, R. E. A., Song, C. C. S., Kjeldsen, M., He, J., and Keller, A. Instability of partial cavitation: A numerical/experimental approach. *National Academies Press*, 2000.
- Arndt, R. E. A., Kawakami, D., Wosnik, M., Perlin, M., Admiraal, D. M., and García, M. H. *Springer Handbook of Experimental Fluid Mechanics*, chapter Hydraulics. Springer, 2007. ISBN 978-3-540-25141-5.
- ASTM Standard G32-10. Standard Test Method for Cavitation Erosion Using Vibratory Apparatus. *ASTM International, West Conshohocken*, 2010.
- Auret, J. G., Damm, O. F. R. A., Wright, G. J., and Robinson, F. P. A. The pressure and velocity dependence of flow-type cavitation erosion. *Wear*, 170:185–190, 1993.
- Ausoni, P. *Turbulent Vortex Shedding from a Blunt Trailing Edge Hydrofoil*. PhD Thesis, EPFL, Lausanne, Switzerland, 2009.
- Auton, T. R. The Lift Force on a Spherical Body in a Rotational Flow. *Journal of Fluid Mechanics*, 183:199–218, 1987.
- Auton, T. R., Hunt, J. C. R., and Prud’Homme, M. The Force Exerted on a Body Moving in an Inviscid Unsteady Non-Uniform Rotational Flow. *Journal of Fluid Mechanics*, 183: 241–257, 1988.

- Berchiche, N., Franc, J. P., and Michel, J. M. A Cavitation Erosion Model for Ductile Materials. *Journal of Fluids Engineering*, 124(3):601, 2002. ISSN 00982202. doi: 10.1115/1.1486474.
- Berchiche, N., Grekula, M., and Bark, G. Concept of Focusing of Collapse Energy - Application to Cavitation Observations. In *Proceedings of the Fifth International Symposium on Cavitation*, 2003.
- Bernitt, M. and Heinke, H.-J. Freifahrt- und Kavitationsversuche mit dem Festpropellermodell P1225. Technical Report 1475, Schiffbau-Versuchsanstalt Potsdam, 1983.
- Besant, W. *Hydrostatics and Hydrodynamics*. Cambridge University Press, 1859.
- Billet, M. L., Turnock, S. R., Briançon-Marjollet, L., Chang, B. J., Friesch, J., and Wilczynński, L. The Specialist Committee on Cavitation Erosion on Propellers and Appendages on High Powered/High Speed Ships. In *Proceedings of the 24th ITTC - Volume II*, 2005.
- Biluš, I., Bizjan, B., Lešnik, L., Širok, B., Pečnik, B., and Dular, M. Non-Contact Method for Analysis of Cavitating Flows. *Ultrasonics*, 81(March):178–186, 2017. ISSN 0041624X. doi: 10.1016/j.ultras.2017.03.011.
- Bjerknes, V. *Die Kraftfelder*. Friedrich Vieweg und Sohn, Braunschweig, 1909.
- Blake, J. R. Bjerknes Forces in Stationary Sound Fields. *The Journal of the Acoustic Society of America*, 21(5):551, September 1949a.
- Blake, J. R. The Onset of Cavitation in Liquids. Technical Report 12, Acoustics Res. Lab., Harvard Univ., 1949b.
- Boussinesq, J. Essai sur la théorie des eaux courantes. *Mémoires présentés par divers savants à l'Académie des Sciences*, 23(1):1–680, 1877.
- Brackbill, J. U., Kothe, D. B., and Zemach, C. A Continuum Method for Modeling Surface Tension. *Journal of Computational Physics*, 100:335–354, 1992.
- Brehm, A., Uhlenbrock Janse, S., Wienke, J., and el Moctar, O. Teilprojekt MICRUD im Verbundvorhaben “Hydrodynamische und strukturmechanische Untersuchung von Rudern großer, schneller Schiffe (XXI-Ruder)”. Technical Report NB-EF 2009.060, Germanischer Lloyd AG, 2009.
- Brennen, C. E. *Cavitation and Bubble Dynamics*, volume 9. 1995. ISBN 0195094093. doi: 10.1017/CBO9781107338760.
- Brennen, C. E. *Fundamentals of Multiphase Flows*. Cambridge University Press, 2005. ISBN 0521 848040.
- Briggs, L. J. Limiting Negative Pressure of Water. *Journal of Applied Physics*, 21(7):721–722, 1950. ISSN 00218979. doi: 10.1063/1.1699741.

## Bibliography

- Brujan, E. A., Keen, G. S., Vogel, A., and Blake, J. R. The Final Stage of the Collapse of a Cavitation Bubble Close to a Rigid Boundary. *Physics of Fluids*, 14(1):85–92, January 2002.
- Budich, B., Schmidt, S. J., and Adams, N. A. Numerical simulation and analysis of condensation shocks in cavitating flow. *Journal of Fluid Mechanics*, 838:759–813, 2018. doi: 10.1017/jfm.2017.882.
- Callenaere, M., Franc, J.-P., Michel, J.-M., and Riondet, M. The Cavitation Instability Induced by the Development of a Re-entrant Jet. *Journal of Fluid Mechanics*, 444:223–256, 2001.
- Caretto, L. S., Gosman, A. D., Patankar, S. V., and Spalding, D. B. Two calculation procedures for steady, three-dimensional flows with recirculation. In *Proceedings of the Third Int. Conf. Numer. Methods Fluid Dyn., Paris, France, 1972*.
- Carnelli, D., Karimi, A., and Franc, J.-P. Application of Spherical Nanoindentation to Determine the Pressure of Cavitation Impacts from Pitting Tests. *Journal of Materials Research*, 27(1):91–99, 2012. ISSN 08842914. doi: 10.1557/jmr.2011.259.
- Chahine, G. L. *Advanced Experimental and Numerical Techniques for Cavitation Erosion Prediction*, chapter Modeling of Cavitation Dynamics and Interaction with Material. Springer, 2014a. ISBN 978-94-017-8538-9.
- Chahine, G. L. *Advanced Experimental and Numerical Techniques for Cavitation Erosion Prediction*, chapter Modeling of Material Response. Springer, 2014b. ISBN 978-94-017-8538-9.
- Chahine, G. L. and Hsiao, C.-T. Modelling Cavitation Erosion Using Fluid–Material Interaction Simulations. *Interface Focus*, 5(5):1–21, 2015. ISSN 20428901. doi: 10.1098/rsfs.2015.0016.
- Chahine, G. L., Franc, J.-P., and Karimi, A. *Advanced Experimental and Numerical Techniques for Cavitation Erosion Prediction*, chapter Cavitation and Cavitation Erosion. Springer, 2014a. ISBN 978-94-017-8538-9.
- Chahine, G. L., Franc, J. P., and Karimi, A. *Advanced Experimental and Numerical Techniques for Cavitation Erosion Prediction*, chapter Mass Loss and Advanced Periods of Erosion. Springer, 2014b. ISBN 978-94-017-8538-9.
- Chesters, A. K. and Hofman, G. Bubble Coalescence in Pure Liquids. *Applied Scientific Research*, 38:353–361, 1982.
- Choi, J. K., Jayaprakash, A., and Chahine, G. L. Scaling of Cavitation Erosion Progression with Cavitation Intensity and Cavitation Source. *Wear*, 278-279:53–61, 2012. ISSN 00431648. doi: 10.1016/j.wear.2012.01.008.
- Church, C. C. A Method to Account for Acoustic Microstreaming When Predicting Bubble Growth Rates Produced by Rectified Diffusion. *J. Acoust. Soc. Am.*, 84:1758–1764, 1988.

- Corrsin, S. and Lumley, J. On the Equation of Motion for a Particle in Turbulent Fluid. *Applied Scientific Research, Section A*, 6(2–3):114–116, 1956.
- Dandy, D. S. and Dwyer, H. A. A Sphere in Shear Flow at Finite Reynolds Number: Effect of Shear on Particle Lift, Drag, and Heat Transfer. *Journal of Fluid Mechanics*, 216:381–410, 1990.
- Darmana, D., Deen, N. G., and Kuipers, J. A. M. Parallelization of an Euler-Lagrange Model Using Mixed Domain Decomposition and a Mirror Domain Technique: Application to Dispersed Gas-Liquid Two-Phase Flow. *Journal of Computational Physics*, 220:216–248, 2006.
- Dular, M. and Coutier-Delgosha, O. Numerical Modelling of Cavitation Erosion. *International Journal for Numerical Methods in Fluids*, 61:1388–1410, February 2009.
- Dular, M. and Petkovšek, M. On the Mechanisms of Cavitation Erosion - Coupling High Speed Videos to Damage patterns. *Experimental Thermal and Fluid Science*, 68:359–370, 2015. ISSN 08941777. doi: 10.1016/j.expthermflusci.2015.06.001.
- Dular, M., Širok, B., and Stoffel, B. The Influence of the Gas Content of Water and the Flow Velocity on Cavitation Erosion Aggressiveness. *Journal of Mechanical Engineering*, 51(3): 132–145, 2005.
- Dular, M., Stoffel, B., and Širok, B. Development of a Cavitation Erosion Model. *Wear*, 261: 642–655, February 2006.
- Dular, M., Požar, T., Zevnik, J., and Petkovšek, R. High Speed Observation of Damage Created by a Collapse of a Single Cavitation Bubble. *Wear*, 2018. ISSN 0043-1648. doi: <https://doi.org/10.1016/j.wear.2018.11.004>.
- Dupont, P. *The dynamics of cavitation partial to the prediction of erosion in hydraulic turbo-machines*. PhD Thesis, EPFL, Lausanne, Switzerland, 1991.
- Eçã, L. and Hoekstra, M. A Procedure for the Estimation of the Numerical Uncertainty of CFD Calculations Based on Grid Refinement Studies. *Journal of Computational Physics*, 262:104–130, 2014.
- Eçã, L., Vaz, G., and Hoekstra, M. Code Verification of ReFRESKO with a Statistically Periodic Manufactured Solution. In *Proceedings of ASME 33rd International Conference on Ocean, Offshore and Arctic Engineering, OMAE2014*, 2014.
- Eçã, L., Klaij, C. M., Hoekstra, M., and Pereira, F. S. On Code Verification of RANS Solvers. *Journal of Computational Physics*, 310:418–439, 2016.
- el Moctar, O. and Schellin, T. E. Prediction of Rudder Cavitation Based on CFD and Full-Scale Observations. *Proc. Int. Conf. on Marine CFD, Royal Society of Naval Architects, Southampton*, 2008.
- Ferziger, J. H. and Perić, M. *Computational Methods for Fluid Dynamics*. Springer, 2002. ISBN 3-540-42074-6.

## Bibliography

- Field, J. E. The Physics of Liquid Impact, Shock Wave Interactions with Cavities, and the Implications to Shock Wave Lithotripsy. *Physics in Medicine and Biology*, 36(11):1475–1484, 1991.
- Fortes-Patella, R., Reboud, J.-L., and Briancon-Marjollet, L. A Phenomenological and Numerical Model for Scaling the Flow Aggressiveness in Cavitation Erosion. *EROCAV Workshop, Val de Reuil, France*, 2004.
- Franc, J. P. Partial Cavity Instabilities and Re-Entrant Jet. In *Proceedings of the 4th International Symposium on Cavitation, Pasadena, USA*, ed. by C. E. Brennen, R. E. A. Arndt, L. S. Ceccio, 2001.
- Franc, J.-P. and Michel, J.-M. *Fundamentals of Cavitation*. Kluwer Academic Publishers, 2005. ISBN 1-4020-2233-6.
- Franc, J.-P. and Riondet, M. Incubation Time and Cavitation Erosion Rate of Work-Hardening Materials. In *Proceedings of the 6th International Symposium on Cavitation, CAV2006, Wageningen, Netherlands*, 2006.
- Franc, J.-P., Riondet, M., Karimi, A., and Chahine, G. Impact Load Measurements in an Erosive Cavitating Flow. *Journal of Fluids Engineering*, 133(12), 2011.
- Franc, J.-P., Riondet, M., Karimi, A., and Chahine, G. Material and Velocity Effects on Cavitation Erosion Pitting. *Wear*, 274–275:248–259, 2012.
- Franc, J.-P., Chahine, G. L., and Karimi, A. *Advanced Experimental and Numerical Techniques for Cavitation Erosion Prediction*, chapter Pitting and Incubation Period. Springer, 2014. ISBN 978-94-017-8538-9.
- Ganesh, H., Mäkiharju, S. A., and Ceccio, S. L. Interaction of a Compressible Bubbly Flow with an Obstacle Placed Within a Shedding Partial Cavity. *Journal of Physics: Conference Series*, 656(1):2–6, 2015. ISSN 17426596. doi: 10.1088/1742-6596/656/1/012151.
- Ganesh, H., Mäkiharju, S. A., and Ceccio, S. L. Bubbly shock propagation as a mechanism for sheet-to-cloud transition of partial cavities. *Journal of Fluid Mechanics*, 802:37–78, 2016.
- Germanischer Lloyd. *Rules for Classification and Construction II, part 1: Materials and Welding*, chapter 5: Materials for Propeller Fabrication, section 1: Propellers Made of Cast Copper Alloys. 2009.
- Ghahramani, E., Arabnejad, M. H., and Bensow, R. E. Realizability Improvements to a Hybrid Mixture-Bubble Model for Simulation of Cavitating Flows. *Computers & Fluids*, 174:135–143, 2018. ISSN 00457930. doi: 10.1016/j.compfluid.2018.06.025.
- Gilmore, F. R. The Collapse and Growth of a Spherical Bubble in a Viscous Compressible Liquid. Technical Report 26-4, California Institute of Technology Hydrodynamics Laboratory, 1952.

- Godderidge, B., Tan, M., Turnock, S., and Earl, C. A Verification and Validation Study of the Application of Computational Fluid Dynamics to the Modelling of Lateral Sloshing. Technical Report 140, University of Southampton, Fluid Structure Interaction Research Group, 2006.
- Golf, R. Kavitationsuntersuchung am DTC Propeller. Bachelor's thesis, Universität Duisburg-Essen, Duisburg, Germany, 2018.
- Grekula, M. and Lindell, P. Cavitation Erosion Damage – Running the Risk of Costly Recurrent Repairs on Semi-Spade Rudders. *The Swedish Club Letter, Loss Prevention*, pages 6–7, 2007. ISSN 0954-4070. doi: 10.1177/0954407011416904.
- Groß, T. F. and Pelz, P. F. Diffusion-Driven Nucleation from Surface Nuclei in Hydrodynamic Cavitation. *Journal of Fluid Mechanics*, 830:138–164, 2017. ISSN 14697645. doi: 10.1017/jfm.2017.587.
- Haberman, W. L. and Morton, R. K. An Experimental Investigation of the Drag and Shape of Air Bubbles Rising in Various Liquids. Technical Report 802, The David W. Taylor Model Basin, Navy Department, 1953.
- Haller Knežević, K. *High-Velocity Impact of a Liquid Droplet on a Rigid Surface: The Effect of Liquid Compressibility*. PhD Thesis, Swiss Federal Institute of Technology Zurich, Zurich, Switzerland, October 2002.
- Hao, J., Zhang, M., and Huang, X. The Influence of Surface Roughness on Cloud Cavitation Flow around Hydrofoils. *Acta Mechanica Sinica*, 34(1):10–21, 2018. ISSN 16143116. doi: 10.1007/s10409-017-0689-0.
- Hasuike, N., Yamasaki, S., and Ando, J. Numerical study on cavitation erosion risk of marine propellers operating in wake flow. In *Proceedings of the 7th International Symposium on Cavitation, CAV2009, Ann Arbor, Michigan, USA, 2009*.
- Hattori, S. and Takinami, M. Comparison of Cavitation Erosion Rate with Liquid Impingement Erosion Rate. *Wear*, 269(3-4):310–316, 2010. ISSN 00431648. doi: 10.1016/j.wear.2010.04.020.
- Hattori, S., Takinami, M., and Otani, T. Comparison of Cavitation Erosion Rate with Liquid Impingement Erosion Rate. In *Proceedings of the 7th International Symposium on Cavitation, CAV2009, Ann Arbor, Michigan, USA, 2009*.
- Heinke, H.-J. Untersuchung von Schicht-, Blasen- und Wolkenkavitation und die damit verbundenen Erosionsprobleme – Teilvorhaben: Weiterentwicklung der Versuchsmethodik für Erosionsuntersuchungen. Technical Report 2730, Schiffbau-Versuchsanstalt Potsdam, 2001.
- Heinke, H.-J., Schulze, R., and Klose, R. Akustische Direktmessungen für die Erosionsprognose mit den Propellern P1225 und P1226. Technical Report 4219, Schiffbau-Versuchsanstalt Potsdam, 2013.

## Bibliography

- Heinz, S. Turbulent Supersonic Channel Flow: Direct Numerical Simulation and Modeling. *American Institute of Aeronautics and Astronautics Journal*, 44(12):3040–3050, 2006.
- Hsiao, C.-T., Chahine, G. L., and Liu, H.-L. Scaling Effect on Bubble Dynamics in a Tip Vortex Flow: Prediction of Cavitation Inception and Noise. Technical Report 98007-1, Dynaflo, Inc., 2000.
- Hsiao, C.-T., Chahine, G. L., and Liu, H.-L. Scaling Effect on Prediction of Cavitation Inception in a Line Vortex Flow. *Journal of Fluids Engineering*, 125:53–60, 2003.
- Hsiao, C.-T., Ma, J., and Chahine, G. L. Multi-Scale Two-Phase Flow Modeling of Sheet and Cloud Cavitation. In *30th Symposium on Naval Hydrodynamics, Hobart, Tasmania, Australia*, 2014.
- Hsiao, C.-T., Ma, J., and Chahine, G. L. Simulation of Sheet and tip vortex cavitation on a rotating propeller using a multiscale two-phase flow model. In *Proceedings of the 4th International Symposium on Marine Propulsors*, number JUNE, 2015a.
- Hsiao, C.-T., Ma, J., and Chahine, G. L. Simulation of sheet and tip vortex cavitation on a rotating propeller using a multiscale two-phase flow model. In *Proceedings of the 4th International Symposium on Marine Propulsors, Austin, Texas, USA*, 2015b.
- Issa, R. I. Solution of the Implicitly Discretised Fluid Flow Equations by Operator-Splitting. *Journal of Computational Physics*, 62:40–65, 1986.
- Isselin, J. C., Alloncle, A. P., and Autric, M. On Laser Induced Single Bubble Near a Solid Boundary: Contribution to the Understanding of Erosion Phenomena. *Journal of Applied Physics*, 84(10):5766–5771, 1998. ISSN 00218979. doi: 10.1063/1.368841.
- ITTC. Uncertainty Analysis in CFD Verification and Validation, Methodology and Procedures. Technical Report 7.5-03-01-01, International Towing Tank Conference, 2017.
- Jamaluddin, A. R., Ball, G. J., Turangan, C. K., and Leighton, T. G. The Collapse of Single Bubbles and Approximation of the Far-Field Acoustic Emissions for Cavitation Induced by Shock Wave Lithotripsy. *Journal of Fluid Mechanics*, 677:305–341, 2011. ISSN 00221120. doi: 10.1017/jfm.2011.85.
- Jasak, H. *Error Analysis and Estimation for the Finite Volume Method with Applications to Fluid Flows*. PhD Thesis, Imperial College, London, Great Britain, 1996.
- Jian, W., Petkovšek, M., Houlin, L., Širok, B., and Dular, M. Combined Numerical and Experimental Investigation of the Cavitation Erosion Process. *Journal of Fluids Engineering*, 137(5):051302, 2015. ISSN 0098-2202. doi: 10.1115/1.4029533.
- Johnson, V. E. and Hsieh, T. The Influence of the Trajectories of Gas Nuclei on Cavitation Inception. In *Proceedings of the Sixth Symposium on Naval Hydrodynamics (Office of Naval Research), Washington, DC, USA*, page 163, 1966.

- Joukowsky, N. Über den hydraulischen Stoss in Wasserleitungsröhren (On the hydraulic hammer in water supply pipes). *Mémoires de l'Académie Impériale des Sciences de St.-Pétersbourg (1900), Series 8, 9(5):1–71, 1898.*
- Keil, T., Pelz, P. F., Cordes, U., and Ludwig, G. Cloud Cavitation and Cavitation Erosion in Convergent Divergent Nozzle. In *Proceedings of the WIMRC 3rd International Cavitation Forum, 2011.*
- Keller, A. P., Rott, H. K., Stoffel, B., and Striedinger, R. Maßstabeffekte bei der Strömungskavitation. *Forschung im Ingenieurwesen, 65:48–57, 1999.*
- Keller, J. B. and Kolodner, I. I. Damping of Underwater Explosion Bubble Oscillations. *Journal of Applied Physics, 27(10):1152–1161, 1956.*
- Kennedy, J. E. High-Intensity Focused Ultrasound in the Treatment of Solid Tumours. *Nature Reviews Cancer, 5:321–327, 2005.*
- Kiefer, S. W. Sound Speed in Liquid-Gas Mixtures: Water-Air and Water-Steam. *Journal of Geophysical Research, 82:2895–2904, July 1977.*
- Kimura, K., Kawamura, T., Fujii, A., Taketani, T., and Huang, Z. Study on unsteady cavitating flow simulation around marine propeller using a rans cfd code. In *Proceedings of the 7th International Symposium on Cavitation, CAV2009, Ann Arbor, Michigan, USA, 2009.*
- Kjseldsen, M., Arndt, R. E. A., and Effertz, M. Spectral Characteristics of Sheet / Cloud Cavitation. *Journal of Fluids Engineering, 122:481–487, 2000.*
- Knapp, R. T., Daily, J. W., and Hammitt, F. G. *Cavitation.* McGraw-Hill, Inc., 1970.
- Koch, M., Lechner, C., Reuter, F., Köhler, K., Mettin, R., and Lauterborn, W. Numerical Modeling of Laser Generated Cavitation Bubbles with the Finite Volume and Volume of Fluid Method, Using OpenFOAM. *Computers & Fluids, 126:71–90, 2016.* ISSN 00457930. doi: 10.1016/j.compfluid.2015.11.008.
- Konno, A., Kato, H., Yamaguchi, H., and Maeda, M. Observation of Cavitation Bubble Collapse by High-Speed Video. In *Proceedings of The Fifth Asian Symposium on Visualization, pages 134–139, 1999.*
- Koopmann, L., Schwarz-Beutel, J., and Cura Hochbaum, A. Maßstabeffekte und Umwelteinflüsse bei der Vorhersage des Manövrierverhaltens seegehender Schiffe – Teilvorhaben: Verbesserung der Vorhersage des Manövrierverhaltens von Schiffen auf Basis von virtuellen gefesselten Versuchen. Technical report, Technische Universität Berlin, 2015.
- Koukouvini, P., Bergeles, G., and Gavaises, M. A New Methodology for Estimating Cavitation Erosion: Application on a High Speed Cavitation Test RIG. In *11th World Congress on Computational Mechanics (WCCM XI), Barcelona, Spain, 2014.*
- Kuiper, G. Cavitation in Ship Propulsion. [<https://ocw.tudelft.nl/courses/cavitation-ship-propellers/>], 2010.

## Bibliography

- Kunz, R. F., Boger, D. A., Stinebring, D. R., Chyczewski, T. S., Lindau, J. W., Gibeling, H. J., Venkateswaran, S., and Govindan, T. R. A Preconditioned Navier-Stokes Method for Two-Phase Flows with Application to Cavitation Prediction. *Computers & Fluids*, 29:849–875, 2000.
- Lantermann, U. *Simulation der Transport- und Dispositionsvorgänge von Nanopartikeln in der Gasphase mittels Partikel-Monte-Carlo- und Lattice-Boltzmann-Methoden*. PhD Thesis, University of Duisburg-Essen, Duisburg, Germany, 2006.
- Lauer, E., Hu, X. Y., Hickel, S., and Adams, N. A. Numerical Investigation of Collapsing Cavity Arrays. *Physics of Fluids*, 24(5), 2012a. ISSN 10706631. doi: 10.1063/1.4719142.
- Lauer, E., Hu, X. Y., Hickel, S., and Adams, N. A. Numerical Modelling and Investigation of Symmetric and Asymmetric Cavitation Bubble Dynamics. *Computers & Fluids*, 69:1–19, 2012b. ISSN 00457930. doi: 10.1016/j.compfluid.2012.07.020.
- Lauder, B. E. and Sharma, B. I. Application of the Energy Dissipation Model of Turbulence to the Calculation of Flow Near a Spinning Disc. *Letters in Heat and Mass Transfer*, 1(2): 131–138, 1974.
- Lauterborn, W. and Bolle, H. Experimental Investigations of Cavitation-Bubble Collapse in the Neighbourhood of a Solid Boundary. *Journal of Fluid Mechanics*, 72:391–399, 1975.
- Lauterborn, W. and Kurz, T. Physics of Bubble Oscillations. *Reports on Progress in Physics*, 73(10), 2010. ISSN 00344885. doi: 10.1088/0034-4885/73/10/106501.
- Lauterborn, W. and Vogel, A. *Bubble Dynamics and Shock Waves*, chapter Shock Wave Emission by Laser Generated Bubbles. Springer, 2013. ISBN 978-3-642-34296-7.
- Leclercq, C., Archer, A., Fortes-Patella, R., and Cerru, F. Numerical Cavitation Intensity on a Hydrofoil for 3D Homogeneous Unsteady Viscous Flows. *International Journal of Fluid Machinery and Systems*, 10(3):254–263, 2017.
- Li, Z. R. *Assessment of Cavitation Erosion with a Multiphase Reynolds-Averaged Navier-Stokes Method*. PhD Thesis, Delft University of Technology, Delft, Netherlands, June 2012.
- Lidtko, A. K. *Predicting Radiated Noise of Marine Propellers Using Acoustic Analogies and Hybrid Eulerian-Lagrangian Cavitation Models*. PhD Thesis, University of Southampton, Southampton, Great Britain, 2017.
- Lohrberg, H. *Messung und aktive Kontrolle der erosiven Aggressivität der Kavitation in Turbomaschinen*. PhD Thesis, Technical University of Darmstadt, Darmstadt, Germany, 2001.
- Louisnard, O. and González-García, J. *Ultrasound Technologies for Food and Bioprocessing*, chapter Acoustic Cavitation. Springer, 2011. ISBN 978-1-4419-7472-3.
- Lu, N.-X., Svennberg, U., Bark, G., and Bensow, R. E. Numerical simulations of the cavitating flow on a marine propeller. In *Proceedings of the 8th International Symposium on Cavitation, CAV2012, Singapore*, 2012.

- Lush, P. A. Impact of a Liquid Mass on a Perfectly Plastic Solid. *Journal of Fluid Mechanics*, 135:373–387, 1983.
- Ma, J., Hsiao, C.-T., and Chahine, G. L. Euler–Lagrange Simulations of Bubble Cloud Dynamics Near a Wall. *Journal of Fluids Engineering*, 137(4):041301, 2015a. ISSN 0098-2202. doi: 10.1115/1.4028853.
- Ma, J., Hsiao, C.-T., and Chahine, G. L. Euler–Lagrange Simulations of Bubble Cloud Dynamics Near a Wall. *Journal of Fluids Engineering*, 137(4):041301, 2015b. ISSN 0098-2202. doi: 10.1115/1.4028853.
- Ma, J., Hsiao, C.-T., and Chahine, G. L. Shared-Memory Parallelization for Two-Way Coupled Euler–Lagrange Modeling of Cavitating Bubbly Flows. *Journal of Fluids Engineering*, 137(12):121106, 2015c. ISSN 0098-2202. doi: 10.1115/1.4030919.
- Ma, J., Hsiao, C.-T., and Chahine, G. L. A Physics Based Multiscale Modeling of Cavitating Flows. *Computers & Fluids*, 145:68–84, 2017. ISSN 00457930. doi: 10.1016/j.compfluid.2016.12.010.
- Maisonhaute, E., Prado, C., White, P. C., and Compton, R. G. Surface Acoustic Cavitation Understood via Nanosecond Electrochemistry. Part III: Shear Stress in Ultrasonic Cleaning. *Ultrasonics Sonochemistry*, 9(6):297–303, 2002. ISSN 13504177. doi: 10.1016/S1350-4177(02)00089-5.
- Mäkiharju, S. A., Ganesh, H., and Ceccio, S. L. Effect of Non-Condensable Gas Injection on Cavitation Dynamics of Partial Cavities. *Journal of Physics: Conference Series*, 656(1), 2015. ISSN 17426596. doi: 10.1088/1742-6596/656/1/012161.
- Marschall, H. B., Morch, K. A., Keller, P. A., and Kjeldsen, M. Cavitation Inception by Almost Spherical Solid Particles in Water. In *Proceedings of the 4th International Symposium on Cavitation, Pasadena, USA, ed. by C. E. Brennen, R. E. A. Arndt, L. S. Ceccio*, 2001.
- Menter, F. R. Two-Equation Eddy-Viscosity Turbulence Models for Engineering Applications. *AIAA Journal*, 32(8):1598–1605, 1994.
- Merkle, C. L., Feng, J. Z., and Buelow, P. E. O. Computational Modeling of the Dynamics of Sheet Cavitation. In *Proceedings of the 3rd International Symposium on Cavitation, Grenoble, France*, 1998.
- Mettin, R., Akhatov, I., Parlitz, U., Ohl, C.-D., and Lauterborn, W. Bjerknes Forces Between Small Cavitation Bubbles in a Strong Acoustic Field. *Physical Review E*, 56(3):2924–2931, 1997.
- Mihatsch, M., Schmidt, S. J., Thalhamer, M., Adams, N. A., Skoda, R., and Iben, U. Collapse Detection in Compressible 3-D Cavitating Flows and Assessment of Erosion Criteria. *WIMRC 3rd International Cavitation Forum*, 2011.

## Bibliography

- Mihatsch, M., Schmidt, S. J., Thalhamer, M., and Adams, N. A. Quantitative Prediction of Erosion Aggressiveness through Numerical Simulation of 3-D Unsteady Cavitating Flows. In *Proceedings of the 8th International Symposium on Cavitation, CAV2012, Singapore*, 2012.
- Mihatsch, M. S. *Numerical Prediction of Erosion and Degassing Effects in Cavitating Flows*. PhD Thesis, Technische Universität München, Germany, 2017.
- Mihatsch, M. S., Schmidt, S. J., and Adams, N. A. Cavitation Erosion Prediction Based on Analysis of Flow Dynamics and Impact Load Spectra. *Physics of Fluids*, 27(103302), 2015.
- Miller, W. and Wilczyński, L. Model - Full Scale Correlations of the Cavitation Erosion of Ship Propeller – a Container Vessel Case Study. In *Proceedings of the 6th International Symposium on Cavitation, CAV2006, Wageningen, Netherlands*, 2006.
- Mottyll, S. *Numerical 3D Flow Simulation of Cavitation at Ultrasonic Horns and Assessment of Flow Aggressiveness, Erosion Sensitive Wall Zones and Incubation Time*. PhD Thesis, Ruhr-Universität Bochum, Germany, 2017.
- Mouvanal, S., Chatterjee, D., Bakshi, S., Burkhardt, A., and Mohr, V. Numerical Prediction of Potential Cavitation Erosion in Fuel Injectors. *International Journal of Multiphase Flow*, 104:113–124, 2018.
- Neppiras, E. A. *Acoustic Cavitation*. North-Holland Publishing Company, Amsterdam, 1980.
- Neppiras, E. A. and Noltingk, B. E. Cavitation Produced by Ultrasonics: Theoretical Conditions for the Onset of Cavitation. *Proc. Phys. Soc., London*, 64B:1032–1038, 1951.
- Noack, J. and Vogel, A. Single-Shot Spatially Resolved Characterization of Laser-Induced Shock Waves in Water. *Applied Optics*, 37(19):4092–4099, 1998.
- Nohmi, M., Iga, Y., and Ikohagi, T. Numerical prediction method of cavitation erosion. In *Proceedings of FEDSM 2008, Jacksonville, Florida, USA*, 2008.
- Oberhagemann, J. *On Prediction of Wave-Induced Loads and Vibrations of Ship Structures with Finite Volume Fluid Dynamics Methods*. PhD Thesis, Universität Duisburg-Essen, Duisburg, Germany, 2017.
- Oh, J., Lee, H. B., Shin, K., Lee, C., Rhee, S. H., Suh, J. C., and Kim, H. Rudder Gap Flow Control for Cavitation Suppression. In *Proceedings of the 7th International Symposium on Cavitation, CAV2009, Ann Arbor, Michigan, USA*, 2009.
- Ohl, C.-D., Kurz, T., Geisler, R., Lindau, O., and Lauterborn, W. Bubble Dynamics, Shock Waves and Sonoluminescence. *Philosophical Transactions of The Royal Society A*, 357: 269–294, 1999.
- Ohl, C.-D., Tjink, A., and Prosperetti, A. The Added Mass of an Expanding Bubble. *Journal of Fluid Mechanics*, 482:271–290, 2003.
- OpenCFD Ltd (ESI Group). OpenFOAM. [<http://www.openfoam.com/>], 2018.

- Osterman, A., Dular, M., and Širok, B. Numerical Simulation of a Near-Wall Bubble Collapse in an Ultrasonic Field. *Journal of Fluid Science and Technology*, 4(1):210–221, 2009. ISSN 1880-5558. doi: 10.1299/jfst.4.210.
- Oweis, G. F., van der Hout, I. E., Iyer, C., Tryggvason, G., and Ceccio, S. L. Capture and Inception of Bubbles Near Line Vortices. *Physics of Fluids*, 17, 2005.
- Pelz, P. F., Keil, T., and Ludwig, G. *Advanced Experimental and Numerical Techniques for Cavitation Erosion Prediction*, chapter On the Kinematics of Sheet and Cloud Cavitation and Related Erosion. Springer, 2014. ISBN 978-94-017-8538-9.
- Pelz, P. F., Keil, T., and Groß, T. F. The transition from sheet to cloud cavitation. *Journal of Fluid Mechanics*, 817:439–454, 2017.
- Pereira, F. M. S. *Towards Predictive Scale-Resolving Simulations of Turbulent External Flows*. PhD Thesis, Universidade de Lisboa, Portugal, 2018.
- Peters, A. and el Moctar, O. Numerical Prediction of Cavitation-Induced Erosion Using a Multi-Scale Euler-Lagrange Method. *revised manuscript submitted to Journal of Fluid Mechanics*, 2019.
- Peters, A., Lantermann, U., and el Moctar, O. Numerical Modelling and Prediction of Erosion Induced by Hydrodynamic Cavitation. *Journal of Physics, conference series*, 656(1), 2015a.
- Peters, A., Lantermann, U., Sagar, H., Lange, S., and el Moctar, O. Entwicklung von numerischen und experimentellen Methoden zur Vorhersage von kavitationsbedingter Erosion an Schiffsanhängen – KonKav III: Schlussbericht zum Teilvorhaben Entwicklung von numerischen Methoden zur Berechnung von kavitationsbedingter Erosion – NumEro. Technical report, Universität Duisburg-Essen, Institut für Schiffstechnik, Meerestechnik und Transportsysteme, 2015b.
- Peters, A., Sagar, H., Lantermann, U., and el Moctar, O. Numerical Modelling and Prediction of Cavitation Erosion. *Wear*, 338–339:189–201, 2015c.
- Peters, A., Lantermann, U., and el Moctar, O. Numerical Prediction of Cavitation Erosion on a Ship Propeller in Model- and Full-Scale. *Wear*, 408–409:1–12, 2018a.
- Peters, A., Lantermann, U., and el Moctar, O. Simulation of an Internal Nozzle Flow Using an Euler-Lagrange Method. In *Proceedings of the 10 International Symposium on Cavitation, CAV2018, Baltimore, Maryland, USA*, 2018b.
- Petkovšek, M. and Dular, M. Simultaneous Observation of Cavitation Structures and Cavitation Erosion. *Wear*, 300:55–64, 2013.
- Philipp, A. and Lauterborn, W. Cavitation Erosion by Single Laser-Produced Bubbles. *Journal of Fluid Mechanics*, 361:75–116, 1998.
- Plesset, M. S. The Dynamics of Cavitation Bubbles. *Journal of Applied Mechanics*, 16: 277–282, 1949.

## Bibliography

- Plesset, M. S. and Chapman, R. B. Collapse of an Initially Spherical Vapor Cavity in the Neighborhood of a Solid Boundary. *Journal of Fluid Mechanics*, 47(2):283–290, 1971.
- Plesset, M. S. and Zwick, S. A. The Growth of Vapor Bubbles in Superheated Liquids. *Journal of Applied Physics*, 25(4):493–500, 1954.
- Pöhl, F., Mottyll, S., Skoda, R., and Huth, S. Evaluation of Cavitation-Induced Pressure Loads Applied to Material Surfaces by Finite-Element-Assisted Pit Analysis and Numerical Investigation of the Elasto-Plastic Deformation of Metallic Materials. *Wear*, 330-331:1–11, 2015. ISSN 00431648. doi: 10.1016/j.wear.2014.12.048.
- Ponkratov, D. DES Prediction of Cavitation Erosion and its Validation for a Ship Scale Propeller. *Journal of Physics, conference series*, 656(1), 2015.
- Ponkratov, D. and Caldas, A. Prediction of cavitation erosion by detached eddy simulation (des) and its validation against model and ship scale results. In *Proceedings of the 4th International Symposium on Marine Propulsors, Austin, Texas, USA*, 2015.
- Poritsky, H. The Collapse or Growth of a Spherical Bubble or Cavity in a Viscous Fluid. In *Proc. First Nat. Cong. in Appl. Math.*, pages 813–821, 1952.
- Prince, M. J. and Blanch, H. W. Bubble Coalescence and Break-Up in Air-Sparged Bubble Columns. *AIChE Journal*, 36(10):1485–1499, 1990.
- Rao, P. V. and Buckley, D. H. Cavitation Erosion Size Scale Effects. *Wear*, 96:239–253, 1984.
- Rayleigh, J. W., Lord (Strutt). On the Pressure developed in a liquid during the collapse of a spherical cavity. *Philosophical Magazine and Journal of Science*, 34:94–98, 1917.
- Reboud, J.-L., Stutz, B., and Coutier-Delgosha, O. Two phase flow structure of cavitation: Experiment and modeling of unsteady effects. In *Proceedings of the 3rd International Symposium on Cavitation, Grenoble, France*, 1998.
- Reemts, J. and Johannsen, C. KonKav III – Entwicklung von numerischen und experimentellen Methoden zur Vorhersage von kavitationsbedingter Erosion an Schiffsanhängen – Vorhaben: Verbesserte Erosionsprognosen aus dem Modellversuch. Technical Report 1687, Hamburgische Schiffbau-Versuchsanstalt GmbH, 2015.
- Reuter, F. and Mettin, R. Mechanisms of Single Bubble Cleaning. *Ultrasonics Sonochemistry*, 29:550–562, 2016. ISSN 1350-4177. doi: <https://doi.org/10.1016/j.ultsonch.2015.06.017>.
- Reuter, F., Cairós, C., and Mettin, R. Vortex Dynamics of Collapsing Bubbles: Impact on the Boundary Layer Measured by Chronoamperometry. *Ultrasonics Sonochemistry*, 33: 170–181, 2016. ISSN 1350-4177. doi: <https://doi.org/10.1016/j.ultsonch.2016.04.023>.
- Reuter, F., Lauterborn, S., Mettin, R., and Lauterborn, W. Membrane Cleaning with Ultrasonically Driven Bubbles. *Ultrasonics Sonochemistry*, 37:542–560, 2017. ISSN 1350-4177. doi: <https://doi.org/10.1016/j.ultsonch.2016.12.012>.

- Reuter, F., Lesnik, S., Ayaz-Bustami, K., Brenner, G., and Mettin, R. Bubble Size Measurements in Different Acoustic Cavitation Structures: Filaments, Clusters, and the Acoustically Cavitated Jet. *Ultrasonics Sonochemistry*, 2018. doi: 10.1016/j.ultsonch.2018.05.003.
- Rhie, C. M. and Chow, W. L. Numerical Study of the Turbulent Flow Past an Airfoil with Trailing Edge Separation. *AIAA Journal*, 21(11):1525–1532, 1983.
- Saffman, P. G. The Lift on a Small Sphere in a Slow Shear Flow. *Journal of Fluid Mechanics*, 22(2):385–400, 1965.
- Sagar, H. J. *Numerical and Experimental Investigation of Laser-Induced Cavitation Bubbles and Induced Damage*. PhD Thesis, Universität Duisburg-Essen, Duisburg, Germany, 2018.
- Sagar, H. J., Hanke, S., Underberg, M., Feng, C., el Moctar, O., and Kaiser, S. A. Experimental and Numerical Investigation of Damage on an Aluminum Surface by Single-Bubble Cavitation. *Materials Performance and Characterization*, 7(5):985–1003, 2018.
- Sakamoto, N. and Kamiirisa, H. Estimations of propeller cavitation noise by cfd. In *Japanese Society of Naval Architects and Ocean Engineers Annual Autumn Meeting, Tokyo, Japan*, volume 21, 2015.
- Sauer, J. *Instationär kavitierende Strömungen – Ein neues Modell, basierend auf Front Capturing (VoF) und Blasendynamik*. PhD Thesis, Universität Karlsruhe, Germany, 2000.
- Sauer, J. and Schnerr, G. H. Unsteady Cavitating Flow - a New Cavitation Model Based on Modified Front Capturing Method and Bubble Dynamics. In *Proceedings of FEDSM, 4th Fluids Engineering Summer Conference*, 2000.
- Schenke, S., Melissaris, T., and van Terwisga, T. J. C. On the Relevance of Kinematics for Cavitation Implosion Loads. *Physics of Fluids*, 31, 2019.
- Schlichting, H. and Gersten, K. *Boundary-Layer Theory*. Springer, 2017. ISBN 978-3-662-52919-5.
- Shal'nev, K. K., Varga, I. I., and Sebestyen, D. A Discussion on Deformation of Solids by the Impact of Liquids, and its Relation to Rain Damage in Aircraft and Missiles, to Blade Erosion in Steam Turbines, and to Cavitation Erosion – Investigation of the Scale Effects of Cavitation Erosion. *Philosophical Transactions of the Royal Society of London. Series A, Mathematical and Physical Sciences*, 260(1110):256–266, 1966.
- Shams, E., Finn, J., and Apte, S. V. A Numerical Scheme for Euler-Lagrange Simulation of Bubbly Flows in Complex Systems. *International Journal for Numerical Methods in Fluids*, 67(12):1865–1898, 2011. ISSN 02712091. doi: 10.1002/flid.2452.
- Singhal, A. K., Athavale, M. M., Li, H., and Jiang, Y. Mathematical Basis and Validation of the Full Cavitation Model. *Journal of Fluids Engineering*, 124:617–624, September 2002.
- Sommerfeld, M., Bourloutski, E., and Bröder, D. Euler/Lagrange Calculations of Bubbly Flows with Consideration of Bubble Coalescence. *The Canadian Journal of Chemical Engineering*, 81:508–518, 2008. ISSN 00084034. doi: 10.1002/cjce.5450810324.

## Bibliography

- Soyama, H., Sekine, Y., and Saito, K. Evaluation of the Enhanced Cavitation Impact Energy Using a PVDF Transducer with an Acrylic Resin Backing. *Measurement*, 44(7):1279–1283, 2011.
- Sridhar, G. and Katz, J. Effect of Entrained Bubbles on the Structure of Vortex Rings. *Journal of Fluid Mechanics*, 397:171–202, 1999.
- Steller, J. and Kaczmarzyk, P. Phenomenological Models of Cavitation Erosion Progress. *International Cavitation Erosion Test Seminar*, June 2000.
- Supponen, O., Obreschkow, D., Tinguely, M., Kobel, P., Dorsaz, N., and Farhat, M. Scaling Laws for Jets of Single Cavitation Bubbles. *Journal of Fluid Mechanics*, 802:263–293, 2016.
- Supponen, O., Obreschkow, D., Kobel, P., Tinguely, M., Dorsaz, N., and Farhat, M. Shock Waves from Nonspherical Cavitation Bubbles. *Physical Review Fluids*, 2(9):1–31, 2017. ISSN 2469990X. doi: 10.1103/PhysRevFluids.2.093601.
- Tait, P. G. Report on some of the physical properties of fresh water and sea water. *Rept. Sci. Results Voy. H.M.S. Challenger Years 1873-76: Phys. Chem.*, 1889.
- Tezel, A. and Mitragotri, S. Interactions of Inertial Cavitation Bubbles with Stratum Corneum Lipid Bilayers during Low-Frequency Sonophoresis. *Biophysical Journal*, 85(6):3502–3512, 2003. ISSN 00063495. doi: 10.1016/S0006-3495(03)74770-5.
- The OpenFOAM Foundation Ltd. OpenFOAM. [<http://www.openfoam.org/>], 2018.
- Tomita, Y. and Shima, A. On the Behavior of a Spherical Bubble and the Impulse Pressure in a Viscous Compressible Liquid. *Bulletin of the JSME*, 20(149):1453–1460, 1977.
- Truckenbrodt, E. *Fluidmechanik Band 1 – Grundlagen und elementare Strömungsvorgänge dichtebeständiger Fluide*. Springer, 2008. ISBN 978-3-540-79018-1.
- Ubbink, O. *Numerical Prediction of Two Fluid Systems with Sharp Interfaces*. PhD Thesis, Imperial College, London, Great Britain, 1997.
- Ukon, Y., Fujisawa, J., Kawanami, Y., Sakoda, M., and Yamasaki, S. Prevention of Root Erosion for High-Speed Ship Propellers. In *Proceedings of the 6th International Symposium on Cavitation, CAV2006, Wageningen, Netherlands*, 2006.
- Usta, O., Aktas, B., Maasch, M., Turan, O., Atlar, M., and Korkut, E. A study on the numerical prediction of cavitation erosion for propellers. In *Proceedings of the 5th International Symposium on Marine Propulsors, Espoo, Finland*, 2017.
- Vallier, A. *Simulations of Cavitation – From the Large Vapour Structure to the Small Bubble Dynamics*. PhD Thesis, Lund University, Lund, Sweden, 2013.
- van Terwisga, T. J. C., Fitzsimmons, P. A., Li, Z., and Foeth, E. J. Cavitation Erosion – A Review of Physical Mechanisms and Erosion Risk Models. *Cav2009*, (41):1–13, 2009.

- Vaz, G., Hally, D., Huuva, T., Bulten, N., Muller, P., Becchi, P., Herrer, J. L. R., Whitworth, S., Macé, R., and Korsström, A. Cavitating flow calculations for the e779a propeller in open water and behind conditions: Code comparison and solution validation. In *Proceedings of the 4th International Symposium on Marine Propulsors, smp'15, Austin, Texas, USA, 2015*.
- Vogel, A. and Lauterborn, W. Acoustic Transient Generation by Laser-Produced Cavitation Bubbles Near Solid Boundaries. *The Journal of the Acoustical Society of America*, 84(2): 719—731, 1988.
- Vogel, A., Busch, S., and Parlitz, U. Shock Wave Emission and Cavitation Bubble Generation by Picosecond and Nanosecond Optical Breakdown in Water. *The Journal of the Acoustical Society of America*, 100(1):148–165, 1996. ISSN 0001-4966. doi: 10.1121/1.415878.
- Waclawczyk, T. and Koronowicz, T. Comparison of CICSAM and HRIC High-Resolution Schemes for Interface Capturing. *Journal of Theoretical and Applied Mechanics*, 46(2): 325–345, 2008.
- Wang, Y. C. and Brennen, C. E. Numerical Computation of Shock Waves in a Spherical Cloud of Cavitation Bubbles. *Journal of Fluids Engineering*, 121(4):872–880, 1999.
- Weller, H. G. Pressure-Velocity Solution Algorithms for Transient Flows. Technical report, OpenCFD, 2005.
- Weller, H. G. Bounded Explicit and Implicit Second-Order Schemes for Scalar Transport. Technical report, OpenCFD, 2006.
- Weller, H. G. A New Approach to VOF-based Interface Capturing Methods for Incompressible and Compressible Flow. Technical report, OpenCFD, 2008.
- Wilcox, D. C. Re-Assessment of the Scale-Determining Equation for Advanced Turbulence Models. *AIAA Journal*, 26(11):1299–1310, 1988.
- Yakubov, S., Cankurt, B., Maquil, T., Schiller, P., Abdel-Maksoud, M., and Rung, T. Euler-Euler and Euler-Lagrange Approaches To Cavitation Modelling in Marine Applications. *International Conference on Computational Methods in Marine Engineering, MARINE*, pages 544–555, 2011.
- Yakubov, S., Cankurt, B., Abdel-Maksoud, M., and Rung, T. Hybrid MPI/OpenMP parallelization of an Euler-Lagrange approach to cavitation modelling. *Computers & Fluids*, 80(1):365–371, 2013. ISSN 00457930. doi: 10.1016/j.compfluid.2012.01.020.
- Yasui, K., Iida, Y., Tuziuti, T., Kozuka, T., and Towata, A. Strongly Interacting Bubbles Under an Ultrasonic Horn. *Physical Review E*, 77(016609):1–10, 2008. doi: 10.1103/PhysRevE.77.016609.
- Zalesak, S. T. Fully Multidimensional Flux-Corrected Transport Algorithms For Fluids. *Journal of Computational Physics*, 31(3):335–362, 1979.

## *Bibliography*

- Žnidarčič, A., Mettin, R., Cairós, C., and Dular, M. Attached Cavitation at a Small Diameter Ultrasonic Horn Tip. *Physics of Fluids*, 26(2):1–17, 2014. ISSN 10897666. doi: 10.1063/1.4866270.
- Zoetewij, M. L., van der Donck, J., and Versluis, R. Particle removal in linear shear flow: Model prediction and experimental validation. *Journal of Adhesion Science and Technology*, 23(6):899–911, 2009. doi: 10.1163/156856109X411247.
- Zwart, P. J., Gerber, A. G., and Belamri, T. A Two-Phase Flow Model for Predicting Cavitation Dynamics. In *Proceedings of the International Conference on Multiphase Flow, ICMF 2004, Yokohama, Japan*, number 152, 2004.

# DuEPublico

Duisburg-Essen Publications online

UNIVERSITÄT  
DUISBURG  
ESSEN

*Offen im Denken*

ub | universitäts  
bibliothek

Diese Dissertation wird über DuEPublico, dem Dokumenten- und Publikationsserver der Universität Duisburg-Essen, zur Verfügung gestellt und liegt auch als Print-Version vor.

**DOI:** 10.17185/duepublico/71156

**URN:** urn:nbn:de:hbz:464-20200109-140841-4

Alle Rechte vorbehalten.